WTAP and YTHDC1: non-redundant regulators of adult brain functioning

Dissertation zum Erwerb des Doctor of Philosophy (Ph.D.) an der
Medizinischen Fakultät der Ludwig-Maximilians-Universität München

Fabian Stamp

2022

Mit Genehmigung der Medizinischen Fakultät der

Ludwig-Maximilians-Universität München

First supervisor: *Prof. Dr. Alon Chen*

Second supervisor*:* *Prof. Dr. Dr. med. Elisabeth Binder*

Dean: Prof. Dr. med. Thomas Gudermann

Datum der Einreichung:

03.09.2021

Datum der Verteidigung:

10.03.2022

ORCiD: 0000-0003-2928-7386

MAX-PLANCK-GESELLSCHAFT

IMPRS
Translational Psychiatry

LMU
LUDWIG-
MAXIMILIANS-
UNIVERSITÄT
MÜNCHEN

LUDWIG-
MAXIMILIANS-
UNIVERSITÄT
MÜNCHEN

Dean's Office
Medical Faculty

MMRS
MUNICH MEDICAL RESEARCH SCHOOL

Affidavit

Stamp, Fabian
Surname, first name

Max Planck Institut für Psychiatrie, Kraepelinstraße 2-10
Street

80804, München
Zip code, town

Deutschland
Country

I hereby declare, that the submitted thesis entitled

WTAP and YTHDC1: non-redundant regulators of adult brain functioning

is my own work. I have only used the sources indicated and have not made unauthorised use of services of a third party. Where the work of others has been quoted or reproduced, the source is always given.

I further declare that the dissertation presented here has not been submitted in the same or similar form to any other institution for the purpose of obtaining an academic degree.

München, 04.05.2022
Place, date

Fabian Stamp
Signature doctoral candidate

LMU

LUDWIG-
MAXIMILIANS-
UNIVERSITÄT
MÜNCHEN

Dean’s Office
Medical Faculty

MMRS
MUNICH MEDICAL RESEARCH SCHOOL

Confirmation of congruency between printed and electronic version of the doctoral thesis

Stamp, Fabian
Surname, first name

Max Planck Institut für Psychiatrie, Kraepelinstraße 2-10
Street

80804, München
Zip code, town

Deutschland
Country

I hereby declare that the electronic version of the submitted thesis, entitled

WTAP and YTHDC1: non-redundant regulators of adult brain functioning

is congruent with the printed version both in content and format.

München 04.05.2022
Place, date

Fabian Stamp
Signature doctoral candidate

“Je suis de ceux qui pensent que la Science a une grande beauté.”

“I am among those who think that science has great beauty.”

Marie Curie, 1933

I. Abstract

Advances in the study of covalent RNA modifications have revealed an essential role for N^6-methyladenosine (m^6A) in regulating RNA metabolism. It has been shown that m^6A is involved in shaping developmental programs and various aspects of cellular functioning. Research on the role of m^6A regulation in the brain suggests that it is important for tuning neuronal plasticity and behavior. However, investigations in the mammalian brain have only focused on a few crucial regulators, leaving the contribution of the m^6A regulatory protein WTAP and the m^6A 'reader' YTHDC1 unknown. The research presented in this thesis shows that WTAP and YTHDC1 are non-redundant and important regulators of adult brain functions.

The postnatal deletion of WTAP in Camk2aCre expressing projection neurons reveals that WTAP is involved in regulating protein abundance, metabolic state and brain anatomy. WTAP deficient animals show profound changes in protein expression and circulating metabolites as assessed by liquid chromatography-mass spectrometry (LC-MS), indicating a switch in the metabolic state with early glycolysis products being upregulated, and nicotinamide adenine dinucleotide (NAD^+) being downregulated across brain regions. The observed molecular changes are associated with striking differences in the circadian activity patterns of knockout (KO) animals, aberrant behavior in classical anxiety tests and are accompanied by volumetric changes in the thalamus and auditory cortex, as determined by magnetic resonance imaging (MRI). Complementing these results, the tamoxifen dependent conditional KO in NexCreERT2 positive cells of the dorsal hippocampus, results in large scale changes in gene expression and splicing. Surprisingly, NexCreERT2 WTAP KO animals do not show a learning impairment in a fear conditioning paradigm but exhibit a significantly increased long-term potentiation (LTP).

The comparative study of YTHDC1 using a Camk2aCre expressing mouse line demonstrates the non-redundancy with WTAP. YTHDC1 deficient animals show an overall reduced life expectancy and breeding impairments. KOs exhibit aberrant behaviors across various classical behavior tests measuring anxiety and learning. Structural MRI scans reveal extensive changes in gray matter volume across the cortex and hippocampus. Functionally, KO cells in the medial prefrontal cortex (mPFC) are less sensitive to stimulation as revealed by single cell patching. An LC-MS screening of protein abundance showed large scale region-specific changes in KO animals. Finally, NexCreERT2 KO animals exhibit differential gene expression and splicing.

Overall, the presented results demonstrate that WTAP and YTHDC1 are non-redundant regulators of adult brain functioning. Removing either protein results in specific and far-reaching consequences for gene expression, protein abundance, brain anatomy and behavior. The observation that the deletion of WTAP leads to increased LTP and no learning impairment complements studies showing that disturbances of m^6A regulation are mostly associated with reduced LTP and learning deficits. The fact that the postnatal deletion of YTHDC1 in Camk2aCre expressing neurons affects life expectancy suggests that YTHDC1 might be involved in METTL3 independent regulatory processes. Together, these findings make a substantial contribution to understanding the role of the m^6A regulatory proteins WTAP and YTHDC1 in the mammalian brain.

Keywords: *N^6-Methyladenosine, m^6A, WTAP, YTHDC1, epitranscriptome, epitranscriptomic regulation in the adult brain, neuron, behavior, transcriptomics, proteomics, metabolomics, learning and memory*

II. Zusammenfassung

Fortschritte in der Erforschung kovalenter RNA-Modifikationen haben gezeigt, dass N^6-methyladenosin (m^6A) eine wichtige Rolle in der Regulierung des RNA-Stoffwechsels spielt. Dabei ist m^6A unter anderem für die Verarbeitung, den Transport und den Abbau von Boten-RNA (mRNA) wichtig. Forschungsergebnisse zur Rolle der m^6A-Regulation im Gehirn legen nahe, dass m^6A für die Regulierung neuronaler Plastizität und dem davon abhängigen Lernen wichtig ist. Dabei haben sich die bisherigen Untersuchungen im Gehirn von Mäusen auf einige wenige entscheidende Proteine konzentriert, die zur m^6A-bedingten Regulation beitragen. Die Rolle des m^6A-regulierenden Proteins WTAP und des m^6A Leseproteins YTHDC1 sind bisher unerforscht. Deswegen, war es das Ziel der vorliegenden Dissertation, einen wesentlichen Beitrag zu unserem Verständnis der Funktion von WTAP und YTHDC1 im adulten Gehirn zu leisten. Die hier präsentierten Ergebnisse demonstrieren, dass WTAP und YTHDC1 nicht redundante Regulatoren der Gehirnfunktionen im Erwachsenenalter sind.

Die massenspektrometrische Untersuchung (LC-MS) des medialen präfrontalen Cortex (mPFC) sowie des dorsalen und ventralen Hippocampus (dHPC, vHPC), von Tieren mit einer postnatalen Deletion von WTAP in Camk2aCre-exprimierenden Nervenzellen zeigt, dass WTAP an der Einstellung der Proteinkonzentration und der Regulation des Energiestoffwechsels beteiligt ist. Die beobachteten molekularen Veränderungen sind dabei mit markanten Unterschieden in der zirkadianen Aktivität von Knockout (KO) Tieren verbunden, sowie mit Verhaltensveränderungen in klassischen Angstverhaltenstests. Des Weiteren, wurden mithilfe von Magnetresonanztomographie (MRT) volumetrische Veränderungen im Thalamus und im auditorischen Cortex der KO Tiere identifiziert. Ergänzend zu diesen Ergebnissen, führt der tamoxifen-induzierte KO in NexCreERT2 exprimierenden Nervenzellen des dHPC zu weitreichenden Veränderungen in der Genexpression und dem alternativen Spleißen. Überraschenderweise zeigen NexCreERT2 WTAP KO Tiere dabei keine Einschränkungen beim Lernen, aber eine signifikant erhöhte Langzeitpotenzierung (LTP) im dHPC.

Der Vergleich mit dem Camk2aCre induzierten KO von YTHDC1 zeigt, dass WTAP und YTHDC1 nicht redundant sind. YTHDC1 KO Tiere haben eine reduzierte Lebenserwartung und zeigen Zuchtbeeinträchtigungen. Die Charakterisierung der YTHDC1 KO Tiere mit verschiedenen klassischen Verhaltenstests deutet auf weitreichende Verhaltensstörungen hin. Die strukturelle Untersuchung des Gehirns mithilfe von MRT offenbart umfangreiche Veränderungen des Volumens der grauen Substanz im Cortex und dHPC. Des Weiteren zeigen elektrophysiologische Messungen, dass Nervenzellen durch den Verlust von YTHDC1 weniger erregbar geworden sind. Die Untersuchung von Proteinen und Stoffwechselprodukten mithilfe von LC-MS deutet darauf hin, dass der Verlust von YTHDC1 zu umfassenden und regional spezifischen Veränderungen im Gehirn führt. Zusätzlich, zeigt die Charakterisierung der Genexpression im dHPC von NexCreERT2 KO-Tiere, dass YTHDC1 für die Regulation der Genexpression und des alternativen Spleißens erforderlich ist.

Zusammen deuten die hier präsentierten Ergebnisse darauf hin, dass WTAP und YTHDC1 nicht-redundante Regulatoren im erwachsenen Gehirn sind. Die Entfernung beider Proteine hat spezifische und weitreichende Konsequenzen für die Genexpression, die Proteinkomposition, den Stoffwechsel, die Gehirnanatomie und das Verhalten. Die Beobachtung, dass der Verlust von WTAP zu einer erhöhten LTP und keiner Lernbeeinträchtigung führt, ergänzt Studien, die zeigen, dass Störungen der m^6A-Regulation meist mit einem reduziertem LTP und Lerndefiziten einhergehen. Die Tatsache, dass die postnatale Deletion von YTHDC1 die Lebenserwartung verringert, deutet darauf hin, dass YTHDC1 an METTL3-unabhängigen Regulationsprozessen beteiligt sein könnte. Die in dieser Dissertation vorgetragenen Ergebnisse tragen wesentlich zu unserem Verständnis der Funktion der m^6A-regulatorischen Proteine WTAP und YTHDC1 im Gehirn von Säugetieren bei.

Stichwörter: *N^6-Methyladenosin, m^6A, WTAP, YTHDC1, Epitranskriptom, epitranskriptomische Regulation im adulten Gehirn, Nervenzelle, Verhalten, Transkriptomik, Proteomik, Metabolom, Lernen und Gedächtnis*

III. Acknowledgements

During my doctoral training at the Max Planck Institute of Psychiatry, I had the privilege to work with a group of outstanding researchers and a highly skilled technical staff for which I am extremely grateful. I would especially like to thank my supervisors Prof. Dr. Alon Chen and Prof. Dr. Dr. med. Elisabeth Binder for their guidance and mentorship throughout my PhD. The freedom and independence you gave me allowed me to grow as a researcher and will be one of the most valuable experiences I will take with me.

I would like to thank my thesis advisory committee members: Prof. Dr. Alon Chen, Prof. Dr. Dr. med. Elisabeth Binder, Prof. Dr. Dr. med. univ. Susanne Lucae, Prof. Dr. Jean-Yves Roignant and Dr. Alec Dick for advising me on how to shape my project. I am particularly grateful for the support and advice that I received from Dr. Alec Dick who introduced me to mRNA sequencing.

I am thankful for the support of my research assistant Laura Pohlenz, who supported me with genotyping, tissue processing, microscopy and qPCR. Laura, it has been a real pleasure to work with you!

I would like to express my deep gratitude to the members of the technical staff: to Carola Eggert for teaching me primary cell culture, cloning and ISH; Andrea Parl, Andrea Ressle, Maik Koedel, Susann Sauer, Daniela Harbich, and Bianca Schmid for their continuous support with countless routine work; Nicole Krombholz and Barbara Steigenberger from the LC-MS core facility at the MPI of Neurobiology for their assistance with the proteomic screening; Eviatar Weizman at the INCPM (Weizmann Institute of Science) for his bioinformatic support; Stefanie Unkmeir und Sabrina Bauer for their help with genotyping and mouse colony management; Maria Holzapfel for producing viruses for me that unfortunately did not make it into the final manuscript; the animal caretakers including Albin Varga, Sabine Schatzhuber, Anja Amman, Angelina Rusin, Ludwig Merkl, Johannes Drews, Anton Grüsser, Sandra Deininger and Tanja Hagl for their continued support, reliability and engagement for animal welfare.

I would like to thank Dr. Jan Deussing for providing me with advice on mouse husbandry and the access to a plethora of mouse lines. I am also very grateful to Dr. Rosa Eva Hüttl for her mentorship and help with experiments that were not included in this thesis.

I would like to thank my collaborators for their contribution to this project. It has been a pleasure to work with each one of you. I am grateful to Daniel Heinz for his suggestions and contributions to my projects. Specifically, the membranome purification and the MRI screening; Lea Bartmann for her support with the MRI scans; Tibor Stark for his assistance with the MRI analysis; Dr. Mathias Eder, Dr. Danusa Menegaz and Dr. Silvio Calcagnini for their curiosity and assistance with the electrophysiological assays; Dr. Nils Gassen and Dr. Andreas Zellner for their contribution to the proteomic analysis and Jinqiu Xiao for the analysis of the metabolome.

To my family and friends: I am grateful beyond words for the unconditional love and support you have shown during this challenging time.

IV. Table of content

I. Abstract .... **I**

II. Zusammenfassung .... **II**

III. Acknowledgements .... **IV**

IV. Table of content .... **V**

V. List of abbreviations .... **VIII**

1. Introduction **1**

1.1 The epitranscriptome 1

1.2 N^6-methyladenosine (m^6A) 2

1.3 m^6A regulation by ‘readers’, ‘writers’ and ‘erasers’ 3

1.3.1 The catalytic methyltransferase complex METTL3-METTL14 3
1.3.2 Other m^6A methyltransferases 4
1.3.3 The m^6A demethylase ALKBH5 4
1.3.4 The m^6A demethylases FTO 5
1.3.5 Wilms' tumor 1-associating protein (WTAP) 6
1.3.6 m^6A ‘readers’ 8
1.3.7 m^6A-dependent RNA binding proteins 11

1.4 m^6A: dynamically regulated or ‘hard coded’? 12

1.5 m^6A in the brain 12

1.5.1 m^6A is essential for normal brain development 13
1.5.2 Glia cell differentiation is regulated by m^6A 13
1.5.3 m^6A is required for adult neurogenesis 13
1.5.4 Axon guidance and regeneration depends on m^6A signaling 14
1.5.5 Regulation of synaptic transcripts through m^6A 14
1.5.6 m^6A regulation is involved in learning and memory 16

2. Aims and objectives **18**

3. Material and methods **19**

3.1 Animal husbandry and strain details 19

3.2 Tamoxifen administration 20

3.3 Tissue collection 21

3.4 *In situ* hybridization 23

3.5 Animal behavior 23

3.6 Gene expression analysis 26

3.7 Bioinformatic analysis of RNA sequencing 28

3.8 Proteomic screening using LC-MS/MS 29

3.9 Metabolite screening using LC-MS/MS 32

3.10 Western blot 33

3.11 Immunostaining 33

3.12 Microscopy 34

3.13 Electrophysiology 34

3.14 Magnetic resonance imaging 35

4. Results 37

4.1 Project I: WTAP is required for neuronal gene expression regulation, signaling and behavior 37

- 4.1.1 Camk2aCre expression across the adult mouse brain 37
- 4.1.2 Camk2aCre WTAP KO affects the weight in juvenile males but not females 39
- 4.1.3 WTAO KO alters circadian activity patterns in the home cage 40
- 4.1.4 WTAP KO induces volumetric changes in the cortex and thalamus 45
- 4.1.5 WTAP KO alters the protein composition in the mPFC, dHPC and vHPC 46
- 4.1.6 WTAP KO disturbs the metabolic balance 55
- 4.1.7 NexCreERT2 expression in the adult mouse brain 58
- 4.1.8 Validation of NexCreERT2 induced WTAP KO 59
- 4.1.9 WTAP KO results in reduced global m^{6}A 60
- 4.1.10 WTAP KO induces massive shift in gene expression 60
- 4.1.11 WTAP KO induces shift in splicing events 66
- 4.1.12 WTAP KO shifts composition of the neuronal membranome 69
- 4.1.13 WTAP KO animals show increased long-term potentiation 71
- 4.1.14 WTAP NexCreERT2 KOs show normal behavior 72

4.2 Project II: YTHDC1 is essential for adult survival and a regulator of neuronal functions 78

- 4.2.1 Impaired breeding and premature death of YTHDC1 KO females 78
- 4.2.2 YTHDC1 KO juveniles show reduced weight 79
- 4.2.3 The KO of YTHDC1 reduces the survival probability 80
- 4.2.4 YTHDC1 KO broadly affects behavior 81
- 4.2.5 YTHDC1 KO animals show volumetric changes in the cortex and HPC 87
- 4.2.6 YTHDC1 KO neurons in the mPFC are less excitable 88
- 4.2.7 Depleting YTHDC1 induces global changes in protein abundance 89
- 4.2.8 YTHDC1 KO affects metabolism in mPFC and dHPC 92
- 4.2.9 Validation of NexCreERT2 induced YTHDC1 KO 95
- 4.2.10 YTHDC1 KO induces shift in gene expression 95
- 4.2.11 NexCreERT2 YTHDC1 KO: behavioral assessment 100

5. Discussion 104

5.1 Considerations regarding the targeted KO of m^{6}A regulators in the brain 104

5.2 WTAP is essential for regulating neurons and behavior 105

5.3 YTHDC1 is essential for adult survival and regulates brain functions 115

6. Conclusion and outlook 122

7. Bibliography 125

8. Appendix 142

8.1 Locus and genotyping information 142

8.2 R packages 145

8.3 Material and reagents 146

- 8.3.1 Immunostaining and histology 146
- 8.3.2 RNA extraction and QC reagents 146

8.3.3 RT-qPCR, sequencing and m^{6}A 147
8.3.4 qPCR primers 147
8.4 Circadian activity analysis: model summary 148
8.5 Camk2aCre WTAP KO: proteomic GO analysis full results 149
8.6 Camk2aCre WTAP KO: metabolite analysis full results 152
8.7 NexCreERT2 expression validation using ISH 154
8.8 Comparison of KO efficacy in bulk HPC, dHPC slices and dCA1 155
8.9 NexCreERT2 WTAP KO: qPCR validation of LTP cohort 155
8.10 NexCreERT2 WTAP KO: DESeq2 GO full results 156
8.11 NexCreERT2 WTAP KO: DEXSeq GO full results 157
8.12 Membranome preparation: enrichment for membrane associated terms 159
8.13 NexCreERT2 WTAP KO: GAM model details for cue and contextual fear memory analysis 160
8.14 NexCreERT2 WTAP METTL3 KO: GAM model details for cue and contextual fear memory analysis 161
8.15 Camk2aCre YTHDC1 weight at P15 and week 12 161
8.16 Camk2aCre YTHDC1 KO: GAM model details for cue and contextual fear memory analysis 162
8.17 Camk2aCre YTHDC1 KO: patch clamp recordings full results 163
8.18 YTHDC1 Camk2aCre KO: metabolite analysis full results 163
8.19 NexCreERT2 YTHDC1 KO: DESeq2 GO full results 164
8.20 NexCreERT2 YTHDC1 KO: DEXSeq GO full results 165
8.21 NexCreERT2 YTHDC1 KO: GAM model details for cue and contextual fear memory analysis 165

9. List of figures 167

10. List of tables 170

11. Declaration of author contributions 172

V. List of abbreviations

°C	degree Celsius
a.u.	arbitrary units
ACSF	artificial cerebral spinal fluid
ALKBH5	alkB homolog 5
ANOVA	analysis of variance
AP	action potential
bp	base pairs
BP	Biological Process
CA1	cornu ammonis, subfield 1
CA2	cornu ammonis, subfield 2
CA3	cornu ammonis, subfield 3
caRNAs	chromosome-associated RNAs
CC	Cellular Component
cDNA	complementary DNA
CDS	coding sequence
cm	centimeter
cpm	counts per minute
Cre	Cre recombinase
CreERT2	tamoxifen-inducible Cre recombinase
Ct	cycle threshold
dCA1	dorsal cornu ammonis, subfield 1
dHPC	dorsal hippocampus
DL	dark/light
DNA	deoxyribonucleic acid
DNase	deoxyribonuclease
dNTP	deoxynucleoside triphosphate
EDTA	ethylenediaminetetraacetic acid
EEG	electroencephalography
EPM	elevated plus maze
eV	electronvolt
FC	fear conditioning
FDR	false discovery rate
fEPSP	field excitatory postsynaptic potential
FTO	fat mass and obesity associated
FWE	family-wise error
g	g-force
GAM	generalized additive model
gDNA	genomic deoxyribonucleic acid
GO	gene ontology
GΩ	giga-ohm
h	hour
HPC	hippocampus
Hz	Hertz
i.p.	intraperitoneal
ISH	*in-situ* hybridization
kDa	kilo Dalton
kg	kilogram
kHz	kilohertz
KO	knockout
l	liter
L2FC	Log2FoldChange
LC-MS	liquid chromatography–mass spectrometry
lncRNA	long non-coding RNA
LTP	long-term potentiation
M	molar
m/z	mass-to-charge ratio
m^{1}A	N^1-methyladenosine
m^{6}A	N^6-Methyladenosine
m^{6}Am	N^6,2'-O-dimethyladenosine
MACOM	m^{6}A-METTL-associated complex
METTL14	methyltransferase like 14
METTL3	methyltransferase like 3 (MT-A70)
MF	Molecular Function
mg	milligram
min	minute
ml	milliliter
mm	millimeter
mM	millimolar
mPFC	medial prefrontal cortex
MRI	magnetic resonance imaging
mRNA	messenger ribonucleic acid
MS	mass spectrometry
ms	millisecond
mt-mRNA	mitochondrial mRNA
mV	millivolt
MWM	Morris water maze
MΩ	Mega-ohm
NAD$^+$	nicotinamide adenine dinucleotide

ncRNA	noncoding RNA
NE	north-east
ng	nanogram
NGS	normal goat serum
nl	nanoliter
ns	not significant
NTC	no template control
NTP	nucleoside triphosphate
NW	north-west
OD	optical density
OF	open field
p.adj.	p-value adjusted
P15	postnatal day 15
PBS	phosphate-buffered saline
PCA	principal component analysis
PCR	polymerase chain reaction
PFC	prefrontal cortex
poly-(A)	polyadenylation
PPI	pre-pulse inhibition
ppm	parts per million
Pr(>|z|)	p-value
pre-mRNA	precursor mRNA
QC	quality control
qPCR	quantitative polymerase chain reaction (synonymously used for RT-qPCR)
RBM15	RNA binding motif protein 15
RNA	ribonucleic acid
RNase	ribonuclease
rRNA	ribosomal ribonucleic acid
RT	room temperature
RT-qPCR	reverse transcription-quantitative polymerase chain reaction
s	second
SACSF	sucrose-supplemented artificial cerebrospinal fluid
SAH	S-adenosylhomocysteine
SAM	S-adenosylmethionine
SCN	suprachiasmatic nucleus
SDC	sodium deoxycholate
SE	south-east
seq.	sequencing
SSC	saline-sodium citrate
SW	south-west
T	tesla
TBS	theta-burst stimulation
TH	thalamus
Th	Thomson
tRNA	transfer RNA
UHPLC	ultra-high performance liquid chromatography
UTR	untranslated region
V	volt
vHPC	ventral hippocampus
Vs	volt-second
W	watt
WB	western blot
WT	wild type
WTAP	Wilms tumor 1 associated protein
YTHDC1	YTH domain containing 1
YTHDC2	YTH domain containing 2
YTHDF1	YTH N^6-methyladenosine RNA binding protein 1
YTHDF2	YTH N^6-methyladenosine RNA binding protein 2
YTHDF3	YTH N^6-methyladenosine RNA binding protein 3
ZC3H13	zinc finger CCCH-type containing 13
µl	microliter
µM	micromolar

1. Introduction

In this chapter, I will provide a review of our current knowledge on the overall role N^6-methyladenosine (m^6A) has in regulating the RNA metabolism. I will briefly touch upon the ascribed functions of various m^6A regulators and provide a comprehensive overview of our current knowledge in respect to the role m^6A has in shaping neural functions and behavior. The scope of this review will set the stage for the main question addressed in this thesis: What is the role of the m^6A regulators WTAP and YTHDC1 in the adult mammalian brain?

1.1 The epitranscriptome

Originally described by Francis Crick, the 'central dogma' of molecular biology states that information can be transferred between nucleic acids and from nucleic acids to proteins but not between proteins or from protein to nucleic acids[1–3]. Today, the 'central dogma' is often referred to as the flow of genetic information from DNA to RNA, with proteins as the functional output[3]. The scientific advances of the last couple of decades have elucidated that this flow of information from DNA to protein is highly regulated. Chemical modifications of nucleobases, so-called 'epigenetic marks', shape gene expression[4] and can be passed down generations[5].The methylation of cytosine to 5-methylcytosine (5mC), its metabolite 5-hydroxymethylcytosine (5hmC) and the more recently discovered N^6-methyladenine (6mA) have been shown to regulate gene expression by shaping the accessibility of genomic regions[4]. Together with histone modifications, most notably methylation[6] and acetylation[7] that modulate chromatin structure, these epigenetic modifications are essential regulators of developmental programs[8] and variations have been associated with adverse health outcomes[9].

On the RNA level, 143 distinct modifications have been identified that potentially enable the post transcriptional fine tuning of gene expression through the regulation of protein RNA interactions. Together referred to as the 'epitranscriptome', RNA modifications are present across all classes of RNA, with 111 modifications having been detected in transfer RNAs (tRNA), 33 in ribosomal RNAs (rRNA), 17 in messenger RNAs (mRNA), and 11 in noncoding RNAs (ncRNA)[5]. While the biological function of many of these modifications remains to be determined, largely due to a lack in suitable detection methods, methodological advances have now enabled us to study the role of a selected few. Among these, the most abundant RNA modification pseudouridine (Ψ), mostly present in non-coding RNAs and less frequently in mRNAs[10], has been shown to be essential for stabilizing the structure of tRNAs and rRNAs[5,11]. Other modifications such as N^1-methyladenosine (m^1A), N^6,2'-O-dimethyladenosine (m^6Am) and N^6-methyladenosine (m^6A) appear to be integral for regulating the mRNA metabolism and represent a post-transcriptional mechanism for fine-tuning gene expression[12–15].

An overview of our current understanding of how the flow of genetic information from DNA to protein is shaped by the presence of epigenetic and epitranscriptomic regulation, is shown in Figure 1.

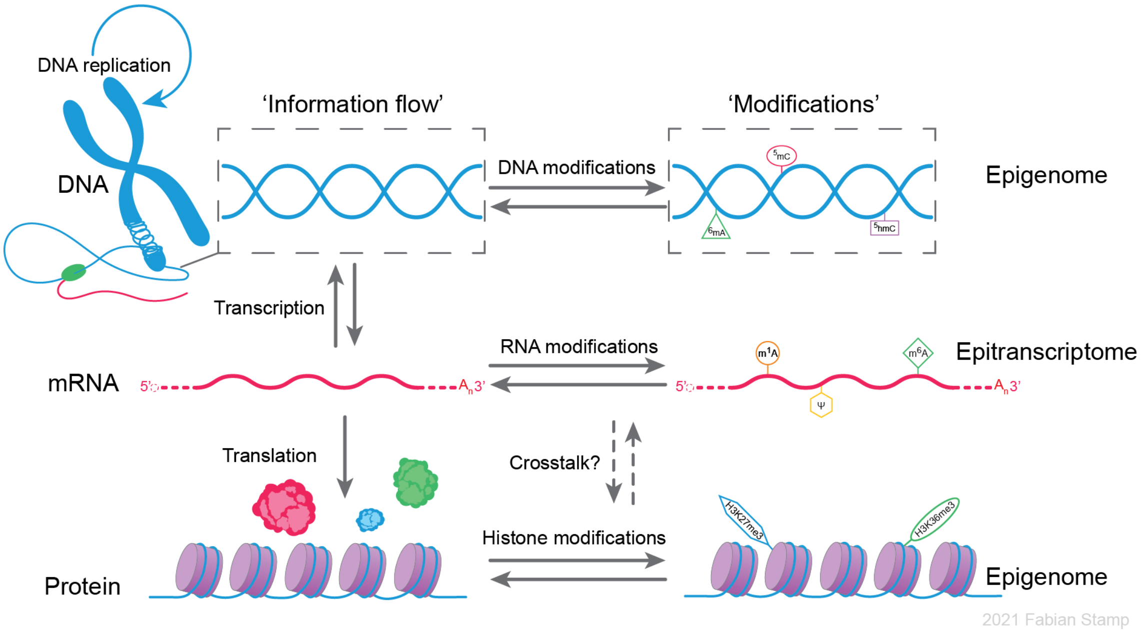

Figure 1: The flow of genetic information from DNA to protein

The flow of genetic information from DNA to protein, here updated with insights from epigenetic and epitranscriptomic research. The transfer of information from DNA to RNA with proteins as the functional output has been shown to be modulated by chemical modifications present in nucleic acids and on proteins. The methylation status of genetic regions within the DNA regulates transcription. On the level of RNA, the reversible addition of chemical groups has been demonstrated to affect various aspects of the RNA metabolism and to modulate translation efficiency. Post-translation modifications of histones determine the packing of DNA and shape chromatin structure. The entirety of chemical modifications within the DNA and histones is referred to as the epigenome while the sum of modifications present in RNA constitutes the epitranscriptome. Concept adapted from Fu et al., 2014[16].

In this thesis, two proteins integral to the regulation and function of the RNA methylation mark m^{6}A are studied within the adult mammalian brain. Therefore, in the following, I will give an overview of the current state of the research into m^{6}A, with a focus on previous research into its involvement in regulating brain functions.

1.2 N^6-methyladenosine (m^{6}A)

The addition of a methyl group at the N^6-position of adenosine, known as m^{6}A, is the most abundant internal modification in mRNA with an estimated occurrence of 3-5 marks per transcript[16]. Originally discovered in the 1970s[17,18], a lack of quantitative detection methods hindered in depth investigations at the time. Systematic research into the biological function of m^{6}A only took off after the identification of MT-A70 (also known as METTL3) as the principal m^{6}A methyltransferase of mRNA[19,20] and the discovery of fat mass and obesity-associated protein (FTO) as the first m^{6}A demethylase[21]. The possibility that m^{6}A could be dynamically regulated, depending on cellular states or induced as adaptation to alterations in the environment, sparked interest across biological disciplines. With the advent of antibody-based high throughput m^{6}A sequencing[13,15], revealing more than 10,000 distinct m^{6}A sites mapping to over 7,000 genes, the stage was set for what can only be described as the m^{6}A gold rush. Over 2,800 articles have been published on the topic, of which 2,500 were within the last 5 years (Figure 2).

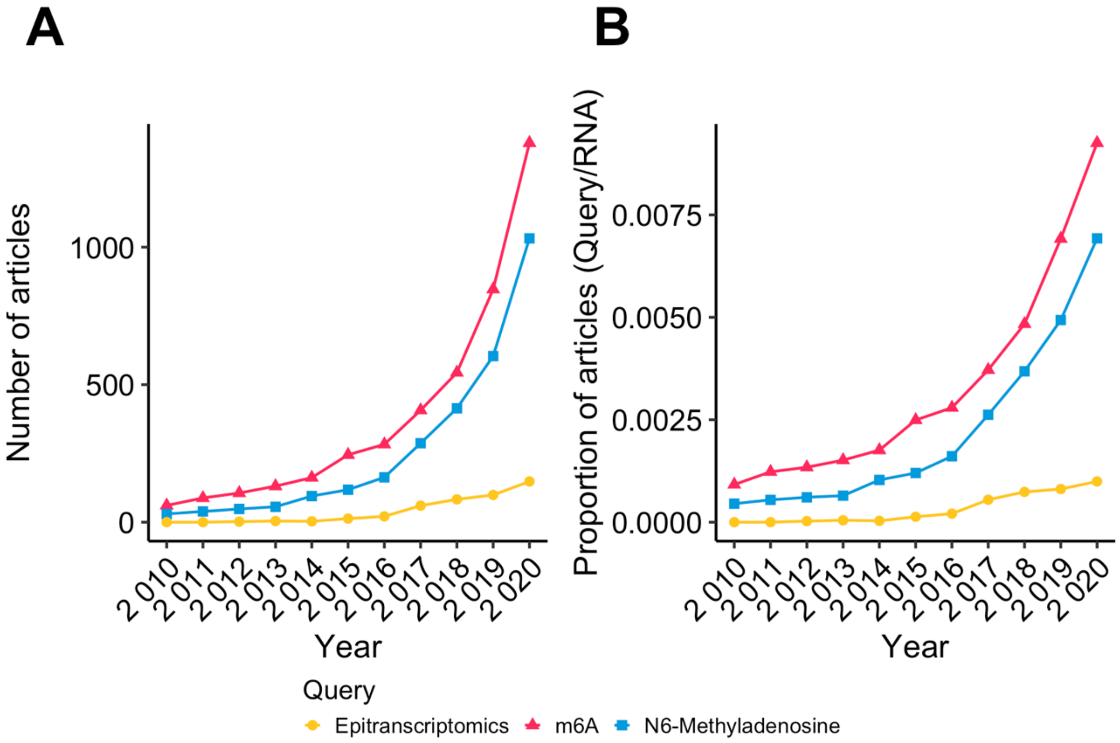

Figure 2: Research into N^6-Methyladenosine has exponentially grown since 2010

(A) The total number of research articles returned for the query terms 'Epitranscriptomics', 'm^{6}A' and 'N^6-methyladenosine' in Europe PubMed Central for the time period 2010 to 2020. (**B)** The proportion of articles returned for the search terms of interest in relation to the overall articles returned for the query 'RNA' showing that within the broad field of RNA, research into epitranscriptomics and m^{6}A has steadily increased over the last 10 years.

Since the discovery of the first components of the m^{6}A regulatory complex, research has grown exponentially. The observation that many m^{6}A regulators are evolutionary conserved, with orthologue enzymes having been described across eukaryotes[22], suggests that m^{6}A provides a universal mechanism for post transcriptional regulation of gene expression. While initial investigations focused on understanding the implications of m^{6}A for the regulation of the RNA processing, the role of m^{6}A is now increasingly investigated in other branches of biology. The expanding area of research into the function of m^{6}A includes, among others, stem cell regulation [23,24], organismal development[25–27], neuronal signaling and higher cognitive functions[28–30]. Furthermore, an increasing number of studies have demonstrated the involvement of m^{6}A regulation in viral infections[31], cancer[32] and metabolic disorders[33,34].

1.3 m^{6}A regulation by 'readers', 'writers' and 'erasers'

The regulation of the RNA metabolism by m^{6}A is mediated by dedicated 'writers' that establish the methylation, 'readers' that interact with RNA in an m^{6}A-dependent manner and 'erasers' that remove m^{6}A. In the following section, I will give an overview of important m^{6}A regulatory proteins, including the main 'readers', 'writers' and 'erasers'.

1.3.1 The catalytic methyltransferase complex METTL3-METTL14

m^{6}A is established by a multiprotein 'writer complex' and occurs within a dedicated consensus motif (5'-DRm^{6}ACH-3': D = A/G/U, R = A/G, H = A,C/U) which is enriched near the stop codon and in the 3′ untranslated region (3' UTR)[13,15,35]. The core 'writer complex' establishing the methylation consists of the catalytically active methyltransferase like 3 (METTL3) and the associated methyltransferase like 14 (METTL14)[36,37]. METTL3 has been shown to reside within the nucleus and cytoplasm and has different functions depending on its localization[38,39]. In the nucleus, METTL3 is involved in establishing m^6A, whereas cytoplasmic METTL3 promotes the translation of a subset of m^6A containing mRNAs through the recruitment of eIF3 to the translation initiation complex[39]. In contrast, the localization of METTL14 is restricted to the nucleus[39] where it is required for the recognition of target RNAs and the stabilization of the heterodimer[40]. Together, the METTL3-METTL14 complex binds to the DRACH motif in target mRNAs and transfers a methyl group from the methyl donor S-adenosylmethionine (SAM) to an adenosine[40]. This has been shown to occur, at least to some extent, co-transcriptionally[41], possibly mediated through an interaction of METTL14 with the histone modification H3K36me3[42]. The depletion of either METTL3 or METTL14 results in a strong reduction in m^6A levels, suggesting that a large part of cellular m^6A depends on METTL3-METTL14 activity[23,36].

For the core methyltransferase to establish m^6A, it depends on a multiprotein complex consisting of Wilms' tumor 1-associating protein (WTAP), vir like m^6A methyltransferase associated (VIRMA), RING-type E3 ubiquitin transferase hakai (HAKAI), RNA binding motif protein 15/B (RBM15/B) and zinc finger CCCH-type containing 13 (ZC3H13)[43–45]. Together these proteins form a complex referred to as m^6A-METTL-associated complex (MACOM) that interacts with the METTL3-METTL14 dimer and is required for the m^6A methyltransferase activity[44].

1.3.2 Other m^6A methyltransferases

Recently, two more m^6A methyltransferases were identified that place m^6A in a subset of precursor mRNAs (pre-mRNA) and non-coding RNAs[46–49]. The nuclear methyltransferase methyltransferase like 16 (METTL16) has been shown to require a structural motif within pre-mRNAs and various non-coding RNAs to catalyze the addition of m^6A[46–48]. In contrast, METTL3-METTL14 mediated methylation is directed solely by a sequence motif. METTL16 has been shown to be integral for the regulation of the methyl donor (SAM) levels[50]. In the presence of SAM, METTL16 deposits m^6A on the SAM synthetase transcript *Mat2a* resulting in the retention of the terminal intron and subsequent transcript degradation. In contrast, low SAM levels reduce the chance of methylation. Consequently, METTL16 binds to a conserved hairpin structure within *Mat2a* inducing the splicing of the terminal intron that results in the up-regulation of SAM synthetase protein levels. This regulation of *Mat2a* expression levels has been shown to be essential for early development with a depletion of METTL16 resulting in the developmental arrest at around the blastocyst stage[48].

The second recently identified m^6A methyltransferases is zinc finger CCHC-type containing 4 (ZCCHC4) which is localized in the nucleoli where it catalyzes the methylation of rRNA and specifically the addition of the only m^6A mark that is present in 28S rRNA[49,51]. The *in vitro* depletion of ZCCHC4 results in the loss of 28s RNA methylation, decreased translation and impaired proliferation suggesting that ZCCHC4 is required for ribosomal functioning[49].

1.3.3 The m^6A demethylase ALKBH5

Removal of m^6A is catalyzed by the alpha-ketoglutarate-dependent dioxygenases alkb homolog 5 (ALKBH5)[52] and FTO[21]. The m^6A demethylase ALKBH5 is predominantly located in the nucleus[53] and co-localizes with nuclear speckles[52], the site of pre-mRNA processing and m^6A methylations. ALKBH5 is ubiquitously expressed with its highest expression levels found in the lungs and testes[52]. ALKBH5 knockout (KO) mice are viable but show a reduction in testes size, accompanied by increased apoptosis and abnormal spermatozoa suggesting an important role of ALKBH5 in spermatogenesis[52]. Furthermore, ALKBH5 activity has been reported to promote nuclear retention, with the depletion of ALKBH5 resulting in a decrease in nuclear localized RNA[52].

1.3.4 The m^{6}A demethylases FTO

FTO catalyzes the removal of m^{6}A and m^{6}Am[54,55] in mRNA, as well as m^{1}A in tRNA[56]. FTO is detected mostly in the nucleus where it co-localizes with nuclear speckles[21]. Depending on the cell type, FTO has also been detected in the cytoplasm, where its primary targets appear to be m^{6}Am and m^{1}A[56]. In addition to its role in neuronal processes that will be addressed below, FTO is involved in the regulation of the energy homeostasis, with FTO full KO mice being viable but showing an overall reduction in size and body weight[57]. Conversely, FTO overexpression has been reported to result in increased food intake and obesity[57]. Mechanistically, FTO, has been shown to regulate m^{6}A sites that determine the isoform expression of the adipogenic Runt-related transcription factor 1 (RUNX1T1). Further support for the involvement of FTO in regulating metabolic processes comes from the observation that *Fto* expression and protein abundance depend on the glucose levels in mice[58] and patients diagnosed with type 2 diabetes[59]. Recently it has been demonstrated that the introduction of the human *FTO* gene into rice and potato plants increases yield and biomass by ~ 50 % in field trials[60]. *FTO* activity was shown to enhance the growth of roots, improve the efficiency of photosynthesis and make plants more resistant to droughts. Mechanistically, *FTO* promotes open chromatin, increases transcription and the demethylation of mRNA and nuclear RNA species[60]. Complementing these results, genome-wide association studies have linked variants of the *FTO* gene with an increased body mass index and risk for obesity [33,34]. Together, this evidence strongly supports a central role of FTO in regulating the metabolism.

A concise overview of the methylation and demethylation reaction of adenosine to m^{6}A is shown in Figure 3.

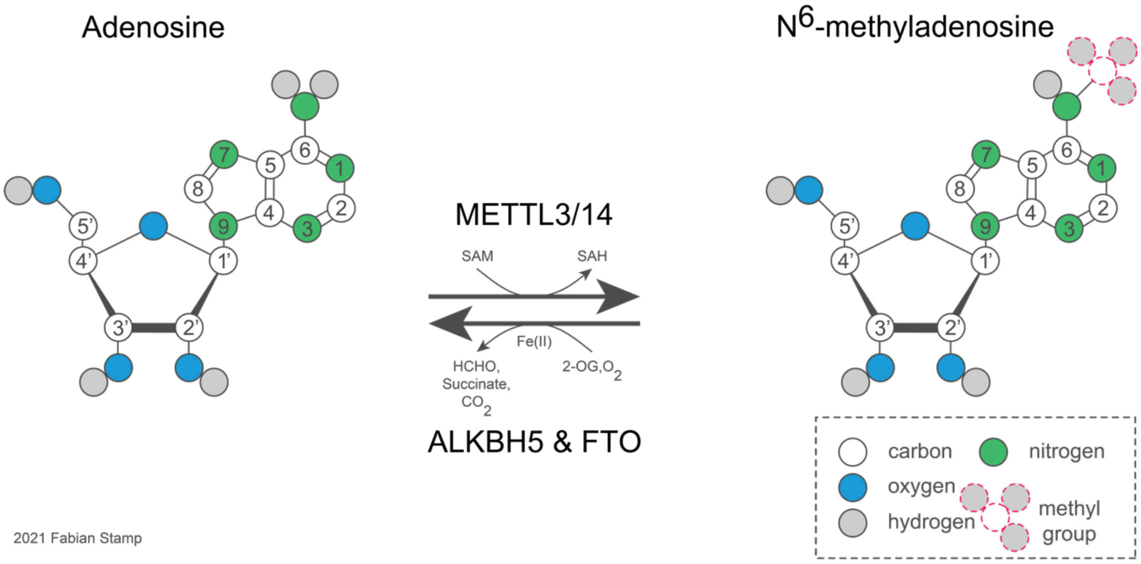

Figure 3: The conversion of adenosine to N^6-methyladenosine by 'writers' and the removal through 'erasers'

The addition of a methyl group at position N^6 is catalyzed by the methyltransferase heterodimer METTL3-METTL14 and requires the methyldonor S-adenosylmethionine (SAM), which is converted to S-adenosylhomocysteine (SAH). This process can be reversed by the demethylases ALKBH5 and FTO, which catalyze the Fe(II) and 2-oxoglutarate (2-OG) dependent demethylation of m^{6}A.

1.3.5 Wilms' tumor 1-associating protein (WTAP)

WTAP, whose functions in the brain is investigated in this thesis, was initially identified as an interaction partner of the transcription factor Wilms' tumor-1 (WT-1), which plays an important role in the development of the urogenital system[61]. The *Wtap* gene encodes two isoforms that result from alternative splicing, with the short isoform producing no functional protein. Both isoforms are expressed *in vitro* (short ~70 %, long ~ 30 %) and it has been suggested that WTAP expression is regulated through an autoregulatory feedback loop that changes the ratio of its transcripts[43]. WTAP is an ubiquitously expressed nuclear protein located in the nucleoplasm and nuclear speckles, where it co-localizes with various splicing factors and METTL3[43,61]. The overexpression of WTAP induces apoptosis of vascular smooth muscle cells, while the depletion of WTAP increases cell proliferation[62,63]. This suggests that WTAP might be involved in regulating the cell cycle and the viability of dividing cells. Accordingly, in the mouse, WTAP is essential for embryonal development and the depletion of WTAP results in defects in the differentiation of the endoderm and mesoderm and embryonal lethality[64,65]. Similar observations were made for the zebra fish WTAP and the fly orthologue Fl(2)d in which WTAP loss results in developmental defects[37,66].

As a regulatory subunit of the m^{6}A-methylation complex, WTAP interacts with the METTL3-METTL14 heterodimer[36,37] via an N-terminal coiled-coil region[67]. While WTAP does not possess catalytical activity[36], it is essential for methylation activity and was shown to be required for METTL3-METTL14 to be localized in the nuclear speckles[37]. Aberrant METTL3 levels have been reported to affect WTAP expression[68], while the *in vitro* depletion of WTAP using siRNAs has been suggested to not alter METTL3 protein levels[37].

The depletion of WTAP has consistently been reported to result in a significant decrease in m^{6}A levels[36,37,69] demonstrating that WTAP is necessary for m^{6}A methylation. Interestingly, several independent studies have reported that the removal of WTAP results in a stronger reduction of m^{6}A levels than observed after METTL3 depletion[36,37,69]. Why this is the case remains to be determined. However, it is conceivable that WTAP might be involved in the regulation of other m^{6}A-methyltransferases such as METTL16.

Crosslinking experiments have shown that WTAP interacts with various mRNAs, ~50 % of which are also targeted by METTL3 suggesting that WTAP might facilitate the recruitment of RNAs to the methylation complex[37]. Furthermore, WTAP is involved in the regulation of gene expression and splicing in cell culture. The *in vitro* depletion of WTAP changes the expression and splicing of several thousand genes[37] and shows an overlap with the effects observed after METTL3 depletion (expression ~45 %, splicing ~50 %)[37].

Together, these observations suggest that WTAP is an essential component of the m^{6}A methyltransferase complex and is involved in the regulation of gene expression and splicing. The fact that WTAP can be found outside of the m^{6}A ‘writer complex’, as part of the MACOM complex[44], suggests that WTAP might be involved in m^{6}A independent regulation.

An overview of m^{6}A regulation through ‘writers’ ‘readers’ and ‘erasers’ is shown in Figure 4.

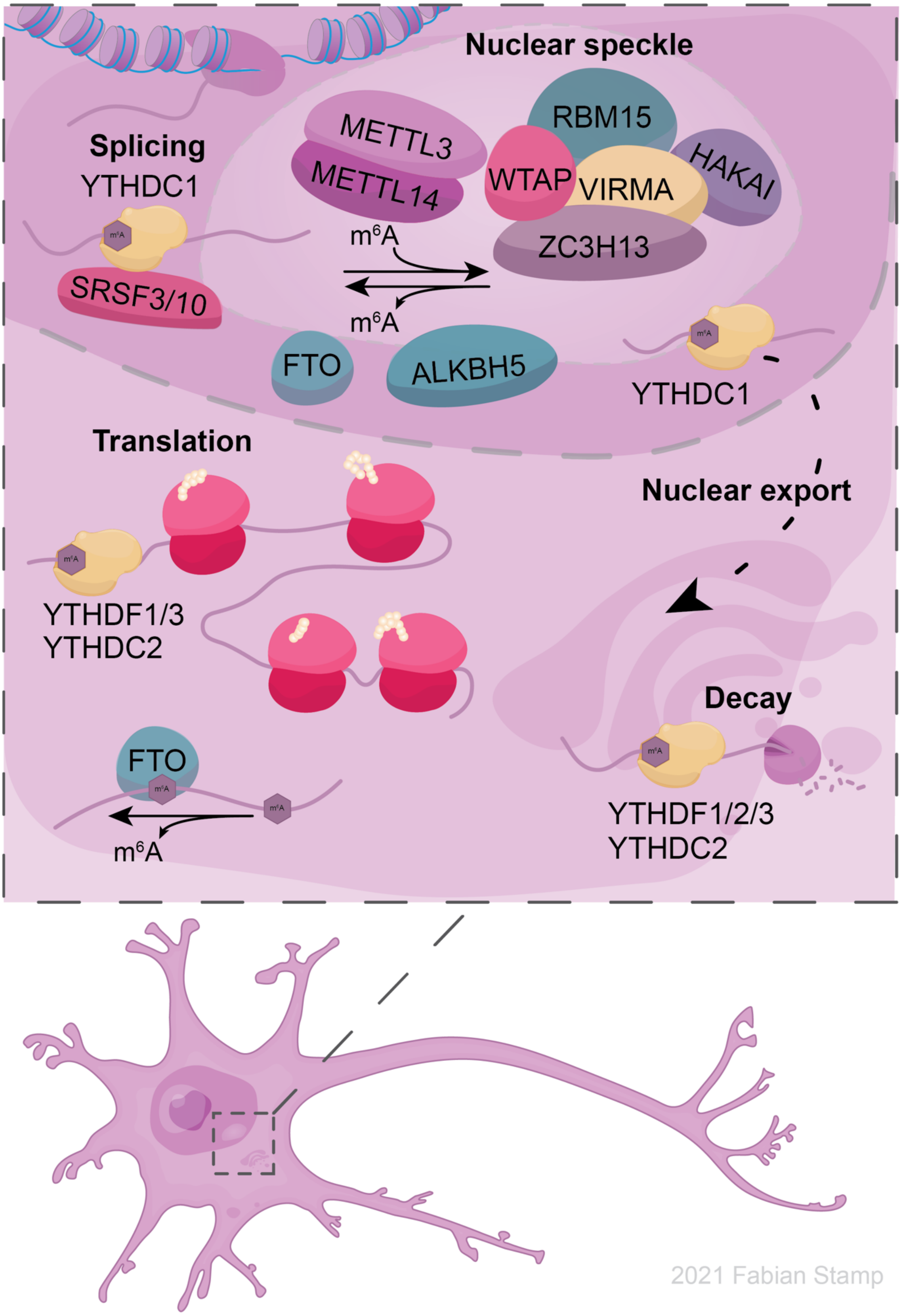

Figure 4: Overview of the m^{6}A regulation by ‘writers’, ‘readers’ and ‘erasers’

m^{6}A is established by a ‘writer complex’ located in the nuclear speckles. The core ‘writer complex’ consists of METTL3 and METTL14 and interacts with the associated proteins WTAP, RBM15/B, ZC3H13, HAKAI and VIRMA. In the nucleus, the m^{6}A ‘reader’ YTHDC1 promotes mRNA processing via recruitment of splicing factors (e.g., SRSF3) and facilitates the nuclear export of methylated transcripts. In the cytoplasm, the m^{6}A ‘readers’ YTHDF1-3 and YTHDC2, regulate mRNA turnover and translation.

1.3.6 m^{6}A ‘readers’

The regulatory effects of m^{6}A on RNA metabolism are mediated by various ‘reader’ proteins. m^{6}A ‘readers’ can be largely separated into two categories, proteins that directly bind to m^{6}A through a dedicated binding domain and ‘readers’ that interact with RNA in an m^{6}A-dependent manner. In the following section, I will give an overview of both classes of m^{6}A ‘readers’.

YTH domain containing m^{6}A readers

The YTH (YT521-B homology) domain containing m^{6}A ‘readers’ were originally discovered in an affinity chromatography and mass spectrometry screening with methylated RNA baits[13] and derive their name from the family defining YTH-domain that interacts with m^{6}A. The YTH domain is evolutionary conserved[70] and there are five different YTH domain containing m^{6}A ‘readers’ in mammals. Four of the YTH domain containing m^{6}A ‘readers’ have been shown to locate in the cytoplasm (YTHDC2, YTHDF1, YTHDF2, YTHDF3), while one (YTHDC1) is located in the nucleus.

YTHDC1

YTH domain containing 1 (YTHDC1) is a ubiquitously expressed protein and the only nuclear m^{6}A ‘reader’. Within the nucleus, YTHDC1 has been shown to accumulate in distinct nuclear structures termed YT bodies[71]. YT bodies are sites of active transcription found in the proximity of nuclear speckles where the m^{6}A methylation machinery is located. YTHDC1 is essential for mammalian development with a KO resulting in early embryonal lethality[72]. Furthermore, the conditional depletion of YTHDC1 in the germ line results in sterility and changes in alternative splicing and polyadenylation[72]. In addition, YTHDC1 interacts with the X-inactivation regulating RNA Xist *in vitro* and is required for Xist-mediated transcriptional silencing[25]. Mechanistically, YTHDC1 regulates splicing, nuclear export and chromatin regulation as outlined in the following paragraphs.

YTHDC1: splicing

Findings from several independent studies have demonstrated that YTHDC1 is involved in the regulation of alternative splicing[70,72,73], which is concentration dependent[73], with elevated YTHDC1 levels promoting exon inclusion and the depletion of YTHDC1 resulting in exon skipping[70]. Consistent with these observations, YTHDC1 has been shown to interact with different splicing regulators, including SAM68, SRSF1, SRSF3, SRSF7, SRSF9, and SRSF10[73–76]. Mechanistically, YTHDC1 binds to a motif containing G(m^{6}A)C in pre-mRNA[77] and promotes exon inclusion through an interaction with the splicing factor SRSF3[74]. YTHDC1 and SRSF3 have been shown to preferentially bind methylated transcripts and to compete with the m^{6}A-independent splicing factor SRSF10, which promotes exon skipping[74]. The conditions under which YTHDC1 dependent regulation of splicing is most important and whether this plays a role in regulating neuronal processes remain to be determined.

YTHDC1: nuclear export

In addition to regulating alternative splicing, YTHDC1 facilitates the nuclear export of methylated transcripts[76]. This is supported by the observation that the removal of YTHDC1 selectively increases the amount of nuclear m^{6}A, while cytoplasmic m^{6}A levels are reduced[76]. Conversely, an overexpression has been shown to have the opposite effect[76]. The YTHDC1 mediated transport of RNA has been suggested to involve the nuclear RNA export factor 1 (NXF1) and SRSF3[76]. Independently, the relocation of YTHDC1 to the cytoplasm had previously been described to depend on the phosphorylation of YTHDC1 at a tyrosine residue[78].

YTHDC1: chromatin regulation

An increasing number of studies support a role of YTHDC1 in chromatin regulation[27,79–82]. In a recent study, Jun Liu and colleagues showed that the m^{6}A-dependent regulation of chromosome-associated RNAs (caRNAs) requires YTHDC1[79]. caRNAs include various ncRNAs that are either associated with gene regulatory elements or are transcribed from transposable elements. While individually differing in functions, these caRNAs are believed to exert regulatory control on gene expression[79]. Using various *in vitro* assays, Jun Liu and colleagues showed that the depletion of either METTL3 or YTHDC1 results in increased chromatin accessibility. Mechanistically, YTHDC1 is believed to bind to a subset of methylated caRNAs and to facilitate degradation by the nuclear exosome targeting (NEXT) complex. This appears to be of particular importance for the regulation of long interspersed element-1 (LINE1) transposable elements. LINE1 elements are involved in the regulation of transcription during early embryonal developmental[83,84] and the sex-specific response to early life stress[85,86]. Besides the METTL3/YTHDC1 dependent regulation of retrotransposons, there is evidence for a YTHDC1 driven regulation of a subset of METTL3 independent LINE1 caRNAs[82]. In support of this, experiments in mouse embryonic stem cells have shown that YTHDC1 binds to METTL3 independent m^{6}A sites on LINE1 caRNAs, with the depletion of YTHDC1 resulting in reduced levels of H3K9me3 marks associated with transcriptional repression[82]. While the origin of these METTL3 independent marks is not entirely clear, they are potentially installed by METTL16, which has been shown to act on pre-mRNA and ncRNAs[47,82].

YTHDC1: histone modifications

Several independent studies support an involvement of YTHDC1 in the regulation of histone modifications[27,79–81]. YTHDC1 has been suggested to direct the histone methyltransferase SETB1 to specific retrotransposons, promoting their silencing through installment of the repressive H3K9me3 mark[80], and the presence of m^{6}A appears to destabilize transcripts encoding histone modifiers in some contexts[27]. Furthermore, YTHDC1 has been shown to co-transcriptionally downregulate H3K9me2 levels in an m^{6}A-dependent way, through the recruitment of the histone demethylase KDM3B[81] and the *in vitro* KO of either METTL3 or YTHDC1 has been shown to results in an upregulation of transcription promoting marks, namely H3K4me3 and H3K27a[79].

Overall, YTHDC1 seems to play a central role in the control of chromatin state, splicing and nuclear export. While it has been established that YTHDC1 is essential for stem cell identity and early development, the role YTHDC1 plays in post mitotic cells such as neurons, remains to be determined.

YTHDC2

YTH domain containing 2 (YTHDC2) is the only YTH family protein containing a helicase domain and is highly expressed in the testes[87,88]. YTHDC2 was identified as a cytoplasmic m^{6}A ‘reader’ that is essential for the maturation of gametes and YTHDC2 KO mice are viable but sterile[87,89,90]. YTHDC2 is required for the progression from the mitotic to the meiotic stage during germ line development[90,91] and the *in vitro* depletion of YTHDC2 attenuates protein synthesis[88,89]. Mechanistically, YTHDC2 binds to m^{6}A marks within the coding sequence (CDS) opening mRNA secondary structures and with this facilitating translation[88]. This observation complements previous results showing that m^{6}A within the CDS modulates tRNA mediated translation dynamics[92]. Furthermore, it has been reported that YTHDC2 interacts with the small ribosomal subunit[87] and recruits the mRNA decay inducing exoribonuclease XRN1[87,89,93]. Therefore, YTHDC2 might, depending on cellular context, promote translation and/or facilitate mRNA clearance. As with YTHDC1, the role of YTHDC2 in neurons has not been systematically investigated.

YTHDF1, YTHDF2, YTHDF3

The YTH-domain containing m^{6}A ‘readers’ YTHDF1-3 are cytoplasmic m^{6}A ‘readers’, which have been proposed to mediate the cytosolic effects of m^{6}A through regulating the translation and decay of methylated transcripts[94–96]. In the following paragraphs, I will discuss the proposed function of individual YTHDF ‘readers’ and recent evidence that suggests a high degree of redundancy among individual YTHDF proteins.

YTHDF1: translation efficiency

YTH N^6-methyladenosine RNA binding protein 1 (YTHDF1) has been suggested to interact with the translation initiation factor eIF3 and to promote the translation of methylated transcripts[95]. In support of this, it has been reported that the depletion of YTHDF1 impairs the translation of its target transcripts[95]. However, recent results challenge the involvement of YTHDF1 in the regulation of translation[97]. The potential role of YTHDF1 regulating neuronal functioning[30,98] is addressed below.

YTHDF2: mRNA decay

YTH N^6-methyladenosine RNA binding protein 2 (YTHDF2) binds to the consensus motif G(m^{6}A)C and regulate the stability of methylated transcripts[76,94]. Mechanistically, the binding of YTHDF2 results in the accumulation of transcripts within sites of RNA degradation[94] and YTHDF2 has been suggested to recruit the CCR4-NOT deadenylase complex resulting in an accelerated degradation of the target mRNA[99]. During oocyte maturation, YTHDF2 is required for the dosing of maternal mRNA levels[100] and YTHDF2 has been shown to be involved in the clearance of m^{6}A-tagged maternal transcripts during the maternal to zygotic transition in zebra fish[101]. Therefore, YTHDF2 might generally accelerate the rapid clearance of m^{6}A tagged transcripts from the cytoplasm and this appears to be of particular importance during state transitions such as the activation of the embryonic genome. Under heat shock conditions, YTHDF2 relocates to the nucleus where it facilitates the cap-independent translation of heat shock induced genes[102]. The fact that YTHDF2 shows an ~50 % overlap in binding targets with YTHDF1, suggests that enhanced translation and subsequent degradation might be coordinated[95]. In regards to human health, a polymorphism in the *YTHDF2* gene was associated with an increased life span in humans[103].

YTHDF3: concerted regulation of mRNA translation and decay

YTH N^6-methyladenosine RNA binding protein 3 (YTHDF3) is structurally very similar to YTHDF1 and YTHDF2, and has been reported to share more than 50 % of its targets with either protein[96]. YTHDF3 might act in concert with YTHDF1 and YTHDF2 to regulate translation and mRNA decay[96]. In support of this, the *in vitro* depletion of YTHDF3 using siRNA has been shown to impair the translation of YTHDF3 targets[96]. Furthermore, YTHDF3 has been reported to interact with the ribosome and to facilitate the translation of shared YTHDF1/DF3 targets[104]. Recently, it has been proposed that YTHDF3 might also act as m^{1}A ‘reader’, facilitating transcript decay[105].

YTHDF1-3: controversy about functions

The prevailing model of YTHDF ‘reader’ functions suggests that each ‘reader’ has a specific function and targets a selected subset of transcripts. Challenging this model, Zaccara and Jaffrey recently proposed that YTHDF1-3 are redundant in function and selectivity and mainly promote mRNA decay[97]. To demonstrate this, the authors compared the binding affinity of individual YTHDF ‘readers’ and found no unique preference for particular m^{6}A sequence contexts. Using immunostainings the authors showed that all YTHDF ‘readers’ are located within the same defined structures in the cytoplasm, some of which were identified as sites of RNA degradation. The comparison of YTHDF ‘reader’ interacting proteins showed a high degree of overlap and ranking interactions by confidence revealed high-confidence interactions for factors involved in RNA decay and low confidence interactions with components of the translation initiation complex. An *in vitro* depletion of individual ‘readers’ showed only subtle effects on the abundance and stability of methylated transcripts while the combined KO of all three markedly increased the abundance and stability of methylated transcripts. This led the authors to conclude that YTHDF ‘readers’ are somewhat redundant and can compensate for each other. Furthermore, the reanalysis of ribosome profiling data previously published by Wang et al.[95] did not replicate the proposed effects on translation. Instead, it points towards a mistake in the original data analysis. To confirm this, the authors performed their own ribosome profiling experiment after depletion of individual YTHDF ‘readers’. No translation promoting effect was observed for either candidate. Based on these observations, the authors conclude that YTHDF ‘readers’ are mostly redundant in sequence preference, location and function.

1.3.7 m^{6}A-dependent RNA binding proteins

Besides the YTH-domain family, a diverse group of RNA binding proteins has been suggested to either bind directly to m^{6}A or interact with transcripts in an m^{6}A-dependent manner.

HNRPs

The heterogeneous nuclear ribonucleoprotein (HNRNP) family includes a diverse group of nuclear RNA-binding proteins that are important regulators in many aspects of RNA processing[106,107]. Dysregulation of HNRNPs is associated with various diseases, including cancer[108] and neurodegeneration[109,110].

Recently, it has been shown that members of the HNRP family interact with mRNA in an m^{6}A-dependent manner[111]. Unlike members of the YTH-domain family, HNRNPs do not directly interact with m^{6}A but depend on structural changes induced by the presence of m^{6}A. Specifically, m^{6}A opens up secondary structures and allow HNRNPS to effectively bind to their individual binding motifs. This mechanism, referred to as ‘m^{6}A-switch’, has been suggested to regulate over 39,000 binding sites of HNRNPC[111]. For the lncRNA MALAT1, an ‘m^{6}A-switch’ regulates the hairpin structure containing a HNRNPC binding motif [112]. Similarly, HNRNPA2B1 has been shown to bind m^{6}A containing primary-miRNAs and regulate their processing[113]. While originally proposed as a m^{6}A ‘reader’[113], crystallographic and bioinformatic analyses support the ‘m^{6}A-switch’ dependent binding also for HNRNPA2B1[114].

FMRP

Fragile X mental retardation protein (FMRP) is an RNA-binding protein known for its importance in brain development and dysregulation in the neurodevelopmental fragile X syndrome[115,116]. FRMP regulates the editing, transport and translation of mRNA and controls the expression of chromatin modifying enzymes[117]. FMRP has a binding motif that overlaps with the m^{6}A consensus sequence and recent studies have reported that FMRP acts as context dependent m^{6}A ‘reader’[118,119]. It has been suggested that FMRP binding to methylated transcripts, facilitates nuclear export[120], regulates translation[118] and modulates mRNA stability[119]. In the brain, FMRP has been shown to regulate neuronal differentiation in an m^{6}A-dependent manner[120] and in *D. melanogaster,* the fly homolog Fmr1 has been reported to repress the translation of mRNA involved in the regulation of axon growth, through an interaction with the fly m^{6}A ‘reader’ protein Ythdf[121].

eIF3 and METTL3

Cytoplasmic METTL3 has been shown to associate with the ribosomes and to recruit eIF3, facilitating the translation of selected m^{6}A containing mRNAs[39]. Mechanistically, METTL3 has been suggested to bind in proximity of the stop codon where it facilitates the formation of a translation enhancing closed-loop structure via a direct interaction with eIF3[122]. In addition, under cellular stress conditions, eIF3 directly binds to m^{6}A within the 5′ untranslated region (5'UTR) and enables cap-independent translation[123].

1.4 m^{6}A: dynamically regulated or 'hard coded'?

While it has been generally accepted that m^{6}A is established by the 'writer complex', bound by various 'reader' proteins and removed by 'erasers', the dynamic nature of m^{6}A regulation remains a topic of debate[124–126]. One of the questions that has not been resolved yet is whether m^{6}A is deposited in a site-specific manner or solely tuned on a global level through the expression of the 'writer complex'. Addressing this question, a recent publication by Garcia-Campos and colleagues used an antibody independent sequencing approach to demonstrate that for 16-25 % of methylation sites, the sequence context reliably predicts the methylation status[126]. This supports the idea that the methylation status of many m^{6}A marks is hard coded. However, it does not preclude that a subset of m^{6}A sites are regulated by targeted mechanisms. Another open question concerns the extent to which a dynamic regulation of m^{6}A marks takes place during pre-mRNA processing. Regarding this, the *in vitro* comparison of chromatin associated pre-mRNAs and mature mRNAs has been reported to show little differences in the location and stoichiometry of m^{6}A marks[124]. This suggests that m^{6}A marks which are established during early stages of pre-mRNA processing, remain mostly unchanged throughout later stages.

It is well documented that cellular steady states are characterized by a high correlation between mRNA and protein levels[127] and under these conditions, the dynamic regulation of m^{6}A might not be required. In contrast, during state transitions such as during the maternal to zygotic transition when maternal transcripts have to be rapidly degraded, m^{6}A is used for transcript sorting and facilitates decay[101]. Similarly, cellular heat shock stress requires a prioritization of a small number of transcripts and m^{6}A has been shown to facilitate the cap-independent translation initiation of selected transcripts[102].

Therefore, when faced with challenges to the equilibrium cells might utilize m^{6}A-dependent transcript and site-specific regulation to efficiently prioritize the processing of a subsets of RNAs. In conclusion, while a large number of m^{6}A sites are most likely 'hard coded' and remain unchanged throughout pre-mRNA processing, it is possible that dynamic m^{6}A regulation is required during state transitions or the stress response.

1.5 m^{6}A in the brain

The comparison of different brain regions revealed the existence of brain region-specific m^{6}A patterns and differences in the methylation levels of transcripts[28,128]. Mechanistically, the involvement of m^{6}A in regulating mRNA processing and turnover makes it a prime candidate for coordinating the axonal mRNA transport[129] and regulating the stimulus induced local translation of synaptic proteins[130]. Therefore, in recent years, an increasing number of studies has investigated the role of m^{6}A in regulating central nervous system processes.

1.5.1 m^{6}A is essential for normal brain development

m^{6}A is highly enriched in the mammalian brain[15,128], with methylation levels steadily increasing during development[15]. An analysis of m^{6}A marks in the embryonic mouse cortex revealed an enrichment for genes associated with neurodevelopmental processes[26] and in the cerebellum the m^{6}A landscape has been shown to be developmentally regulated[131]. A crucial role of m^{6}A in the development of the nervous system was demonstrated by several KO studies. The depletion of METTL3 disrupts cerebellar development and results in defective Purkinje cells, the apoptosis of granule cells and increased lethality before P20[132]. Similarly, the depletion of METTL14 results in attenuated proliferation and premature differentiation of neuronal precursor cells during embryonal development[27]. METTL14 KO animals show a reduction in overall brain size with a decrease in late-born neurons and lethality within the first postnatal week[27]. Mechanistically, m^{6}A may destabilize the transcripts of genes coding for histone modifiers that are involved in regulating neuronal development[27]. Accordingly, the depletion of the mRNA degradation promoting m^{6}A ‘reader’ YTHDF2 results in neurodevelopment dysregulation and prenatal lethality[133]. In contrast, the *in vitro* depletion of the m^{6}A demethylases FTO and ALKBH5 does not impair neuronal stem cell proliferation[27]. This suggests that the essential role of m^{6}A for the regulation of neuronal stem cells does not depend on the demethylases FTO and ALKBH5.

In addition, m^{6}A has been shown to regulate postnatal neurogenesis. NestinCre METTL14 KO animals exhibit a prolonged postnatal cortical neurogenesis and an extended cell cycle of radial glia cells[26]. Similar results were obtained for METTL3 depletion[26]. Together, these studies point towards a central role of m^{6}A in shaping neurogenesis and neuronal differentiation, possibly via facilitating the rapid clearance of developmentally regulated transcripts.

1.5.2 Glia cell differentiation is regulated by m^{6}A

Although most investigations into the role of m^{6}A in the brain have focused on neurons, there is some evidence suggesting an involvement of m^{6}A in the regulation of glia cells. The depletion of either METTL3 or METTL14 in glia precursor cells has been shown to result in a prolonged cell cycle of radial glia and decreased numbers of astrocytes[26]. For the oligodendrocyte lineage, the conditional deletion of METLL14 was reported to result in hypomethylation and a reduction in the number of mature oligodendrocytes[134]. In addition oligodendrocyte precursor cells lacking METTL14 were unable to differentiate into mature oligodendrocytes *in vitro*[134]. Complementing these results, a recent study in which the suggested m^{6}A ‘reader’ protein PRRC2A was removed, reported dysregulated oligodendrocyte development and myelination deficits[135]. Together, this points towards a crucial role of m^{6}A in the postmitotic differentiation of glia.

So far, no studies have been published regarding the role of m^{6}A in glia cells of the adult brain. Given the remarkable diversity of glia cells and their involvement in regulating homeostatic processes and neuronal signaling, this remains an intriguing unexplored area.

1.5.3 m^{6}A is required for adult neurogenesis

Adult neurogenesis in the mammalian brain has remained a topic of debate since it was first proposed in the 1960s[136,137]. Today, an increasing body of evidence has been accumulated supporting the existence of adult neurogenesis, particularly in the dentate gyrus of the hippocampus (HPC)[137]. Given the function m^{6}A has been shown to have in regulating stem cell state in embryonal tissue[23,24] and brain development[26,131,132], a similar role in regulating adult neural stem cells is conceivable. This idea is supported by KO studies showing that m^{6}A-dependent regulation is required for the proliferation and differentiation of adult neuronal stem cells. Specifically, FTO KO animals show a reduction in the proliferation and differentiation of adult neural stem cells and deficits in learning and memory[138]. Similarly, the conditional knockdown of METTL3 using shRNA inhibits the *in vitro* proliferation of isolated adult neural stem cells[139]. Interestingly, the depletion of METTL3 was accompanied by a decrease in the histone methyltransferase EZH2 and H3K27me3 marks and the overexpression of EZH2 resulted in a phenotypic 'rescue', providing further evidence that m^{6}A-dependent histone modifications are involved in regulating neurogenesis. Constitutive KO models, as well as *in vitro* experiments are useful for hypothesis formulation but cannot substitute targeted *in vivo* experiments. To unequivocally determine the role of m^{6}A in adult neurogenesis, further experiments are required that investigate this question within the mature adult brain.

1.5.4 Axon guidance and regeneration depends on m^{6}A signaling

Coordinated axon guidance is a prerequisite for the normal development of the nervous system and mutations in axon guidance factors have been associated with neurological disorders[140]. Recently it has was shown that *Fto* transcripts are locally enriched and translated within axons and that a depletion of axonal FTO results in increased m^{6}A levels and shorter axons[141]. Removing the m^{6}A 'writer complex' components METTL3 or METTL14 has the opposite effect and induces axonal overgrowth at the neuromuscular junction in *D. melanogaster*[121]. This suggest that m^{6}A is required for containing axonal growth within normal levels. In the fly, this regulation may be mediated via the fly orthologs *Ythdf* and *Fmr1*, with no involvement of the YTH domain 'reader' protein *Ythdc1* fly homologue[121].

A recent study of peripheral nerve lesions suggests that m^{6}A has the opposite effect in the nervous system's response to injury[142]. Sciatic nerve lesion triggers an increase in methylation levels and translation of transcripts required for nerve regeneration. The deletion of either METTL14 or YTHDF1 has been reported to repress this response[142] suggesting that m^{6}A signaling is required for axon regeneration. Similarly, in the central nervous system, *Pten* deletion induced axon regeneration of retinal ganglion cells is disrupted by shRNA mediated knockdown of *Mettl14*[142]. Together, this suggests that m^{6}A can either repress or facilitate axonal growth, depending on the developmental stage and context.

The effect of m^{6}A on axon guidance might be mediated through the regulation of transcripts encoding axon guidance factors. For the axon guidance factor Robo3, the targeted mutation of selected methylation sites, or respectively a depletion of METTL3 using shRNA, resulted in reduced protein levels without affecting mRNA abundance[98]. Conversely, an overexpression of YTHDF1 had the inverse effect, suggesting that Robo3 levels are regulated through an m^{6}A-dependent mechanism involving YTHDF1[98]. This raises the question whether other axon guidance molecules such as ephrins, netrins and semaphorins are similarly regulated and how a differential regulation could be achieved.

1.5.5 Regulation of synaptic transcripts through m^{6}A

While the molecular mechanisms of learning and memory are not fully understood, it is established that experience driven changes in synaptic connectivity play a central role. To establish the long lasting changes in synaptic strength required for learning, the production of new proteins is required[143–145]. Since neurons have to be able to tune the individual strength of synaptic connections, translation has to be regulated locally. For this to happen, transcripts associated with synaptic plasticity have to be selectively processed in response to neuronal activity. Recently, it has been proposed that m^{6}A might be involved in the local translation at the synapse[130]. This idea was supported by the observation that in the mouse forebrain hypermethylated transcripts are enriched for synaptic functions, with 4,469 m^{6}A sites being detected within 2,921 synaptosomal transcripts[130]. Functionally, the depletion of the dendritically localized 'reader' proteins YTHDF1 and YTHDF3 resulted in reduced spine volume, attenuated miniature excitatory post synaptic potentials and a reduction of synaptically located PSD-95 and Glu[130]. Together, these observations point towards an m^{6}A-dependent local regulation of synaptic proteins.

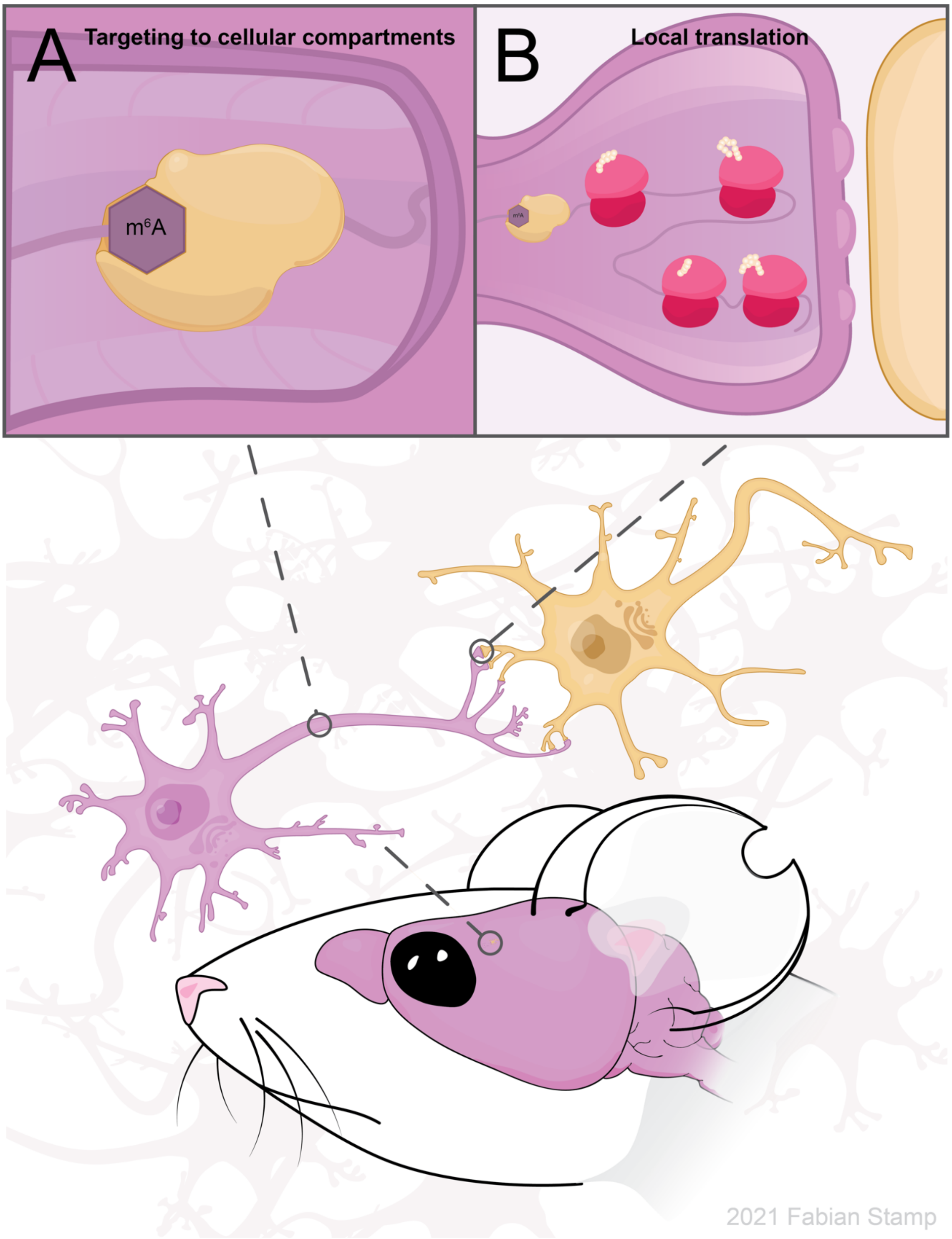

Figure 5: Tentative roles of m^{6}A in regulating neuronal functions

Among the tentative roles suggested for m^{6}A in the brain are the targeting of methylated transcripts to different neuronal compartments[129] **(A)** and the regulation of local translation in axons and at the synapse[130,141] **(B)**.

1.5.6 m^{6}A regulation is involved in learning and memory

Region-specific m^{6}A patterns and differences in methylation levels have been described for the cortex, amygdala and cerebellum[28,128] and recently it has been shown that the m^{6}A landscape shows brain region-specific changes in response to experience. Specifically, emotional stress induced an overall upregulation of m^{6}A marks in the mPFC and conversely a downregulation in the amygdala[28]. This raises the intriguing possibility that experience induced differential m^{6}A regulation plays a role in regulating synaptic plasticity. In support of this idea, an increasing number of studies has shown that disturbances of m^{6}A regulation modulate learning and memory[28–30,138,146,147].

The majority of studies that have been published on the role of m^{6}A regulation in behavior have employed contextual fear conditioning paradigms, with a few using delayed fear conditioning, the Morris water maze (MWM) test and other paradigms. One shock fear conditioning has been reported to induce a local downregulation of *Fto* mRNA in the mPFC within half an hour of conditioning, with the FTO protein being selectively depleted in the synaptosomal fraction[147]. Concomitantly, m^{6}A levels in the mPFC are increased temporarily suggesting that m^{6}A regulation might be involved in coordinating the transcriptomic response required for learning. Conversely, the knockdown of FTO in the dCA1 with Cas9-Fto or shRNA has been found to enhance contextual fear memory[147]. This finding was corroborated by experiments using a NexCreERT2 driver line that targets projection neurons in the cortex and HPC[28]. Surprisingly, here the increased contextual memory of FTO KO animals was accompanied by a decrease in HPC LTP[28]. In contrast, constitutive FTO KO animals, despite being viable, show pronounced learning and memory deficits[138]. Given the importance of m^{6}A regulation for normal development and neuronal differentiation, this might be attributed to altered developmental trajectories. In the midbrain, FTO has been shown to be involved in regulating dopaminergic signaling, with DAT-Cre KO animals showing a reduced locomotor response to cocaine[148].

Studies targeting components of the m^{6}A ‘writer complex’ have focused on manipulations of METTL3 and METTL14. The conditional KO of METTL3 using a NexCreERT2 floxed mouse line has been shown to result in increased cue but not contextual fear memory, with METTL3 KO animals showing impaired fear extinction, normal short-term plasticity and LTP[28]. Complementing these observations, Camk2aCre METTL3 KO animals exhibit reduced contextual fear memory, attenuated learning in the MWM and show a significantly decreased LTP in the dCA1[29]. Considering the differences in timing and penetrance of the KO, NexCreERT2 is chemically induced while the Camk2aCre driven KO starts around the third postnatal week[149], these results might not contradict each other but underline the context dependent role of m^{6}A regulation. In addition, the depletion of METTL14 in the striatum has been reported to result in increased excitability and attenuated spike frequency adaptation of striatonigral neurons as well as impaired striatum-dependent learning[150]. A study of the m^{6}A ‘reader’ YTHDF1 reported impaired spatial learning of KO animals in the MWM[30]. YTHDF1 full KO mice showed an increased latency to find the hidden platform across training days and reduced time in the target quadrant during the probe test. In addition, KO animals were reported to show impaired contextual fear learning, impaired LTP and decreased spontaneous miniature excitatory postsynaptic currents in the dCA1. These phenotypes were ‘rescued’ by AAV mediated overexpression of YTHDF1 in the HPC. As with the learning impairments reported for METTL3[29], the observed alterations in behavior were subtle and most evident under challenging learning conditions. Molecularly, Shi et al. reported a reduction of key glutamate receptor subunits and other proteins required for synaptic plasticity.

The study of m^{6}A regulators in the brain shows that m^{6}A is regulating the processing of neuronal transcripts and protein synthesis. As a result, alterations in the levels of m^{6}A regulators affect plasticity processes and this is most evident in learning and memory tasks. Considering that manipulations of the ‘writer’ component METTL3 and the ‘reader’ YTHDF1 result in phenotypically similar outcomes raises the question whether manipulations of other YTH-family m^{6}A ‘readers’ recapitulate this phenotype. Overall, more research will be required to disentangle the contribution of individual m^{6}A regulators to neuronal processes.

2. Aims and objectives

Previous research on m^{6}A regulation in the mammalian brain has focused on a few crucial regulators. These include the catalytic core complex (METTL3-METTL14), the m^{6}A ‘eraser’ FTO and the m^{6}A ‘reader’ YTHDF1. The contribution of other m^{6}A regulatory factors, including WTAP and YTHDC1 has not been reported so far.

The main aim of this thesis is to make a substantial contribution to our understanding of the role the m^{6}A regulatory proteins WTAP and YTHDC1 play in the mammalian brain. To this end, the effect of losing either regulator on gene expression, protein abundance, metabolism, neuronal signaling, brain anatomy and behavior was investigated. For this, two conditional KO mouse strains were used that allow the cell type specific depleting of WTAP or YTHDC1 in either Camk2Cre or NexCreERT2 expressing neurons.

The thesis has the following objectives: (1) To characterize changes in gene expression and splicing following the loss of WTAP and YTHDC1 respectively, with poly (A) RNA sequencing. (2) To assess whether changes in gene expression affect protein abundance using LC-MS. (3) To investigate the effect the KO has on the metabolic state of the tissue with LC-MS. (4) To explore the consequences for neuronal signaling and brain anatomy using electrophysiological measurements and MRI. (5) To identify changes in behavior arising from the observed molecular alterations, with classical tests and home cage activity monitoring.

3. Material and methods

3.1 Animal husbandry and strain details

Animal husbandry and ethics

Animal housing and handling followed national regulations. Animal handling and experimental procedures were carried out by trained personal only. Mouse strains were bred at the Max Planck breeding facilities located in-house and in Martinsried (Planegg, Germany). Animals were housed in groups of 4-5 in individually ventilated cages (IVC, 30 x 16 x 16 cm) at 22 ± 2 °C (50-60 % humidity) on a 12:12 h light-dark cycle with food and water ad libitum. If not otherwise specified, experimental groups consisted of adult (≥ 8 weeks), group housed, same sex, age-matched animals.

Genotyping

The genotype of transgenic animals was determined using gel-based genotyping. Genomic DNA was extracted from tail biopsies. Samples were incubated with 100 µl 50 mM NaOH for 30 min at 95-99 °C in 96 well plates using a thermal cycler. Reactions were neutralized with 30 µl 1 M Tris-HCl (pH 7.0) and stored at -20 °C until further use. For the PCR, 1 µl of DNA extract was incubated with 0.04 µl of each primer, 0.4 µl deoxynucleoside triphosphate (dNTP: 10 mM, Invitrogen), 2 µl of reaction buffer (10X DreamTaq Buffer, ThermoFischer Scientific), 18 µl of ddH$_2$O and 0.1 µl of DreamTaq-DNA-Polymerase (ThermoFischer Scientific).

The PCR amplicons were separated using agarose gel electrophoresis (300 mA, 160 V, 1.5-2 h, 1.5-3.5 % agarose gel) and visualized with an ethidium bromide staining (5 µl / 500 ml, Carl Roth) under UV light.

Mouse strains

A detailed overview of the genetic loci of the floxed lines used in the presented thesis, as well as the description and details of the genotyping can be found in Appendix 8.1.

C57BL/6 and CD1

C57BL/6 and CD1 male mice obtained from the Max Planck Institute of Psychiatry breeding facility (Martinsried, Germany) were used for generating tissue for control experiments. CD1 mice were also used for breeding with C57BL/6 transgenic lines to obtain white-furred animals.

Camk2aCre

Tg(Camk2a-Cre)93Kln. (MGI:2176754) C57BL/6 males[149] were backcrossed with CD1 females over several generations to obtain white animals. Cre driver animals where then crossed with *Wtap*$^{tm1c(EUCOMM)Hmgu}$ and *Ythdc1*$^{tm1c(EUCOMM)Wtsi}$ mice, to acquire white animals for behavior and molecular screenings.

NexCreERT2

Neurod6$^{tm2.1(cre/ERT2)Kan}$ (MGI:5308766) Cre-driver mice[151] were crossed with *Wtap*$^{tm1c(EUCOMM)Hmgu}$ and *Ythdc1*$^{tm1c(EUCOMM)Wtsi}$ mice, resulting in tamoxifen inducible, conditional KO strains.

Ai9

Gt(ROSA)26Sor$^{tm9(CAG\text{-}tdTomato)Hze}$ mice (MGI:3809523) carrying a reporter construct consisting of a loxP-flanked STOP cassette controlling the expression of the red fluorescent tdTomato protein inserted into the Rosa26 locus was used as endogenous Cre reporter[152]. This strain was crossed with Camk2aCre and NexCreERT2 carrying animals to visualize Cre activity.

Mettl3

The *Mettl3*$^{tm1c(KOMP)Wtsi}$ strain, derived from *Mettl3*$^{tm1a(KOMP)Wtsi}$ (MGI: 4363451), originally generated by Geula and colleagues[24], was used for the conditional METTL3-WTAP KO experiments. In this strain a critical region, containing exon 4, is flanked by two loxP sites that can be recognized by the Cre recombinase, resulting in a functional deletion of the METTL3 protein.

Wtap

Wtap$^{tm1a(EUCOMM)Hmgu}$ (MGI:4434984) KO first allele animals were obtained from MRC Harwell (Oxford, UK). The tm1a KO-first allele contains two FRT sites flanking a LacZ and neomycin cassette between exon 3 and 4, as well as two loxP sites flanking exon 4 and 5. *Wtap* tm1a animals were crossed with mice carrying the Flp recombinase resulting in the deletion of the neomycin and lacZ cassettes located between the FRT sites. The resulting tm1c mice were bred to NexCreERT2 and Camk2aCre driver lines to obtain experimental cohorts. For phenotypic screening, C57BL/6 Wtap tm1c males were backcrossed over several generations with CD1 females before the respective Cre drivers on CD1 background were crossed into the line. *Wtap*-NexCreERT2 animals were generated by crossing *Wtap* tm1c mice with C57BL/6 NexCreERT2 animals. CD1-*Wtap*-Camk2aCre animals were acquired by crossing *Wtap* tm1c animals with CD1-Camk2aCre animals. *Wtap*-*Mettl3*-NexCreERT2 double floxed animals were created by crossing *Wtap*-NexCreERT2 tm1c animals with *Mettl3* tm1c animals.

Experimental animals were Cre-positive (lox/lox, +/Cre) and Cre-negative (lox/lox, +/+) littermates obtained by breeding heterozygous Cre-carrying animals (lox/lox, +/Cre) with Cre-negative (lox/lox, +/+) animals.

Ythdc1

Ythdc1$^{tm1a(EUCOMM)Wtsi}$ (MGI:4432642) KO first allele animals were obtained from CAM-SU GRC (Soochow University, China). The tm1a KO-first allele contains two FRT sites flanking a LacZ and neomycin cassette upstream of exon 5. The critical exons 5-7 are flanked by two loxP sites. *Ythdc1* tm1a animals were crossed with Flp deleter mice, resulting in the deletion of the neomycin and lacZ cassettes located between the FRT sites. The resulting tm1c mice were bred to NexCreERT2 and Camk2aCre drivers to obtain experimental cohorts.

Experimental animals were Cre-positive (lox/lox, +/Cre) and Cre-negative (lox/lox, +/+) littermates obtained by breeding heterozygous Cre-carrying animals (+/lox, +/Cre) with Cre-negative (lox/lox, +/+) animals.

3.2 Tamoxifen administration

The tamoxifen-inducible Cre recombinase (CreERT2) was activated as previously described[151]. In brief, a solution of 10 mg/ml Tamoxifen was prepared from tamoxifen powder (Sigma-Aldrich) which was first dissolved in 100 % ethanol (5 % of final volume, Fisher BioReagents) before sterile filtered corn oil (Sigma-Aldrich) was added. Complete dissolution was achieved by incubating the tamoxifen solution for several hours at 50 °C in a water bath. During this incubation, the solution was vortexed from time to time. The tamoxifen solution was prepared fresh before each experiment and aliquots were stored at -20 °C until further use. Tamoxifen was administered via i.p. injections following the approved experimental protocol.

For the induction of CreERT2 activity, animals were injected on 5 consecutive days with 100 mg/kg tamoxifen each day (i.p.). The weight of animals was closely monitored and the dosage adapted for each day. The induction was followed by a 14 day wash out period, after which tamoxifen is not detectable anymore in the blood plasma of mice[153]. However, it has to be noted that residual tamoxifen is retained in adipose tissue and has been shown to exert CreERT2 nuclear translocation even two months after the last dosage[154]. To control for potentially confounding effects of tamoxifen persisting after the wash out period, all experimental groups received tamoxifen.

3.3 Tissue collection

Animals were euthanized with isoflurane (CP-Pharma) following the approved animal protocol. Depending on further processing, animals were either decapitated using a pair of scissors, or prepared for perfusion. Two pieces of tail were collected per animal for re-genotyping.

Fresh tissue dissections

Immediately after decapitation the brains were dissected from the cranial cavity using fine scissors and transferred into sterile filtered ice-cold phosphate-buffered saline (PBS) slush (< 4 °C). The time of sacrifice was noted, and a stop watch set to record the dissection time. Brains were cut in coronal slices using a 1 mm brain matrix (Zivic instruments; 5325) and commercial razor blades (Wilkinson Sword). For dissections of the HPC, the first cut was made at approximately Bregma -3.8 mm. Using multiple razor blades several 1 mm sections were cut with the brain remaining in the metal matrix. For dissections of the mPFC, the whole brain was cut into 1 mm slices. The slices where quickly transferred onto a 6 % agar filled plate covered in ice cold sterile filtered PBS slush. Using a brush, slices were sorted and arranged on the agar plate. The coordinates of individual cuts were noted, and slices fixed to the agar using 30 G sterile syringes (BD). The dissection of regions of interest, as illustrated in Figure 6, was conducted under a binocular using a medical °15 stab knife (Tecfen Medical). Tissue samples were collected in 1.5 ml DNA/protein low bind tubes and immediately transferred to dry ice. The duration of dissection was noted for each individual sample. Depending on the number of regions to dissect per brain, the average dissection time ranged from 5 to 20 min. Samples were stored at -80 °C until further use.

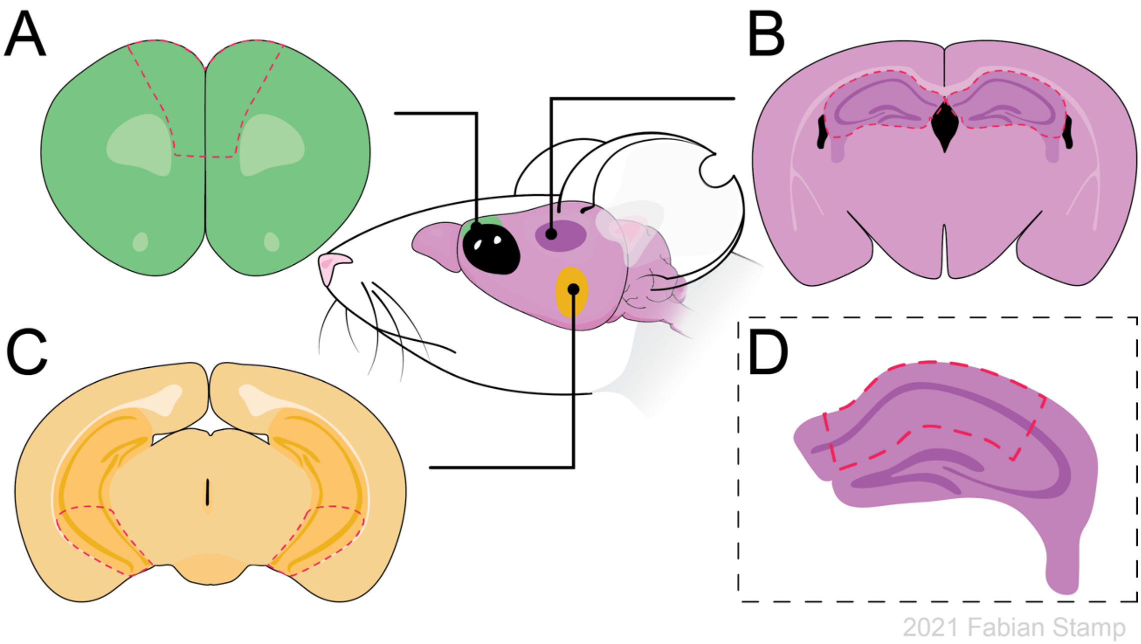

Figure 6: Fresh tissue dissection for molecular analysis
(A) mPFC representative dissection area. **(B)** dHPC representative dissection area. **(C)** vHPC representative dissection area. **(D)** dCA1 representative dissection area.

Frozen tissue collection

Brains were quickly dissected from the sculls after decapitation and dropped into a beaker filled with pre-chilled methyl butane for flash freezing. After a few seconds, the brains were removed using a metal scoop and transferred into multiwell plates on dry ice. Brains were stored at -80 °C until further use. For region-specific samples, frozen brains were cut using a cryostat at -12 to -16 °C. Regions of interest were punched from 200 µm slices using stainless steel punchers (0.35 mm, 0.5 mm, 0.8 mm, 1 mm) and collected in DNA low bind tubes. After processing, samples were kept at -80 °C until further use. For *in-situ* hybridization (ISH) brains were cut in 20 µm slices using a cryostat and collected at room temperature (RT) on glass slides. After drying at RT, slides were stored at -20 °C until further use.

Fixed tissue collection

For the perfusion, animals were euthanized as described above and the rib cage opened to grant access to the heart. The left heart ventricle was punctured using a syringe and the mouse was flushed with saline (0.9 % NaCl, 300 USP heparin / l, Sigma-Aldrich) using a perfusion pump system. The right atrium of the heart was cut open to allow the solution to exit. After flushing (~ 5 min), the mouse was perfused with 4 % paraformaldehyde (PFA, Carl Roth) in PBS for 4-5 min. The brain was dissected from the cranial cavity and collected in a 15 ml falcon tube containing 4 % PFA for post fixation on a shaker (4 °C, overnight). Afterwards, brains were dehydrated in 30 % saccharose at 4 °C (1-3 days). Depending on further processing, brains were either snap frozen in methylbutane or cut using a vibratome. For cutting with the vibratome, brains were embedded in 5 % agarose in 1 x PBS. Coronal/sagittal slices (50 µm) were cut and either directly mounted on SuperFrost Plus™ slides (Thermo Scientific), or stored in anti-freezer (250 ml ethylene glycol, 250 ml glycerol, 500 ml 1 x PBS) at -20 °C.

3.4 *In situ* hybridization

The location and efficacy of Cre-mediated exon deletions was assessed with radioactive ISH as previously described[155,156]. Briefly, flash frozen brains were cut on a cryostat (Leica Biosystems) at -14 to -16 °C into 20 µm coronal sections. Slices were thaw-mounted in 4 series on SuperFrost Plus™ slides (Thermo Scientific), dried and stored at -20 °C until further use. Sections were fixed with 4 % PFA (Carl Roth), acetylated (0.25 % acetic anhydride in 0.1 M in triethanolamine-HCl) and dehydrated in a graded series of ethanol. Complementary riboprobes were transcribed from linearized plasmids and sections incubated with 100 µl of hybridization mix (50 % formamide, 20 mM Tris-HCL pH 8.0, 300 mM NaCl, 5 mM EDTA pH 8.0, 10 % dextran sulphate, 0.02 % Ficoll 400, 0.02 % PVP40, 0.02 % BSA, 0.5 mg/ml tRNA, 0.2 mg/ml carrier DNA, 200 mM DTT) containing 35,000-70,000 cpm/ µl ^{35}S-labeled riboprobes overnight at 55 °C. On the next day, sections were washed with 4 x saline-sodium citrate (SSC), treated with RNaseA (20 µg/ml) and washed with SSC solutions of decreasing stringency at RT. At last, sections were dehydrated with a graded series of ethanol and air dried. Slides were exposed to BioMax MR films (Eastman Kodak Co.) for several days before development.

The following exon-spanning, antisense ^{35}S UTP-labeled ribonucleotide probes were used for ISH: *Mettl3* (exon 4, 175 bp,[28]), *Wtap*,(exon 4-5, 170 bp), *Ythdc1* (Exon 5-7, 232 bp). Details can be found in Appendix 8.7.

3.5 Animal behavior

All preclinical procedures were conducted in accordance with the recommendations of the Federation for Laboratory Animal Science Associations (FELASA), the Society of Laboratory Animal Sciences (GV-SOLAS) and authorized by the ethics committee of the government of higher Bavaria (Munich). Animal behavior was assessed during dark phase if not otherwise specified. The experimenter was blind to the genotype during handling and testing of animals.

Open field test

The open field (OF) test is used to assess locomotor activity, exploratory drive and anxiety-like behaviors[157]. The test was performed using a gray, plastic box with dim lighting (50 × 50 × 50 cm, 10-15 lux). Animals were recorded for 10 min and the time spent in the center zone (innermost 25 x 25 cm) vs the outer zone was determined using the automated ANY-Maze video tracking software. The parameters compared between experimental groups include total distance travelled and time in the center. Before each test the arena was cleaned with soap water, water and then wiped dry.

Elevated plus maze

The elevated plus maze (EPM) is used to test exploratory drive and anxiety-like behaviors[158]. Animals were placed in an EPM in which they could freely choose between two enclosed and two open arms. This test was performed using a custom-made, gray, plastic maze with medium lighting (50 × 50 cm, elevated 25 cm, 10 lux closed arms, 40 lux open arms). Animals were placed in the mace facing the entry of a closed arm and recorded for 10 min using ANY-Maze. The time spent in the closed/open arms and the overall activity was compared between experimental groups to assess anxiety-like behaviors. Before each test the arena was cleaned with soap water, water and then wiped dry.

Dark/light transition test

The dark/light transition test takes advantage of the aversion mice have for brightly lit areas, as well as the innate exploratory drive to asses anxiety-like traits in mice[159,160]. Animals were placed in the dark compartment (15 x 27 x 28 cm, < 5 lux) of a two-chamber box consisting of a dark and a brightly lit arena and recorded for 10 min. The latency until the first exit from the dark compartment, the number of transitions, the time spent in and distance travelled in the lit compartment (31 x 27 x 28 cm, ~140 lux) were recorded using ANY-Maze. Before each test, the arena was cleaned using soap water, water and then wiped dry.

Fear conditioning

Fear conditioning was assessed using an established screening procedure that combines the assessment of conditioned and contextual fear[28,161]. Animals were fear conditioned using the Ugo Basile Fear Conditioning system and EthoVision XT software (Noldus). Conditioning was performed in context A (plastic cubicle with metal grid floor 17 x 17 x 36 cm, light 30 %) cleaned with 70 % ethanol prior to each trial. Contextual memory was assessed by returning the animals to context A. Cue memory was measured in a neutral context B, consisting of a hexagonal cubicle (diameter: 13, height: 30 cm; light 5 %) with fresh bedding and cleaned with 1 % acetic acid prior to each trial. If not otherwise indicated, animals were conditioned with a 2 s shock applied via the metal floor grid. The shock intensity varied between 0.6-0.8 mA, as specified in the respective experimental details. Except for the contextual memory test, each test started with a habituation phase of 3 min and ended with a post stimulus period of at least 60 s. For assessing memory strength, freezing was quantified using EthoVision XT. Changes in individual pixels between consecutive frames are registered and an activity score (% change in pixels between two frames) is calculated. The experimenter determines the activity threshold separating noise from animal movement. For the presented results, freezing is defined as the absence of any movement for a period of at least 1 s. The data analysis was performed in R as described below.

Delay fear conditioning protocol

Delay fear conditioning refers to paradigms in which a cue and shock are presented simultaneously[161]. On the day of conditioning (day 0), animals are placed in context A for 3 min of habituation. A neutral stimulus (tone: ~9-10 kHz, 70-80 dB) is presented for 20 seconds and co-terminated with a shock (2s, 0.6-0.8 mA). Animals remained in the conditioning context for another minute before being returned to their home cage. Cued and contextual memory are tested on the following two days. On day 1, animals are introduced to a neutral environment (context B) for a habituation of 3 min after which the tone is presented for 3 min, followed by a post-cue period of 1 min. On day 2, animals are returned to the conditioning context (context A) for 5 min to assess contextual memory.

Morris water maze

Mice were trained in the MWM[162] using a circular, white pool (diameter 150 cm, height 40 cm) filled with temperate tab water (21-23 °C). The pool was divided into four quadrants of equal size (NW, NE, SW, SE) with a transparent platform placed into the NW quadrant (12 cm diameter, submerged ~1 cm below water level). The walls of the experimental room were dimly lit (~ 15 lux), to reveal distinct geometric shapes (square, cross, circle, triangle) serving as landmarks for orientation.

Animals were trained in navigating to the hidden platform in 4 trials each day on 6 consecutive days. For each trial animals pseudo-randomly started from alternating quadrants (balanced design across quadrants) with each trial lasting a maximum of 60 s. Mice that failed to find the platform during a trial where guided towards the platform using a spatula. Animals had to remain on the platform for at least 10 seconds before being returned to their home cage. In between trials animals were allowed to recover for at least 15 min before being tested again. During that time animals were free to choose between a cool or an infrared lit warm area in their home cage. The position of animals during trials was tracked using ANY-maze to determine the time spent in each quadrant, as well as the distance, the direction and latency to reach the platform.

At the start of the 4th and 7th day, animals were tested for their spatial memory. Therefore, the platform was removed from the pool and mice were placed into the pool for a trial of 60 s. Following the 6-day training, animals were subjected to reversal learning. For this, the platform was placed in the opposite quadrant (SW) and animals were trained for 3 consecutive days (starting on day 7) to memorize the new position. On day 10 reversal learning was assessed with one 60s trial. 7 days after the last test, animals were returned for one more trial (60s), to assess memory retention.

Visible platform training

Impairments in the vision of animals was tested using the visible platform training which is often used to habituate animals to the water before a classical MWM training. For this, the MWM setup described above was used, with the visible landmarks being removed from the walls of the test room. Animals underwent 4 trials (60 s), starting from a fixed location while the position of a visible platform was altered across trials. The latency to reach the platform was recorded and animals that failed to find the platform within the test time, were gently guided towards it. In between trials, animals were allowed to recover as described above.

Home cage activity screening

Home cage activity of individual animals was assessed using passive ultra-compact infrared sensors (INFRA-E-MOTION GmbH, Germany; firmware: 3.7). Animals were single-housed for 7 consecutive days, with additional bedding but without tunnel and nesting material. The infrared sensor located on top of the feeding tray detects activity with a resolution of 1 s, returning the number of events per 60 s. During the recording, the setup and animals were checked daily while avoiding any disturbance. The data was analyzed as described below.

Behavior data analysis

If not otherwise indicated, all statistical data analysis was conducted with R in RStudio[163,164]. Details regarding the packages used for data manipulation, statistical analysis and visualization can be found in Appendix 8.2.

For group comparisons, the results were visualized as box plots with whiskers showing individual sample values, the median (horizontal line) and group means (diamond). For time series, mean group values were plotted per time bin with the 95 % confidence intervals indicated by the error bars if not otherwise indicated.

Comparison of two groups

The data were first tested for normality (Shapiro-Wilk test) and homogeneity of variance (Levene’s test). For normally distributed data, the independent two-sample t-test or Welch's t-test (assumption of homoscedasticity violated) was used. For non-normal distributed data, the non-parametric Wilcoxon test was used. Multiple testing correction was applied using the false discovery rate (FDR, Benjamini and

Hochberg adjustment). Significance levels are indicated as: not significant (ns) $p > 0.05$; *: $p \leq 0.05$; **: $p \leq 0.01$; ***: $p \leq 0.001$; ****: $p \leq 0.0001$.

Comparison of more than two groups

Data were first analyzed using linear regression analysis in R. in brief, linear models were constructed and the fit, as well as assumptions of linearity and homoscedasticity examined. Reported in this thesis is the analysis of variance (ANOVA) that was applied for normally distributed data if not otherwise indicated. A Tukey's post hoc test for multiple comparisons was used to determine groups that significantly differ from each other. For non-normally distributed data, the non-parametric Kruskal-Wallis test was applied, followed by the Dunn post-hoc test. Significance levels are shown as: not significant (ns) $p > 0.05$; *: $p \leq 0.05$; **: $p \leq 0.01$; ***: $p \leq 0.001$; ****: $p \leq 0.0001$.

Generalized additive models

For the analysis of continuous fear conditioning data and home cage activity the data were analyzed in R using generalized additive models (GAM).

For the analysis of freezing across time, a logistic regression analysis was performed with freezing per second as the dependent variable (0/1) and genotype, sex as the dependent variables with a random intercept for animal. Time and tone were included in the models smoothing terms without assuming linearity. The model formula and results are reported in the respective sections of the Appendix.

The continuous recordings from the home cage activity measurement were also analyzed using GAMs with the dependent variable mean activity (10 min bins), the independent variables genotype, sex and time.

3.6 Gene expression analysis

RNA extraction, quality control and quantification

Total RNA was extracted from brain samples using QIAzol Lysis Reagent (QIAGEN) and RNeasy mini kits (QIAGEN), according to manufacturer's specification. Residual gDNA was removed either on a column using the RNase-Free DNase Set (QIAGEN), or after extraction using TURBO DNase (ThermoFisher Scientific: AM2238). RNA yield was measured using the Qubit™ RNA BR/HS Assay (Thermo Fisher Scientific) and sample purity measured with the Nanodrop 2000 spectrophotometer (Thermo Scientific). The integrity of RNA used for poly-(A) sequencing was assessed with the 2200 TapeStation (Agilent) or 2100 Bioanalyzer (Agilent).

Primer design and validation

For validating changes in gene expression and splicing, targeted primers were designed. Whenever possible, exon spanning primer pairs were chosen to prevent the amplification of residual gDNA. qPCRs with non-exon spanning primers were run with DNase treated samples. For genes containing multiple exons, primers were picked preferentially for the last exons that are more likely detectable in partially degraded RNA. Primers were designed based on the sequence information provided by the UCSC Genome Browser and with the help of the website Primer3web (https://primer3.ut.ee). For qPCR application, the amplicon size was set to 75-250 base pairs (bp). The specificity of primer pairs was verified using the primer-blast service from NCBI (https://www.ncbi.nlm.nih.gov/tools/primer-blast/). Additionally, an in-silico PCR was performed using the UCSC in silico PCR tool (http://genome.ucsc.edu/cgi-bin/hgPcr).

For each target 2-3 primer pairs were designed and validated for their efficiency and specificity using qPCR before application in an experiment. Therefore, a 1:5 dilution series with 6 steps were prepared from wild type (WT) brain cDNA (RNA stock: 20 ng/µl). SYBR green master mixes were prepared according to manufactures specifications and with primers diluted to 10 µM. The standard curve was run as quadruplicates in 10 µl reaction volumes on a 384 well plate using QuantStudio 7. Two no template controls (NTC) were included for each primer pair, to identify contaminations. To calculate the slope of the standard curve, Ct values of individual dilution steps were averaged and plotted against the log values of the dilutions. At least 4 dilution steps were used for calculating primer efficiency. The primer efficiency (%) was calculated using the formula:

$$Efficiency\ (\%) = [10^{\frac{-1}{slope}} - 1] * 100$$

Primers with an efficiency of 90-110 % were considered for experimental application. The specificity of primers was assessed by checking the melt curve and running the PCR product on an agarose gel (2-3.5 % agarose). Primers showing evidence of primer dimers (at Ct 25-30), or multiple products after electrophoresis, were excluded.

Reverse transcription quantitative PCR (RT-qPCR)

Changes in gene expression were measured using quantitative reverse transcription PCR (RT-qPCR). Therefore, total RNA was converted to cDNA using the High-Capacity cDNA Reverse Transcription Kit with RNase Inhibitor (Applied Biosystems) according to manufacturer’s instructions. The cDNA was diluted (1:20-1:40) and measured using the SYBR dye (QIAGEN) in 10 µl reaction volumes (384-well format) on the QuantStudio™ 7 Flex Real-Time PCR System (Applied Biosystems). Samples were measured with technical duplicates/triplicates and NTCs.

qPCR data analysis

The relative gene expression of KO compared to WT samples was calculated using the delta-delta Ct ($2^{-\Delta\Delta Ct}$) method. Mean CT values across technical replicates per sample were calculated for each gene. For the normalization of gene expression, *Rpl13a* and *Polr2b* were chosen as reference genes. The DCT (ΔCt = Ct (gene of interest) - geometric mean (Ct reference genes)) and DDCT (ΔΔCt = ΔCt (average KO sample) - ΔCt (average WT samples)) was calculated and used to determine the relative fold gene expression (FoldChange: 2^-(ΔΔCt)). Before testing for group differences, the data were transformed to the log2 scale (Log2FoldChange). All statistics were run on the Log2FoldChange of normalized expression values using the appropriate parametric or non-parametric tests. In brief, the log2-transformed data were first tested for normality (Shapiro-Wilk Test) and homogeneity of variance (Levene’s Test). For normally distributed data, the Student’s independent two-sample t-test or Welch's t-test (assumption of homoscedasticity violated) was used. For non-normal distributed data, the non-parametric Wilcoxon test was used. Multiple testing correction was applied using the false discovery rate (FDR, Benjamini and Hochberg adjustment). Significance levels are shown as: not significant (ns) $p > 0.05$; *: $p \leq 0.05$; **: $p \leq 0.01$; ***: $p \leq 0.001$; ****: $p \leq 0.0001$.

Poly(A) RNA sequencing

RNA Sequencing libraries were prepared using the NEBNext Ultra II Directional RNA Library Prep Kit for Illumina platforms (New England Biolabs) according to manufacturer’s instructions, with an initial input amount of 200 ng DNase I treated total RNA. For the *Wtap*-NexCreERT2 samples, libraries were sequenced on 2 x lanes of the Hiseq4000 (1 x 75 bp, single end). The output was ~ 56 million reads per sample.

The *Ythdc1*-NexCreERT2 libraries were prepared using the same kit and treated with Illumina's Free Adapter Blocking Reagent (Illumina) and sequenced on 1 x lane of the NovaSeq 6000 (2 x 100 bp, paired end). The output was ~78 million reads per sample.

3.7 Bioinformatic analysis of RNA sequencing

The pre-processing of the raw data and differential expression analysis was done with support from the Israel National Center for Personalized Medicine (INCPM) at the Weizmann Institute of Science (Israel). Specifically, the bioinformatic pre-processing and analysis using DESeq2 and DEXSeq were performed by E. Weizmann. Subsequent analysis steps, including the pathway analysis, data interpretation and visualization were done by F. Stamp. Below is a summary of the processing and analysis steps.

Pre-processing, differential expression and exon count analysis

The pre-processing and differential expression analysis was done as previously described[165] and the analysis pipeline was run using snakemake[166]. In brief, poly-A/T stretches and Illumina adapters were trimmed from the reads using cutadapt[167] and resulting reads shorter than 30 bp were discarded. The trimmed reads were mapped to the *M. musculus* reference genome GRCm38 using STAR[168], supplied with gene annotations downloaded from Ensembl (EndToEnd option, outFilterMismatchNoverLmax = 0.04). Expression levels for each gene were quantified using htseq-count[169].

Differentially expressed genes were identified using DESeq2[170] with the betaPrior, cooksCutoff and independentFiltering parameters set to ‘False’. All statistics were run on the Log2FoldChange of normalized expression values. Shrinkage of the observed effect sizes (Log2FoldChanges) was applied for visualization and ranking of results to reduce the high variability often observed in lowly expressed genes[170]. The obtained p-values were corrected for multiple testing using the Benjamini and Hochberg method.

Genes with differential exon usage were identified using DEXS-seq[171]. This approach does not look at splicing events and cannot estimate isoform abundance but instead tests for differences in exon usage. For this the relative exon usage is defined as:

$$\frac{Reads\ mapping\ to\ the\ target\ exon}{Reads\ mapping\ to\ any\ other\ exon\ of\ the\ same\ gene}$$

In brief, the number of reads mapping to a specific exon are counted, as well as the number of reads mapping to any other exon of that gene. The resulting ratio is compared first across replicates and then between conditions to determine relative changes in exon usage. If the overall expression of the target gene changes but the abundance of an exon remains the same, this ratio will not change. It is important to note that DEXSeq does not run the statistics on the ratio but uses the counts in the numerator and denominator. Therefore, the magnitude information contained in the individual values is preserved and the resulting estimates are more reliable.

To test for differential exon usage, DEXSeq calculates the dispersion estimates (within group variability) and size factors and fits a generalized linear model of the negative binomial family. A comprehensive description of the method can be found in the original publication[171]. An example of the analysis output is shown in Figure 7.

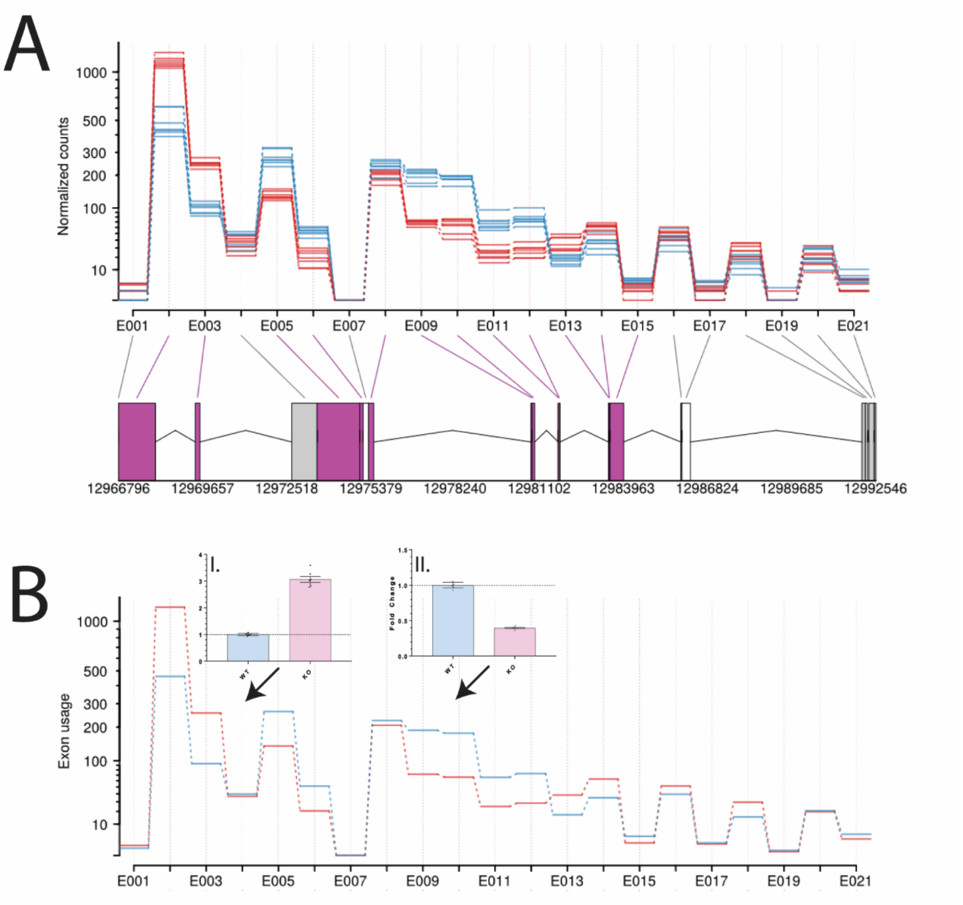

Figure 7: Differential exon usage analyzed with the DEXSeq R package

(A) Normalized read counts mapped to the individual exons of the *Wtap* gene. **(B)** Exon usage calculated with DEXSeq shows differences in the exon usage of KO, compared to WT animals for the *Wtap* gene with the results from the qPCR for the floxed exons 4 and 5 (I.) and the isoform specific exons 7 and 8 (II.).

Gene Ontology (GO) analysis

Enrichment analysis was used to identify biological themes associated with the three gene ontologies (GO) Cellular Component (CC), Molecular Function (MF) and Biological Process (BP)[172,173]. Therefore, a gene/protein universe was defined, comprising all genes/proteins that were detected in the experiment. The enrichment analysis was performed with differentially expressed transcripts passing the cut off: FDR < 0.05, Log2FoldChange ≥ 0.5, base mean ≥ 20. For the DEXSeq results, the cut off was set at: FDR < 0.05, Log2FoldChange ≥ 0.5, exon base mean ≥ 5. Similarly, proteins included in the pathway analysis were filtered for FDR < 0.05.

The analysis was conducted in R with the package clusterProfiler[174] using the setting: minGSSize = 15, maxGSSize = 1000, AdjustMethod = 'fdr', qvalueCutoff = 0.05. Semantic similarity analysis was performed with GOSemSim[175] using the graph-based Wang's method with the setting: threshold = 0.7.

3.8 Proteomic screening using LC-MS/MS

The proteomic screening was done with support from the Core Facility / Mass Spectrometry at the Max Planck Institute of Biochemistry (Martinsried, Germany) and in collaboration with D. Heinz, A. Zellner and N. Gassen, as previously described[176]. The sample preparations for the membranome characterization were conducted by F. Stamp and D. Heinz. Sample measurements were performed by N.

Krombholz and B. Steigenberger and the bioinformatic processing was done by A. Zellner under supervision of N. Gassen. Data interpretation, pathway analysis and visualization were done by F. Stamp. The methods descriptions below were kindly provided by N. Krombholz, B. Steigenberger and A. Zellner and adapted for this thesis.

Sample preparation: bulk tissue

The tissue collection and sample preparation for the LC-MS bulk tissue analysis was conducted as previously described[176]. In brief, the tissue was collected as described above and stored at -80 °C. Samples were incubated with 400 µl pre-heated SDC buffer (1 % sodium deoxycholate, 40 mM 2-cloroacetamide, 10 mM Tris(2-carboxyethyl)phosphine, 100 mM Tris, pH 8.0.) for 2 min at 95 °C. Samples were lysed with an ultrasonicator (2 min, pulse: 0.5 s, pause: 2 s, intensity: 50 %; Sonopuls, Bandelin) at RT, incubated for 2 min at 95 °C and sonicated a second time. Samples were subsequently diluted (1:2) with MS grade water (VWR) and proteins digestion with LysC (1 µg, Labchem-Wako) for 3 h at 37°C, followed by an overnight incubation with trypsin (3 µg, Promega) at 37 °C. Afterwards, 25 % of the sample volume was acidified using trifluoroacetic acid (final concentration: 1 %, pH; < 2, TFA; Merck). Samples were centrifuged to remove precipitated SDC and subsequently purified using SCX StageTips [177]. The resulting peptide mix was vacuum dried and re-suspended in buffer A (final volume: 10 µl, formic acid: 0.1 %) in MS grade water (VWR).

Sample preparation: membranome

The purification of membrane bound proteins was performed following a previously published protocol, with few modifications[178]. In brief, animals were euthanized with isoflurane (CP-Pharma) and decapitated using a mouse guillotine. Brains were quickly dissected from the sculls and collected in pre-chilled, oxygenated sucrose-supplemented artificial cerebrospinal fluid (SACSF) (250 mM sucrose, 2.5 mM KCl, 1.2 mM NaH_2PO_4, 1.2 mM $MgCl_2$, 2.4 mM $CaCl_2$, 26 mM $NaHCO_3$, and 11 mM glucose, 95 % O_2, 5 % CO_2). Using a vibratome, 300 µm sections of the dorsal HPC (dHPC) region were cut (Bregma: -1.46 mm to -2.92 mm). Slices were transferred onto an agar plate filled with SACSF slush and the dorsal CA1 area was quickly dissected using a binocular, as described for the fresh tissue collection. Using a fire-polished Pasteur pipette, tissue sections were transferred to custom made, mesh-bottomed incubation chambers (volume: 100 ml) containing temperate artificial cerebrospinal fluid (ACSF, 2.5 mM KCl, 1.2 mM NaH_2PO_4, 1.2 mM $MgCl_2$, 2.4 mM $CaCl_2$, 26 mM $NaHCO_3$, and 11 mM glucose, 95 % O_2, 5 % CO_2, 30 °C). Slices were subjected to a 40 min recovery period at 30 °C in continuously oxygenated ACSF before labelling. Following recovery, slices were transferred to a 12 well plate and washed 3x with ice cold ACSF. Labelling of proteins was performed by incubating samples with 1.0 mg/ml sulfo-NHS-SS-biotin in ice cold ACSF, prepared freshly from stock (200 mg/ml in DMSO, stored at -20 °C, Sigma-Aldrich), for 45 min at 4 °C. The labelling reaction was quenched by washing samples 3 x with ice cold slice quench buffer (ACSF supplemented with 100 mM glycine), followed by 2 x 25 min incubations in slice quench buffer on ice. Next, slices were washed 3x in ice cold ACSF and transferred to protein LoBind tubes. After pelleting (200 x g, 1 min) the remaining ACSF was aspirated and the tissue lysed in ice cold RIPA buffer (Merck). Afterwards, cellular debris was removed by centrifugation and the protein concentration of the lysate measured using the BCA protein assay (Thermo Fisher Scientific) according to manufacturer's specifications. Next, 400 mg of protein was incubated overnight with equilibrated streptavidin beads (25 µl/ sample, ThermoFisher). On the next day, beads were pelleted and air dried after 3 x washing with RIPA. Samples were stored at -20 °C.

PBS washed magnetic beads were incubated with SDC buffer (1 % sodium deoxycholate, 40 mM 2-cloroacetamide, 10 mM Tris(2-carboxyethyl)phosphine, 100 mM Tris, pH 8.0.) for 20 mins at 37 °C, diluted (1:2) with MS grade water (VWR) and digested overnight with trypsin (0.5 µg, Promega) at 37 °C. Afterwards, the beads were separated using a magnetic rack, the supernatant was collected and acidified using trifluoroacetic acid (final concentration: 1 %, pH; < 2, TFA; Merck). Samples were centrifuged to remove precipitated SDC and subsequently purified using SCX StageTips[177]. The resulting peptide mix was vacuum dried and re-suspended in buffer A (final volume: 10 µl, formic acid: 0.1 %) in MS grade water (VWR).

LC-MS/MS data acquisition

The LC-MS data acquisition and analysis was conducted, with few modifications, as previously described[176]. In brief, twenty percent volume of the purified, desalted peptides were loaded onto a 30 cm column: inner diameter: 75 microns; packed in-house with ReproSil-Pur C18-AQ 1.9-micron beads, Dr. Maisch GmbH via the autosampler of the Thermo Easy-nLC 1000 (Thermo Fisher Scientific) at 60 °C. Peptides that were eluted were sprayed onto the timsTOF Pro (Bruker Daltonics). For the data acquisition, samples were loaded with buffer A (formic acid: 0.1 %) at 400 nl/min and buffer B (acetonitrile: 80 %, formic acid: 0.1 %) was slowly increased from 5 % to 25 % over 90 min followed by an increase to 35 % over 30 min, an increase to 58 % across 5 min, to a final volume of 95 % over 5 min. The buffer composition of buffer B at 95 % was maintained for 5 more mins.

The data acquisition with timsTOF Pro was conducted with timsControl and the mass spectrometer was operated in data-dependent PASEF mode (one survey TIMS-MS, ten PASEF MS/MS scans per acquisition cycle). The analysis was conducted with a mass scan range of 100-1,700 m/z and an ion mobility range of 1/K0 = 1.6-0.6 Vs cm^{-2} using equal ion accumulation and ramp time in the dual TIMS analyzer of 100 ms each at a spectra rate of 9.43 Hz. The precursor ions for the MS/MS analysis were isolated in a window of 2 Th for m/z < 700 and 3 Th for m/z > 700 by rapidly switching the quadrupole position in sync with the elution of precursors from the TIMS device. The collision energy was lowered as a function of ion mobility, starting from 59 eV for 1/K0 = 1.6 Vs cm^{-2} to 20 eV for 0.6 Vs cm^{-2}. Single charged precursor ions were excluded using a polygon filter mask and the m/z and ion mobility information was used for dynamic exclusion to avoid re-sequencing of precursors that reached a target value of 20,000 a.u. Finally, the ion mobility dimension was calibrated linearly using three ions from the Agilent ESI LC/MS tuning mix (m/z, 1/K0: 622.0289, 0.9848 Vs cm^{-2}; 922.0097 Vs cm^{-2}, 1.1895 Vs cm^{-2}; 1221.9906 Vs cm^{-2}, 1.3820 Vs cm^{-2}).

LC-MS/MS data analysis

The raw data were processed using the MaxQuant computational platform (version 1.6.17.0[179] with standard settings for ion mobility data[180]. In brief, the list of identified peaks was submitted to the Uniprot database (Mouse SwissProt: 17048 entries; download: November 2020, precursor mass deviation: 10 ppm, fragment mass deviation: 20 ppm) with individual peptide mass tolerances enabled. Cysteine carbamidomethylation was defined as static modification, and methionine oxidation, deamidation and N-terminal acetylation were set as variable modifications. Proteins were quantified across samples using the label-free quantification algorithm (MaxQuant, match-between-run option: enabled) that calculates label-free quantification intensities. For proteins, identified by at least two ratio counts of unique peptides in at least three samples of each group, intensities were log2-transformedm, and a one-way ANOVA was performed with permutation-based FDR correction. Afterwards, a two-sided Student's t test was applied. The following significance threshold were used: p value < 0.05. Multivariate statistical analysis was performed with s0 = 0 and, FDR < 0.05.

3.9 Metabolite screening using LC-MS/MS

The metabolite screening was conducted in collaboration with J. Xiao at the Max Planck Institute of Psychiatry. Sample preparation, measurements and bioinformatic analysis were performed by J. Xiao and the data visualization and interpretation was done by F. Stamp. The methods description below outlining the sample preparation, measurement and data analysis was kindly provided by J. Xiao and adapted for this thesis.

Extraction of metabolites from brain tissue

The tissue used for the metabolic analysis was freshly dissected as outlined above and stored at −80 °C until use. The metabolite extraction was conducted as previously described[181]. In brief, tissue samples were incubated with 500 µl ice cold (−80 °C) methanol (80 %) and homogenized with a bullet blender (Next Advance) for 2 min (speed: 6). Samples were incubated for 4 h at −80 °C and centrifuged with 14,000 g for 10 min at 4 °C. The supernatant was transferred to a fresh tube and the remaining precipitate was incubated with 400 µl ice cold (−80 °C) methanol (80 %) at −80 °C for 30 min, centrifuged at 14,000 g for 10 min at 4 °C and the resulting supernatant from both centrifugations were combined. Subsequently, the combined supernatants were dried using the SpeedVac (SC210A, Thermo Savant) without heat. Finally, samples were reconstituted in 120 µl 75 % acetonitrile, centrifuged at 14,000 g for 10 min at 4°C and the supernatant split into equal aliquots for two independent measurements.

Metabolomics quantification

The sample analysis was performed with hydrophilic interaction liquid chromatography (HILIC) using the positive negative ion-modes. For quality control and to determine technical variations, a sample pool containing each sample in equal amounts was measured at the beginning and after every tenth measurement.

The samples were measured was with the Bruker Elute UHPLC and Bruker Impact II TOF MS systems (Bruker Daltonik GmbH) that are operated with the Bruker Hystar Software (version: 5.0). The samples were analyzed using the XBridge Amide column (150 mm x 2.1 mm, 2.5 µm, Waters) with a VanGuard Pre-column (Waters) at 30 °C. For the measurement, 5 µl of each sample were used with the autosampler set to 4 °C. Metabolites were separated using a 30 min gradient at a flow rate of 0.4 ml / min using two eluents (eluent A: 10mM ammonium formate, 0.1 % formic acid, 5 % acetonitrile in H_2O, eluent B: 10mM ammonium formate, 0.1 % formic acid, 90 % acetonitrile in in H_2O). The following eluent compositions were used across the measurement: eluent B: 99 % 0-2 min, 99 % -50 % 20 min, 50 % 3min, 50 % -99 % 0.2 min, 99 % 4.8 min (Eluent A = 100 % - B). Electrospray ionization source settings: end plate offset 500 V; capillary voltage 4500 V (positive mode) | 3,500 V (negative mode); nebulizer nitrogen gas flow 10 l / min; nebulizer 2.5 bar; dry temperature 240 °C. Metabolic profiles were acquired with the Bruker Compass 3.0 (spectra rate: 1 Hz, mass range: 50-1,300 m/z). QC samples were run in MS2 mode and the 3 most intense ions were selected for fragmentation within a mass range of ±4-6 Da. Collision energy settings: 16 eV for ions with m/z of 100; 25 eV for ions with m/z of 500; 40 eV for ions with m/z 1,000 and larger, with linear energy interpolation and a spectra rate of 5 Hz.

Metabolomics data processing and statistical analysis

The data analysis, including the calibration, feature extraction and metabolite annotation were performed with MetaboScape (version: 4.0). Metabolic features were extracted using the following settings: intensity threshold 1,500, minimum peak length 10, minimum peak length 8 (recursive), mass range 50-1300 m/z, 0.8 EIC correlation. Only features detected in at least 70 % of all samples were included. For the annotation of metabolites, a custom metabolite library, based standards measured with the same platform, was used with default settings for tolerance and scoring. The annotated tables obtained with MetaboScape were further processed with Perseus (version:1.6.14.0) as previously described[182]. For the statistical analysis, the intensity values of individual metabolite features were median normalized and log2 transformed and a two-sample Student's Independent two-sample t-test with a Benjamini and Hochberg FDR cutoff of q-value < 0.1 was used to determine group differences.

3.10 Western blot

The western blot was performed as described previously[28]. In brief, tissue was dissected into in ice cold RIPA buffer (150 mM NaCl, 1 % NP-40, 0,5 % Sodium deoxycholate, 0,1 % SDS, 50 mM Tris-HCl pH 8 with cOmplete, EDTA-free Protease Inhibitor Cocktail Mini, Roche Applied Science), homogenized with a with Bullet Blender (Next Advance, NY, USA) and lysed for 10 min on ice. After centrifugation (max speed, 10 min) the protein content of the supernatant was quantified using the Pierce BCA Protein Assay (Thermo Fisher Scientific). Next, 25 µg total protein was incubated in Laemmli buffer (final concentration: 62.5 mM Tris-HCl pH 6.8, 2 % SDS, 10 % glycerol, 5 % β -mercaptoethanol) at 95 °C for 10 min. Proteins were separated with a Tris-Glycine SDS-PAGE (Bio-Rad Laboratories) and transferred to a nitrocellulose membrane (Amersham Pro-tran, Millipore). The membrane was blocked in in 1 x tris-buffered saline with Tween20 (TBST, 5 % dry milk) for 1 h, at RT on a shaker. Blots were incubated with the primary antibody (anti WTAP: Proteintech 60188-1-Ig 1:1000; anti-Vinculin 1:5000) in 1 x TBST containing 5 % dry milk at 4 °C overnight. After washing with TBST (3x), the membrane was incubated with the horse-radish-peroxidase-coupled secondary antibody (Cell Signaling Technology) for 2 h, at RT. Blots were developed with enhanced chemiluminescence (ECL Plus, GE Healthcare Life Sciences) using the ChemiDoc Imaging System XRS+ (Bio-Rad). Membranes were first incubated with anti-WTAP antibody, striped after analysis (0.2 M glycine, 3.5 mM SDS, 1 % Tween in H_2O 20 min at RT), then blocked again and processed with anti-Vinculin antibody.

3.11 Immunostaining

Dehydrated and fixed sections were retrieved from storage (-20 °C) and washed 3 x in PBS to remove anti-freezer. Samples were blocked for 30-35 min (10 % normal goat serum (NGS), 0.5 % Triton® X-100 in 1 x PBS) and washed 3 x in 1 x PBS. Sections were incubated with primary antibodies (antibody in 1.5 % NGS, 0.5 % Triton® X-100 in 1 x PBS) on a shaker at 4 °C, overnight. On the next day, sections were washed 3 x in PBS and incubated with the secondary antibodies (antibody in 1.5 % NGS, 0.5 % Triton® X-100 in 1 x PBS) on a shaker for 2-3 h. Finally, sections were washed 3 x with 1 x PBS and mounted on SuperFrost Plus™ slides (Thermo Scientific) with 4′, 6-diamidin-2-phenylindol (DAPI) containing Fluoromount-G® (SouthernBiotech). Used antibodies: anti WTAP (Proteintech 60188-1-Ig 1:400); Alexa 488 goat anti mouse (ThermoFisher #A28175 1:500).

3.12 Microscopy

Slide scanner

The Olympus BX61VS Research Slide Scanner (Olympus) was used take overview images with a magnification of 4x and 10x. Light was generated with a X-Cite exacte illumination system (Excelitas Technologies). Filters: DAPI, Alexa 488, Alexa 594, Alexa 647. Images were acquired with the Olympus VS-ASW software (version 2.9).

Confocal microscopy

The Zeiss LSM 800 upright confocal microscope with spectral detector array was used for high resolution imaging. The objectives used are as follows: Plan-Apochromat 10x/0.45, Plan-Apochromat 40x/1.4 Oil DIC, αPlan-Apochromat 63x/1.46 Oil TIRF. A tunable Ti:Sapphire laser and HXP 120 V halogen lamp were employed to generate light of the following wavelengths: 405 nm, 488 nm, 561 nm, 647 nm and registered by a high sensitivity spectral detector (GaAsP). Filters: DAPI, Alexa 488, Alexa 594, Alexa 647. The Zen 2.3 Software was used to operate the system (version 2.3).

3.13 Electrophysiology

Electrophysiological recordings were conducted by an experimenter blind to the genotype at the core facility for electrophysiology, Max Planck Institute of Psychiatry. LTP measurements were conducted by S. Calcanini and patch clamp recordings were performed by D. Menegaz. The data were analyzed by M. Eder and the statistics and visualization were performed by F. Stamp. The methods description was provided by M. Eder and adapted for this thesis.

In brief, experimental animals (age: 8-12 weeks) were taken from their holding rooms immediately prior to the experiment and euthanized as described above. Brains were quickly collected in pre-chilled (< 4 °C), carbogenated SACSF (87 mM NaCl, 2.5 KCl mM, 25 mM NaHCO3, 1.25 mM NaH2PO4, 0.5 mM CaCl2, 7 mM MgCl2, 10 mM glucose, and 75 mM sucrose, 95 % O2, 5 % CO2). Then 350 µm coronal sections of the mPFC (Bregma: 1.94 mm to -1.34 mm) and dHPC dHPC (Bregma: -1.34 mm to -1.82 mm) were cut using a vibratome (HM650V, Thermo Scientific) and collected in ice cold (< 4 °C), carbogenated SACSF. Sections were allowed to recover for 30 min at 34°C in carbogenated ACSF (125 mM NaCl, 2.5 mM KCl, 25 mM NaHCO3, 1.25 mM NaH2PO4, 2 mM CaCl2, 1 mM MgCl2, and 10 mM glucose, 95 % O2, 5 % CO2), followed by 30 min incubation at ambient temperature (23-25°C).

Long term potentiation

For the paired-pulse facilitation and LTP measurements, tissue sections were superfused with carbogenated ACSF (flow rate: 4-5 ml / min) at room temperature (23-25°C). Field excitatory postsynaptic potentials (fEPSPs) at the CA3-CA1 synapses were induce with the stimulation electrode placed in the Schaffer collateral-commissural pathway, using square-pulse electrical stimuli (pulse width: 50 µs) delivered via a bipolar tungsten electrode (pole diameter: 50 µm, nominal impedance: ~0.5 MΩ). fEPSPs were recorded with a glass microelectrode (solution: ACSF, open-tip resistance: ~1 MΩ) placed in the stratum radiatum (dCA1).

Slices were stimulated every 15 s for 20 min and fEPSPs measured to establish a baseline recording and the intensity of voltage stimulation for the measurements was titrated to induce a fEPSP of ~50 % of the amplitude at which a population spike appeared. LTP was induced by theta-burst stimulation (TBS). TBS consisted of bursts of four pulses at 100 Hz delivered 10x with an inter-burst interval of 200 ms. This stimulation train was applied 3x with an inter-train interval of 10 s, resulting in a total number of 120 pulses. Paired-pulse facilitation was recorded with an inter stimulus interval of 25, 50, 100, 200 and 400 ms. The paired-pulse ratio was calculated as fEPSP 2 slope / fEPSP 1 slope. The recorded data were low-pass filtered at 1 kHz and digitized at 5 kHz. Per animal, 3-4 slices were used for recordings. For each slice, the mean fEPSP slope/amplitude was calculated per minute (mean of 4 values) and statistical analysis was performed using the mean fEPSP slope/ amplitude of the last 10 min of LTP recordings (min 71-80). Group comparisons were performed using the appropriate tests, as detailed in the corresponding results section.

Patch clamp recordings

Experiments were conducted in 1-3 slices per animal at RT (23-25°C) in carbogenated ACSF (flow rate: 2-3 ml / min) containing NBQX (5 µM) and picrotoxin (100 µM). Layer V mPFC pyramidal neurons were identified (pyramidal shape, presence of single apical dendrite projecting towards layer 2 and 3) using infrared video microscopy. Somatic whole-cell current-clamp recordings were obtained using an EPC 10 amplifier (HEKA) and the following settings: seal resistance ≥1 GΩ, series resistance < 20 MΩ, 3 kHz low-pass filter, 15 kHz sampling rate. Patch pipettes (open tip resistance: 3-5 MΩ) were filled with a solution containing: 135 mM KMeSO4, 8 mM NaCl, 0.3 mM EGTA, 10 mM HEPES, 2 mM Mg-ATP, 0.3 mM Na-GTP and current injections were used to depolarize or hyperpolarize the neuron under investigation. All potentials were corrected for a liquid junction potential of 10 mV. Group comparisons were performed using the appropriate tests, as detailed in the corresponding results section.

3.14 Magnetic resonance imaging

The MRI was conducted as previously described[183,184]. Recordings were obtained by F. Stamp, D. Heinz, L. Bartmann at the Max Planck Institute of Psychiatry and the analysis was performed by T. Stark. In brief, animals were anesthetized using isofluorane (~1.5 % isoflurane, CP-Pharma) and fixed onto the MRI-tray, carrying a heat pad for body temperature control, using a stereotactic frame. To protect the eyes, Bepanthen ointment (BAYER AG) was applied prior to the scan. The anesthesia was maintained via a breathing mask (1.5-1.8 % isoflurane, air flow: 1.3 l/min) and the body temperature and respiration were monitored throughout the process. Structural scans were recorded with the operating system Paravision (version: 6.0.1, Bruker Corporation) using a BioSpec 94/20 animal MRI system (Bruker BioSpin GmbH) containing a 9.4 T scanner. In detail, scans were acquired using a 3D gradient echo sequence (repetition time (TR): 34.1 ms, echo time (TE): = 6.25 ms, excitation pulse angle: 10°, number of averages (NA): 2, matrix dimension: 256 x 166 x 205, isotropic pixel resolution: 77 µm). Before processing, each scan was visually inspected. Scans containing motion artifacts, or showing pronounced structural abnormalities (e.g., hydrocephalus, inflated ventricular space) were excluded. The Statistical Parametric Mapping software (SPM12, Wellcome Department of Cognitive Neurology, London, UK, version: 7219) was used for the analysis. Scans were converted to the NIFTI format with a 10x inflation of voxel size, reoriented and co-registered to the structural Hikishima C57Bl6 template[185]. Brain extraction was performed in two steps. First, images were segmented and corrected for bias using the Hikishima C57Bl6 template1 consisting of 5 tissue classes. Using the cat12 toolbox of SPM (www.neuro.uni-jena.de/cat), bias corrected images were filtered using a spatial adaptive non-local means denoising filter[186]. Gray matter, white matter and cerebrospinal fluid probability maps were summed and binarized for image intensities > 0.3, holes were filled using the imfill function in MATLAB and subsequently dilated by 5 voxels to create a brain mask that was applied to the bias corrected spatially filtered images. The resulting images were again segmented with a modified version of the

Hikishima template for which the original cerebrospinal fluid template was divided into two sub-templates, one containing the ventricular inner cerebrospinal fluid (ventricles) and the other the surface cortical cerebrospinal fluid (skull-brain interface). Gray matter, white matter and ventricular inner cerebrospinal fluid were summed, binarized (threshold > 0.1) and remaining holes were filled using MATLAB's imfill function to create a second mask. This mask was dilated and applied to the original bias corrected, spatially filtered images. The resulting brain-extracted 3D images were segmented using the 'Old Segment function' of SPM12 with the three compartments gray matter, white matter and inner ventricular cerebrospinal fluid. DARTEL normalization was used to generate flow-fields and a template based on the gray matter, white matter segments (7 iterations). Flow-fields were converted to Jacobian determinant fields and spatially smoothed (Gaussian kernel: 2 µm). The total intracranial volume (TIV) was approximated as the sum of all modulated tissue probabilities, excluding the olfactory bulb and cerebellum. The statistical analysis was performed using general linear models (GLM) with the TIV as a covariate to calculate coefficients that were then tested for group differences using a two-sample independent t-test. The thresholds for spatial voxel-wise maps of t-values (t-maps) were set at either $p < 0.005$ or $p < 0.001$ (uncorrected). Cluster comparisons were done with the adjusted extent thresholds to obtain FWE-corrected ($p < 0.05$) clusters. The obtained results were visualized using the MRIcro software (Chris Rorden, version 1.9.1).

4. Results

The following section contains selected results obtained during my PhD and is divided into two main parts. In the first part (Project I), I present the results obtained in my study of the m^{6}A 'writer complex' associated protein WTAP and its role in regulating gene expression, splicing, protein abundance, the metabolism, brain anatomy, neuronal signaling and behavior. In the second part (Project II), I present my findings regarding the role of the m^{6}A 'reader' YTHDC1, demonstrating that it is essential for adult survival and normal brain function. Due to the interdisciplinary nature of my research, many of the presented results were obtained in collaboration with an outstanding team of researchers. Their contribution to the presented work is highlighted in the authors contribution section.

4.1 Project I: WTAP is required for neuronal gene expression regulation, signaling and behavior

Despite almost a decade of research into the regulation and function of m^{6}A, little is known about the unique contribution of WTAP. Previously it has been shown that WTAP interacts with the METTL3-METTL14 core complex and is necessary for its localization to the nuclear speckles[25,37]. Functionally, WTAP is considered an adapter that connects the m^{6}A core complex with regulatory proteins, including RBM15 and ZC3H13[44] and its role outside of the m^{6}A machinery is largely unexplored. However, previous studies investigating WTAP have shown that it interacts with other targets, most famously WT1[61] and in recent years it has been suggested that WTAP might exist outside of the m^{6}A 'writer complex' forming a structure termed MACOM that may be involved in METTL3-METTL14 independent regulation[44]. To date, no studies have systematically explored the unique contribution of WTAP to regulating neuronal functions in the mouse brain.

The goals of the research presented below are: (1) To characterize the effect of WTAP KO on the different levels of biological organization, from gene expression to behavior. Towards this goal, two Cre driver lines are employed that enable the conditional deletion of WTAP in the forebrain (Camk2aCre) and in the cortex and HPC (NexCreERT2). (2) to identify unique contributions of WTAP to neuronal regulation in the mammalian brain.

4.1.1 Camk2aCre expression across the adult mouse brain

The Camk2aCre driver line used in the presented experiments, expresses Cre in pyramidal neurons of the neocortex, HPC (CA1-CA3, dentate gyrus) and to a lesser extent in the striatum and amygdala with sparse recombination being observed in the cerebellum[149]. The onset of the KO occurs postnatally, starting around the 3rd postnatal week[149,187] when most of the brain development has concluded[188]. Previous investigations have shown that the Camk2aCre activity continuous to increase until around P70[187].

For the presented thesis, the expression pattern of Camk2aCre was validated in adult (> 8 weeks) Camk2aCre-Ai9 reporter mice using fluorescent microscopy. A representative overview of the Camk2aCre expression is shown in Figure 8.

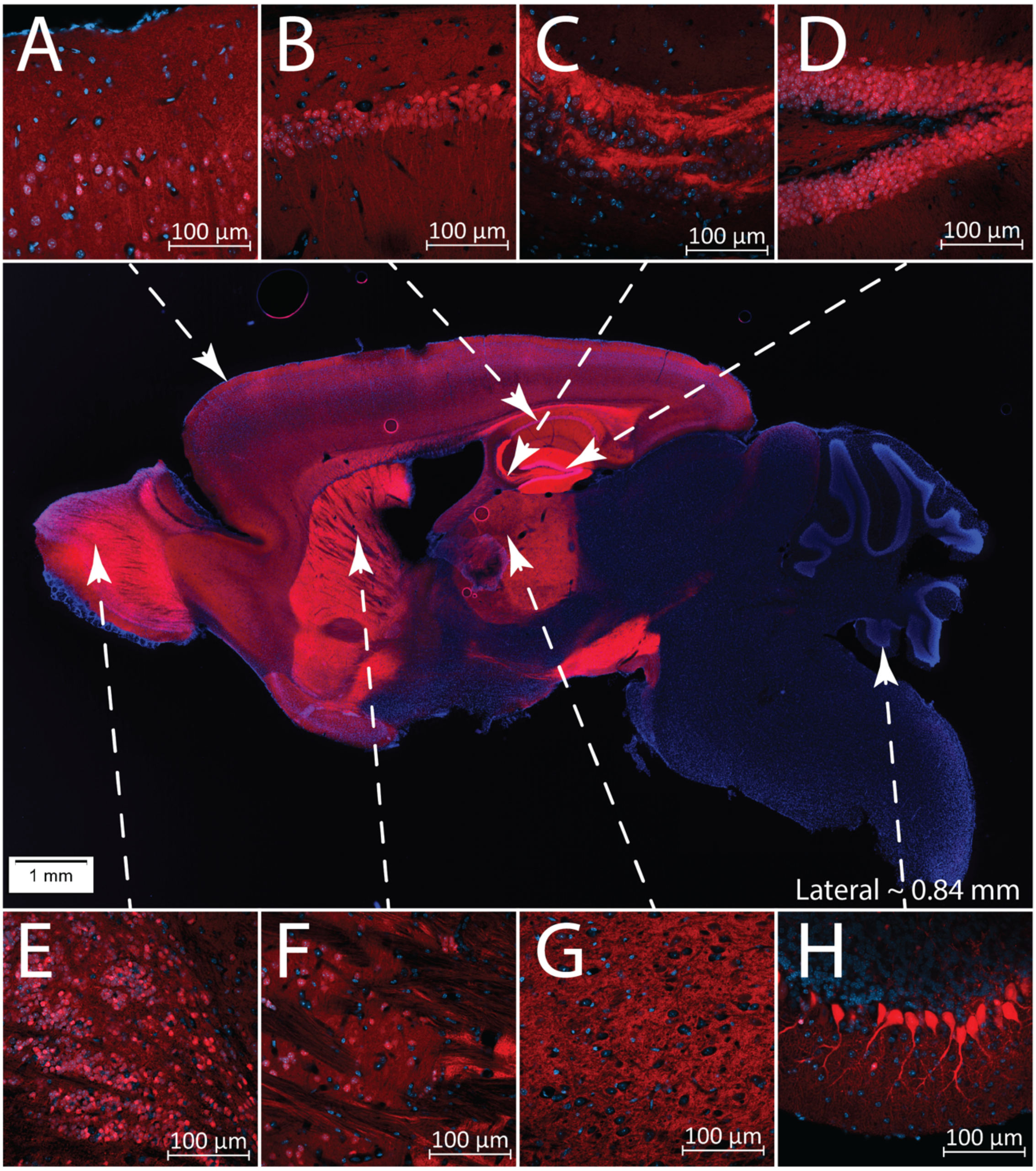

Figure 8: Camk2aCre expression across the adult mouse brain
(A) In the cortex, pyramidal neurons are clearly labelled by tdTomato. **(B-D)** A strong Camk2aCre expression is present in the HPC, with the majority of neurons being labelled in the dCA1 **(B)** while little recombination is detected in dCA3 neurons **(C)**. Clear labelling is also observed for the neurons of the dentate gyrus **(D)**. **(E-H)** Strong labelling is present across the olfactory bulb **(E)**, with fewer cells being labelled in the striatum **(F)** and no cells being labelled in the thalamus **(G)**. Sparse labelling is detected in the cerebellum, with a distinct subset of Purkinje cells being labelled in the 10th cerebellar lobule **(H)**. Images were acquired using a Camk2aCre-Ai9 expressing mouse strain with a magnification of 4x and 40x respectively.

The observed Camk2aCfre activity, as indicated by tdTomato, is largely in accordance with what has been reported previously[149]. In addition, many regions in which no cell bodies show dTomato expression, are densely innervated by Camk2aCre expressing neurons. An example of this is in the thalamus, which is innervated tightly by tdTomato projections but lacks positively labelled cell bodies. Furthermore, across the brainstem and cerebellum, there are scattered Camk2aCre expressing cells which are not visible in the images shown in Figure 8.

4.1.2 Camk2aCre WTAP KO affects the weight in juvenile males but not females

Considering that the Camk2aCre driven KO of WTAP starts around the 3rd postnatal week[149,187] and could potentially affect the maturation of brain circuits, a cohort of juvenile animals was followed post-weaning to determine differences in behavior, physical appearance and monitor weight gain. For this, juvenile animals were assessed weekly post-weaning from week 4 to week 8. While there were no obvious physical or behavioral differences apparent between WT and KO animals, a significant reduction in the weight of juvenile males was detected. The weight data were analyzed using a linear model in R with the dependent variable weight and the independent variables date, sex and genotype. Reported below are the results for the three-way ANOVA. An overview of the results is shown in Figure 9.

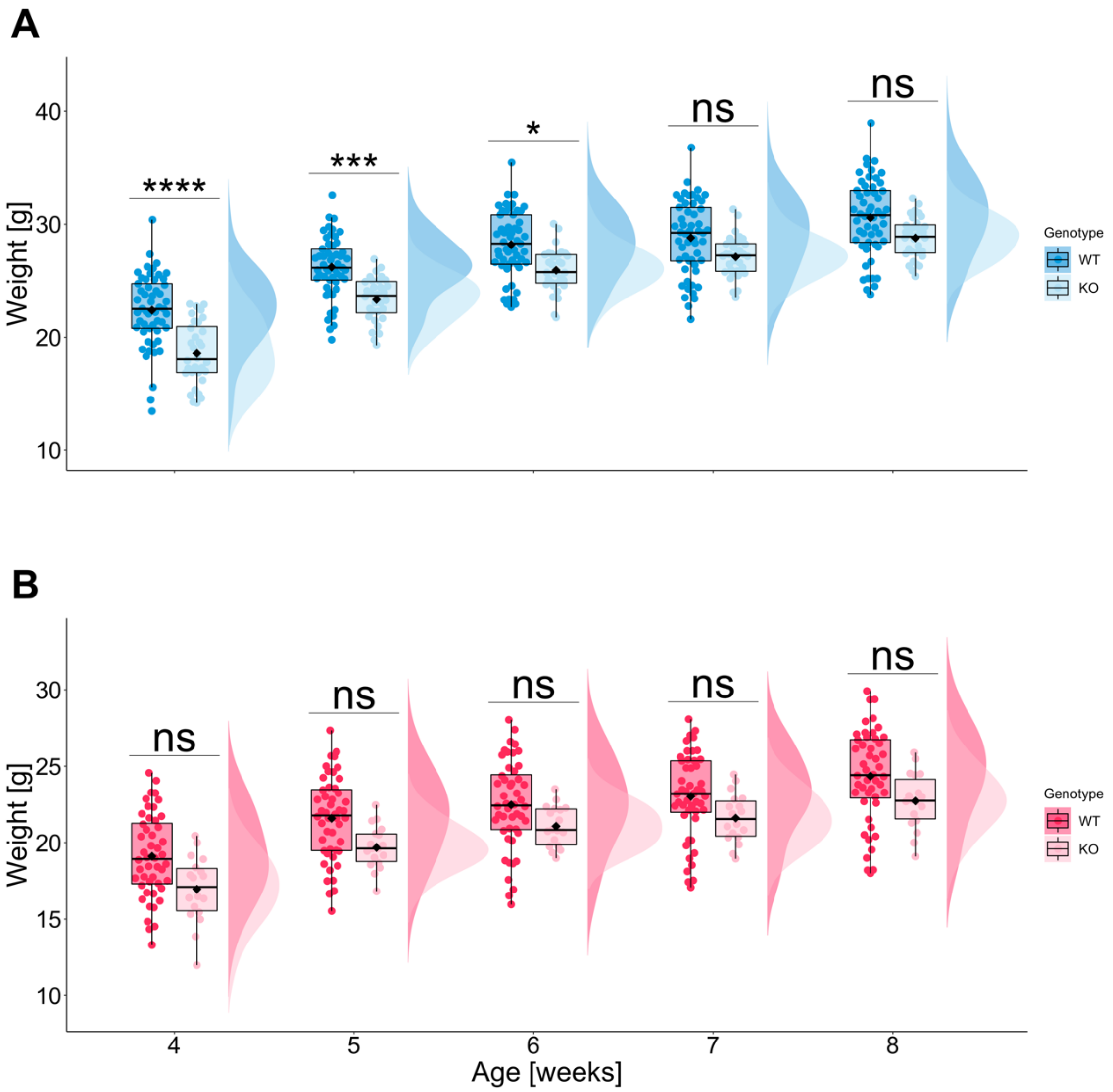

Figure 9: Camk2aCre WTAP KO juvenile males show decreased weight

(A) Weight of male Camk2aCre WTAP WT and KO animals (WT = 53, KO = 32). **(B)** Weight of female Camk2aCre WTAP WT and KO animals (WT = 48, KO = 18). Significance levels from the Tukey's post-hoc test: ns = not significant, *: $p < 0.05$. **: $p < 0.01$, ***: $p < 0.001$, ****: $p < 0.0001$.

A significant main effect of sex and genotype was identified, with males being heavier than females and KO animals being overall lighter than WT animals (sex: $F_{1,754} = 598.5$, $p < 0.0001$; genotype: $F_{1,754} =$

59.741 $p < 0.0001$). In addition, a trend for an interaction of genotype and sex was detected but the significance levels was not reached (genotype:sex: $F_{1, 754} = 3.331$, $p = 0.068$). Furthermore, a significant interaction of genotype and date (genotype:date: $F_{4, 754} = 2.989$, $p = 0.018$) and sex and date (sex:date: $F_{4, 754} = 9.379$, $p < 0.0001$) were found. Applying a Tukey's test for multiple comparisons showed that KO males show a significantly reduced weight at week 4 (p.adj. < 0.0001), week 5 (p.adj. = 0.0004) and week 6 (p.adj. = 0.0271), while there was no significant difference detected between the two genotypes for female animals.

4.1.3 WTAO KO alters circadian activity patterns in the home cage

The effect of a Camk2aCre driven KO of WTAP on circadian activity patterns was examined in the home cage using infrared mobility detection. For this purpose, animals were single-housed for 7 consecutive days, during which time the animals remained undisturbed in their home cage. Spontaneous bouts of locomotor activity were recorded using an infrared sensor located on top of the food tray. This experiment was conducted twice with each 8 WT and 8 KO male animals. The resolution of activity measurements was 1 signal / 1 s (YES/NO) and data were collected as activity / minute. For the analysis, the mean activity was calculated per 10 min, per h and per light phase. The time series data were analyzed for periodic effects using a generalized additive model with activity (10 min bins) as the dependent variable and genotype as the independent variable. Time was included in the model as smooth term. The model summaries for the estimated parameters and smooth terms can be found in Appendix 8.4.

Overall, a significant difference in circadian activity was detected with KO animals showing a distinct shift in circadian activity (genotype KO: Estimate 2.91; $t = 19.32$; $Pr(>|t|)$ $1.2e^{-82}$). The results are summarized in Figure 10.

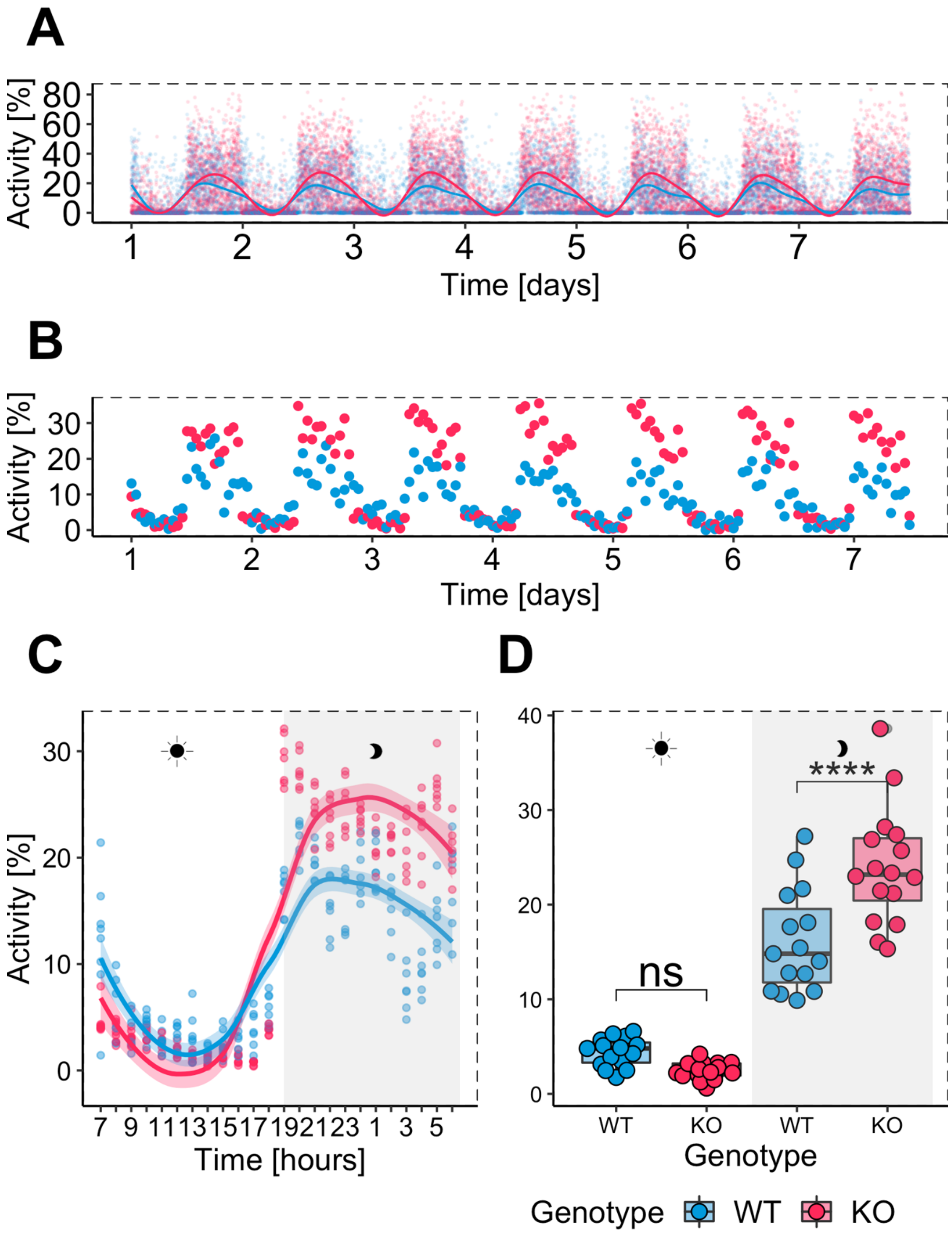

Figure 10: WTAP Camk2aCre WT KO animals show altered circadian activity dynamics

(A) Raw data across 7 days and nights plotted as activity per 10 min for all animals (WT = 15, KO = 16). The GAM model predictions are plotted on top of the raw data, showing the difference across time. **(B)** Mean activity per genotype and hour across 7 days and nights (WT = 8, KO = 8). Here the switch in behavior of the KO animals is most apparent. **(C)** Mean activity per hour plotted for individual days and both genotypes. **(D)** Mean activity during the light and dark phase. Significance levels from the Tukey's post-hoc test: ns = not significant, *: $p < 0.05$. **: $p < 0.01$, ***: $p < 0.001$, ****: $p < 0.0001$.

Interestingly, in addition to differences in the overall activity levels, pronounced differences in circadian kinetics were observed. For WT animals, the overall activity levels follow a sinusoidal pattern with a gradual increase in activity around the start of the dark phase, as well as a gradual decrease in activity at the onset of the light phase. In contrast, KO animals appeared to rapidly switch from an inactive to a highly active state at the beginning of the dark phase, reaching maximum activity levels shortly after light change. The opposite effect can be observed at the start of the light phase, with KO animals showing a sudden drop in activity and maintained low levels throughout the day. In addition to the analysis using a GAM, a linear model was fit with the average activity across nights as dependent variable and the genotype and light state (day/night) as independent variable. The results from a two-way ANOVA show a significant main effect of genotype (genotype: $F_{1,61} = 7.4$, $p = 0.0086$), a pronounced effect of daytime on activity (day.night: $F_{1,61} = 247.24$, $p < 0.0001$), as well as a significant interaction of daytime with genotype (day.night:genotype: $F_{1,61} = 21.04$, < 0.0001). Group comparisons, using a Tukey's test for multiple comparisons reveal a significantly increased activity of KO animals during the dark phase (p.adj. < 0.0001) and no significant difference during the light phase (p.adj. = 0.554).

To determine whether the observed differences in circadian activity are potentially driven by an altered function of the suprachiasmatic nucleus (SCN), the main regulator of circadian rhythms, the expression of Camk2aCre in the SCN was inspected using a Camk2aCre-Ai9 reporter mouse. A representative image is shown in Figure 11.

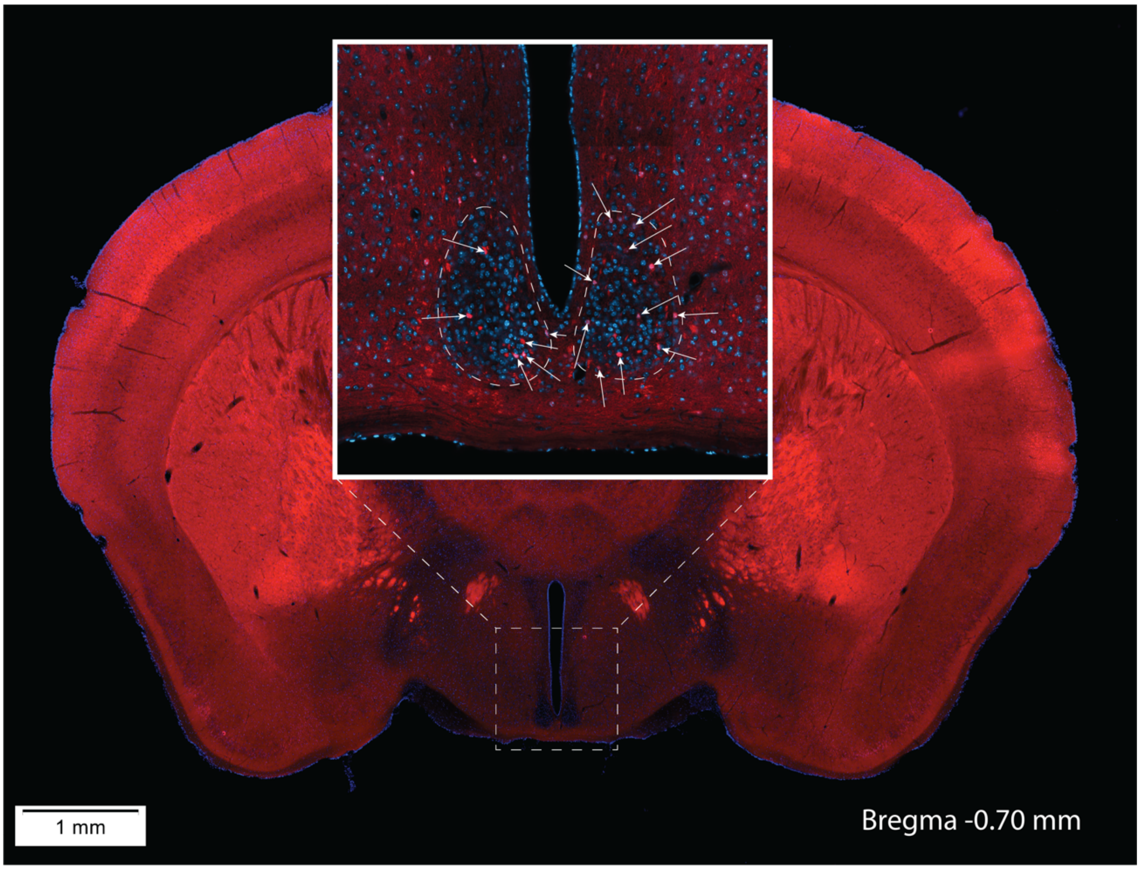

Figure 11: Camk2aCre-Ai9 labelling of the suprachiasmatic nucleus
Representative image of Camk2aCre-Ai9 labelling in the SCN. The white arrows indicate cells that show a co-localization of DAPI (blue: nucleus) and Ai9 (red: tdTomato indicating Cre activity). The overview was obtained with 4x and the detailed view with 40x.

Only a sparse labelling of cells within the SCN was observed, with little to no innervation being visible at 40x.

WTAP KO animals show increased anxiety-like behavior in the OF test

As part of the behavioral assessment, animals were tested using the OF, EPM and DL test. These classical tests are used to assess the exploratory drive, locomotor activity and anxiety-like behavior in mice[157–160].

Animals were first subjected to the OF test to assess differences between WTAP WT and KO animals in locomotion and anxiety-like behaviors. The test was performed with a low light intensity (15 lux) and for a duration of 10 min. Group comparisons were performed using the independent two-sample t-test, Welch's t-test, or Wilcoxon test as appropriate and corrected for multiple testing using the Benjamini and Hochberg method. A summary of the results is shown in Figure 12.

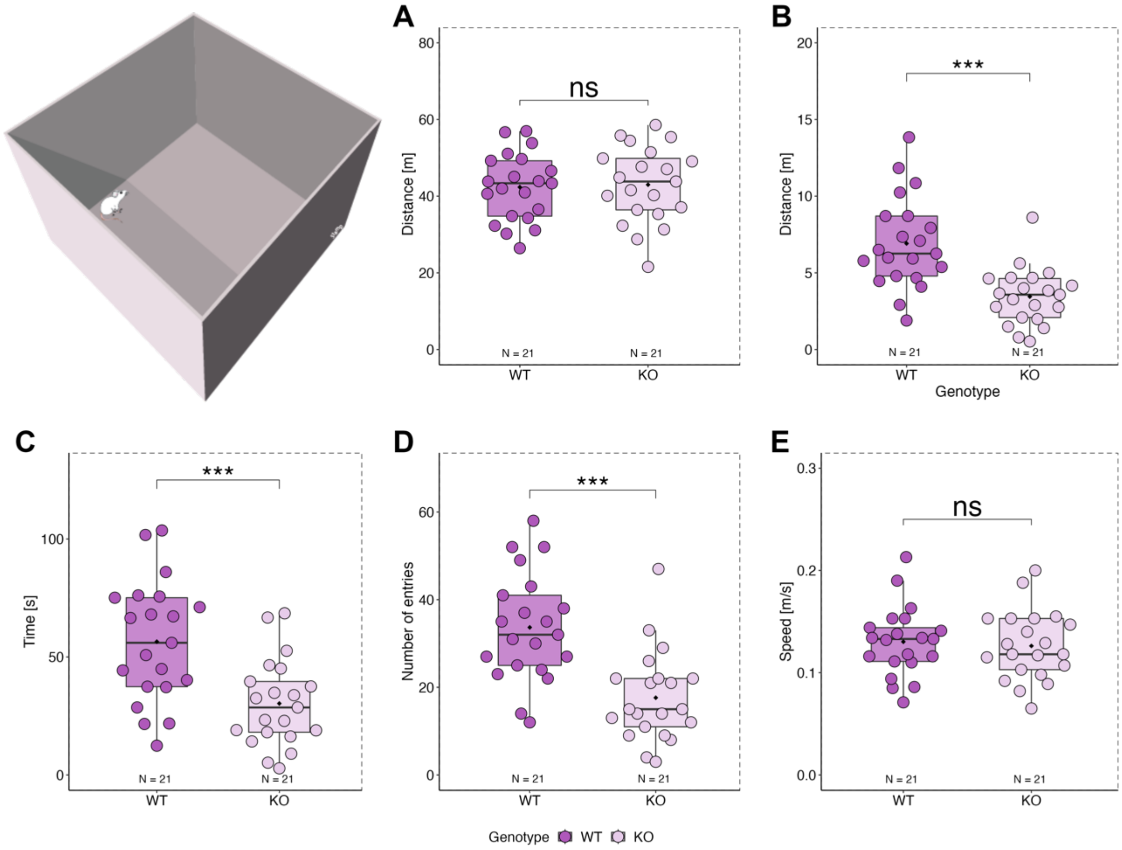

Figure 12: Camk2aCre WTAP KO animals in the open field test

(A) Total distance travelled. **(B)** Distance travelled in the center zone. **(C)** Time spent in the center. **(D)** Number of entries to the center zone. **(E)** Mean speed in the center zone. Individual results are plotted for both genotypes (WT = 21, KO = 21). Ns = not significant, *: p.adj. < 0.05. ** p.adj. < 0.01, *** p.adj. < 0.001, **** p.adj. < 0.000. Adjusted p-values were obtained using either the independent two-sample t-test, Welch's t-test, or Wilcoxon test as appropriate and corrected for multiple testing using the Benjamini and Hochberg method. One animal was excluded due to tracking failure.

There was no difference in the overall locomotion of WT and KO animals across the 10 min of the test (p.adj. = 0.83, independent two-sample t-test). In contrast, KO animals spent significantly less time in the center zone than the WT animals (p.adj. = 0.0008, independent two-sample t-test). This is reflected in the distance the animals spent in the center zone (p.adj. = 0.0001, independent two-sample t-test) and the number of entries (p.adj. = 0.0001, independent two-sample t-test). While in the center zone, WT and KO animals moved at a comparable pace (p.adj. = 0.83, independent two-sample t-test) suggesting no difference in locomotor ability.

WTAP KO animals exhibit hyperactivity in the EPM test

To corroborate the findings from the OF test, animals were subsequently tested in the EPM. The EPM test relies on the exploratory drive of mice to investigate a novel environment and the instinct to avoid exposed positions and is a classical test used to determine anxiety-like behaviors[189]. The test was performed at an ambient lighting of 40 lux and for a duration of 10 mins. Group comparisons were tested using the independent two-sample t-test, Welch's t-test, or Wilcoxon test as appropriate and corrected for multiple testing using the Benjamini and Hochberg method. A summary of the results is shown in Figure 13.

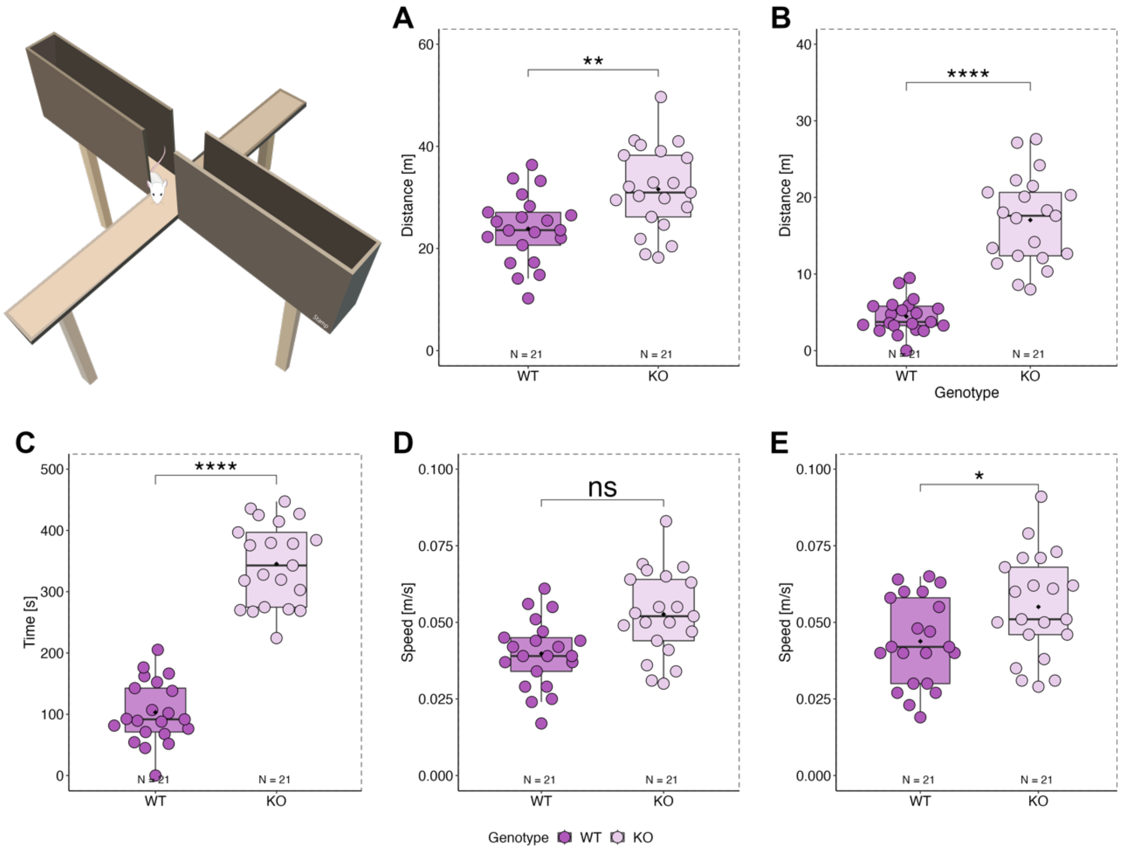

Figure 13: Camk2aCre WTAP KO animals in the EPM test

(A) Total distance travelled. **(B)** Distance travelled in open arms. **(C)** Time spent in the open arms. **(D)** Mean speed in the open arms. **(E)** Mean speed in the closed arms. Individual results are plotted for both genotypes (WT = 21, KO = 21). Ns = not significant, *: p.adj. < 0.05. ** p.adj. < 0.01, *** p.adj. < 0.001, **** p.adj. < 0.000. Adjusted p-values were obtained using either the independent two-sample t-test, Welch's t-test, or Wilcoxon test as appropriate and corrected for multiple testing using the Benjamini and Hochberg method. One animal was excluded due to a tracking failure.

A striking difference in the behavior of KO animals was apparent when observing the animals during testing. While some animals, later identified as WT, showed the expected exploration pattern, including cautious risk assessment, KO animals transferred to the open arms with little hesitation and remained there for large parts of the test. Overall, KO animals exhibited increased levels of activity and showed signs of heightened arousal (hyperlocomotion, hectic abrupt movements etc.). This is reflected in the increased distance travelled in both arms (p.adj. = 0.003, independent two-sample t-test). Interestingly, WTAP KO animals showed a clear preference for the open arm, spending on average more than half of the test time in it (p.adj. < 0.0001, independent two-sample t-test). Accordingly, KO animals traveled a greater distance in the open arm than WT animals (p.adj. < 0.0001, Welch's t-test). Furthermore, KO animals exhibit a significantly increased velocity in the closed arm (p.adj. = 0.03, independent two-sample t-test). In contrast, no significant difference in the velocity within the open arm was determined (p.adj. = 0.03, independent two-sample t-test).

Several KO animals fell off the elevated plus maze during the first two mins of testing and were immediately placed back into the maze. In the presented analysis, these animals are included as the removal of these animals from the analysis does not affect the results.

WTAP KO animals prefer the dark compartment in the DL test

To expand upon the differences in the OF and EPM test, WTAP KO animals were also tested in the DL test. In contrast to the other tests, this experiment is performed with a higher light intensity (~ 140 lux in lit zone and < 5 lux in dark zone, duration: 10 min) and relies on the innate aversion of mice towards brightly lit spaces. As with the other two tests, group comparisons were performed using the independent two-sample t-test, Welch's t-test, or Wilcoxon test as appropriate and corrected for multiple testing using the Benjamini and Hochberg method. A summary of the results is shown in Figure 14.

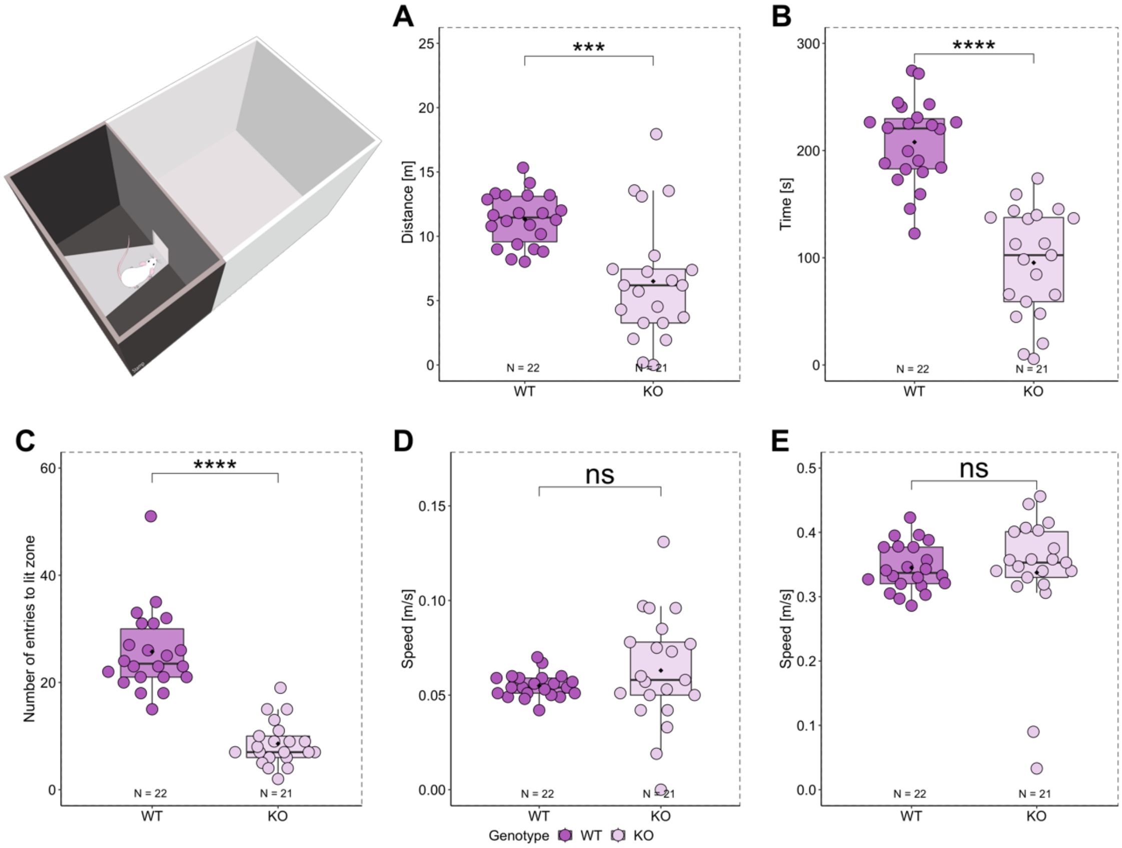

Figure 14: Camk2aCre WTAP KO animals in the DL test

(A) Total distance travelled in the lit compartment. **(B)** Time spent in the lit compartment. **(C)** Number of entries to the lit zone. **(D)** Mean speed in the lit zone. **(E)** Maximum speed in the lit zone. Individual results are plotted for both genotypes (WT = 22, KO = 21). Ns = not significant, *: p.adj. < 0.05. ** p.adj. < 0.01, *** p.adj. < 0.001, **** p.adj. < 0.000. Adjusted p-values were obtained using either the independent two-sample t-test, Welch's t-test, or Wilcoxon test as appropriate and corrected for multiple testing using the Benjamini and Hochberg method.

Across the test duration, KO animals spent significantly less time in the lit compartment, compared to WT controls (p.adj. < 0.0001, independent two-sample t-test). Accordingly, KO animals also made less distance (p.adj. = 0.0003, Welch's t-test) and entered the lit zone fewer times than WT animals (p.adj. < 0.0001, Wilcoxon test). No differences were determined for the average speed in the lit compartment (p.adj. = 0.29, Welch's t-test) and the maximum speed (p.adj. = 0.35, Wilcoxon test).

4.1.4 WTAP KO induces volumetric changes in the cortex and thalamus

To address whether the observed behavioral differences are potentially the result of structural differences in the brain, MRI was performed. For this, the same animals used for the home cage locomotion test (WT= 16, KO = 16) were subjected to structural scans using a 9.4 T scanner (BioSpec, Bruker BioSpin GmbH). For the presented analysis, 4 animals were excluded, because of motion artifacts (3) and hydrocephalus (1). As a result, the results shown below are based on the structural scans of 28 animals (WT = 14, KO = 14). For the analysis, the data were converted to NIFTI format and subsequently analyzed using Statistical Parametric Mapping software (SPM12, Wellcome Department of Cognitive

Neurology, London, UK). Statistics were performed using GLMs to calculate coefficients that are subsequently subjected to an independent two-sample t-test, with the total intracranial volume (TIV) as a covariate. Thresholds for the spatial voxel-wise map of t-values (t-maps) were set at an uncorrected $p < 0.001$ (thalamus) and $p < 0.005$ (auditory cortex) with adjusted extent threshold to obtain significant (FWE-corrected p.adj. < 0.05) clusters. A full description of the acquisition and data analysis can be found in the Methods section. The results were visualized using the MRIcro software (Chris Rorden) and are summarized in Figure 15.

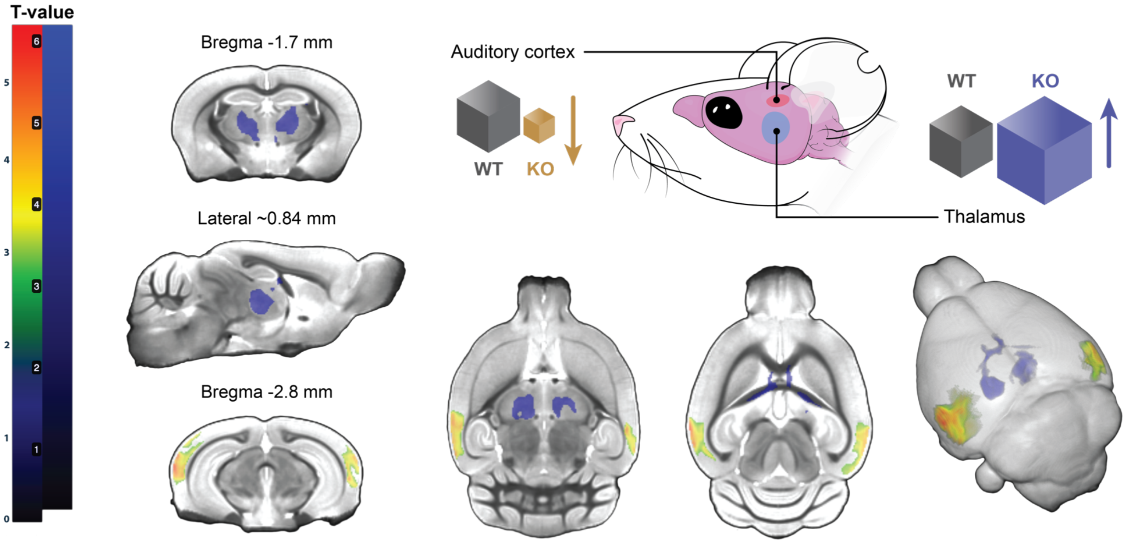

Figure 15: Camk2aCre WTAP KO results in volumetric changes in the thalamus and auditory cortex
Structural imaging of Camk2aCre WTAP KO and WT animals at ~ 9 weeks. The results shown are based on 28 structural scans (WT = 14, KO = 14) and include clusters with FWE-corrected p.adj. < 0.05. Volumetric changes were detected for the thalamus and primary auditory cortex. The color gradients show the T-values, indicative of the relative statistical robustness of changes.

The comparison of WT with KO animals revealed bilateral volumetric changes in two brain regions. Specifically, KO animals showed a significantly increased volume in the thalamus (clusters FWE-corrected p.adj. < 0.05) and a decreased volume in the auditory cortex (clusters FWE-corrected p.adj. < 0.05) compared to WT animals.

The animals tested in the home cage activity and scanned with MRI were split into two cohorts for tissue collection. The tissue of one cohort was used for metabolomic analysis and the tissue of the second cohort was used for the proteomic screening.

4.1.5 WTAP KO alters the protein composition in the mPFC, dHPC and vHPC

To understand the underlying cause of the observed differences in circadian rhythm, classical behavior tests and volumetric changes, a proteomic screening was performed. For this, tissue from 6 WT and 6 KO animals previously used in MRI scan and home cage activity monitoring was freshly dissected from the mPFC, dHPC and ventral HPC (vHPC). The LC-MS measurements were performed at the Core Facility / Mass Spectrometry at the Max Planck Institute of Biochemistry (Martinsried, Germany) and the data were analyzed using the MaxQuant software (version 1.6.17.0)[179] with standard settings as described in the Methods section. In brief, peaks were identified using the SwissProt database and signals were quantified across samples using a label-free quantification algorithm. Proteins with a minimum of two ratio counts of unique peptides in three or more samples of each genotype were included in the statistical analysis. For the statistical evaluation, intensity values were log2-transformed and analyzed using a one-way ANOVA with permutation-based FDR correction. Subsequently, group comparisons were performed using the independent two-sample t-test. Reported below are the results for FDR < 0.05.

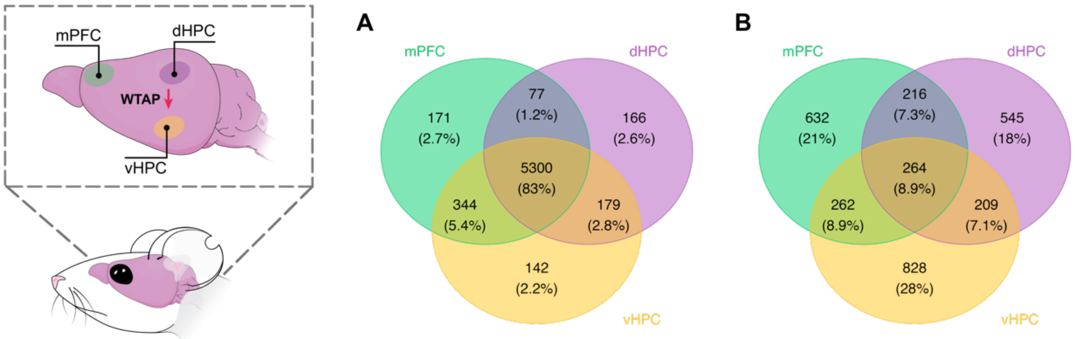

Figure 16: WTAP KO animals show a dysregulated proteome in the mPFC, dHPC and vHPC
(A) Overview of the number of unique proteins identified using label free LC-MS. **(B)** Overlap of differentially expressed proteins across three brain regions (FDR < 0.05).

In total, 6,379 unique proteins were identified, out of which 5,300 (83 %) were detected across brain regions, with 171 (2.7 %) being exclusively detected in the mPFC, 166 (2.6 %) in the dHPC and 142 (2.2 %) in the vHPC respectively. In total, 2,924 unique proteins were found to be significantly dysregulated in the brain of WTAP KOs. An overview of the results is shown in Figure 16 and Figure 17.

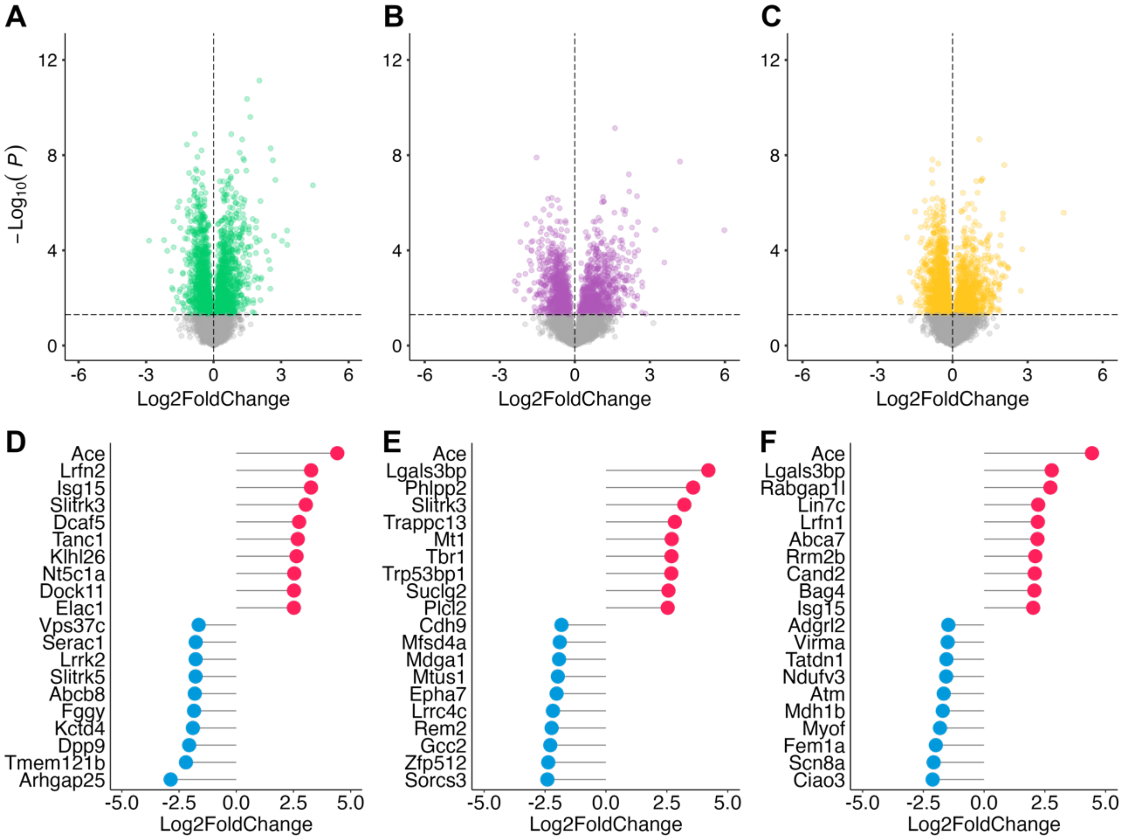

Figure 17: Detailed overview of proteomic changes in the mPFC, dHPC and vHPC of WTAP KO animals
(A-C) Volcano plots showing the differentially regulated proteins in the mPFC **(A)**, dHPC **(B)** and vHPC **(C)** of WTAP KO animals. **(D-F)** The top 10 most up- and downregulated proteins in the mPFC **(D)**, dHPC **(E)** and vHPC **(F)**. Results were filtered for FDR < 0.05.

Considering the overwhelming amount of differentially expressed proteins and the surprising region-specificity of the observed changes, the presented results are restricted to changes that are observed in respect to mitochondria, m^{6}A regulators and selected synaptic scaffolding proteins.

To determine regulated pathways and emerging topics, a GO analysis was performed as described in the Methods section. The results are summarized below for each individual region.

Gene Ontology enrichment analysis reveals enrichment for mitochondrial processes in the mPFC, dHPC and vHPC of WTAP KO animals

Gene Ontology (GO) enrichment analysis is used to identify biological or molecular processes and cellular compartments that are significantly over represented in large scale data sets such as obtained with label free LC-MS. For this, the GO analysis makes use of the GO classification system that annotates genes and their products in respect to their function, location and involvement in biological processes. The annotation is based on the classifications released by the GO consortium which annotates gene products for the three orthogonal ontologies: CC, MF and BP[172,173]. Accordingly, as an example, WTAP is located in the nuclear speckles (CC), protein binding (MF) and involved in mRNA processing (BP). This annotation is available for thousands of genes and can be used to hierarchically cluster, for example, RNA sequencing results within the available ontologies. With this, GO analysis allows to recognize hidden patterns and can be used to generate leads for subsequent hypothesis testing. In this thesis, GO enrichment analysis was applied to the results form sequencing experiments and proteomic screenings.

Since the GO terminology contains a high degree of similarity between closely related terms, semantic similarity analysis was performed to reduce redundancies and reveal overarching topics. Semantic similarity analysis operates on the assumption that the functional similarity of genes is reflected in the degree of similarity in their annotation. In the presented analysis, the R package GOSemSim[175] was used, which employs the graph-based Wang's method. This method calculates semantic similarities based on the topology of the GO graph structure, taking into account the semantic contribution of ancestral terms within the GO topology[190].

In the mPFC,1,359 proteins were differentially regulated in WTAP KO animals (FDR < 0.05) with 694 (51 %) being significantly up- and 665 (49 %) downregulated. The GO analysis performed with the significantly upregulated proteins, did not identify any enrichment, while a strong enrichment for BP, CC and MF terms was determined for the downregulated proteins. A summary of the results is shown in Figure 18, Figure 19 and Figure 20.

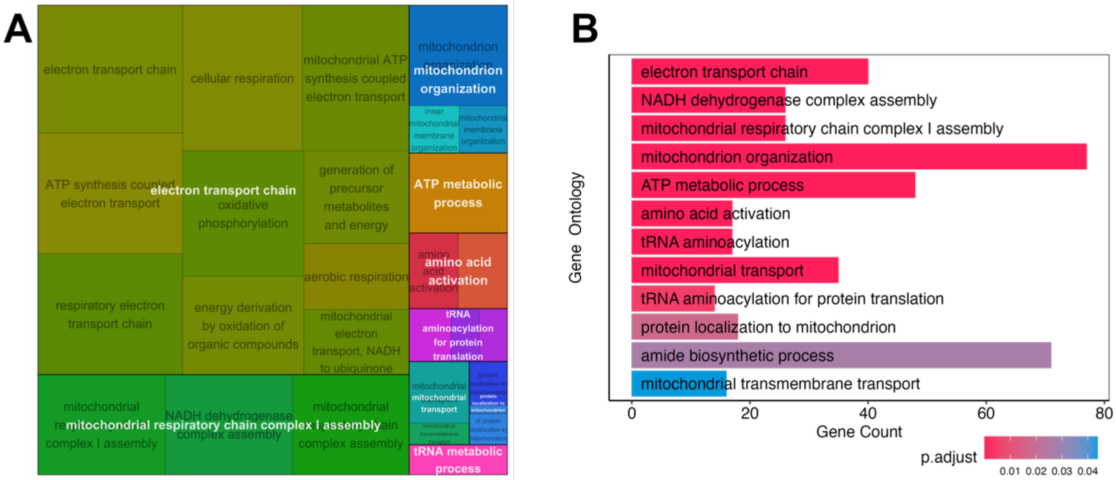

Figure 18: Downregulated proteins in the mPFC of WTAP KOs are enriched for mitochondrial processes

(A) Overview of the GO results for BP after application of semantic similarity analysis (FDR < 0.05). The enriched terms include: electron transport chain, mitochondrial respiratory chain complex I assembly, mitochondrion organization, ATP metabolic process, amino acid activation, tRNA aminoacylation for protein translation, mitochondrial transport, tRNA metabolic process and protein localization to mitochondrion. **(B)** Bar plot showing the number of proteins associated with individual GO terms and their respective p.adj. values.

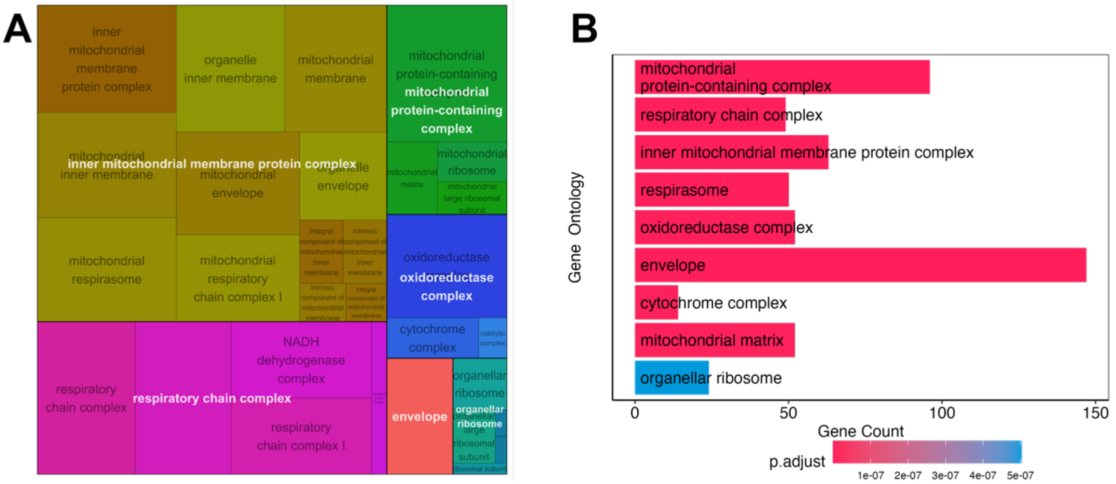

Figure 19: Downregulated proteins in the mPFC of WTAP KOs are enriched for mitochondrial compartments
(A) Overview of the GO results for CC after application of semantic similarity analysis (FDR < 0.05). The enriched terms include: inner mitochondrial membrane protein complex, respiratory chain complex, mitochondrial protein-containing complex, oxidoreductase complex, envelope, organellar ribosome. **(B)** Bar plot showing the number of proteins associated with individual GO terms and their respective p.adj. values.

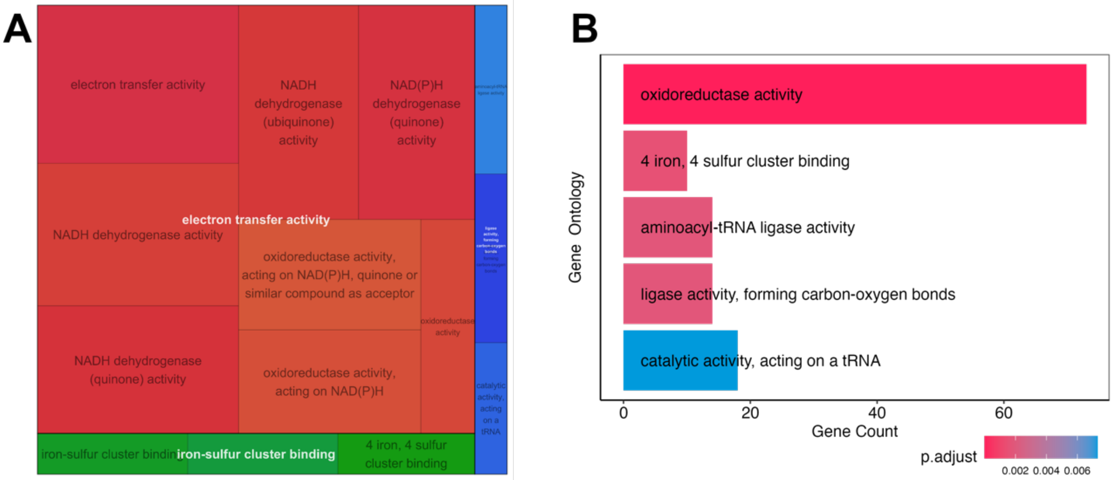

Figure 20: Downregulated proteins in the mPFC of WTAP KOs are enriched for mitochondrial functions
(A) Overview of the GO results for MF after application of semantic similarity analysis (FDR < 0.05). The enriched terms include: electron transfer activity (oxidoreductase activity), iron-sulfur cluster binding, ligase activity forming carbon-oxygen bonds. **(B)** Bar plot showing the number of proteins associated with individual GO terms and their respective p.adj. values.

In the dHPC, 1,214 proteins were differentially regulated in WTAP KO animals (FDR < 0.05) with 660 (54 %) being significantly up- and 554 (46 %) downregulated. The GO analysis performed with the significantly upregulated proteins, did not identify any enrichment, while a clear enrichment for mitochondrial BP, CC and MF terms was determined for the downregulated proteins. A summary of the results is shown in Figure 21, Figure 22 and Figure 23.

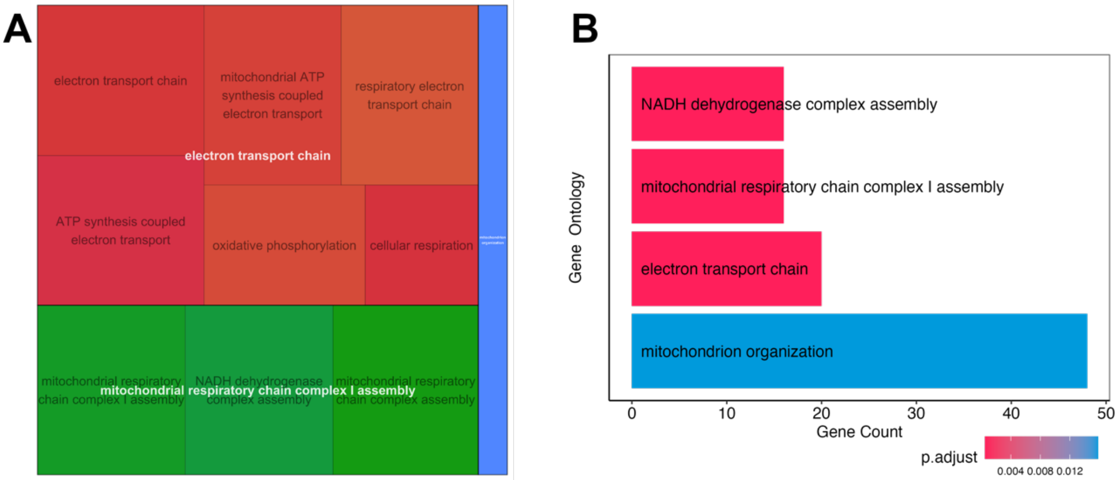

Figure 21: Downregulated proteins in the dHPC of WTAP KOs are enriched for mitochondrial processes

(A) Overview of the GO results for BP after application of semantic similarity analysis (FDR < 0.05). The enriched terms include: electron transport chain, mitochondrial respiratory chain complex I assembly, mitochondrion organization. **(B)** Bar plot showing the number of proteins associated with individual GO terms and their respective p.adj. values.

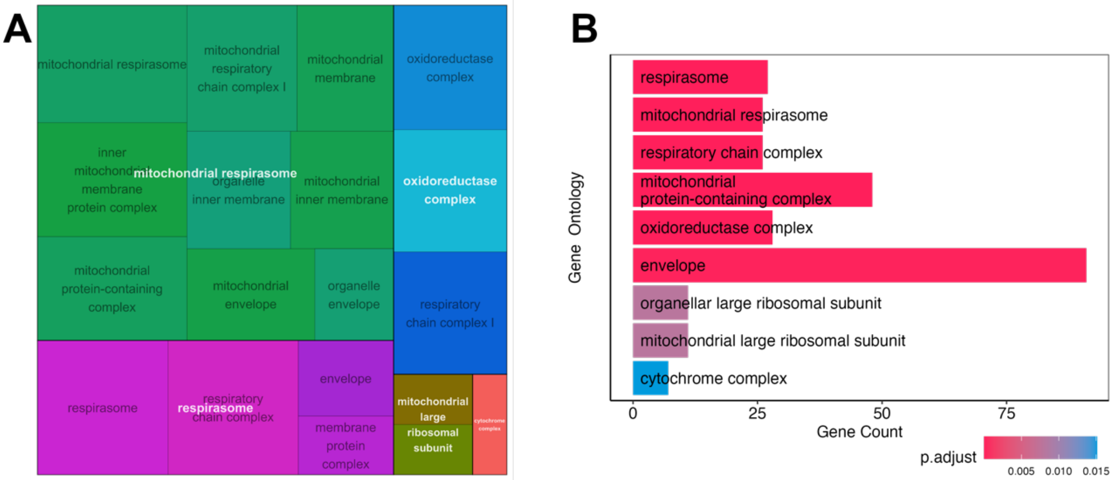

Figure 22: Downregulated proteins in the dHPC of WTAP KOs are enriched for mitochondrial compartments

(A) Overview of the GO results for CC after application of semantic similarity analysis (FDR < 0.05). The enriched terms include: mitochondrial respirasome, respirasome, oxidoreductase complex, mitochondrial large ribosomal subunit, cytochrome complex. **(B)** Bar plot showing the number of proteins associated with individual GO terms and their respective p.adj. values.

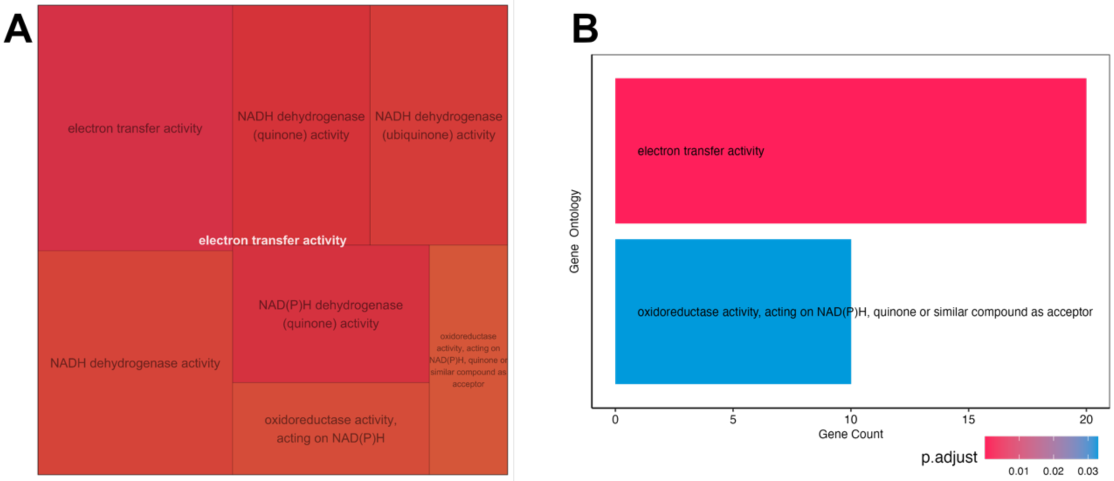

Figure 23: Downregulated proteins in the dHPC of WTAP KOs are enriched for mitochondrial functions
(A) Overview of the GO results for MF after application of semantic similarity analysis (FDR < 0.05). The enriched terms include: electron transfer activity. (**B)** Bar plot showing the number of proteins associated with individual GO terms and their respective p.adj. values.

For the vHPC, 1,546 proteins were differentially regulated in WTAP KO animals (FDR < 0.05) with 657 (42 %) being significantly up- and 889 (58 %) downregulated. The GO analysis performed with the significantly downregulated proteins identified an enrichment for mitochondrial CC terms. For the significantly upregulated proteins an enrichment for neuron specific CC terms was determined. A summary of the results is shown in Figure 24 and Figure 25.

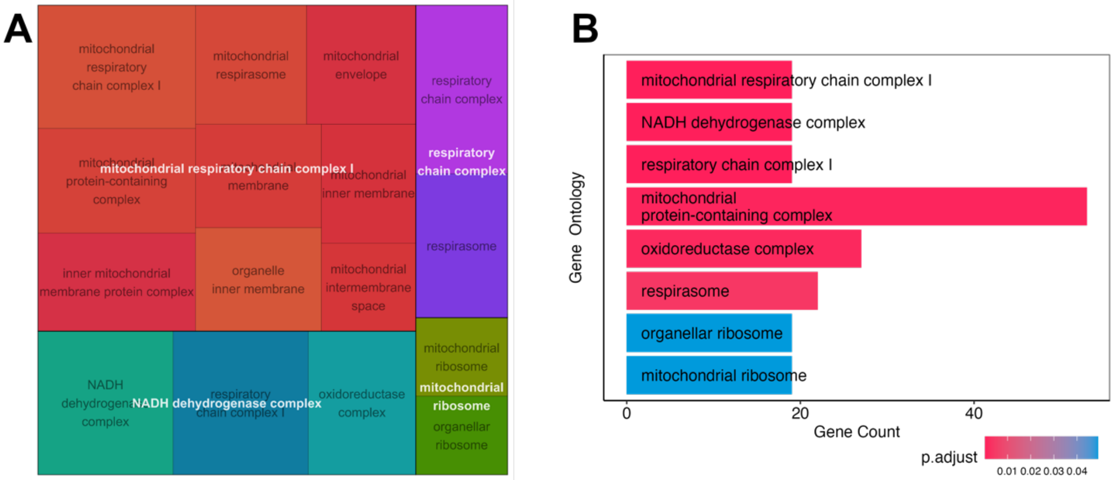

Figure 24: Downregulated proteins in the vHPC of WTAP KOs are enriched for mitochondrial compartments
(A) Overview of the GO results for CC after application of semantic similarity analysis (FDR < 0.05). The enriched terms include: mitochondrial respiratory chain complex I, NADH dehydrogenase complex, respiratory chain complex, mitochondrial ribosome. **(B)** Bar plot showing the number of proteins associated with individual GO terms and their respective p.adj. values.

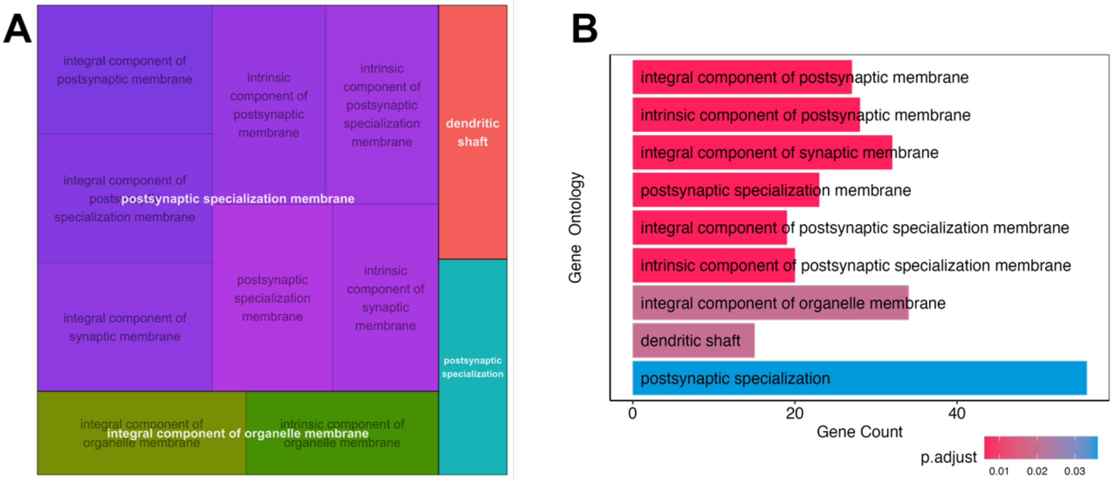

Figure 25: Upregulated proteins in the vHPC of WTAP KOs are enriched for neuron-specific terms

(A) Overview of the GO results for CC after application of semantic similarity analysis (FDR < 0.05). The enriched terms include: postsynaptic specialization membrane, integral component of organelle membrane, dendritic shaft, postsynaptic specialization **(B)** Bar plot showing the number of proteins associated with individual GO terms and their respective p.adj. values.

Across brain regions, an enrichment for mitochondrial themes was observed for proteins that were determined to be significantly depleted in WTAP KO animals. The changes were most pronounced in the mPFC, likely due to the high penetrance of the KO and homogeneity of the tissue. In addition, an enrichment for neuronal compartments was identified among the significantly upregulated proteins in the vHPC.

WTAP KO results in dysregulated mitoribosomes and respiratory chain complex components

The pathway enrichment analysis revealed a strong enrichment for mitochondria associated processes. Two topics that stand out are the mitoribosomes and the electron transport chain. To highlight the observed differences, the changes were qualitatively summarized for the mPFC in Figure 26, Figure 27 and Figure 28.

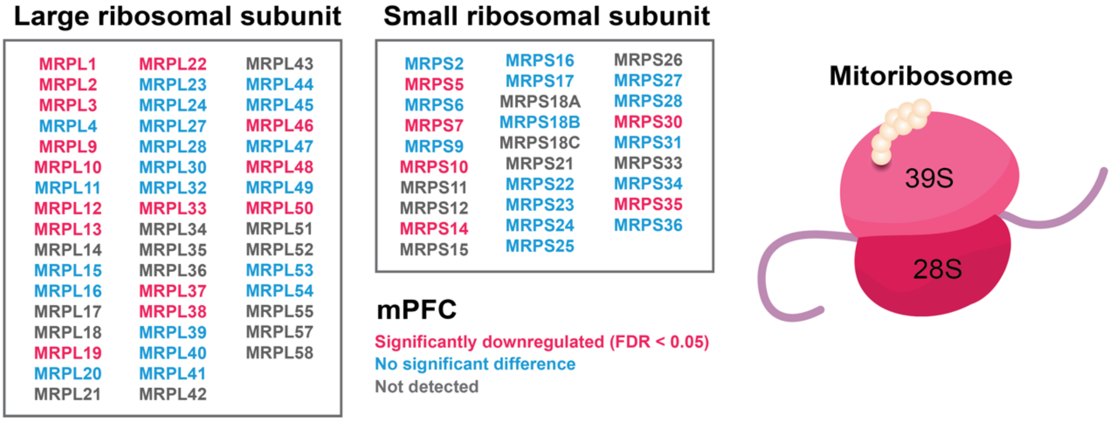

Figure 26: Downregulation of mitoribosome components in the mPFC of WTAP KO animals

Overview of the mitoribosome components detected in the mPFC (WT = 6, KO = 6). Significantly downregulated proteins are highlighted in red (FDR < 0.05), proteins for which no differences between WT and KO were observed are marked in blue and proteins that were not detected are shown in gray. No significantly upregulated proteins were identified.

Overall, there was a pronounced downregulation of mitoribosome components. Interestingly, not a single significantly upregulated protein was identified. Mitoribosomes are essential for the synthesis of mitochondrial encoded genes. The mitochondrial DNA contains the information for the synthesis of 13 mt-mRNAs, 22 tRNAs and 2 rRNAs[191]. All 13 proteins encoded in the mitochondria are components of the respiratory chain complex. Out of these, 6 were detected to be differentially regulate in either the mPFC, dHPC and vHPC of WTAP KO animals, as shown in Figure 27.

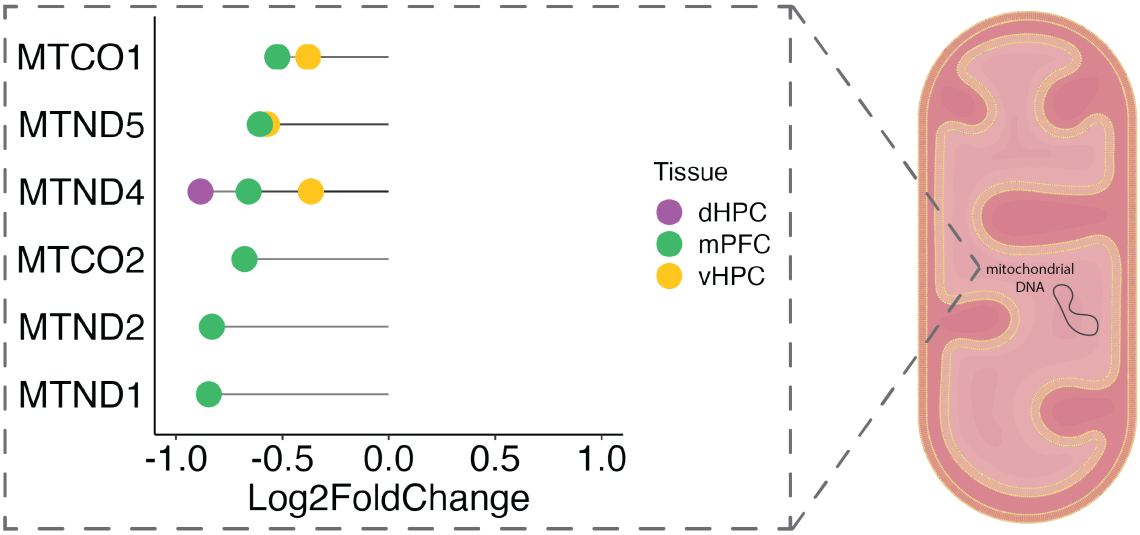

Figure 27: Mitochondrial encoded proteins are downregulated in WTAP KO tissue

Out of 13 mitochondrial encoded proteins 6 were significantly downregulated in the brain of WTAP KO animals (FDR < 0.05). Two more proteins (Mtatp6, Mtatp8) were detected but are not significantly regulated in either region.

In addition to the mitoribosomes, the abundance of proteins that compose the mitochondrial respiratory chain were examined in the mPFC. A qualitative overview of the observed changes is shown in Figure 28.

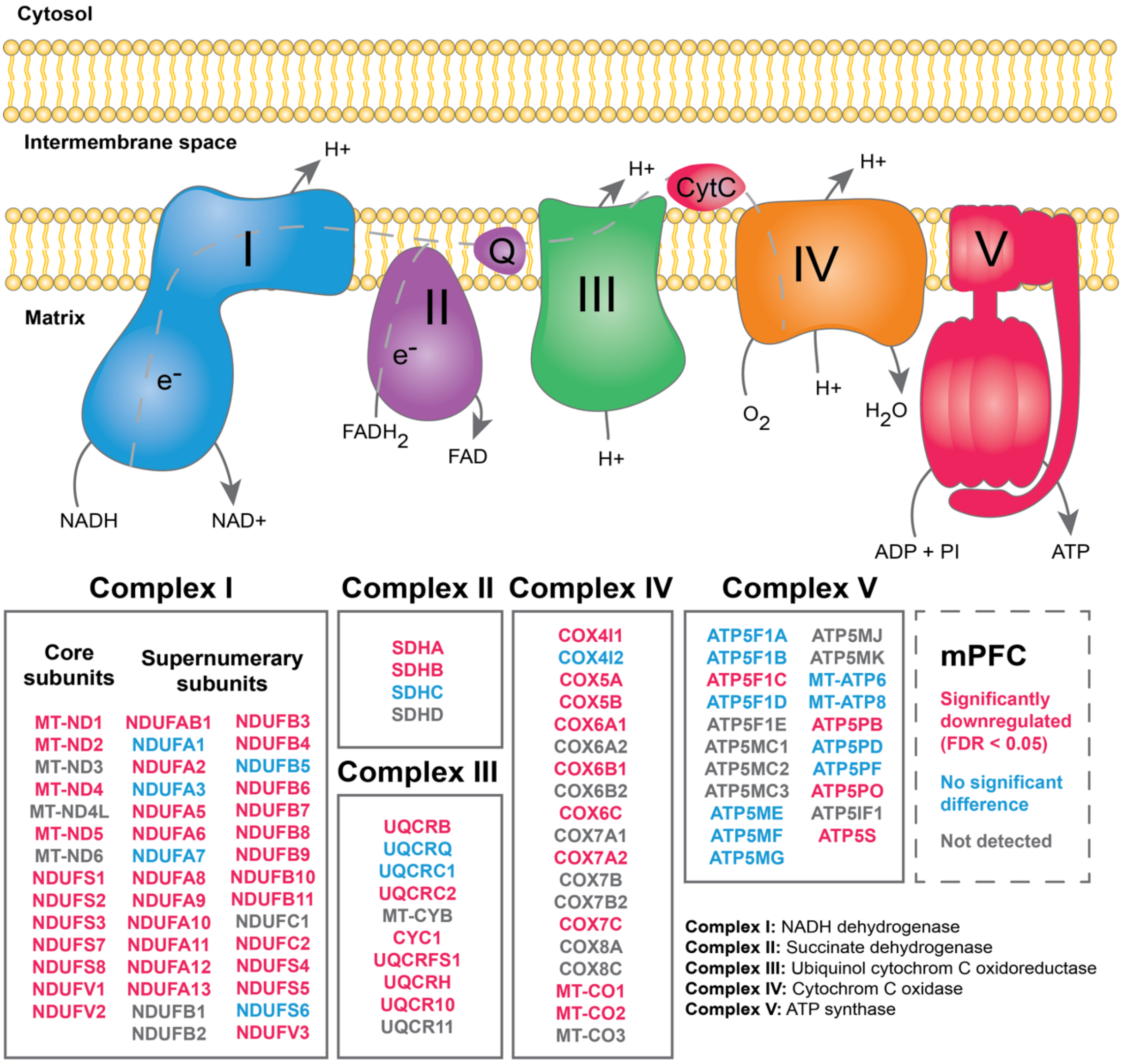

Figure 28: WTAP KO effects on respiratory chain components in the mPFC of WTAP KO animals

Overview of respiratory chain complex components in the mPFC (WT = 6, KO = 6). Significantly downregulated proteins are highlighted in red (FDR < 0.05), proteins for which no differences between WT and KO were observed are marked in blue and proteins that were not detected are shown in gray. No significantly upregulated proteins were identified.

The examination of components of the respiratory chain complexes revealed an overwhelming downregulation of components in all complexes (FDR < 0.05). Most striking were the changes detected in Complex I (NADH dehydrogenase) with the vast majority of components being significantly depleted in KO animals.

WTAP KO driven regulation of m^{6}A ‘regulators’ and ‘readers’

Considering that the depletion of WTAP is expected to interfere with m^{6}A regulation, the protein levels of m^{6}A ‘writers’ ‘readers’ and ‘erasers’ were examined. Several components of the m^{6}A regulatory machinery were determined to be differentially expressed. The most pronounced upregulation was detected for the WTAP interacting protein RBM15 which is significantly upregulated in the mPFC, dHPC and vHPC of WTAP KO animals and the WTAP interacting protein VIRMA, which was significantly downregulated across regions. The m^{6}A demethylase FTO was also found to be significantly upregulated in all three brain regions. In contrast, the YTH-family ‘readers’ show a differential regulation that overall matches the results of the dCA1 sequencing (reported below). An overview of the results is shown in Figure 29. Proteins that were not quantifiable, are reported in the figure legend.

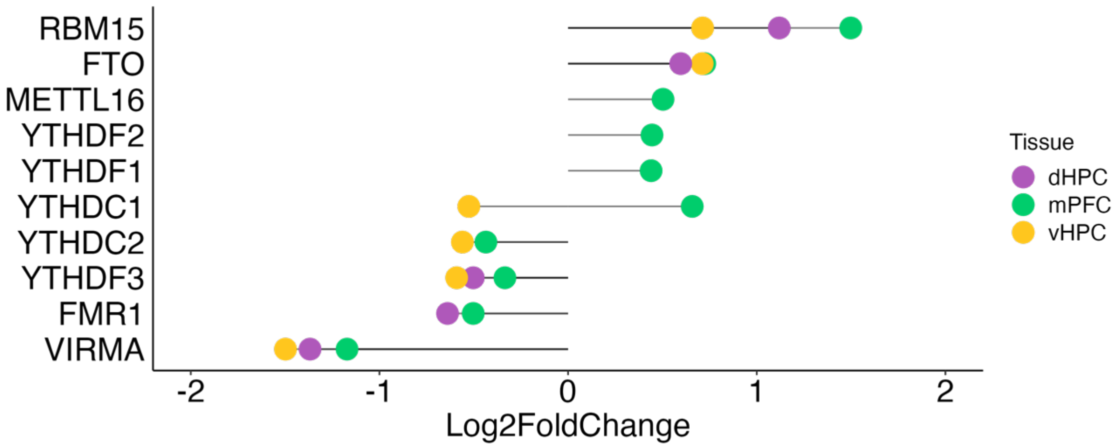

Figure 29: Differential abundance of m^{6}A 'regulators' and 'readers' in WTAP KO animals
Several components of the m^{6}A 'writer complex', as well as m^{6}A 'readers' are differentially regulated in WTAP KO animals (FDR < 0.05). Proteins that were not quantifiable include: Mettl3 (mPFC, dHPC), Mettl14 (all), Rbm15b (mPFC, vHPC), Zc3h13 (all), Alkbh5 (dHPC), Hnrnpa2b (all). No significant difference in expression level was determined for METTL16 (dHPC, vHPC) Alkbh5 (mPFC, vHPC) and Hnrnpc.

WTAP KO alters the abundance of SALM and SLITRK synaptic cell adhesion molecules

Among the top regulated proteins across brain regions were several members of the synaptic adhesion-like molecule (SALM) family and slit and trk-like (SLITRK) family of synaptic cell adhesions molecules. SALM and SLITRK proteins are involved in neurite outgrowth and the development and regulation of excitatory and inhibitory synapses[192–194]. The observed changes are summarized in Figure 30.

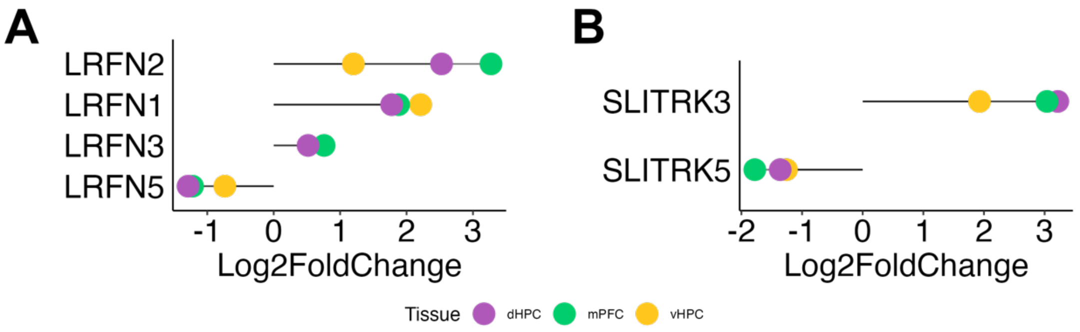

Figure 30: Differential regulation of synaptic scaffolding molecules
(A) Significantly regulated SALM (gene symbol: Lrfn) family members across brain regions (FDR < 0.05). **(B)** Significantly regulated SLITRK family members across brain regions (FDR < 0.05).

Accordingly, LRFN1, LRFN2 and SLITRK3 were also among the strongest upregulated candidates in the membranome analysis that is presented below. In addition, all three were determined to be differentially expressed on the level of mRNA, as demonstrated by poly-(A) sequencing and RT-qPCR.

4.1.6 WTAP KO disturbs the metabolic balance

The day-night cycle of rest and activity requires the adaptation to changing metabolic demands and relies on the harmonization of circadian clocks with metabolic activity[195]. The striking difference in the circadian activity patterns of WTAP KO animals and the pronounced depletion of mitochondrial proteins, poses the question whether there is a fundamental shift in the metabolic state of Camk2aCre KO tissue.

To address this, the mPFC, dHPC and vHPC of 8 WT and 8 KO animals (previously used in MRI scan and home cage activity monitoring) were freshly dissected for a metabolic screening using LC-MS. The metabolite feature extraction was performed using MetaboScape (version 4.0) for metabolites detected in at least 70 % of samples. Annotated features were processed with Perseus 1.6.14.0[182] with the intensity values of features being normalized and log2-transformed before the statistical analysis. Differences between WT and KO were assessed using independent two-sample t-tests with a threshold FDR < 0.1 (commonly used for analyses of the metabolome). An overview of the results across the three brain regions is shown in Figure 31.

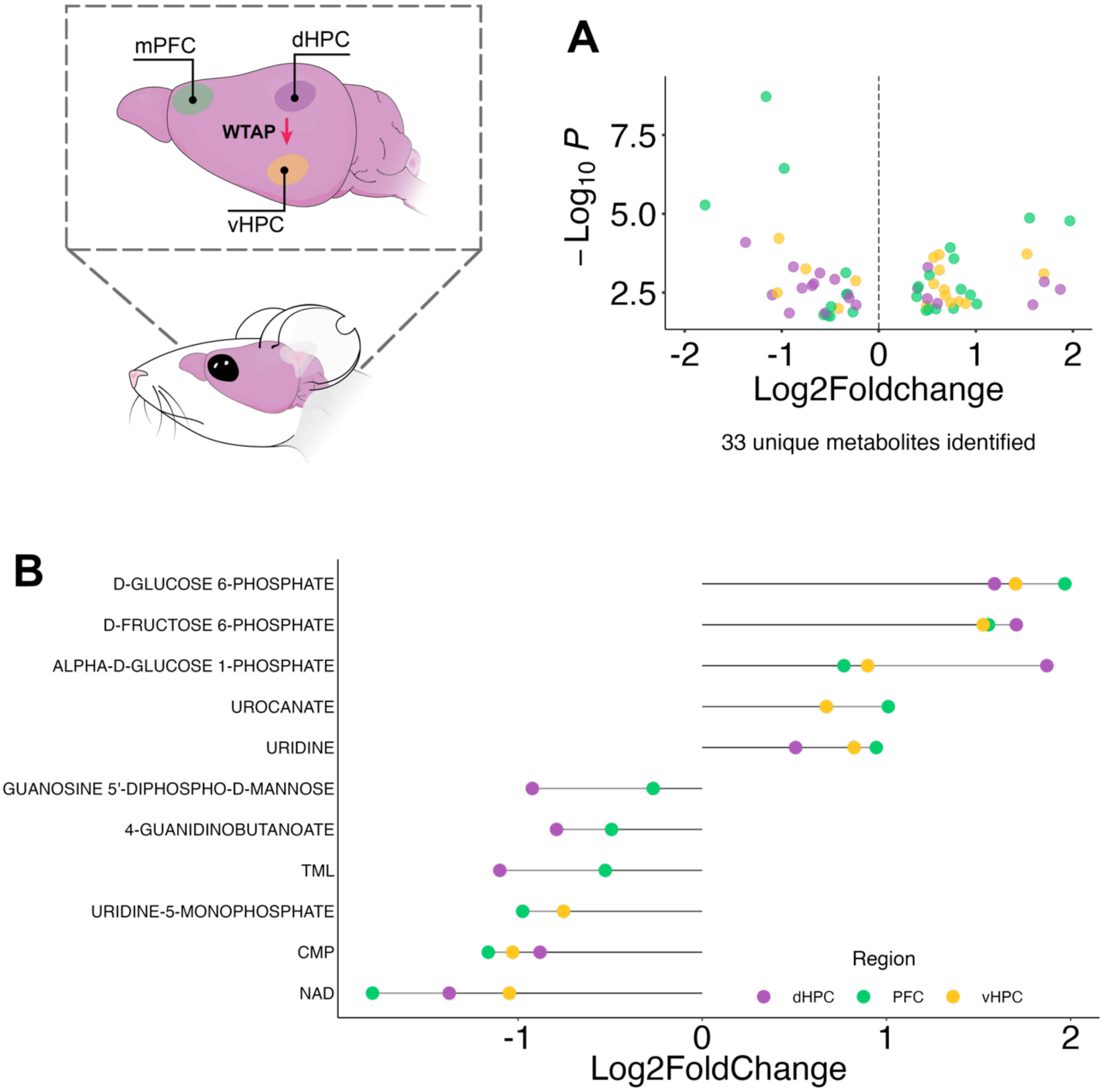

Figure 31: Metabolic dysregulation in Camk2aCre WTAP KO brains

(A) In total, 33 unique metabolites were identified that are dysregulated in the brain (mPFC, dHPC, vHPC) of KO animals. **(B)** Top up- and downregulated metabolites across brain regions. Metabolites were measured in 8 WT and 8 KO animals. Group comparisons shown were obtained by an independent two-sample t-test and are reported for FDR < 0.1. Abbreviations: TML = Nepsilon, Nepsilon, Nepsilon-trimethyllysine; CMP = cytidine monophosphate; NAD = nicotinamide adenine dinucleotide

In total, 123 distinct metabolites were identified across the three brain regions, with 33 unique metabolites being differentially regulated (FDR < 0.1). Overall, a high degree of consistency across regions was observed for the most robust changes. The most pronounced differential upregulation in KO animals was observed for three glycolysis metabolites (glucose-1-phosphate, glucose-6-phosphate, fructose-6-phosphate), while the strongest downregulation was detected for the coenzyme nicotinamide adenine dinucleotide (NAD^+) which, among many other processes, is essential for glycolysis[196]. Fitting this observation, the glucose-6-phosphate synthesizing enzyme hexokinase (HK1) was determined to be significantly downregulated on the level of proteins in the brain of KO animals (mPFC: L2FC = -0.60, p.adj. < 0.0001, dHPC: L2FC = -0.045, p.adj. = 0.0001, dHPC: L2FC = -0.21, p.adj. = 0.1).

In addition to glycolysis metabolites and NAD^+, several amino acids and components of nucleic acids are differentially regulated. A detailed list of all identified metabolites can be found in Appendix 8.6.

4.1.7 NexCreERT2 expression in the adult mouse brain

In addition to the Camk2aCre driven KO in the forebrain, the tamoxifen inducible NexCreERT2 was used for assessing the functional consequences of WTAP and YTHDC1 depletion in the cortex and HPC. For this, the previously described NexCreERT2 driver line[151] was crossed with floxed *Wtap* and *Ythdc1* strains. The experiments reported in this thesis were performed with adult animals (> 8 weeks) following the injection protocol described in the Methods section (5 x i.p., 100 mg/kg per day). The tamoxifen driven recombination of NexCreERT2 expressing cells is restricted to projection neurons of the cortex and HPC as shown in Figure 32. In contrast to the Camk2aCre line, no recombination is detected in the dentate gyrus and in subcortical areas.

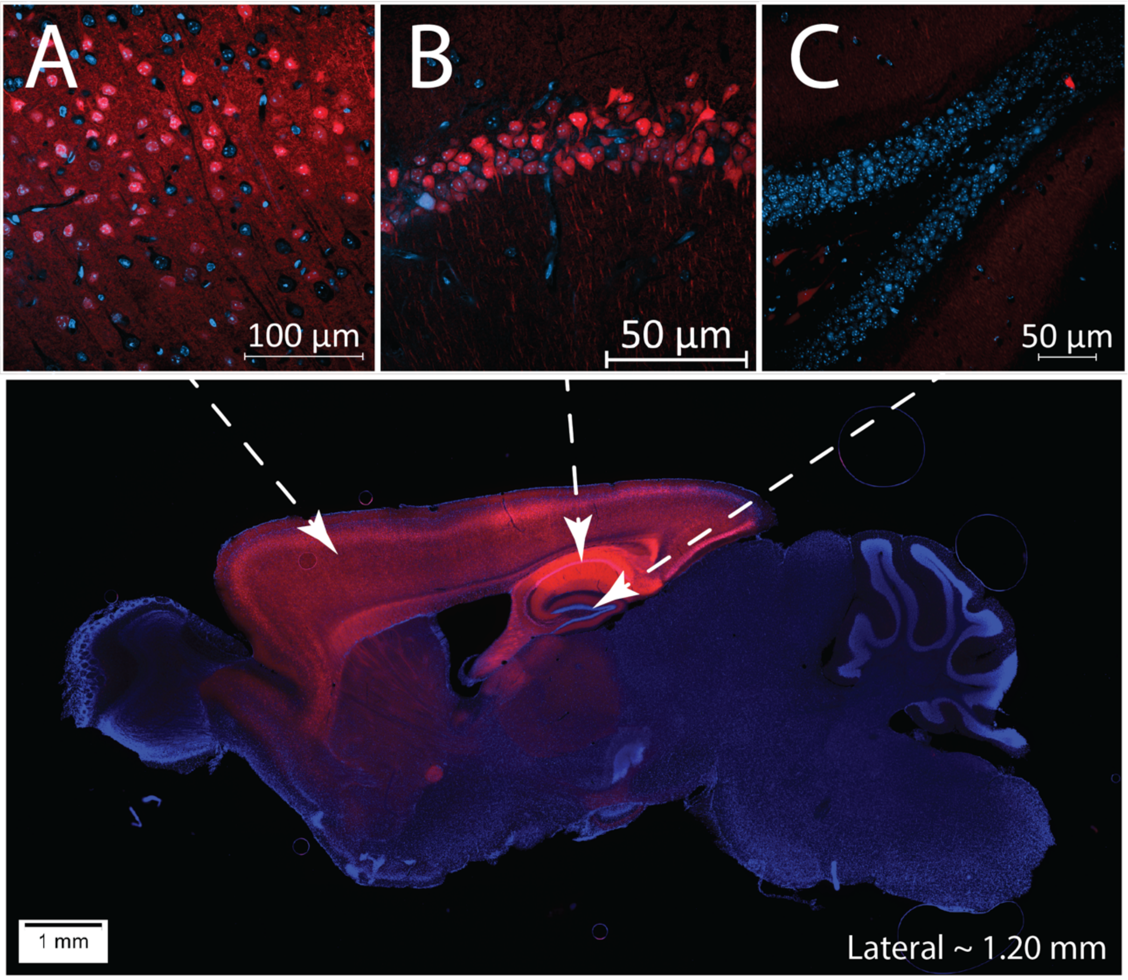

Figure 32: Tamoxifen induces NexCreERT2 recombination in projection neurons of the cortex and HPC **(A)** Sparse labelling of projection neurons is observed across the cortex. **(B)** A strong labelling of projection neurons is detected in the dCA1, with the majority of cells being labelled. **(C)** No labelling was detected in the dentate gyrus granule cell layer. Induction with tamoxifen was performed in an adult animal with 5 x injections (i.p., 100mg/kg per day). The tissue was collected 14 days after the last injection.

The rational for the use of a tamoxifen driven KO is the temporal control of the KO which can be induced in adult animals. In addition, the NexCreERT2 expression is restricted to a smaller subset of neurons than the Camk2aCre driver line. With this in mind, NexCreERT2 KO animals were used for the poly-(A) RNA sequencing and several classical behavior tests.

4.1.8 Validation of NexCreERT2 induced WTAP KO

The NexCreERT2 driven KO of WTAP was induced by administering 100 mg/kg tamoxifen (i.p.) on 5 consecutive days. After a washout period of 14 days, animals were sacrificed for organ collection, or subjected to behavior tests. The efficacy of the CreERT2 driven KO in the HPC was validated on the RNA and protein level. To determine the overall expression patterns of *Wtap*, an ISH was conducted with a probe targeting the floxed exons. As shown in Figure 33 (A), activation of CreERT2 by tamoxifen resulted in a pronounced decrease in the exon signal in the HPC of floxed animals, with the strongest reduction in the dCA1, dCA2 and dCA3. This pattern fits the ISH results for CreERT2 (Appendix 8.7). Notably, no KO was induced in the dentate gyrus.

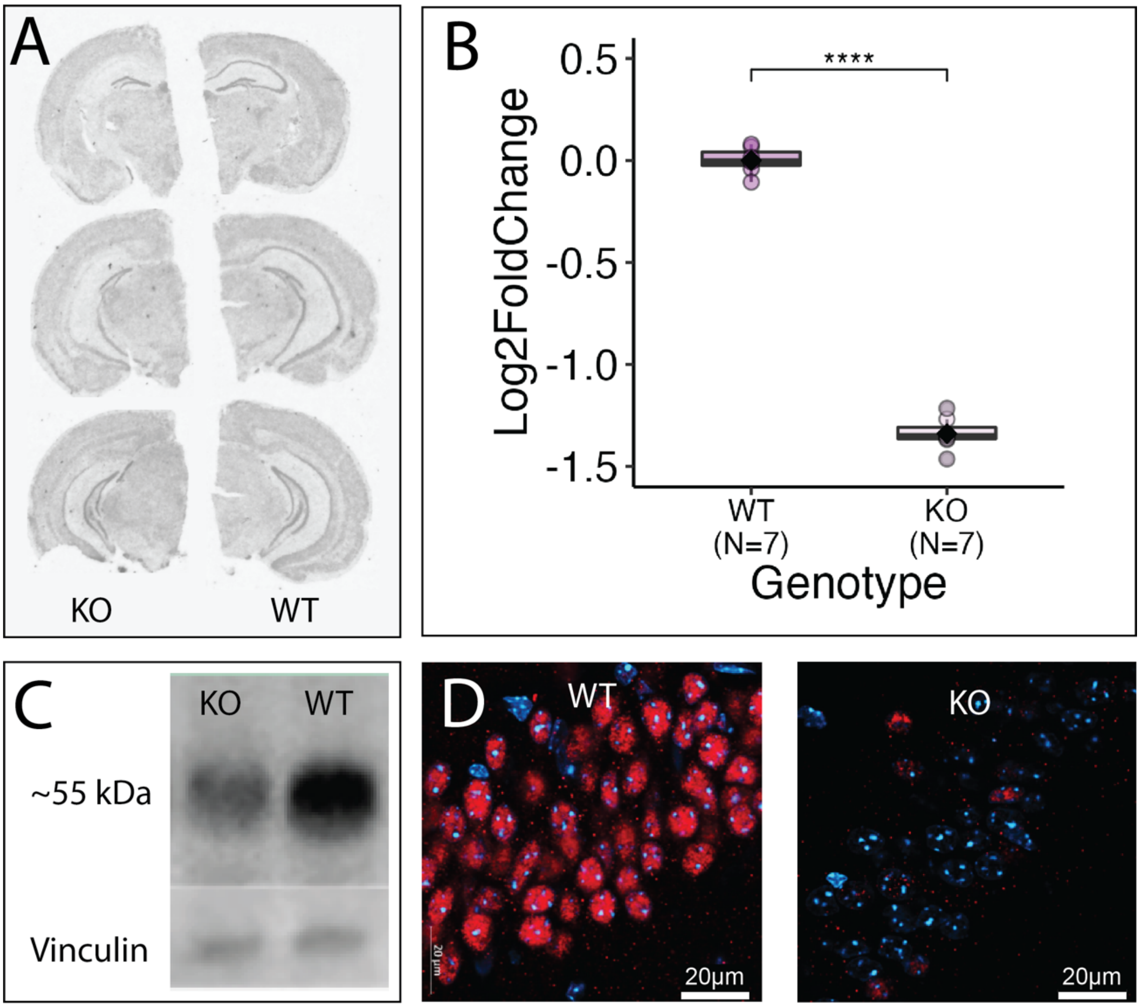

Figure 33: Tamoxifen treatment of NexCreERT2-*Wtap* animals results in a depletion of the floxed exons and WTAP protein

(A) The ISH with a probe targeting the floxed exons 4 and 5 shows a marked decrease in *Wtap* signal in the HPC. **(B)** The KO of cohorts used for gene expression analysis was validated using qPCR. Shown are the results for the samples that were used for RNA sequencing (WT = 7, KO = 7; p.adj. < 0.001, independent two-sample t-test). **(C)** The reduction in WTAP protein levels was demonstrated using western blot (anti WTAP: 1:1000). **(D)** Immunostaining against WTAP in WT (left panel) and KO mice (right panel) shows the nuclear localization of WTAP and the depletion in KO cells of the dCA1 (anti WTAP: 1:400).

To determine the maximal KO efficacy that can be obtained from bulk tissue, a qPCR targeting the floxed exons was performed with RNA obtained from bulk HPC, dHPC slices and dissected dCA1 (Appendix: 8.8). The results show that a fresh dissection of dCA1 results in the strongest reduction in *Wtap* expression. Therefore, the molecular results presented below were obtained with dissected dCA1 tissue, if not otherwise indicated. The KO efficiency of samples that were used for molecular analyses was validated using qPCR and the KO validation for the samples used for RNA sequencing are shown in Figure 33 (B). In addition, the validation for the cohort used for electrophysiological measurements and qPCRs can be found in Appendix 8.9. Furthermore, western blots were used to demonstrate the depletion of WTAP on the protein level as shown in Figure 33 (C). Corroborating these results, an immunostaining against WTAP demonstrated the depletion of WTAP in the majority of neuronal nuclei in the dCA1 Figure 33 (D).

4.1.9 WTAP KO results in reduced global m^{6}A

It has previously been reported that the depletion of WTAP results in a prominent reduction in m^{6}A levels[36,37,69]. Therefore, to demonstrate a functional consequence of WTAP depletion, the m^{6}A levels in the dCA1 of KO and WT animal were quantified using an anti-m^{6}A ELISA (see Figure 34).

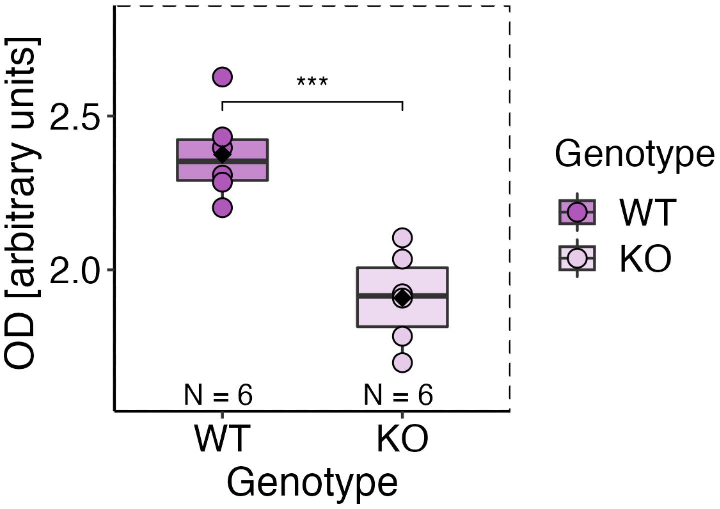

Figure 34: WTAP depletion in the dCA1 reduces m^{6}A levels

The functional consequence of WTAP depletion in the dCA1 was demonstrated using an anti-m^{6}A ELISA kit (WT = 6; KO = 6, $p < 0.001$, independent two-sample t-test). Shown on the y-axis is the optical density (OD) in arbitrary units.

Within the m^{6}A methylation complex, WTAP is essential for localizing the core-complex within the nuclear speckles[37] an important processing site for pre-mRNA. The loss of WTAP results in a marked decrease of m^{6}A levels *in vitro*, likely due to aberrant localization of the methylation machinery[37]. This observation was now confirmed *in vivo*, when WTAP KO animals show a significant reduction in m^{6}A signal in the dCA1, demonstrating that WTAP depletion attenuates m^{6}A methylation levels.

4.1.10 WTAP KO induces massive shift in gene expression

To explore the effects of depleting WTAP on gene expression, poly(A) RNA sequencing was performed as described in the Methods section. In brief, libraries were prepared using the NEBNext Ultra II Directional RNA Library Prep Kit (Illumina) according to manufacturer's instructions, starting from 200 ng DNase I treated total RNA. Samples were sequenced on 2 x lanes of the Hiseq4000 (1 x 75 bp, single end) with an output of ~56 million reads per sample. For the comparison of gene expression 7 WT and 7 KO dCA1 samples, whose KO had been validated with qPCR, were used.

Strong genotype dependent correlation and separation in PCA space of WTAP KO gene expression

The overall sample correlation calculated from the log2-transformed normalized counts showed a clear separation of WT and KO samples, with a high similarity within each genotype and a clear separation between genotypes (Figure 35, panel A). A dimensionality reducing principal component analysis (PCA) was applied to reduce the number of variables and identify individual contributors that explain the observed variance.

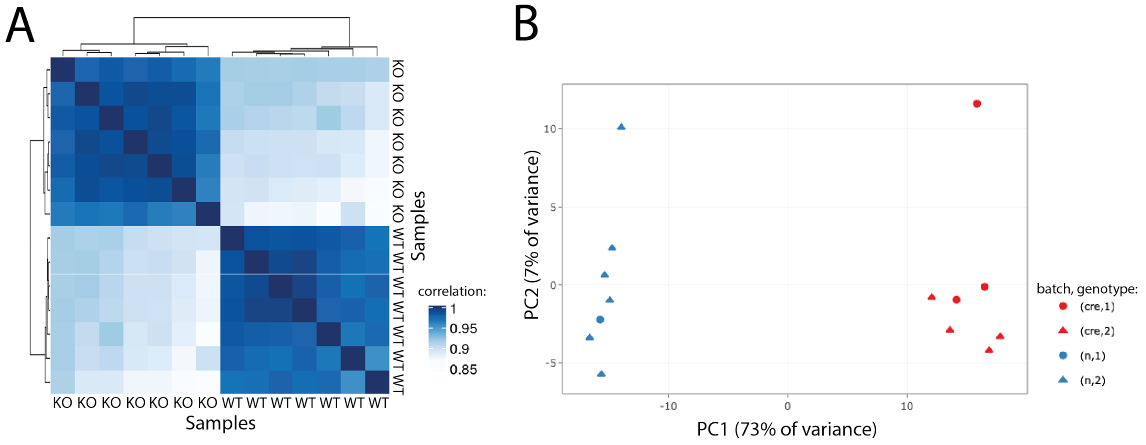

Figure 35: Sequenced samples show strong correlation within genotypes and clear separation in PC space **(A)** The heatmap of sample correlations visualizes the high degree of similarity for samples of the same genotype and clear differences between genotypes. Sample correlations were performed with the log2transformed normalized counts. **(B)** The PCA for the 1,000 most variably expressed genes shows that PC1 explains 73 % of the observed variance. Samples were assigned to two batches, based on their overall expression profile.

The results of the PCA calculated for the 1,000 most variably expressed genes shows a clear separation of WT and KO samples, with principal component 1 (PC1) explaining 73 % of the variance and indicating the genotype driven effect of the KO (Figure 35, panel B).

NexCreERT2 WTAP KO induces massive shift in gene expression in the dCA1

The removal of WTAP induces a massive shift in gene expression with 7,513 transcripts being significantly altered in their abundance in the dCA1 (FDR < 0.05, base mean ≥ 20). For the presented analysis, a cut off was applied. Consequently, only results with Log2FoldChange > 0.5 and a base mean ≥ 20 were considered. With these settings, 2,215 genes are included in the analysis. An overview is shown in Figure 36.

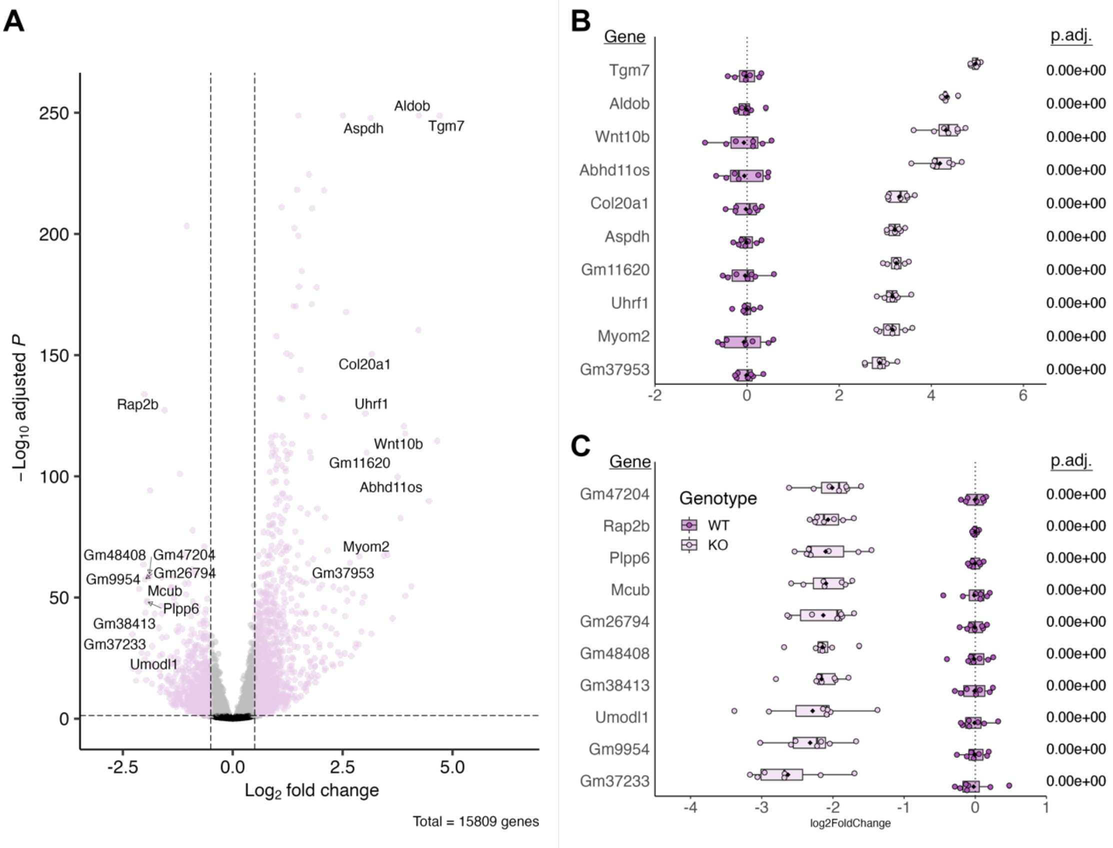

Figure 36: WTAP KO results in a massive transcriptional shift in the dCA1

(A) Volcano plot showing the comparison of KO vs WT animals for 15,809 detected genes. In total, 2,215 genes are differently expressed (FDR < 0.05, Log2FoldChange ≥ 0.5, base mean ≥ 20), with 1,296 transcripts being significantly upregulated and 919 transcripts significantly downregulated. **(B)** Top 10 genes with the greatest upregulation in WTAP KO animals. **(C)** Top 10 genes with the greatest downregulation in WTAP KO animals. Data is shown for WT = 7; KO = 7. For up- and downregulated genes, a cut off was applied (base mean ≥ 20, only genes detected for both genotypes).

Overall, a stronger upregulation than downregulation was observed with 1,353 (58 %) transcripts being upregulated in WTAP KO animals and 978 (42 %) being downregulated. The list of differentially regulated transcripts was used to perform a GO enrichment analysis.

Gene Ontology enrichment analysis reveals enrichment for membrane associated terms

The GO analysis for an enrichment of cellular components showed that differentially expressed transcripts (FDR < 0.05, Log2FoldChange ≥ 0.5, base mean ≥ 20) are significantly enriched for components of the plasma membrane (FDR < 0.05, Figure 37). More specifically, an enrichment for integral components of the post synaptic membrane was observed, with an overrepresentation of ion channel complex components.

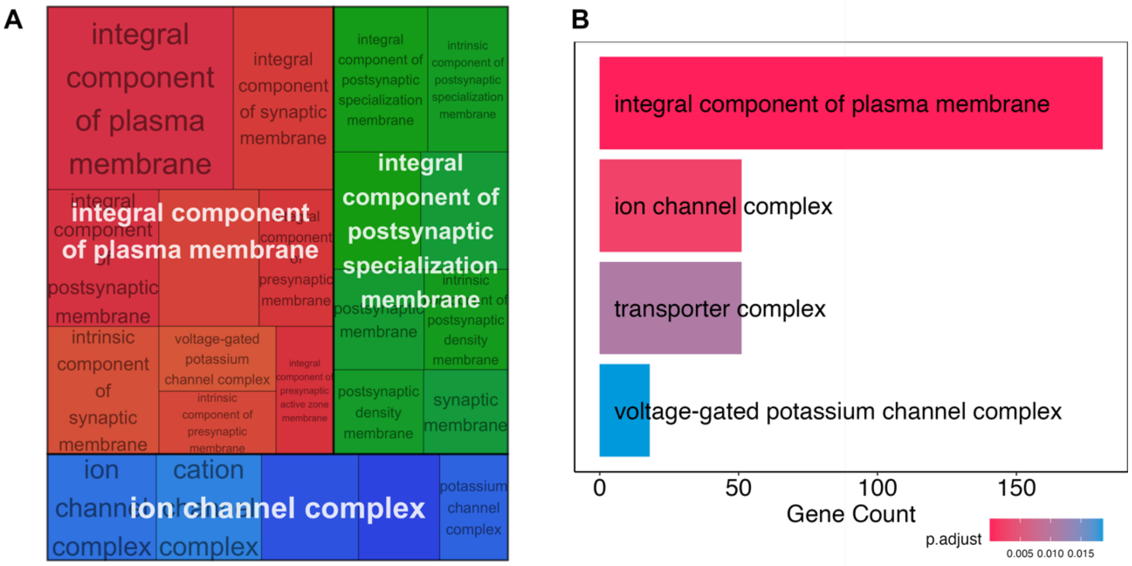

Figure 37: Differentially expressed genes in WTAP KOs are enriched for integral components of the plasma membrane

(A) Overview of the GO results for CC after application of semantic similarity analysis (FDR <0.05). Three main topics emerge: integral components of the plasma membrane, integral components of the postsynaptic specialization membrane and cation channel complex. (**B)** Bar plot showing the number of significantly differentially expressed genes associated with individual GO terms and their respective p.adj.

The GO analysis for MF showed an enrichment for voltage-gated cation channels, G-protein-coupled receptor activity, voltage-gated ion channel activity and sulfotransferase activity (FDR < 0.05, Log2FoldChange ≥ 0.5, base mean ≥ 20), as shown in Figure 38.

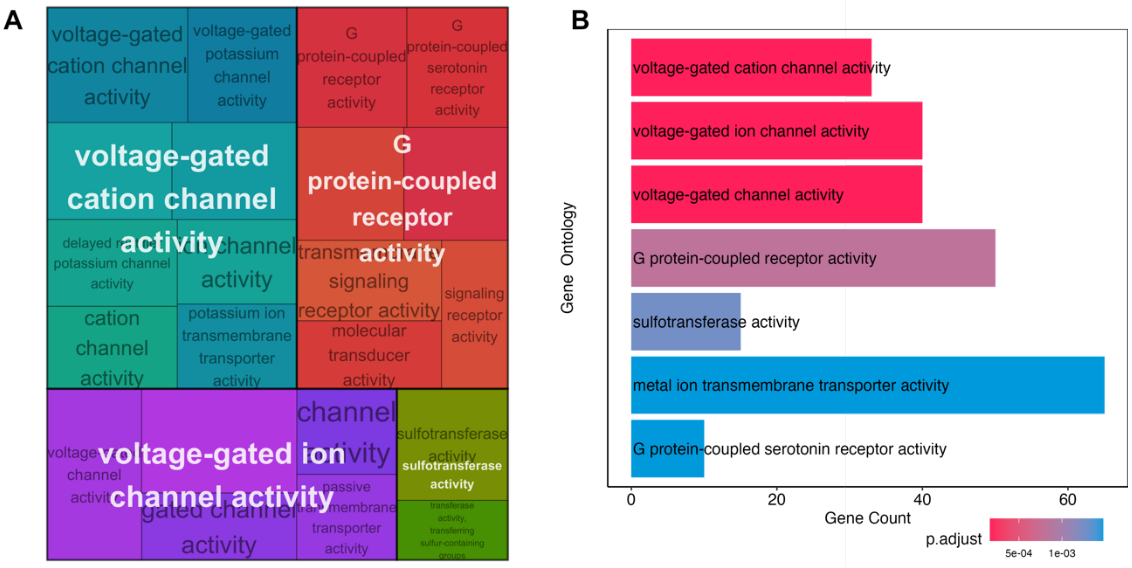

Figure 38: Differentially expressed genes in WTAP KOs are enriched for voltage-gated ion channels and G protein-coupled receptors

(A) Overview of the GO results for MF after application of semantic similarity analysis (FDR < 0.05). The enriched terms include: voltage-gated cation channels, G-protein-coupled receptor activity, voltage-gated ion channel activity and sulfotransferase activity. **(B)** Bar plot showing the number of genes associated with individual GO terms and their respective p.adj. values.

qPCR validation substantiates the observation that WTAP regulates expression of m⁶A regulators

The sequencing of poly-(A) RNA from WTAP KO dCA1, revealed that many of the known m^6A regulating genes are differentially expressed in WTAP KO animals. To validate these findings, an RT-qPCR with tissue from slices used for electrophysiological investigation of LTP in WTAP KO animals was performed (WT = 6; KO = 5). The results of the validation are summarized in Figure 39.

Figure 39: WTAP regulates expression of the m^6A 'writer complex' components and m^6A 'readers'
(A) Essential components of the m^6A methylation complex, as well as associated proteins show shifts in gene expression after WTAP KO. **(B)** Shown are the results from the WTAP KO RNA sequencing (WT = 7, KO = 7) and the qPCR validation (WT = 6, KO = 5). Statistics were performed using the independent two-sample t-test, Wilcox test or Welch's t-test, as appropriate. Reported are the FDR adjusted p-values. ns = not significant, *: $p < 0.05$. **: $p < 0.01$, ***: $p < 0.001$, ****: $p < 0.0001$.

Overall, the results from the qPCR analysis are in accordance with the differences observed in the RNA Seq. data. The replication in a different cohort of animals, using qPCR, strongly supports the findings that the removal of WTAP results in a dramatic shift of gene expresses that includes several crucial m^6A regulators and 'readers'.

Removing METTL3 in WTAP KO animals does not further alter gene expression of selected candidates

To understand the unique contribution of WTAP to cellular functioning, it is important to distinguish the WTAP driven effects from the effects of other m^6A regulators. It has previously been reported that the depletion of METTL3 in the dHPC does not result in major changes in gene expression[28]. Specifically, among the few changes that were reported, no differential regulation was observed for m^6A related genes.

To test for synergistic and/or compensating effects of METTL3 on the observed changes in gene expression, a WTAP-METTL3 double KO was compared, using qPCR, to the results from the WTAP KO sequencing. An overview of the results is shown in Figure 40.

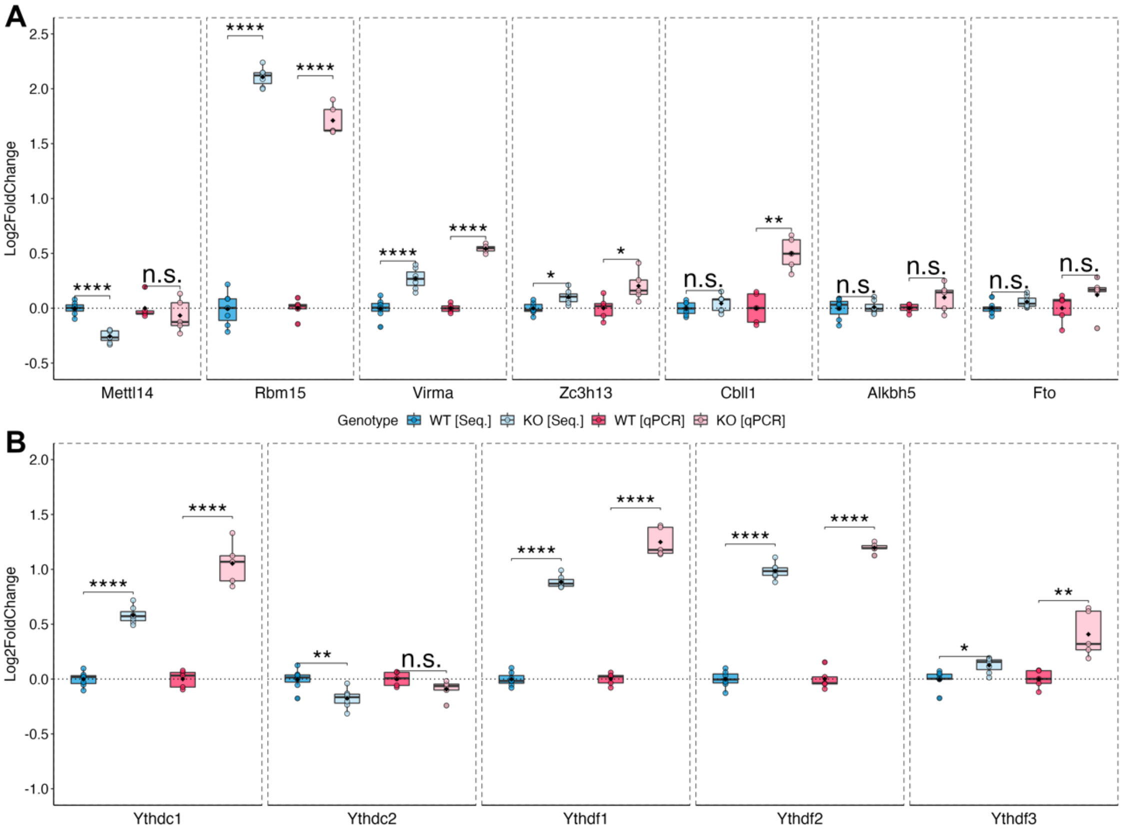

Figure 40: WTAP-METTL3 double KO effects on gene expression of m^{6}A regulators and 'readers'
(A) The effect of depleting WTAP and METTL3 on the expression of m^{6}A regulators, compared with the results from the WTAP KO RNA seq. **(B)** The effect of the double KO on the expression of m^{6}A 'readers'. Shown are the results from the WTAP KO RNA seq. (WT = 7, KO = 7) and the WTAP-METTL3 KO qPCR (WT = 5, KO = 5). Statistics for the qPCR results were performed using the independent two-sample t-test, Wilcox test or Welch's t-test as appropriate. Reported are the FDR adjusted p-values. ns = not significant, *: $p < 0.05$. **: $p < 0.01$, ***: $p < 0.001$, ****: $p < 0.0001$.

As expected, based on previous results[28], no additive effects of the METTL3 KO were detected. The observed changes are comparable to the result for the WTAP KO (Figure 39) supporting the findings that the depletion of WTAP results in distinct changes in gene expression.

NexCreERT2 activity does not alter gene expression in tamoxifen treated WT animals

To rule out that the presence of NexCreERT2 induces the observed shift in gene expression a control experiment was conducted, in which WT animals heterozygous for CreERT2 (+/CreERT2, N = 6) and WT animals without CreERT2 (+/+; N = 6) were subjected to tamoxifen injections (5x, 100 mg/kg tamoxifen). 14 days after the last injection, the dCA1 was collected and RNA extracted following standard procedures. A RT-qPCR was performed for selected target genes showing robust differential expression in WTAP KO animals. The results, summarized in Figure 41, show that no differences were detected for either of the selected genes that are differentially regulated in the WTAP KO.

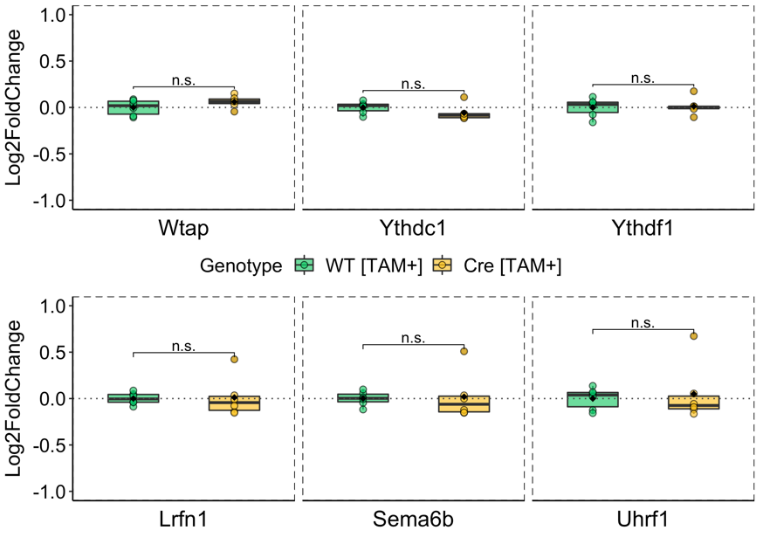

Figure 41: NexCreERT2 activity does not alter gene expression in WT animals
RT-qPCR was performed for selected candidates showing differential expression in Wtap-NexCreERT2 KO samples. WT animals treated with tamoxifen (N = 6) were compared with WT animals carrying CreERT2 and treated with tamoxifen (N = 6). Statistics were performed using the independent two-sample t-test, Wilcox test or Welch's t-test as appropriate. Reported are the FDR adjusted p-values. ns = not significant, *: $p < 0.05$. **: $p < 0.01$, ***: $p < 0.001$, ****: $p < 0.0001$.

The absence of any differential regulation in tamoxifen treated CreERT2 carrying WT mice, supports the claim that the observed changes are the result of WTAP depletion.

4.1.11 WTAP KO induces shift in splicing events

To investigate whether the depletion of WTAP alters splicing in the adult brain, the available mRNA sequencing data were re-analyzed using the Bioconductor package DEXSeq, as described in the Methods section. This approach does not quantify the isoform abundance but instead tests for differences in exon usage and therefore can only be used as an approximation.

The DEXSeq analysis revealed large scale changes in the exon usage between WTAP WT and KO animals. In total, 3402 differentially expressed features, mapping to 1,907 genes were identified (FDR < 0.05; Log2FolgChange ≥ 0.5; base mean ≥ 5). Out of the 3,402 differentially expressed features, 1,763 (52 %) were significantly up- and 1,639 (48 %) downregulated. An overview of the results is shown in Figure 42.

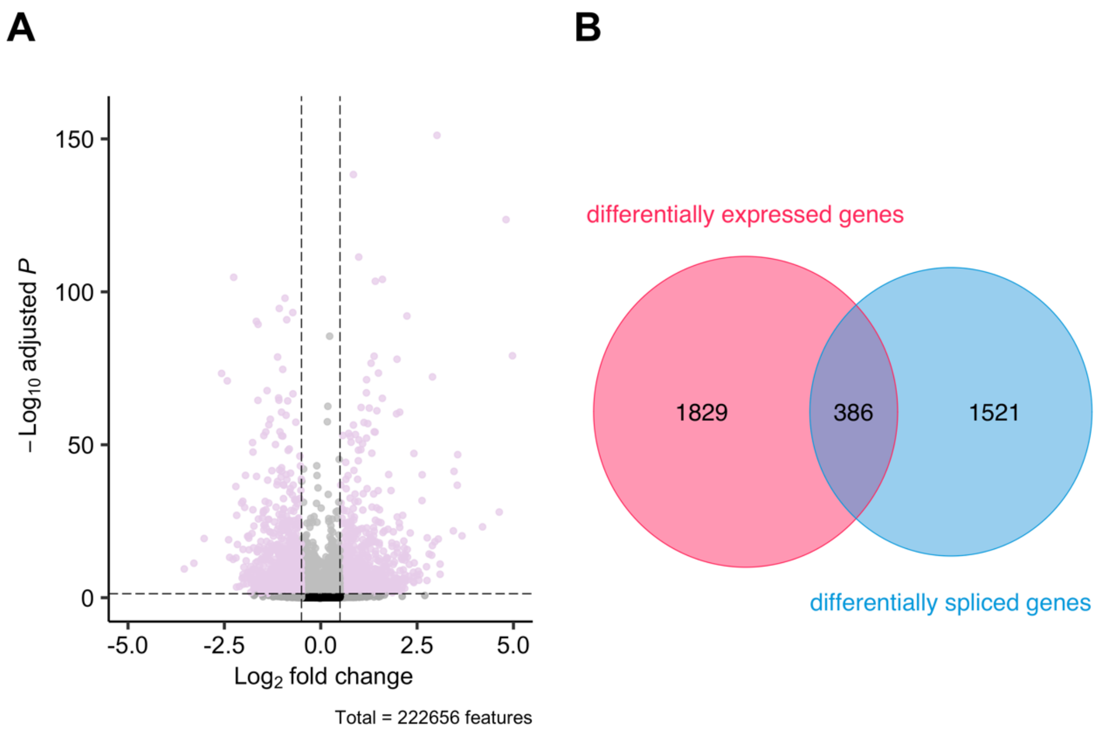

Figure 42: WTAP KO results in large scale changes in exon usage
(A) WTAP KO animals show differences in 3,402 exonic features mapping to 1,907 distinct genes (Log2FoldChance ≥ 0.5, FDR < 0.05, exon base mean ≥ 5). **(B)** Overlap of gene sets for which differential expression was detected (FDR < 0.05, Log2Fold-Change ≥ 0.5, base mean ≥ 20) and genes for which differences in exon usage were observed genes (Log2FoldChance ≥ 0.5, FDR < 0.05, exon base mean ≥ 5).

It is important to note that the changes in exon usage are not reflecting the differential gene expression, since the calculation of differential exon counts is corrected for overall changes in expression levels and therefore, only considers the relative abundance of individual exons.

GO analysis reveals enrichment for neuron specific terms of alternatively spliced transcripts

GO enrichment analysis was performed for genes associated with significantly different exon usage as described for the proteome screening (FDR < 0.05, Log2FoldChange ≥ 0.5, exon base mean ≥ 5). The GO analysis for BP revealed an enrichment for synaptic signaling, synapse organization, synapse assembly, neuron projection morphogenesis to mention the largest clusters (FDR < 0.05). An overview of the results is shown in Figure 43. The list with all results can be found in Appendix 8.11.

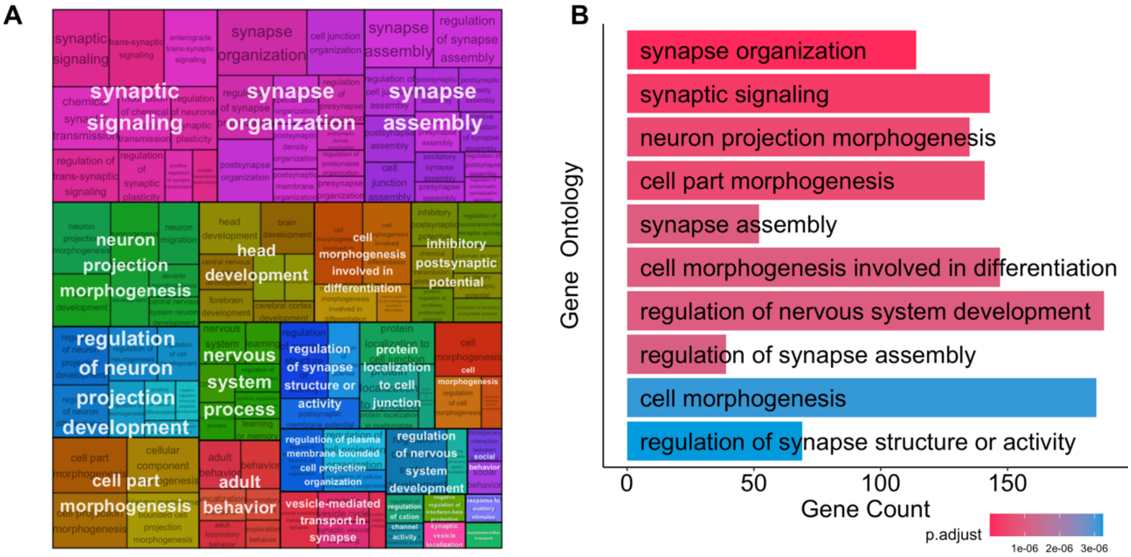

Figure 43: Differentially expressed exons in WTAP KOs are enriched for biological processes associated with synaptic functions and morphogenesis

(A) Overview of the GO results for BP after application of semantic similarity analysis (FDR < 0.05). The enriched topics include synaptic signaling, synapse organization, synapse assembly, neuron projection morphogenesis and others. **(B)** Bar plot showing the number of genes associated with the top 10 GO terms ranked by adjusted p-value.

The GO analysis for CC showed an enrichment for neuron specific cellular components including the glutamatergic synapse, the synaptic membrane, and the axon as the three largest clusters (FDR < 0.05). An overview of the results is shown in Figure 44. The list containing all results can be found in Appendix 8.11.

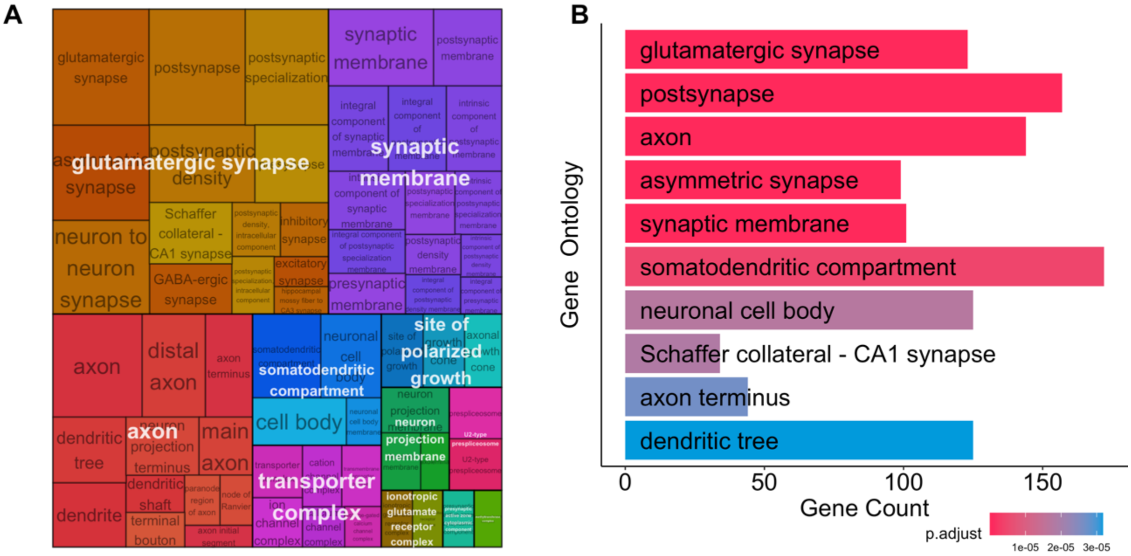

Figure 44: Differentially expressed exons in WTAP KOs are enriched for neuron specific cellular components

(A) Overview of the GO results for CC after application of semantic similarity analysis (FDR < 0.05). The enriched terms include: glutamatergic synapse, synaptic membrane, axon, transporter complex, site of polarized growth and somatodendritic compartment among others. **(B)** Bar plot showing the number of genes associated with the top 10 GO terms ranked by the adjusted p-value.

For MF an enrichment was detected for calcium ion transmembrane transporter activity, voltage-gated channel activity and protein domain specific binding, among others (FDR < 0.05). An overview of the results is shown in Figure 45. The full results can be found in Appendix 8.11.

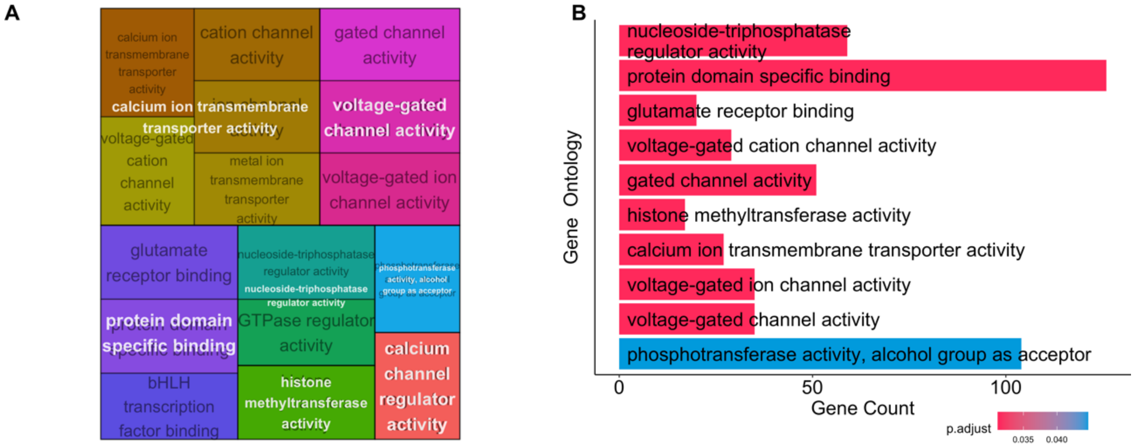

Figure 45: Differentially expressed exons in WTAP KOs are enriched for calcium transport and voltage-gated channel activity

(A) Overview of the GO results for MF after application of semantic similarity analysis (FDR < 0.05) showing the main clusters. The enriched terms include calcium ion transmembrane transporter activity, voltage-gated channel activity and protein domain specific binding. **(B)** Bar plot showing the number of genes associated with the top 10 GO terms ranked by adjusted p-value.

4.1.12 WTAP KO shifts composition of the neuronal membranome

Based on the observation that genes that are differentially expressed or spliced in WTAP KO animals are enriched for membrane associated components and synaptic function, a targeted screen for membrane associated proteins was performed. For this, an enrichment for membrane-bound proteins was achieved by labelling *ex vivo* acute HPC slices of WT and KO animals with biotin, followed by the extraction of biotin labelled proteins with streptavidin coated beads and subsequent LC-MS, as described in the Methods section. This approach was originally developed to interrogate neuronal protein trafficking in the brain[178] but can also be used to determine overall differences in the composition of membrane bound proteins (the membranome). With this label free approach, 2,594 unique proteins were identified with a clear enrichment of membrane associated terms (Appendix 8.12). The analysis of the proteomic data was performed as reported for WTAP Camk2aCre proteomic screening. A summary of the obtained results is shown in Figure 46.

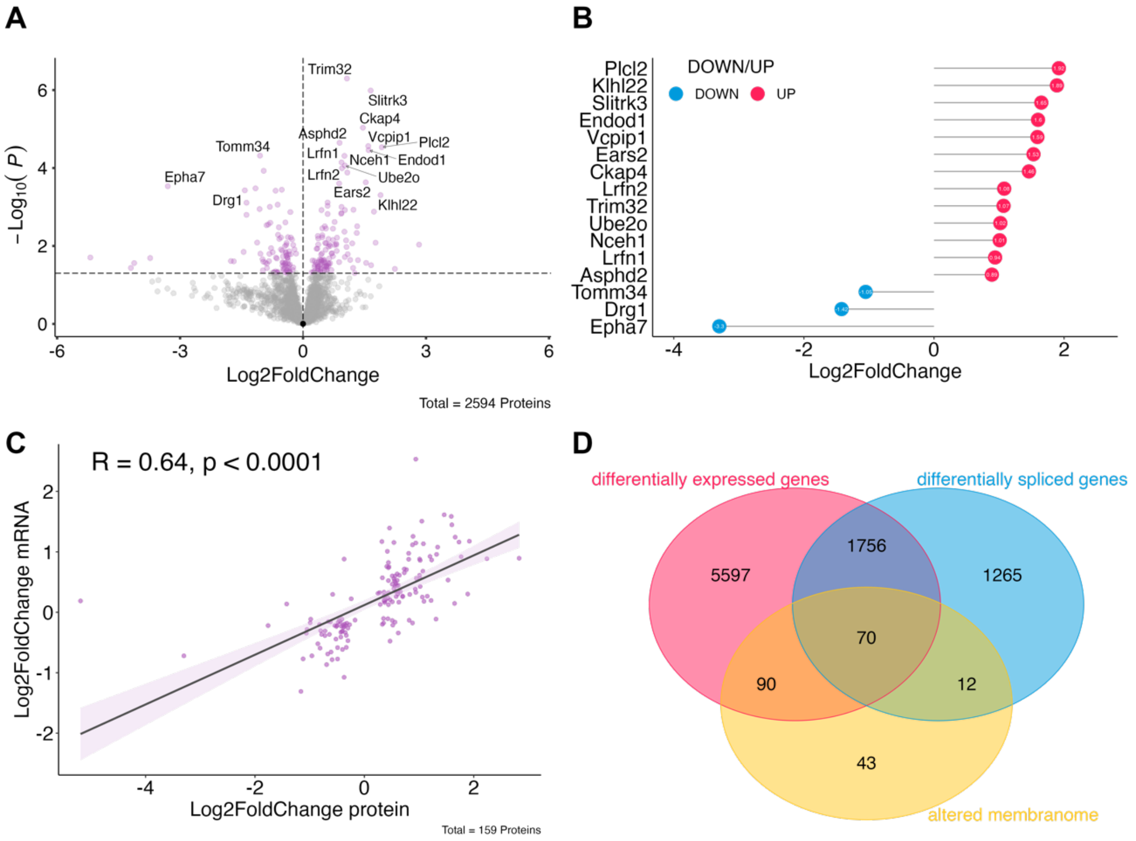

Figure 46: The depletion of WTAP alters the composition of the membranome

(A) Overview of differences in membrane bound proteins for KO vs WT animals (WT = 4, KO = 8). In total, 216 proteins were significantly altered in their abundance ($p < 0.05$, independent two-sample t-test), with 16 candidates remaining after multiple testing correction (FDR < 0.05). **(B)** Candidate list of the top 16 proteins that remained after multiple testing correction. **(C)** Correlation for 159 (159/216) proteins for which differential gene expression was detected in the mRNA seq. **(D)** Overlap of differentially expressed genes, with differences in splicing and membranome composition.

In total, 2,594 proteins were detected from the membrane enriched samples with 216 being significantly altered in expression levels ($p < 0.05$, independent two-sample t-test) and 16 remaining after multiple testing correction (FDR < 0.05). To determine whether the observed changes in RNA expression are predictive of the changes in the composition of the membranome, the results from the proteome screening were compared to the RNA sequencing data. For 159 out of the 216 proteins, differential gene expression had been detected in the poly-(A) RNA seq. Calculating the correlation of the Log2FoldChange in gene expression with the Log2FoldChange of proteins, showed that differential gene expression in WTAP KO is predictive of the observed compositional shift in the membranome ($R = 0.64$, $p < 0.0001$).

qPCR validation: WTAP regulates expression of membrane bound proteins

The differential expression of genes associated with membrane bound proteins that was observed in the mRNA sequencing results, was validated for selected candidates with RT-qPCR as described above. An overview of the results is shown in Figure 47.

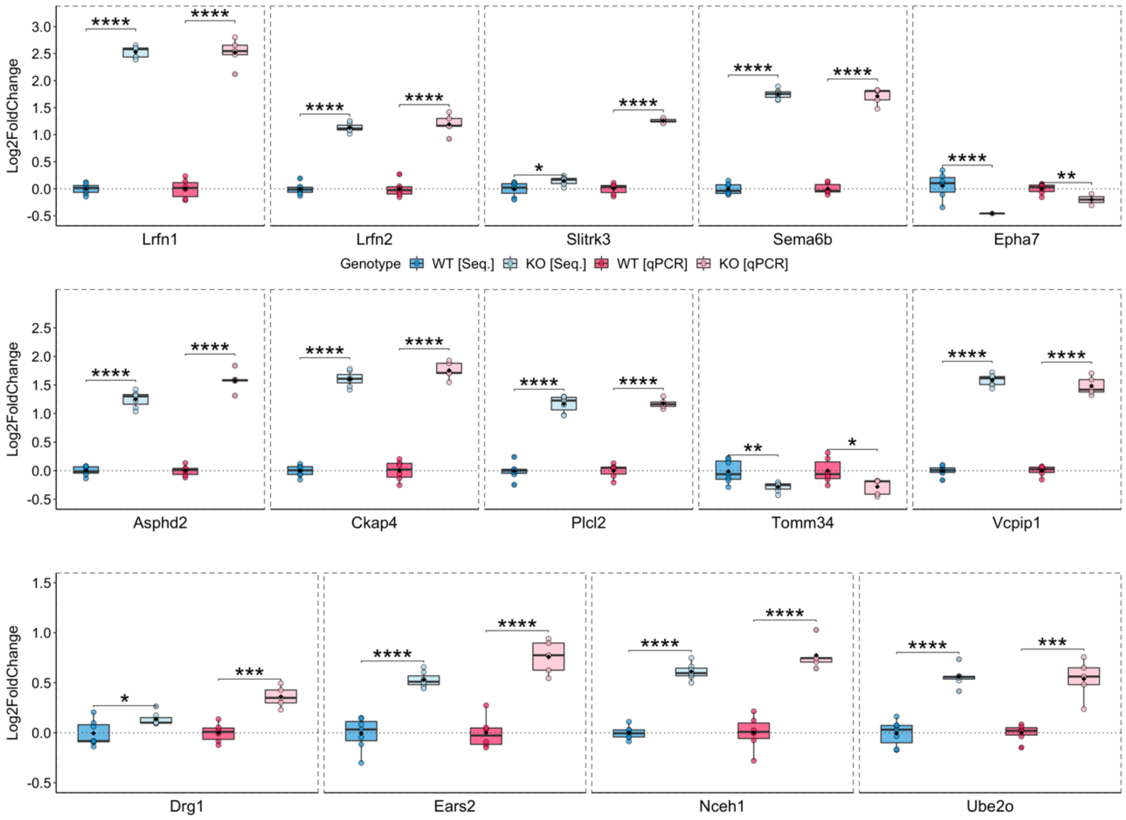

Figure 47: qPCR validation of differentially expressed membrane associated proteins

Shown are the results from the WTAP KO RNA sequencing (7 WT, 7 KO) and the qPCR validation (WT = 6, KO = 5). Statistics were performed using the independent two-sample t-test, Wilcox test or Welch's t-test as appropriate. Reported are the FDR adjusted p-values. ns = not significant, *: $p < 0.05$. **: $p < 0.01$, ***: $p < 0.001$, ****: $p < 0.0001$.

The estimated changes in expression levels from the RNA sequencing analysis were validated for all candidates with comparable effect sizes and with RNA from an independent cohort. Taken together with the validation of m^{6}A-related genes, this suggests a robust alteration in gene expression induced by WTAP KO that is stable across experimental cohorts.

4.1.13 WTAP KO animals show increased long-term potentiation

Given the strong molecular phenotype with an enrichment for synaptic GO terms and changes in synaptic scaffolding proteins, it was hypothesized that NexCreERT2 WTAP KO animals would show changes in the electrical signaling of the dCA1. A classical test to estimate the activity dependent persistent strengthening of excitatory synaptic connections associated with hippocampal learning, is to measure fEPSP at baseline and after TBS. With this, the phenomenon of LTP can be observed. LTP is considered as an important mechanism underlying learning and memory and often used as model system for memory research. Different types of LTP have been described, depending on, among other factors, the brain region and age of the test subject[197]. The presented results were obtained by inducing LTP at the Schaffer collateral-CA1 synapses of the dHPC with a TBS protocol as outlined in the Methods section. LTP is induced by the activation of postsynaptic NMDA receptors resulting in Ca^{2+} influx that activates the $Ca^{2+/}$calmodulin-dependent protein kinase II (CaMKII). CamKII in turn induces the rapid insertion of further AMPA receptors into the post-synaptic membrane. As result, the synaptic connection is strengthened. The results of the LTP measurement are summarized in Figure 48.

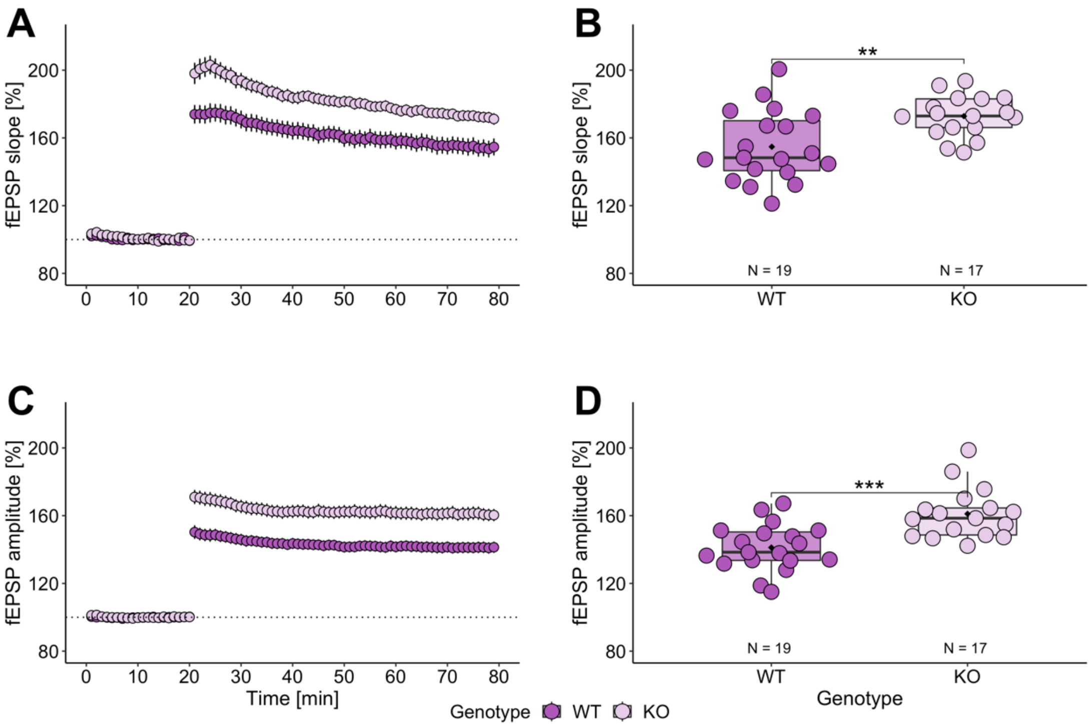

Figure 48: NexCreERT2 WTAP KO animals exhibit increased LTP in the dHPC
(A-B) The slope of fEPSP shows a significant difference after theta burst stimulation for KO animals compared to WT animals. WT = 6 (19 slices); KO = 5 (17 slices). **(C-D)** The amplitude is changed proportionally to the slope after LTP induction with a significant stronger increase in KO compared to WT animals. Statistics were performed on the mean slope and amplitude of the last 10 min of the recordings using the independent two-sample t-test, Wilcox test or Welch's t-test as appropriate. Reported are the FDR adjusted p-values. ns = not significant, *: $p < 0.05$. **: $p < 0.01$, ***: $p < 0.001$, ****: $p < 0.0001$. Error bars in A and C indicate the standard error of the mean.

A significant increase in the slope (p.adj. = 0.0037, independent two-sample t-test) and amplitude (p.adj. = 0.0002, independent two-sample t-test) after tetanic burst stimulation was observed for KO animals. The slices used for recordings were collected on dry ice and used for the RT-qPCR validation of WTAP KO (Appendix 8.9).

4.1.14 WTAP NexCreERT2 KOs show normal behavior

To examine whether the changes in gene expression, splicing and protein levels alter the function of the HPC and cortex, WTAP NexCreERT2 KO animals were subjected to behavioral tests that rely on HPC and cortical integrity.

No impairment of cue and contextual fear memory in WTAP KO animals

It has previously been suggested that a NexCreERT2 driven KO of METTL3 results in an increased cue fear memory and impaired fear extinction[28]. In order to compare a WTAP KO to the effects of METTL3 depletion, the previously published delay fear conditioning protocol was adapted for the presented results. For this, animals were exposed to a moderate foot shock (0.7 mA) at the start of the experiment and the memory was tested 24 h (cue memory) and 48 h (contextual memory) after conditioning.

A logistic regression analysis of the freezing response using GAMs was performed with freezing as the dependent variable (yes/no, resolution: 1 s) and genotype as the independent variable. Time was included in the model as smooth term, as well as a random intercept for each animal. For the cue memory at 24 h, test time was stratified for the occurrence of the cue (tone). The full details of the fitted model can be found in Appendix 8.13.

The logistic regression analysis showed that KO animals do not significantly differ in their fear memory response during the cue memory test (genotype:KO Estimate = -0.1, Z-value = -0.11, Pr(>|z|) = 0.92). Furthermore, when looking at contextual memory, 48 h after conditioning, no difference between WT an KO animals was detected for contextual memory (genotype:KO Estimate = -0.01, Z-value = -0.01, Pr(>|z|) = 0.99). An overview of the results is shown in Figure 49.

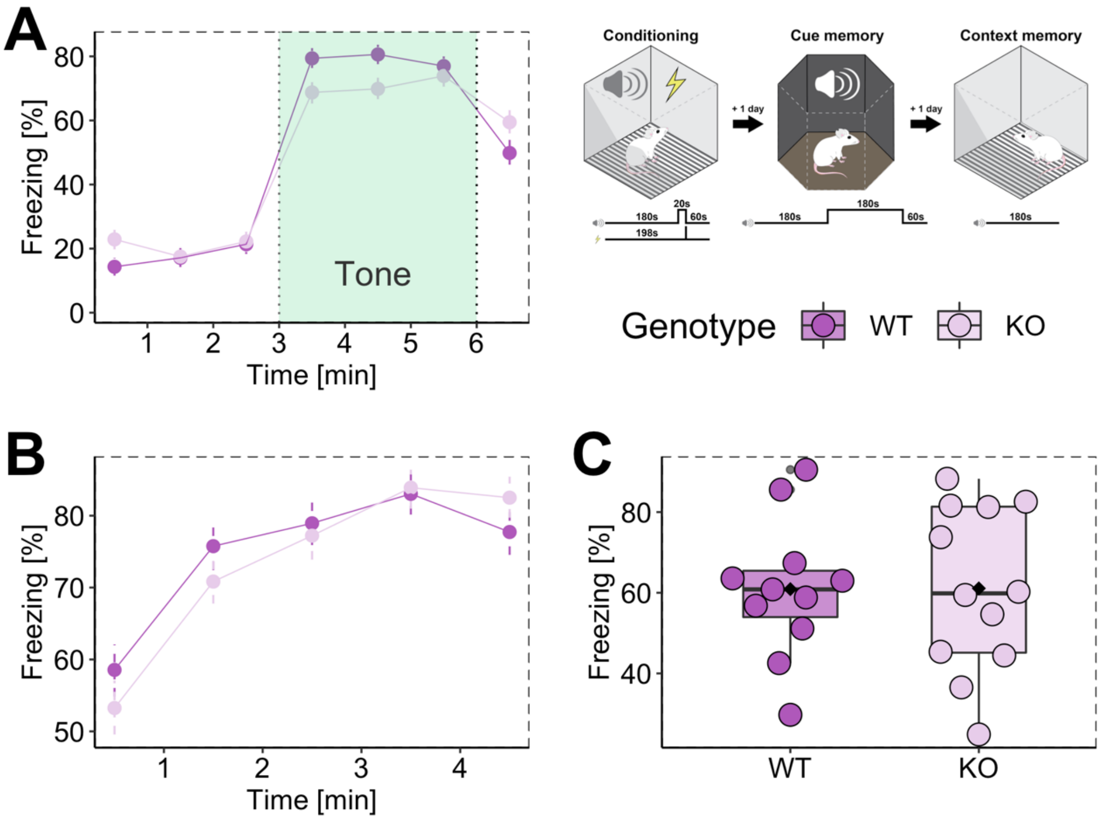

Figure 49: Wtap-NexCreERT2 KO animals show normal delay fear memory

(A) Cue memory across time, 24 h after conditioning (60 s bins). **(B)** Context memory across time, 48 h after conditioning (60 s bins). **(C)** Average contextual memory showing the mean freezing across 5 mins. Individual results are plotted for both genotypes (WT = 11, KO = 12). No significant difference between the two genotypes was detected for cue and contextual fear memory.

Overall, no difference in the fear memory of WTAP NexCreERT2 KO animals was observed. This differs from what has been previously observed for METTL3 NexCreERT2 KO animals[28].

No impairment of cue and contextual fear memory in WTAP-METTL3 double KO animals

Since the removal of WTAP did not alter fear learning, the effect of a double KO for WTAP and METTL3 was investigated. For this, WTAP-METTL3 NexCreERT2 KO animals were tested with the same conditioning paradigm used for WTAP NexCreERT2 KO animals. The results were analyzed using logistic regression analysis and the model summaries for the cue and contextual memory tests are shown in Table 37 and Table 38 (Appendix 8.14).

Here, also no differences were observed in the freezing during the cue memory test (genotype:KO Estimate = -0.34, Z-value = -0.41, Pr(>|z|) = 0.68) and the contextual memory test (genotype:KO Estimate = 0.3, Z-value = 0.35, Pr(>|z|) = 0.73). An overview of the results is shown in Figure 50.

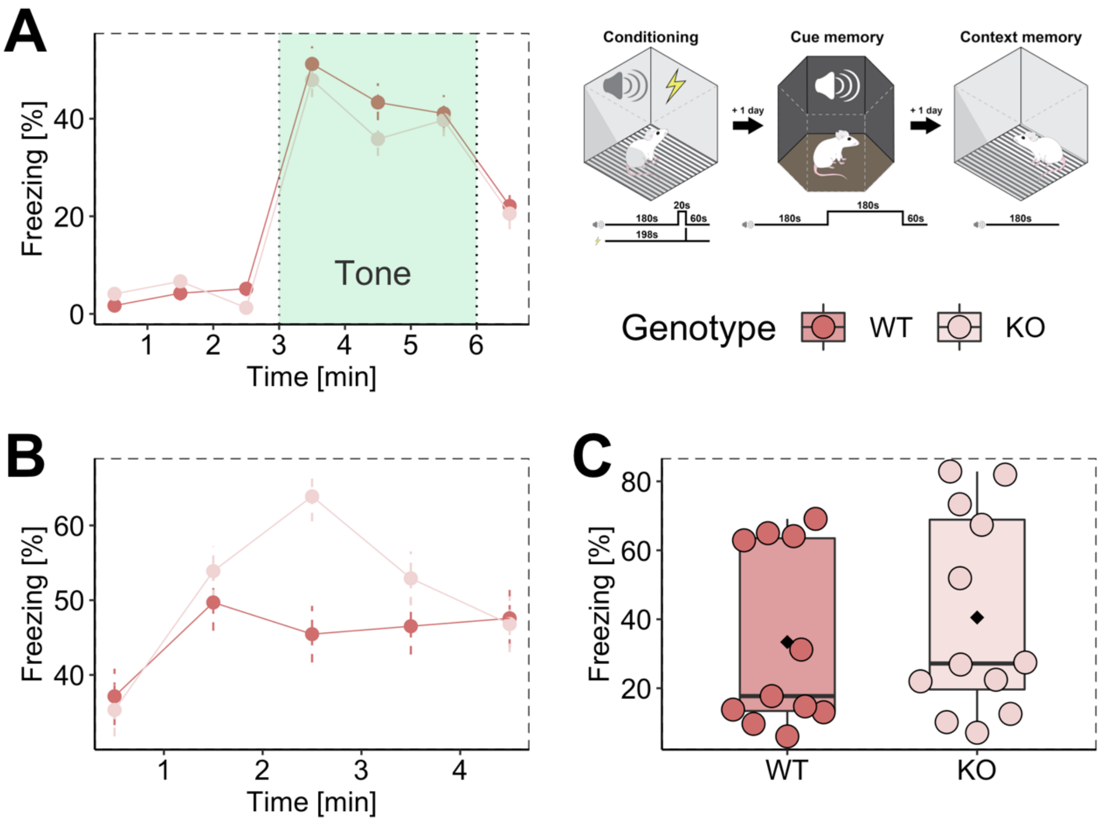

Figure 50: Double KO *Wtap-Mettl3*-NexCreERT2 animals exhibit normal cue and contextual fear memory **(A)** Cue memory across time, 24 h after conditioning (60 s bins). **(B)** Context memory across time, 48 h after conditioning (60 s bins). **(C)** Average contextual memory showing the mean freezing across 5 min. Individual results are plotted for both genotypes (WT = 11, KO = 12, KO). No significant difference between the two genotypes was detected for both cue and contextual fear memory.

WTAP KO animals show normal learning in the Morris Water Maze

It has previously been shown that Camk2aCre METTL3 KO animals exhibit impairments during the training for the MWM test but are able to compensate deficits over time[29]. This suggests that plasticity related processes, which are required for efficient learning, are disturbed but can be compensated for by sufficient training. Here, the MWM test was conducted with CD1-*Wtap*-NexCreERT2 animals, to determine whether a comparable learning impairment is caused by the loss of WTAP in NexCreERT2 expressing neurons.

The paradigm that was used in this study was split into two parts. The first part investigated the formation of spatial reference memory while the second part investigated the reversal of spatial learning[198]. During the first part (day 1-7), animals were trained to locate a submerged platform by relying on visual cues only (4 trials / day: 60 s; inter trial interval > 15 min). The location of the platform was fixed (NW quadrant) while the starting position of the animals changed across trials (pseudorandom, balanced). On day 3 and 7, animals were tested for their memory using a probe trial (test 1, test 2). For this, the platform was removed, and the animals search pattern and quadrant occupancy were recorded for a test period of 60 s.

In the second part (day 7-10), animals were subjected to reversal learning. For this, the platform was moved to the opposite quadrant (SE) and animals were trained for three days to learn the new location. The process of extinguishing the memory of the platform's location and the acquisition of a new or 'updated' memory is measuring an aspect of cognitive flexibility. On day 10 animals were tested for the success of reversal learning in another probe trial (test 3). Lastly, on day 17 animals were tested (test 4) to determine differences in memory retention. The results are summarized in Figure 51.

The data were analyzed using linear models in R. Reported below are the results for the two-way ANOVA.

For the latency during training (day 1-6), there was a significant effect for training day on latency (day: $F_{1,269} = 47.105$, $p < 0.0001$), with no significant main effect of genotype (genotype: $F_{1,269} = 1.171$, $p = 0.28$). Furthermore, no significant interaction of genotype with day was detected (genotype:day: $F_{5,269} = 1.405$, $p = 0.22$). Accordingly, for the latency during reversal training (day 7-9), a significant effect of training day on latency was determined (day: $F_{1,134} = 14.38$, $p < 0.0001$), with no significant main effect of genotype (genotype: $F_{1,134} = 0.163$, $p = 0.69$). Again, no significant interaction of genotype with day was detected (genotype:day: $F_{2,134} = 0.445$, $p = 0.64$).

For the first probe test (day 4), a significant effect of quadrant was observed indicating the training success (quadrant: $F_{3,179} = 69.717$, $p < 0.0001$), with no significant main effect of genotype (genotype: $F_{1,179} = 0.004$, $p = 0.95$). Furthermore, no significant interaction of genotype with quadrant was detected (genotype:quadrant: $F_{3,179} = 0.470$, $p = 0.70$). In accordance, for the second probe test (day 7), a significant effect of quadrant was observed indicating the training success (quadrant: $F_{3,179} = 96.357$, $p < 0.0001$), with no significant main effect of genotype (genotype: $F_{1,179} = 0.001$, $p = 0.98$). Furthermore, no significant interaction of genotype with quadrant was detected (genotype:quadrant: $F_{3,179} = 2.334$, $p = 0.076$).

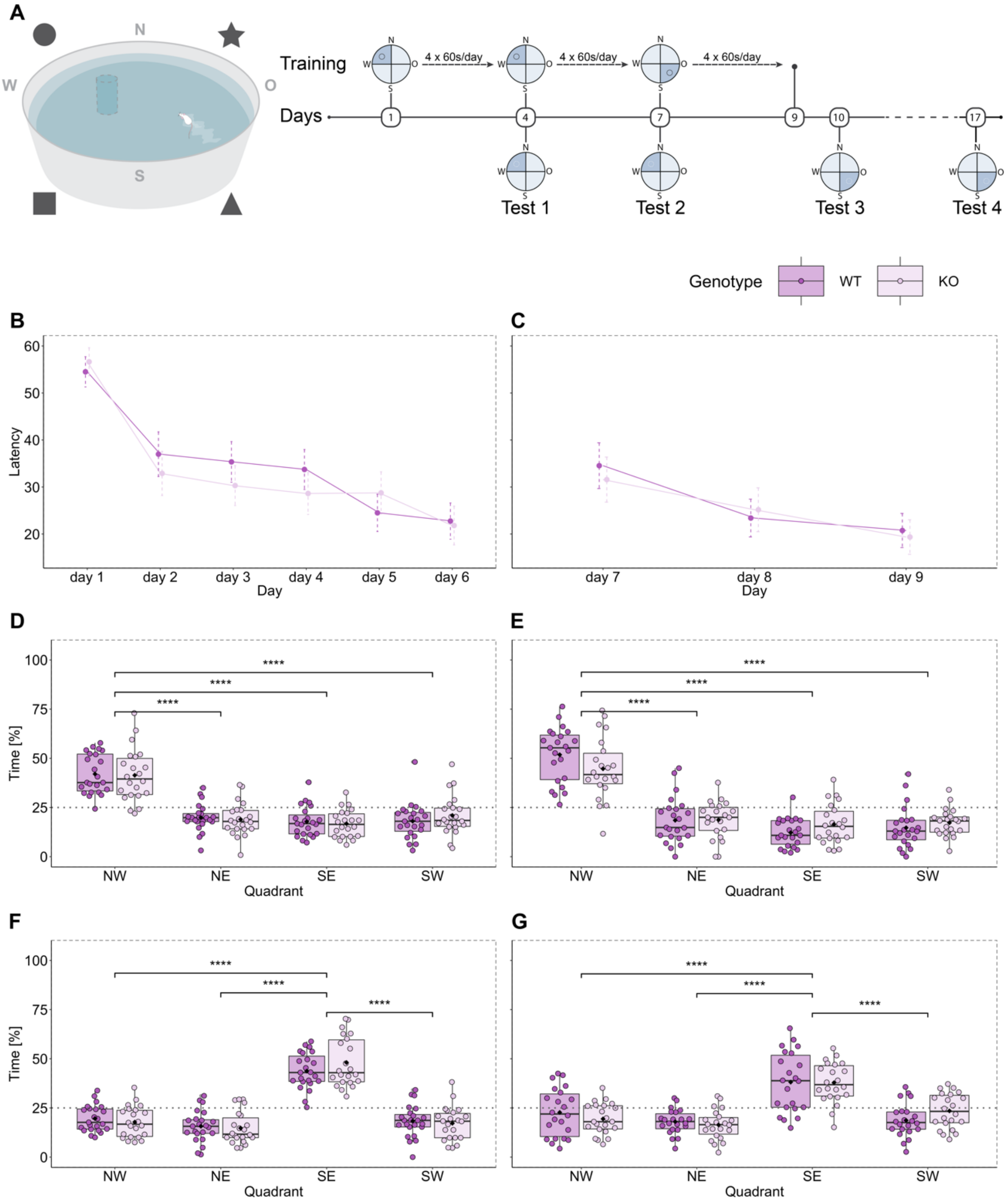

Figure 51: NexCreERT2 WTAP KO animals show normal learning in the MWM test

(A) Overview of the apparatus and paradigm. **(B)** The mean latency to reach the platform is shown for both genotypes across training days. **(C)** Mean latency to reach the platform for the reversal learning. Error bars represent 95 % CI. **(D)** First probe test after 3 days of training (d4). **(E)** Second probe test after 6 days of training (d7). **(F)** First probe test after 3 days of reversal learning (d10). **(G)** Memory retention 7 days after the last test (d17). Individual results are plotted for both genotypes (WT = 23, KO = 22). Significance levels from the Tukey's post-hoc test: ns = not significant, *: $p < 0.05$. **: $p < 0.01$, ***: $p < 0.001$, ****: $p < 0.0001$. One animal was excluded from the analysis, since post mortem verification of the genotype revealed a heterozygous genotype.

For the first reversal learning probe test (day 10), a significant effect of quadrant was observed indicating the successful reversal learning (quadrant: $F_{3,179} = 122.111$, $p < 0.0001$), with no significant main effect of genotype (genotype: $F_{1,179} = 0.01$, $p = 0.92$). Furthermore, no significant interaction of genotype with quadrant was detected (genotype:quadrant: $F_{3,179} = 1.19$, $p = 0.32$).

Also, for the remote memory test (day 17), a significant effect of quadrant was observed indicating the memory retention after one week (quadrant: $F_{3,176} = 38.258$, $p < 0.0001$), with no significant main effect of genotype (genotype: $F_{1,176} = 0.003$, $p = 0.96$). No significant interaction of genotype with quadrant was detected (genotype:quadrant: $F_{3,176} = 1.359$, $p = 0.26$).

In summary, WT and WTAP KO animals performed equally well during the training and probe tests.

4.2 Project II: YTHDC1 is essential for adult survival and a regulator of neuronal functions

Previous studies have established a role of m^6A in cortical and cerebellar development with deficits in the regulation of m^6A resulting in developmental defects[27,132]. Furthermore, the postnatal KO of the m^6A methyltransferase METTL3 in Camk2aCre expressing neurons results in subtle learning impairments in adulthood that can be compensated for by stimulus intensity or sufficient training[29]. Considering that the effects of m^6A are mediated through the action of 'reader' proteins, it can be hypothesized that deficits resulting from m^6A depletion, can be attributed to the failure of downstream 'reader' proteins to accurately regulate the processing of transcripts. So far, the only YTH-family 'reader' that has been systematically investigated in the adult mouse brain is the cytoplasmic m^6A 'reader' YTHDF1[30]. The contribution of the nuclear 'reader' YTHDC1 has not been reported so far.

In the second part of this thesis, the focus lies on understanding the unique contribution of YTHDC1 to brain functioning. Therefore, the effects of a cell-type specific KO of YTHDC1 in Camk2aCre and Nex-CreERT2 expressing cells in the adult mouse brain was investigated.

The goals of the research presented below are: (1) To characterize the effect of YTHDC1 KO on gene expression, protein abundance, metabolism, neuronal signaling, brain anatomy and behavior. (2) To identify unique contributions of YTHDC1 to neuronal regulation in the mammalian brain.

4.2.1 Impaired breeding and premature death of YTHDC1 KO females

During the establishment of the CD1-*Ythdc1*-Camk2aCre mouse line, it was noticed that KO females (genotype: lox/lox, Cre/+) do not breed well. Less than half of all matings with KO females (7 out of 15) were carried to term. Out of 7 litters born, only 2 survived until weaning. An overview of these observations is shown in Figure 52.

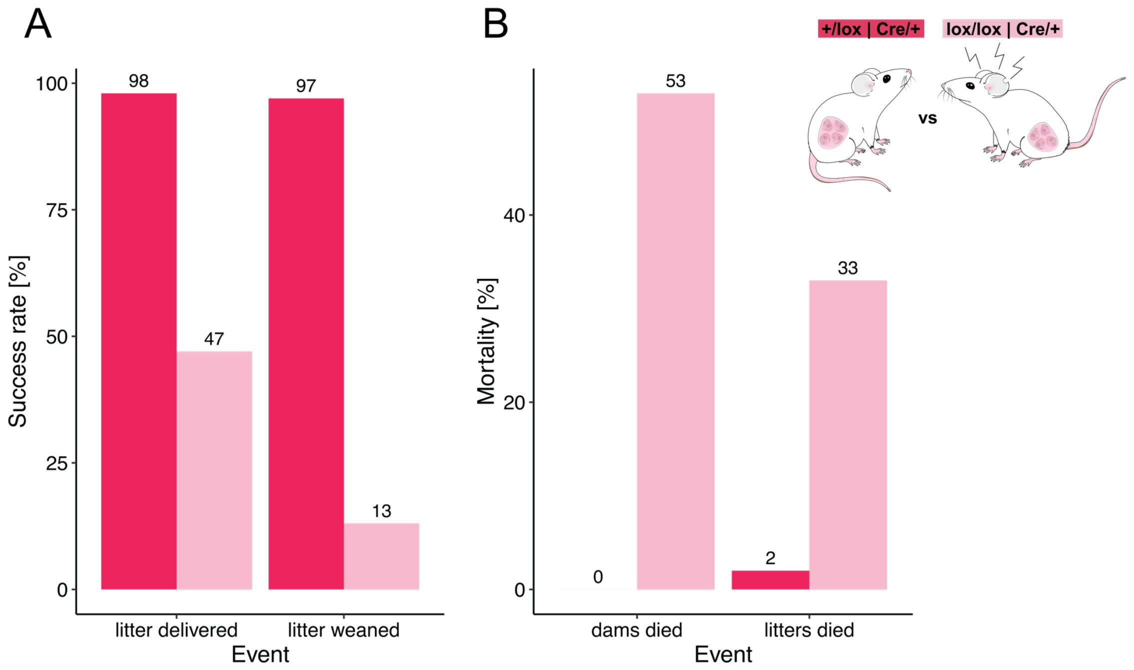

Figure 52: Breeding impairments and premature death in YTHDC1 Camk2aCre KO females

(A) Number of breeding attempts, successful births and weaned litters for females carrying Camk2aCre (Cre/+) with an Ythdc1 +/lox or lox/lox genotype. **(B)** Number of dams and pups that died during breeding or before weaning respectively. Results are shown for 26 heterozygous (+/lox, Cre/+) and 11 homozygous females (lox/lox, Cre/+).

In addition, an increased incidence of premature sudden death was observed in YTHDC1 KO females. Specifically, 8 out of 11 YTHDC1 KO females died during breeding while none of the heterozygous females died. Females used for breeding were between 8 and 24 weeks old and age matched. Since the breeding success of KO females appears to be impaired, experimental cohorts were created by mating heterozygous dams carrying Cre (lox/+, Cre/+) with homozygous Cre negative bucks (lox/lox, +/+).

4.2.2 YTHDC1 KO juveniles show reduced weight

To determine differences in the development of juvenile animals, males and females were examined and weighed from week four to week eight. While there were no obvious physical differences apparent between WT and KO animals, a clear difference in the post-weaning weight was observed (Figure 53). The data presented below was analyzed using a linear model in R with the dependent variable weight and the independent variables date, sex and genotype. Reported below are the results for the three-way ANOVA.

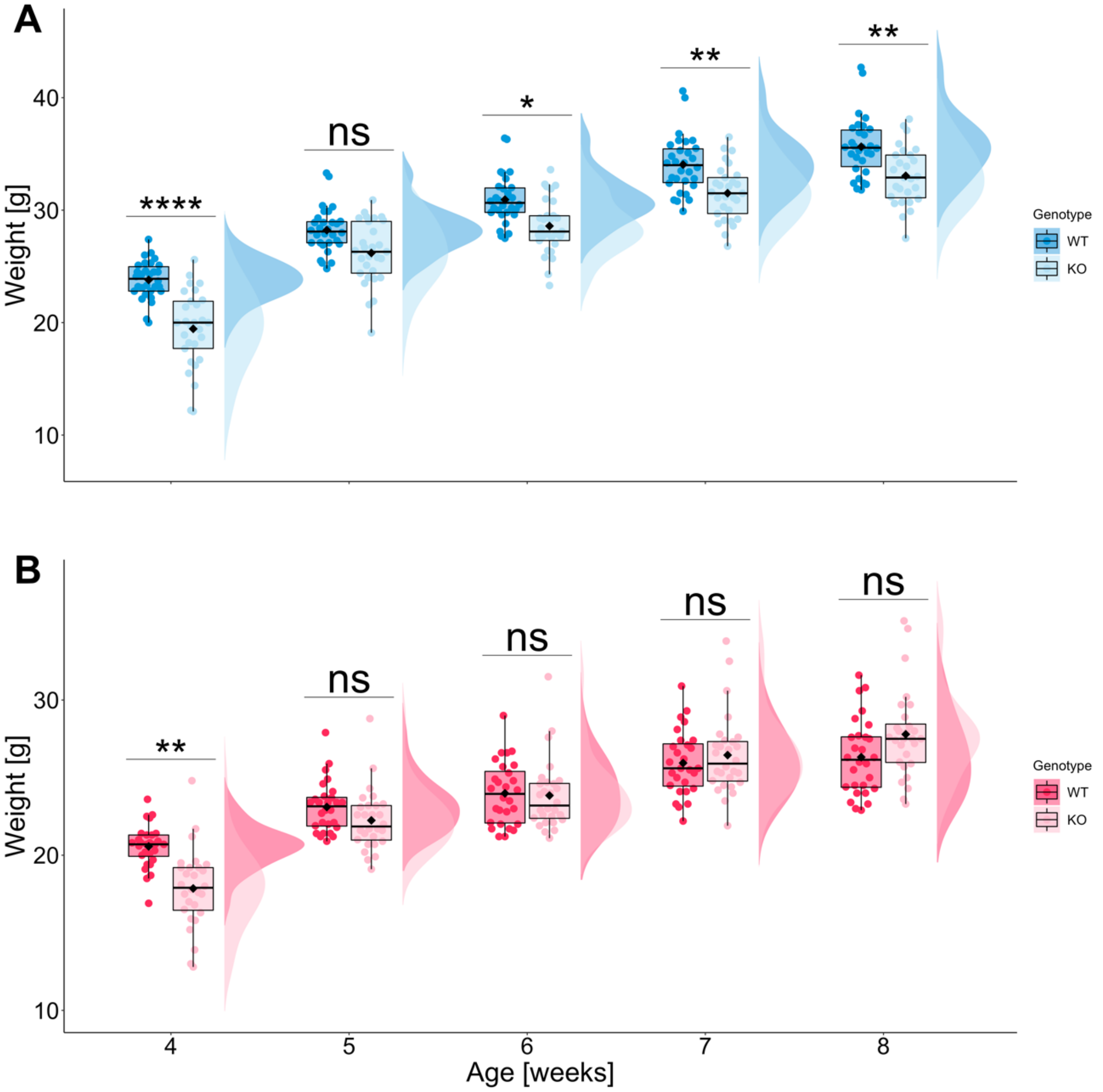

Figure 53: Reduced weight in juvenile YTHDC1 KO animals

(A) Weight of male Camk2aCre YTHDC1 WT and KO animals (WT = 30, KO = 29). **(B)** Weight of female Camk2aCre YTHDC1 WT and KO animals (WT = 28, KO = 28). One weakling that died before week 5 was excluded from the analysis. Significance levels from the Tukey's post-hoc test: ns = not significant, *: $p < 0.05$. **: $p < 0.01$, ***: $p < 0.001$, ****: $p < 0.0001$.

A significant main effect of sex and genotype on weight was observed, with females having an overall lower weight than males and KO animals being overall lighter than WT animals (sex: $F_{1,572} = 721.859$, $p < 0.0001$; genotype: $F_{1,572} = 72.744$ $p < 0.0001$). In addition, a significant interaction of genotype and sex (genotype:sex: $F_{1,572} = 38.060$, $p < 0.0001$), genotype and date (genotype:date: $F_{4,572} = 6.432$, $p < 0.0001$) and sex and date (sex:date: $F_{4,572} = 19.119$, $p < 0.0001$) was determined.

Applying a Tukey's test for multiple comparisons revealed that KO males and females differ significantly in weight at 4 weeks of age (males: p.adj. < 0.0001, females: p.adj. = 0.0035), with KO animals showing reduced weight. Moreover, a sex-specific difference in the weight progression was observed with females showing no differences in weight after week 4, while KO males show a decreased weight at week 6 (p.adj. = 0.022), 7 (p.adj. = 0.0067) and 8 (p.adj. = 0.0068) as shown in Figure 53. Together, this suggests a KO driven effect on post-weaning weight that continues to persist in males into early adulthood.

To determine whether the differences in weight are already present before the onset of Camk2aCre expression, the pre-weaning weight of males and females was determined. No genotype driven difference in the weight for either sex was detected at P15 (males: p = 0.96, independent two-sample t-test; females: p = 0.74, independent two-sample t-test). In addition, adult males were weighed at 12 weeks of age to see if the juvenile difference in weight was retained throughout adulthood. Here, no difference in the weight of WT and KO males was detected (p = 0.12, independent two-sample t-test) suggesting that KO animals catch up with WT animals' weight during adulthood. The detailed results are included in Appendix 8.15.

4.2.3 The KO of YTHDC1 reduces the survival probability

In addition to the initial observation that KO females are less likely to have litters that survive until weaning and the increased occurrence of sudden death during breeding, some unexplained sudden deaths were also observed in males. To distinguish a genotype driven increase in mortality from off target effects arising from the genetic background, the first experimental cohort was systematically monitored for genotype driven differences in the survival probability.

Presented below (Figure 54) are the results from the survival analysis. Survival probabilities were estimated in R using the package 'survminer'[199] that employs the Kaplan-Meier method[200] and compares differences in the survival of groups using a log-rank test.

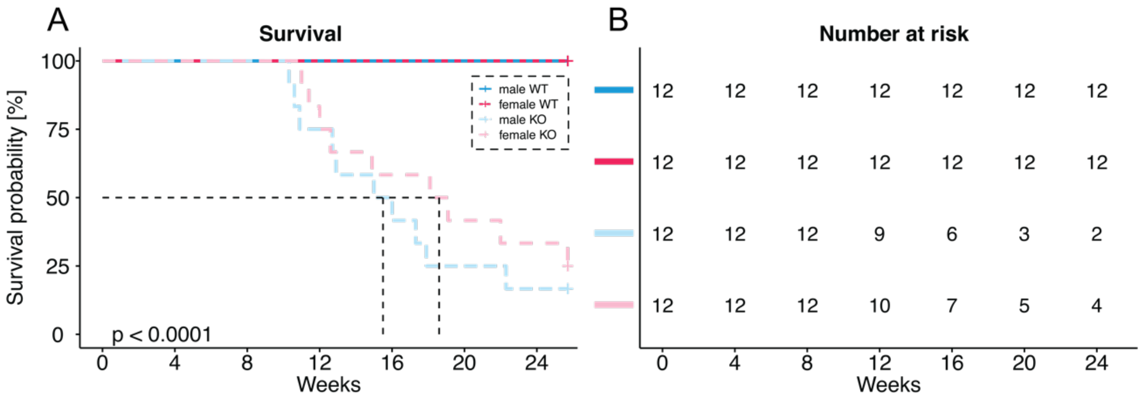

Figure 54: YTHDC1 Camk2aCre KO animals exhibit a decreased survival probability in adulthood

The survival probability estimated by the Kaplan-Meier method is shown for both sexes and genotypes across time. **(A)** The median survival times are indicated for KO males and females by dashed rectangles. **(B)** The number of animals at risk by time. The p-value shown is obtained by a log-rank test for genotype differences.

The survival analysis revealed that KO animals have an increased probability to die prematurely during early adulthood, with an estimated median survival probability of 4-5 months for both sexes. No sudden death was observed in the WT animals during the observation time. Animals that succumbed to sudden death, did not present with any gross morphological difference in size weight, and organ defects as assessed by post-mortem dissections.

The close monitoring of animals revealed that some KO animals succumb to clonic-tonic seizures characterized by escalating uncontrolled movements often followed by complete stiffness of the body. While seizures appeared to occur at random, changes in the environment such as a cage change or behavioral tests seemed to act as triggers in some cases. These events were generally rare during periods of observation and animals always recovered within minutes.

4.2.4 YTHDC1 KO broadly affects behavior

The Camk2aCre driven KO occurs postnatally, with an onset in the 3rd postnatal week[149,187]. As shown with the Camk2aCre-Ai9 reporter mice, the Camk2a driven recombination occurs primarily in pyramidal neurons of the neocortex, HPC (CA1-CA3, dentate gyrus) and to a lesser extend in the striatum and amygdala with sparse recombination in being observed in the cerebellum.

To study the functional relevance of YTHDC1 for adult brain functioning, various behaviors were tested that rely on the function of the cortex and HPC. The performed tests include classical tests for locomotion and anxiety-like behaviors (OF, DL, EPM), a HPC and cortex dependent learning test (FC), and a test of visual impairment and locomotor deficits (visible platform training for the MWM). The results of the individual tests are presented below. If not otherwise indicated, no animals were excluded. Varying sample sizes of KO animals are the result of increased sudden death in early adulthood.

YTHDC1 KO show normal behavior in the open field test

The OF test was conducted to assess overall differences in locomotion and explorative behavior. The test was performed under low light conditions (< 15 lux) and for a duration of 10 min. The data were analyzed using linear models in R with the dependent variables distance or time and the independent variables, sex and genotype. Reported below are the results for the two-way ANOVA.

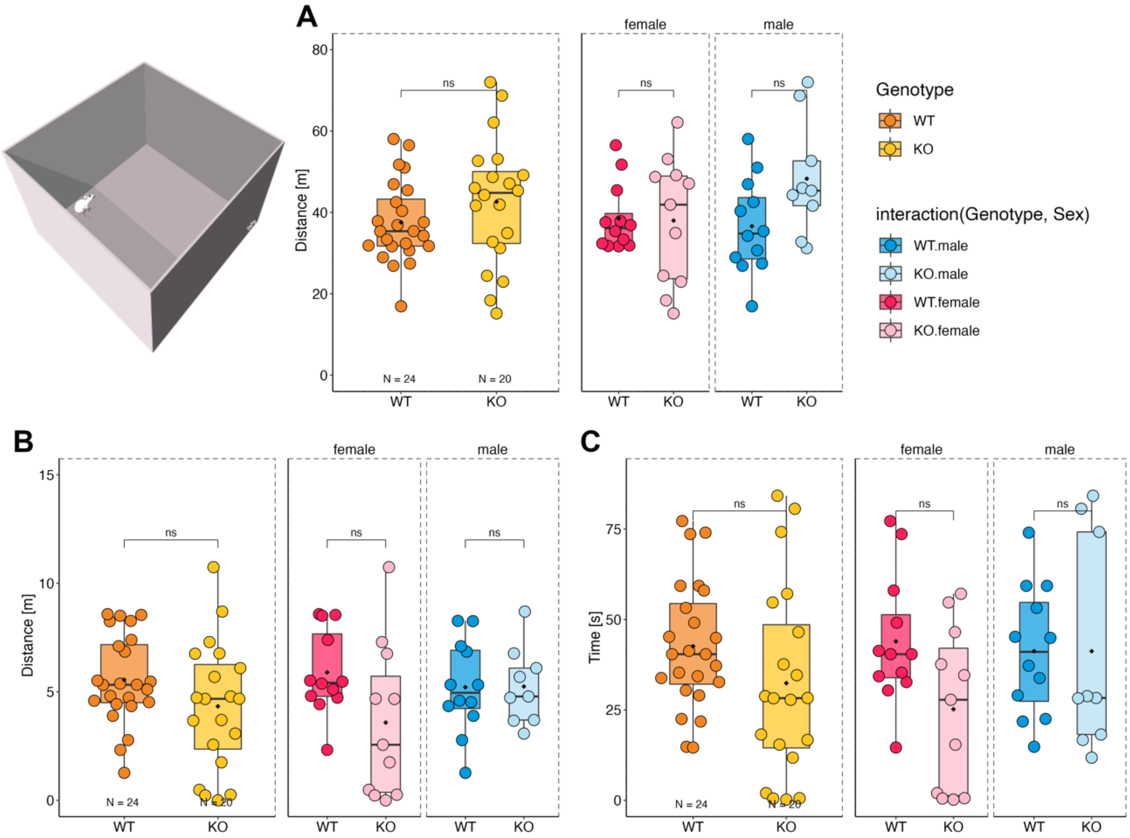

Figure 55. YTHDC1 KO males and females exhibit normal behavior in the open field test
(A) Total distance travelled. **(B)** Distance travelled in the center zone. **(C)** Time spent in the center zone. Individual results are plotted for both genotypes and sexes (WT males = 12, WT females = 12, KO males = 9, KO females = 11). ns = not significant.

There was no significant difference between the genotypes and sexes for distance travelled (genotype: $F_{1,43} = 1.76$, $p = 0.19$; sex: $F_{1,43} = 0.89$ $p = 0.34$, genotype:sex: $F_{1,43} = 2.56$, $p = 0.11$), time in the center zone (genotype: $F_{1,43} = 3.37$, $p = 0.13$; sex: $F_{1,43} = 0.76$ $p = 0.38$, genotype:sex: $F_{1,43} = 1.99$, $p = 0.17$), and distance travelled in the center zone (genotype: $F_{1,43} = 2.76$, $p = 0.11$; sex: $F_{1,43} = 0.252$ $p = 0.61$, genotype:sex: $F_{1,43} = 2.46$, $p = 0.12$).

YTHDC1 KO animals exhibit increased activity in the EPM test

Animals were subjected to the EPM test to assess differences in anxiety-like behaviors between WT and KO animals. The test was performed for a duration of 10 min (40 lux). The data presented was analyzed using linear models in R with the dependent variables distance, distance / s or time and the independent variables, sex and genotype. Animals that jumped off the maze during testing were excluded from the analysis. Reported below are the results for the two-way ANOVA (see Figure 56).

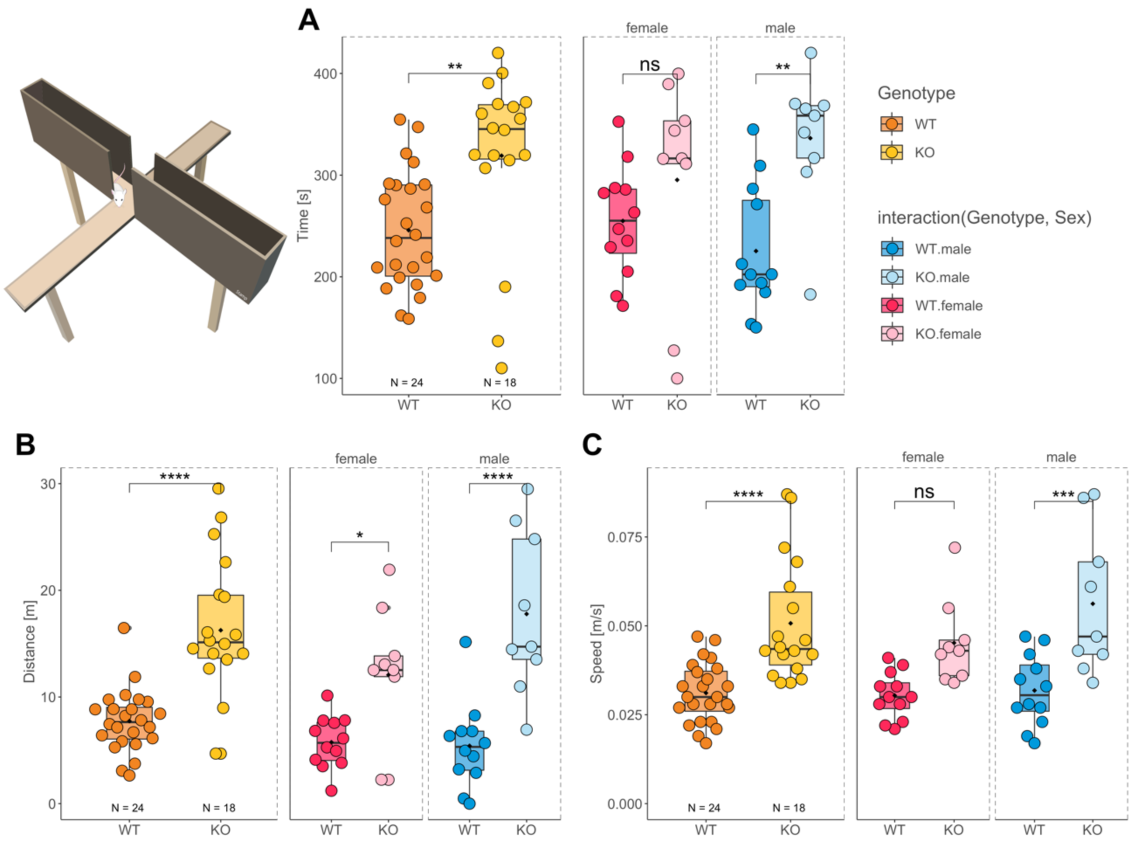

Figure 56: YTHDC1 KO animals spent an increased duration in the open arm of the EPM
(A) Time spent in the open arms. **(B)** Distance travelled in the open arms. **(C)** Mean speed in the open arms. Individual results are plotted for both genotypes and sexes (WT males = 12, WT females = 12, KO males = 9, KO females = 9). Two animals that jumped of the platform during the test were exclude from the analysis. ns = not significant, *: $p < 0.05$. **: $p < 0.01$, ***: $p < 0.001$, ****: $p < 0.0001$.

For the time spent in the open arm, a significant difference between the genotypes was observed, with KO animals spending more time in the open arm (genotype: $F_{1,41} = 10.981$, $p = 0.002$). No significant effect of sex and no interaction of genotype and sex were observed (sex: $F_{1,41} = 0.001$, $p = 0.98$; genotype:sex: $F_{1,41} = 2.389$, $p = 0.13$). A Tukey's test for multiple comparisons revealed a significant main effect of genotype ($p = 0.002$) with KO animals spending an increased time in the open arm compared to WT animals. Specifically, for KO males there was a pronounced difference ($p = 0.007$), while no significant difference between WT and KO females was detected ($p = 0.60$).

For the distance travelled in the open arm, a significant difference between the genotypes was observed, with KO animals travelling more distance in the open arm (genotype: $F_{1,41} = 32.784$, $p < 0.0001$). No significant effect of sex was detected but an interaction of genotype and sex below the significance threshold was observed (sex: $F_{1,41} = 1.948$, $p = 0.17$; genotype:sex: $F_{1,41} = 3.447$, $p = 0.07$). A Tukey's test for multiple comparisons revealed a significant main effect of genotype (p.adj. < 0.0001) with KO animals travelling further than WT animals. Specifically, KO males travelled a greater distance in the open arm (p.adj. < 0.0001) than WT males. Similarly, KO females travelled further than their WT counterparts (p.adj. = 0.04).

Looking at the overall speed when moving in the open arm, a significant difference between the genotypes was observed, with KOs moving faster when in the open arm (genotype: $F_{1,41} = 24.994$, $p < 0.0001$). No significant effect of sex and no interaction of genotype and sex were observed (sex: $F_{1,41} =$

2.027, p = 0.16; genotype:sex: $F_{1,41}$ = 1.494, p = 0.23). The Tukey's test for multiple comparisons indicates a significant main effect of genotype (p.adj. < 0.0001) with KO animals moving faster than WT animals. Here, KO males moved significantly faster in the open arm (p.adj. = 0.0004) than WT males. For females, a trend below the significance threshold was determined (p.adj. = 0.051).

YTHDC1 KO animals spent less time in the lit compartment in the DL test

In order to further examine differences in anxiety-like behaviors and exploratory drive, animals were subjected to the DL test. The test was performed for a duration of 10 min with strong lighting in the lit compartment (~ 140 lux) and no light in the dark compartment (< 5 lux). The data were analyzed using a linear model in R with the dependent variables distance or time and the independent variables, sex and genotype. Reported below are the results for the two-way ANOVA. A summary of the results is shown in Figure 57.

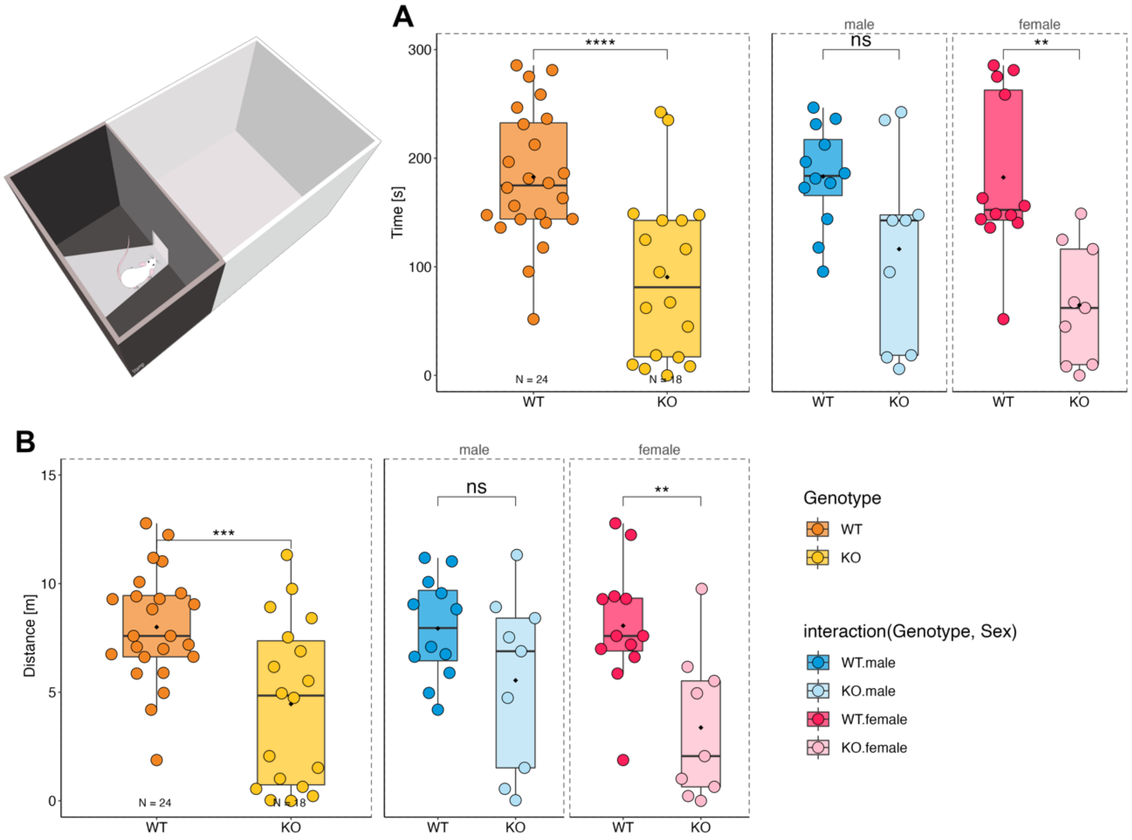

Figure 57: YTHDC1 KO animals spent more time in the dark in the DL test

(A) Time spent in the lit chamber. **(B)** Distance travelled in the lit chamber. Individual results are plotted for both genotypes and sexes (WT males = 12, WT females = 12, KO males = 9, KO females = 9). Significance levels from the Tukey's post-hoc test: ns = not significant, *: p < 0.05. **: p < 0.01, ***: p < 0.001, ****: p < 0.0001.

During the test, there was a significant difference between the genotypes for the time spent in the lit compartment with KO animals spending less time in the illuminated chamber (genotype: $F_{1,41}$ = 19.20, p < 0.00001; sex: $F_{1,41}$ = 1.17 p = 0.28) with no significant interaction of genotype and sex (genotype:sex: $F_{1,41}$ = 1.46, p = 0.24). A Tukey's test for multiple comparisons showed a significant main effect of genotype (p.adj. < 0.0001) with KO females spending significantly less time in the lit compartment than WT females (p.adj. = 0.0016), while no significant difference was detected for the comparison of WT and KO males (p.adj. = 0.13).

For distance travelled in the lit compartment a significant differences between the genotypes was observed with KO travelling less distance (genotype: $F_{1,41} = 13.08$, $p = 0.0009$; sex: $F_{1,41} = 0.79$ $p = 0.38$) with no significant interaction of genotype and sex (genotype:sex: $F_{1,41} = 1.38$, $p = 0.24$). The post hoc analysis showed that there is a significant main effect of genotype ($p = 0.0009$) with KO females travelling significantly less time in the lit compartment than WT females (p.adj. = 0.009), while no significant differences were detected for WT and KO males (p.adj. = 0.32).

YTHDC1 KOs show no impairments in the visible platform training

The assessment of anxiety-like behaviors in the DL and EPM test depends, among other things, on the vision of the animal. In case of visual impairments, these tests are not be reliable and thus may result in false conclusions. The relevance of this, has recently been demonstrated for 'low-anxiety behaving' (LAB) mice that spent extended time in the open arms of the EPM maze. While this alteration could be interpreted as reduced anxiety-like traits, in the case of LAB animals it was reportedly the consequence of complete blindness[201]. Therefore, to avoid any confounds resulting from visual impairments, animals were tested in the visible platform test. This procedure is commonly used to habituate mice before the MWM test and the efficiency in which the task is completed depends on the animal's ability to see the platform. The results presented below were obtained by starting animals from the same position across 4 trials, while altering the position of a visible platform between trials. Animals had 60 s to find and climb on the visible platform which was slightly raised above water level and marked with a distinct black flag. The data were analyzed using a linear model in R with the dependent variable latency and the independent variables, trial, and genotype. Since this was a control experiment and we are not interested in sex dependent differences in swimming, the statistical analysis only considered the effects of genotype and trial. Reported below are the results for the two-way ANOVA (see Figure 58).

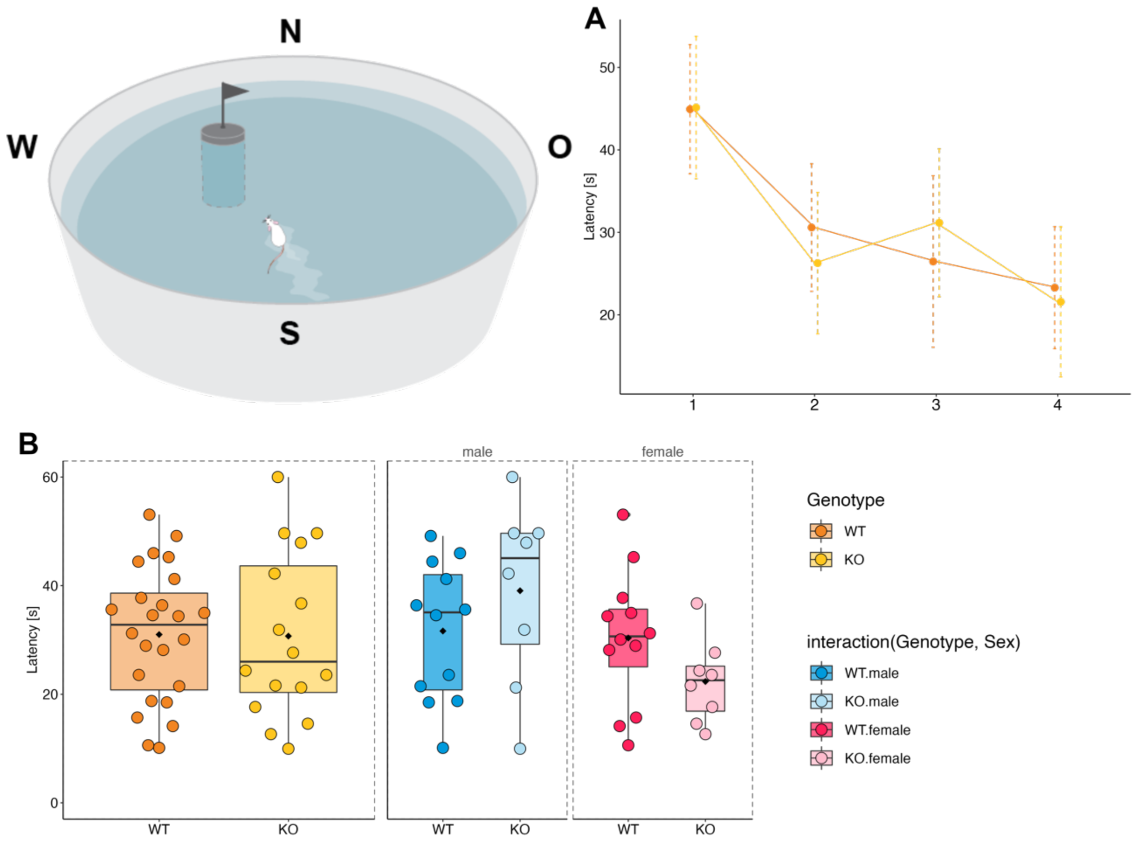

Figure 58: *Ythdc1*-Camk2aCre KO animals don't show impairments of vision in the visible platform training

(A) Latency to reach the platform across 4 trials. **(B)** Mean latency to reach platform. Individual results are plotted for both genotypes and sexes (WT males = 12, WT females = 12, KO males = 8, KO females = 8). ns = not significant, *: $p < 0.05$. **: $p < 0.01$, ***: $p < 0.001$, ****: $p < 0.0001$.

No differences were found between the latency of the WT and KO animals to reach the visible platform across trials. (genotype: $F_{1,157} = 0.002$, $p = 0.97$; Trial: $F_{1,157} = 8.83$, $p < 0.0001$) with no significant interaction between genotype and trial (genotype:trial:$F_{1,157} = 0.33$, $p = 0.81$).

The fact that there was no difference between WT an KO animals in the overall performance across 4 trials, as well as in the improvement during trials, indicates that KO animals have no visual impairment. Furthermore, the comparable latencies also suggest that there are no gross locomotor impairments. Thus, we can assume that the differences observed in the EPM and DL tests are not caused by visual or motor deficits.

YTHDC1 KO animals show increased activity in response to delay fear conditioning

Delay fear conditioning, in which a neutral stimulus (tone) is presented together with an aversive food shock, is commonly used to assess learning and memory and was used here to interrogate cortical and HPC functioning. The results presented below were obtained by using an established screening approach that combines cue and contextual fear conditioning[161]. For the conditioning, animals were exposed to a moderate foot shock (0.7 mA) at the start of the experiment and their memory was tested 24 h (cue memory) and 48 h (context memory) after conditioning. The experiment was conducted using male and female animals. Freezing was defined as periods of complete immobility lasting for at least one second.

A logistic regression analysis using GAMs was performed with freezing as the dependent variable (yes/no resolution: 1 s) and the independent variables genotype and sex. Time was included in the model as a smooth term, as well as a random intercept for the factor animal. Furthermore, for the cue memory, test time was stratified for the occurrence of the cue (tone). A summary of the model results can be found in Appendix 8.16.

The model results show that KO animals show a lower overall freezing during the cue memory test (genotype:KO Estimate = -1.7, Z-value = -7.52, $Pr(>|z|) < 0.0001$) with no main effect of sex (sex:female Estimate = -1.01, Z-value = -0.15, $Pr(>|z|) = 0.88$) but a pronounced interaction of genotype and sex (genotype:KO:sex:female: Estimate = 1.31, Z-value = 4.72, $Pr(>|z|) < 0.0001$). For the contextual memory test, a significant reduction in overall freezing was detected for the KO animals (genotype:KO Estimate = -2.27, Z-value = -7.46, $Pr(>|z|) < 0.0001$) with no main effect of sex (sex:female Estimate = -0.40, Z-value = -0.08, $Pr(>|z|) = 0.93$) and a pronounced interaction of genotype and sex (genotype:KO:sex:female: Estimate = 2.7, Z-value = 7.65, $Pr(>|z|) < 0.0001$).

In addition to the analysis using GAMs, a linear model was fitted for the contextual memory test using mean freezing scores per animal across the test as dependent variable, with sex and genotype as the independent variables. The ANOVA performed on the fitted model showed a main effect of genotype and no effect of sex (genotype: $F_{1,43} = 16.410$, $p = 0.0002$; sex: $F_{1,43} = 0.692$ $p = 0.41$). Here, no significant interaction of genotype and sex was detected (genotype:sex: $F_{1,43} = 0.205$, $p = 0.65$). A Tukey's test for multiple comparisons showed a significant main effect of genotype (p.adj. = 0.0002) with KO males exhibiting significantly less freezing than WT males (p.adj. = 0.016), while comparison of KO and WT females did not reach the significance threshold (p.adj. = 0.07). An overview of the paradigm and all results is shown in Figure 59.

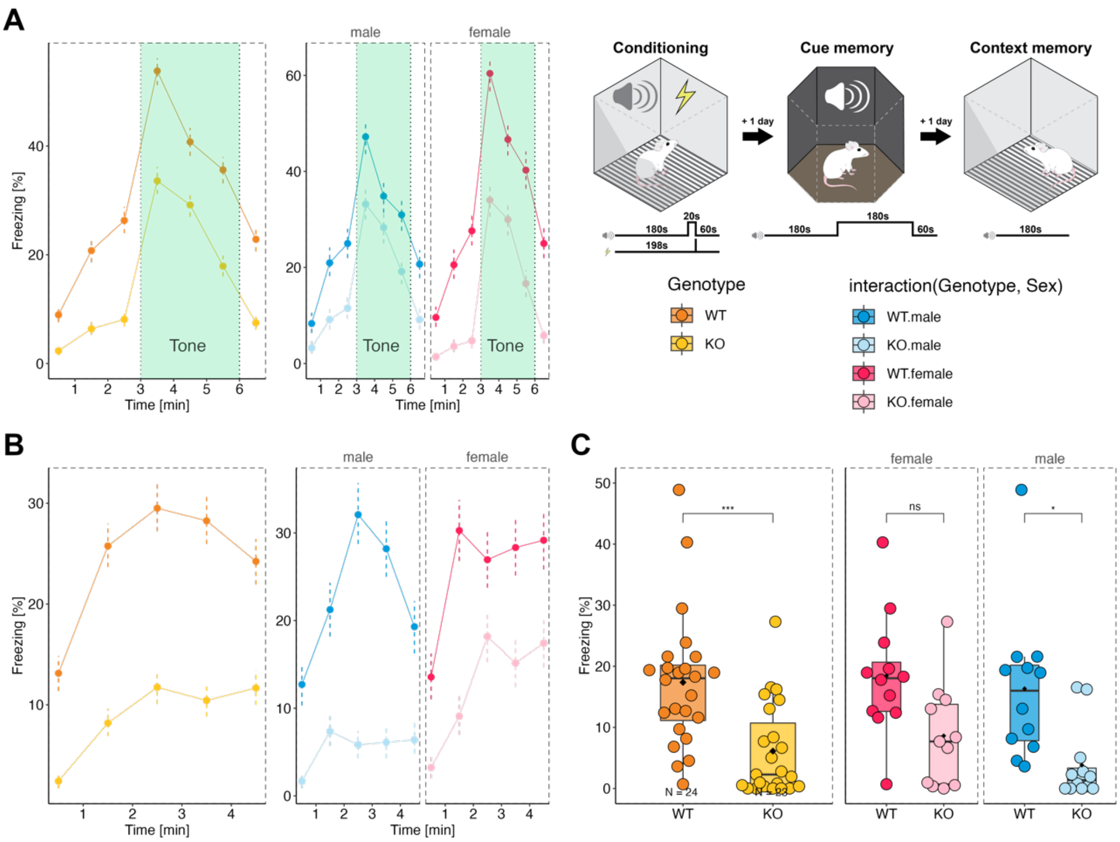

Figure 59: YTHDC1 Camk2aCre KO animals show differences in the fear conditioning response
(A) Cue memory, 24 h after conditioning. **(B)** Context memory, 48 h after conditioning. **(C)** Average contextual memory showing the mean freezing across 5 min. Individual results are plotted for both genotypes and sexes (WT males = 12, WT females = 12, KO males = 12, KO females = 11). Significance levels from the Tukey's post-hoc test: ns = not significant, *: $p < 0.05$. **: $p < 0.01$, ***: $p < 0.001$, ****: $p < 0.0001$.

The results from the fear conditioning should be interpreted with caution. Looking at the overall dynamics, it appears as if YTHDC1 KO show an overall diminished response that follows a similar trajectory. Strikingly, the response to the cue presentation 24h after conditioning shows a comparable response, starting from different basal freezing levels. Besides differences in the fear memory, the observed differences could also indicate an overall difference in arousal or a more active coping response.

4.2.5 YTHDC1 KO animals show volumetric changes in the cortex and HPC

Given the overall changes in behavior, structural MRI was conducted to detect differences in brain anatomy. The results included in this thesis, comprise only half of the collected results (females). The analysis of male animals is currently underway and will not be included due to time constraints.

For this, 23 females (WT = 11, KO = 12) were subjected to structural scans using a 9.4 T scanner (BioSpec, Bruker BioSpin GmbH). The data analysis was performed as described above. No animals were excluded from the analysis. The thresholds for the spatial voxel-wise t-maps were set at an uncorrected $p < 0.005$) with an adjusted extent threshold to obtain FWE-corrected ($p < 0.05$) clusters. The results are summarized in Figure 60.

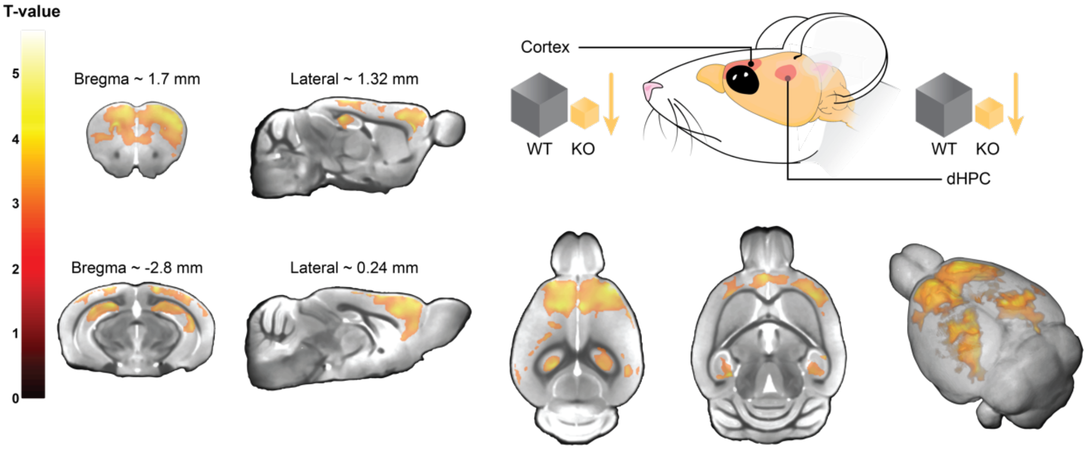

Figure 60: Camk2aCre YTHDC1 KO results in reduced gray matter volume in PFC and dHPC
Structural imaging of Camk2aCre YTHDC1 KO and WT animals at ~ 8 weeks (WT = 11, KO = 12). The results show clusters with FWE-corrected $p < 0.05$. A decrease in volume was detected for the cortex and dHPC. The color gradient shows the T-values, indicative of the relative statistical robustness of changes.

A striking decrease in volume in cortical regions and the dHPC was detected for KO animals compared to WT animals. Strikingly, these changes overlap with the Camk2aCre expression determined with the reporter mice and shown in Figure 8.

4.2.6 YTHDC1 KO neurons in the mPFC are less excitable

The observed differences in the various behavior tests are indicative of fundamental differences in the neuronal activity and prompt the question whether KO animals show differences in the basal properties of neurons. To investigate this, *ex-vivo* patch clamp recordings of layer V pyramidal neurons in the mPFC were performed in adult males (age 8-10 weeks). In total, the responses from 23 WT cells of 3 WT animals and 24 cells of 3 KO animals were analyzed.

No differences in the input resistance (p.adj. = 0.49, Wilcoxon test) nor resting potential (p.adj. = 0.43, Wilcoxon test) were observed. In contrast, parameters indicative of changes in the membrane excitability were found to be altered in KO animals. The rheobase, a threshold measure that constitutes the minimum current given an infinitely long stimulation that would be sufficient to elicit an action potential (AP) was increased in KO neurons (p.adj. = 0.042, independent two-sample t-test). Accordingly, the threshold potential required for triggering an AP showed a significant increase in KO cells (p.adj. = 0.005, Welch's t-test). In addition to the changed excitability, changes in several kinetic parameters were identified. The mean AP amplitude was significantly reduced in KO animals (p.adj. = 0.021, independent two-sample t-test) and the mean AP half-width was increased (p.adj. = 0.005, Wilcoxon test). In addition, the hyperpolarization following an AP showed a decreased undershoot in KO animals (p.adj. = 0.026, independent two-sample t-test). A detailed list of all estimated parameters is given in Appendix 8.17 and the main results are summarized in Figure 61.

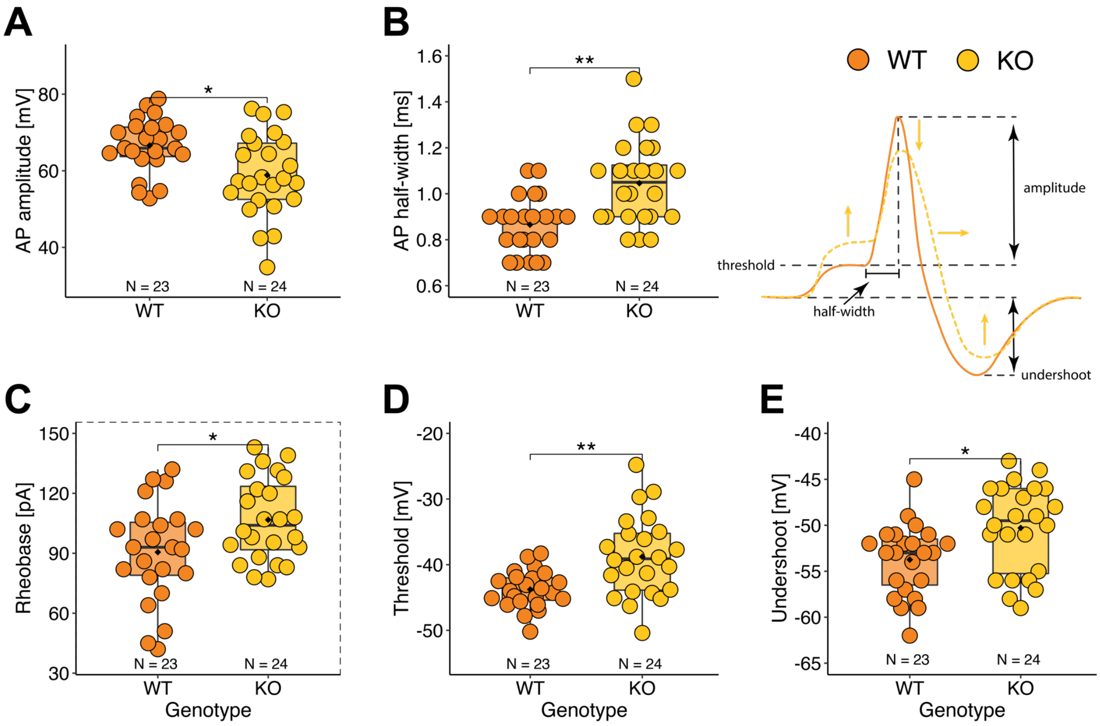

Figure 61: Camk2aCre YTHDC1 KO animals show a reduced excitability of layer V pyramidal neurons in the mPFC

(A) YTHDC1 KO cells show a reduced AP amplitude. **(B)** The AP half-width is significantly increased in KO animals. **(C)** The Rheobase, measuring excitability of neurons is significantly increased in KO animals. **(D)** KO animals show an increased AP threshold. **(E)** The AP undershoot is dampened in KO animals. Cells were patched in layer V of the PFC of WT = 3 (23 cells) and KO = 3 animals (24 cells). Statistics were performed using the independent two-sample t-test, Wilcox test or Welch's t-test as appropriate. Reported are the FDR adjusted p-values.

The observed differences point towards an overall reduced excitability of mPFC layer V pyramidal neurons in YTHDC1 KO animals. The threshold, amplitude and duration of an AP are determined by the properties of the neuronal membrane which in turn is regulated through its protein composition. Therefore, alterations in membrane related properties are likely to be associated with changes in protein abundance.

4.2.7 Depleting YTHDC1 induces global changes in protein abundance

The reduced excitability detected for layer V pyramidal KO neurons is indicative of changes in the protein composition of the cell membrane. To determine whether changes in the proteome of KO animals can explain the electrophysiological phenotype, a proteomic screening using LC-MS was performed as described above. For this, the fresh dissected mPFC, dHPC and vHPC of 6 WT and 5 KO animals was used.

In total 6,521 unique proteins were identified, out of which 6,131 (94 %) were detected across brain regions, with only 72 (1.1 %) being exclusively expressed in the mPFC, 30 (0.46 %) in the dHPC and 48 (0.74 %) in the vHPC respectively. In total, 274 unique proteins were found to be significantly dysregulated in the brain of YTHDC1 KO animals. Out of which, 225 (82 %) proteins were significantly downregulated and 49 (18 %) significantly upregulated. An overview of the results is shown in Figure 62 and Figure 63.

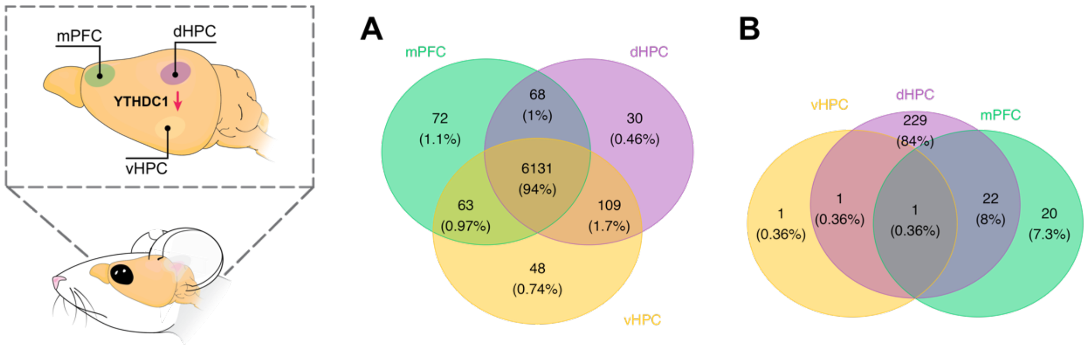

Figure 62: YTHDC1 Camk2aCre KO animals show altered protein abundance in the mPFC, dHPC and vHPC
(A) Overview of the number of unique proteins identified using label free LC-MS. **(B)** Differentially expressed proteins across three brain regions (FDR < 0.05).

In the mPFC, 43 proteins were detected in differing levels in the KO, compared to the WT (FDR < 0.05). For the dHPC and vHPC there were 253 and 3 significant changes detected respectively (FDR < 0.05). A pathway analysis was conducted for the significantly altered proteins (FDR < 0.05) of each brain region. No significant enrichment was detected for any of the three ontologies (CC, MF, BP).

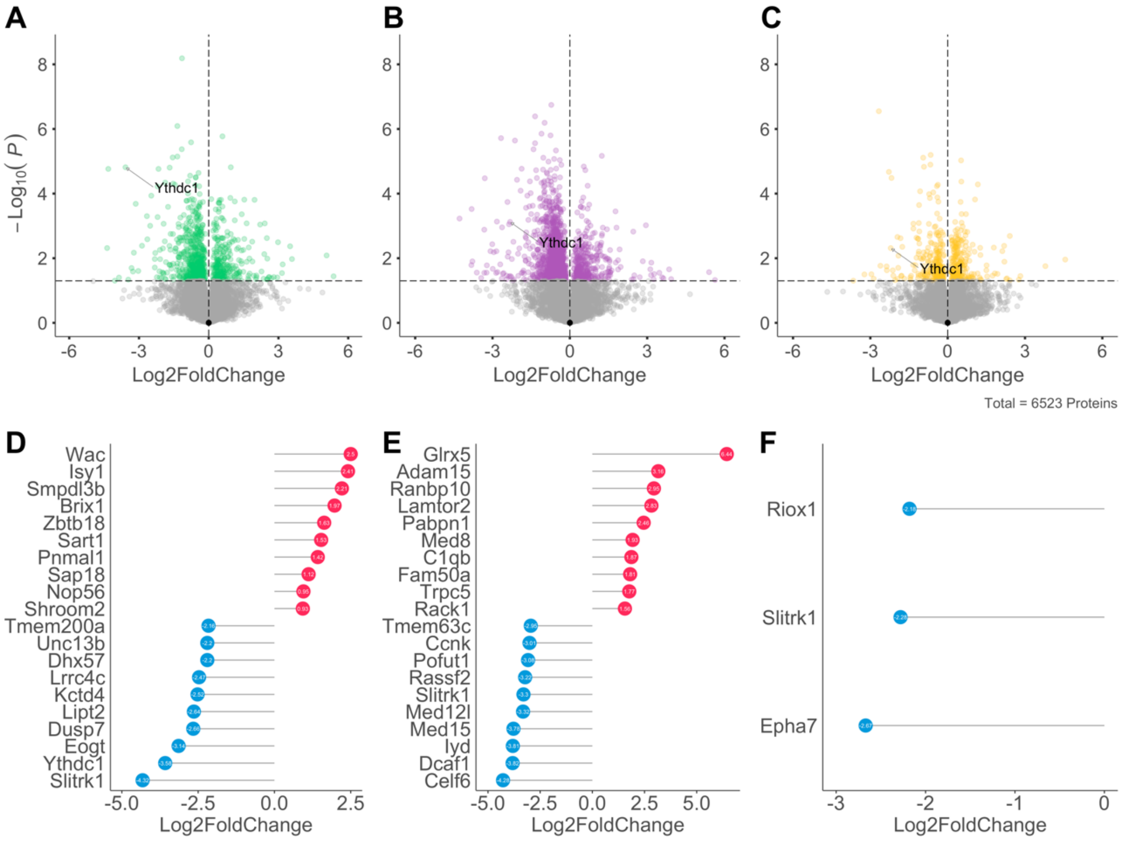

Figure 63: Detailed overview of changes observed in the LC-MS proteomic screening of YTHDC1 KO in the mPFC, dHPC and vHPC
(A-C) Volcano plots showing the differential protein levels in mPFC **(A)**, dHPC **(B)** and vHPC **(C)** YTHDC1 KO animals. **(D-F)** The top 10 most up- and downregulated proteins in the mPFC **(D)**, dHPC **(E)** and vHPC **(F)** (FDR < 0.05).

In addition, the data was mined for differences in protein abundance of genetic risk factors associated with seizures and epilepsy. Interestingly, the risk associated potassium channels KCNQ2 (dHPC: L2FC

= - 0.6, p = 0.005), KCNQ3 (dHPC: L2FC = - 0.78, p = 0.057) as well as the sodium channel SCN1A (mPFC: L2FC = 0.34, p = 0.011; dHPC: L2FC = 0.36, p = 0.019) and the risk associated ubiquitin ligase UBE3A[202] (mPFC: L2FC = -0.5, p = 0.001; dHPC: L2FC = -0.34, p = 0.04) were found to be altered in the brain of KO animals.

In contrast to the WTAP KO, which was observed to alter the abundance of many m^{6}A regulators, only YTHDF3 was determined to be significantly downregulated in the dHPC (FDR < 0.05).

YTHDC1 KO show less changes in mitochondrial proteins, compared to WTAP KO animals

Given the striking changes in mitochondrial protein that were observed in the WTAP KO animals, the effect of YTHDC1 depletion on the abundance of components of the mitoribosome and respiratory chain complex components in the mPFC were examined. For the components of the mitoribosomes, no significant differences were detected after FDR correction. A qualitative overview of all detected proteins is shown in Figure 64.

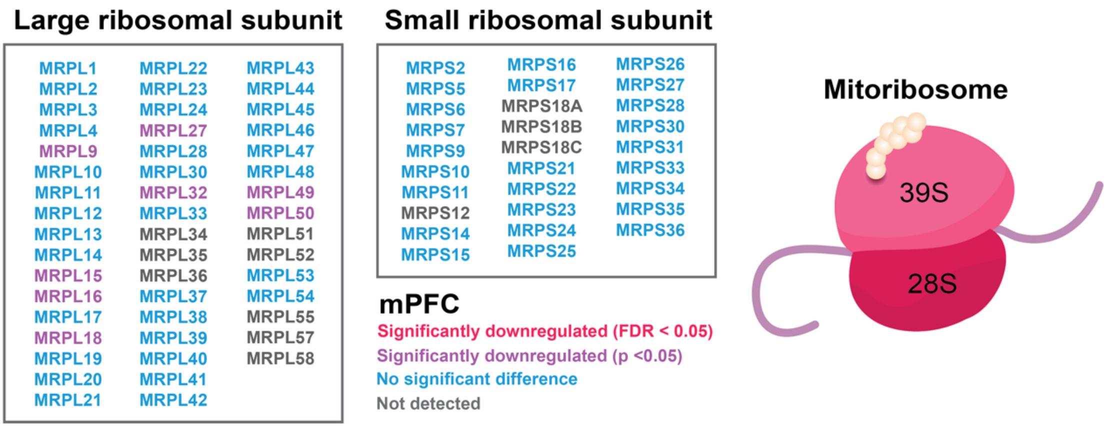

Figure 64: YTHDC1 Camk2aCre KO animals have normal levels of mitoribosomal proteins in the mPFC

Overview of the mitoribosome components detected in the mPFC (WT = 6, KO = 5). Significantly downregulated proteins are highlighted in red (FDR < 0.05), proteins that were determined to be down regulated but did not pass the FDR threshold are shown in purple ($p < 0.05$), proteins for which no differences between WT and KO were observed are marked in blue and proteins that were not detected are shown in gray. No significantly upregulated proteins were identified.

In addition, the components of the respiratory chain complex were examined for differences in the protein abundance. Here, more changes were detected. However, after FDR correction only 3 components of Complex I remained. The results are summarized in Figure 65. Interestingly, as with the WTAP data set, no upregulated proteins were amongst the differentially regulated mitochondrial candidates.

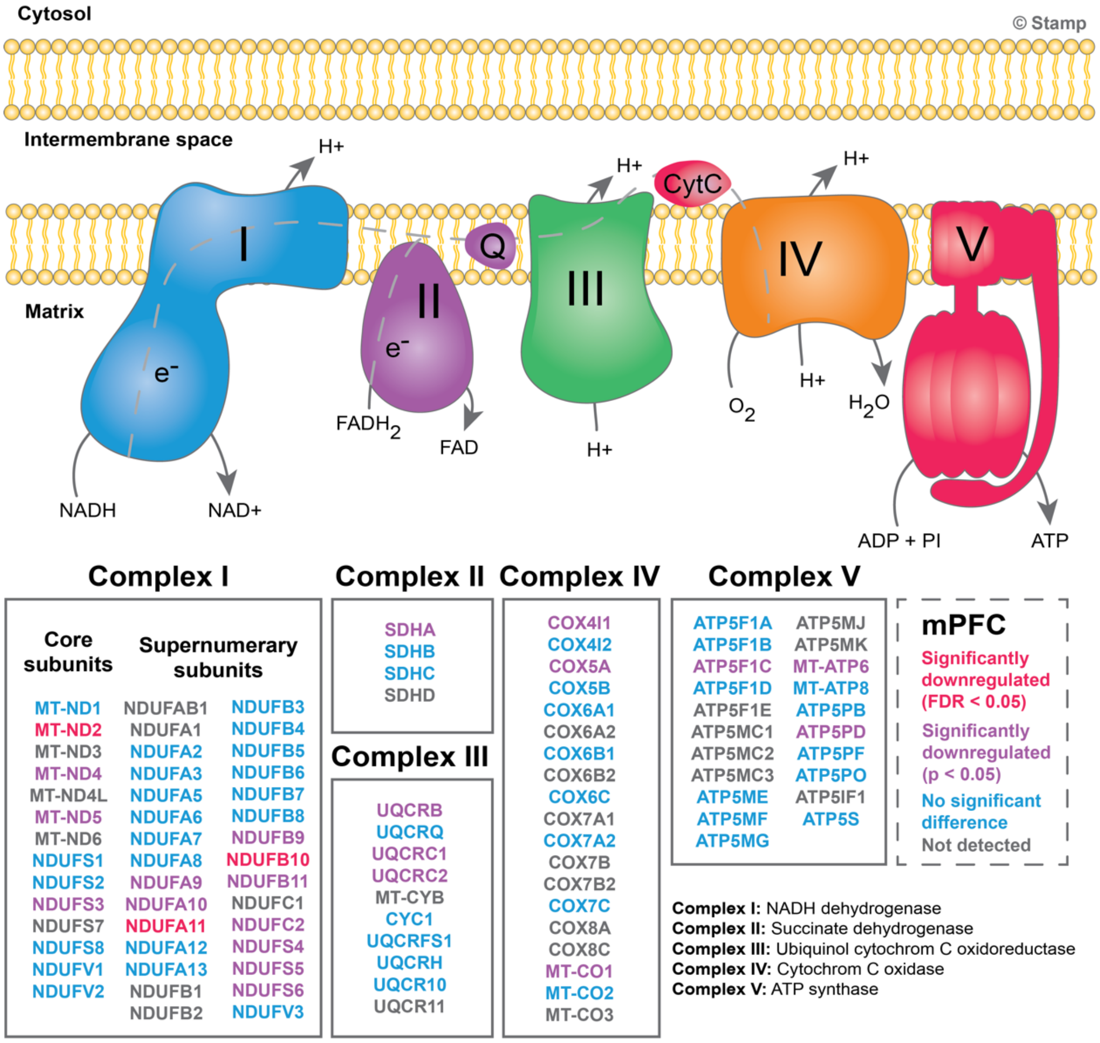

Figure 65: YTHDC1 KO animals show minor changes in the composition of respiratory chain complex

Overview of respiratory chain complex components in the mPFC of YTHDC1 Cam2aCre animals (WT = 6, KO = 5). Significantly downregulated proteins after FDR are highlighted in red (FDR < 0.05), significantly regulated proteins before multiple testing correction are marked in purple ($p < 0.05$), proteins for which no differences between WT and KO were observed are marked in blue and proteins that were not detected are shown in gray. No significantly upregulated proteins were identified.

4.2.8 YTHDC1 KO affects metabolism in mPFC and dHPC

As with the WTAP project, a metabolic screening of YTHDC1 KO tissue was performed to determine the metabolite profile of the mPFC, dHPC and vHPC. For this, the tissue of 8 WT and 8 KO animals were freshly dissected and analyzed as described above. The statistics were performed for metabolites detected in at least 70 % of samples using the independent two-sample t-test. Reported below are results passing the threshold FDR < 0.1. An overview of the significant differences is shown in Figure 66.

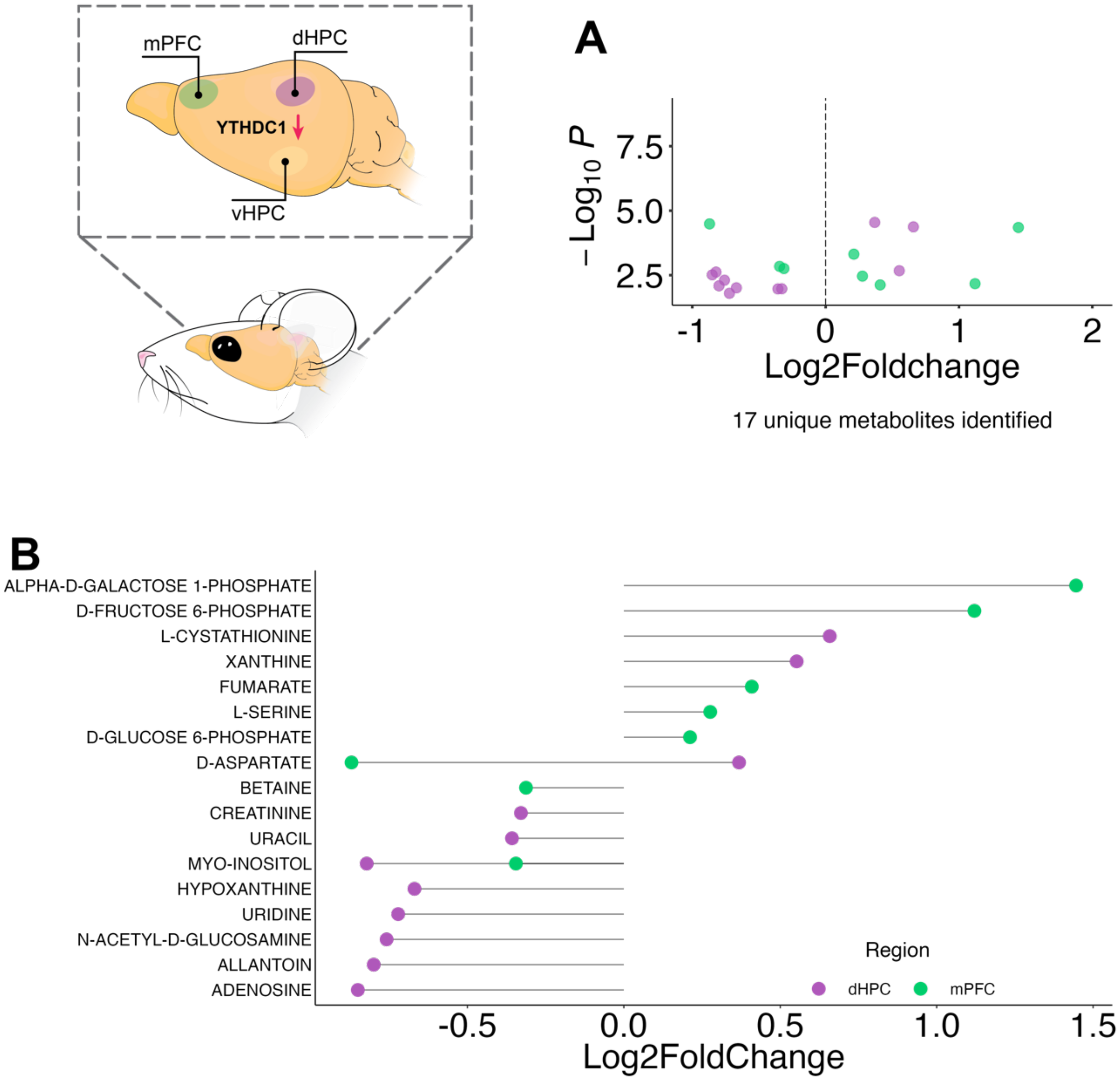

Figure 66: Metabolic dysregulation in Camk2aCre YTHDC1 KO animals

(A) In total 17 unique metabolites were identified that are dysregulated in the mPFC and dHPC of KO animals. No differential regulation was determined for the vHPC. **(B)** Top upregulated and downregulated metabolites across brain regions. Metabolites were measured in 8 WT and 8 KO animals. Group comparisons shown were obtained by an independent two-sample t-test and are reported for FDR < 0.1.

In total, 125 different metabolites were identified across the three brain regions, with 17 unique metabolites being differentially regulated (FDR < 0.1). Strikingly, no differential regulation of metabolites was determined for the vHPC. The majority of differential changes in the mPFC and dHPC appears to be region-specific. In contrast, many changes detected in the WTAP KOs were present across brain regions. A detailed list of all identified metabolites can be found in Appendix 8.18.

An overview of the overlap and differences in differentially regulated metabolites across brain regions for the WTAP and YTHDC1 KO is shown in Figure 67.

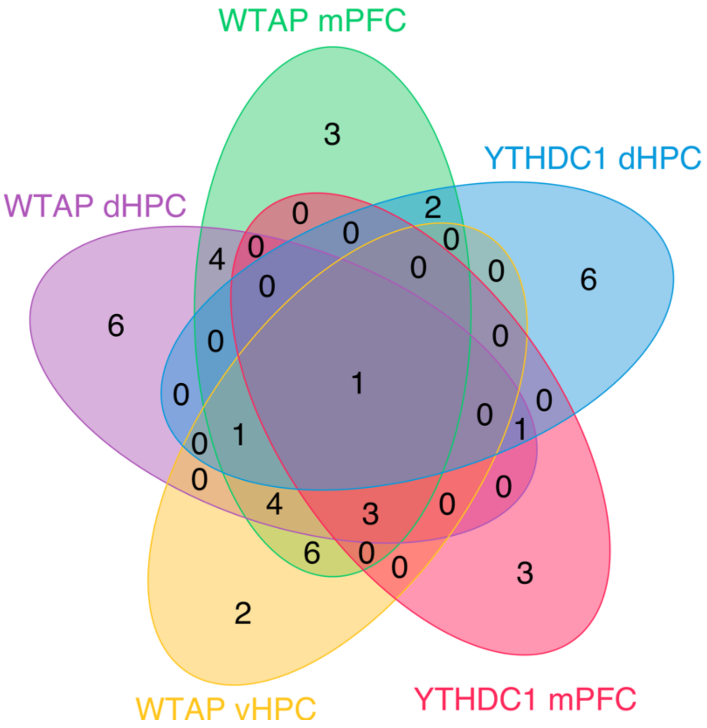

Figure 67: Overlap of differentially regulated metabolites across brain regions for WTAP and YTHDC1 KOs

Overlap of differentially regulated metabolites in the mPFC, dHPC and vHPC of WTAP and YTHDC1 KO animals. Included are results FDR < 0.01.

The comparison of differentially regulated metabolites across brain regions and KOs shows that many of the observed changes are region and KO specific with only one metabolite (D-aspartate) being differentially regulated across regions and KOs. In the brain of WTAP KO animals, D-aspartate is significantly upregulated across regions (mPFC: 0.74, p.adj. = 0.002; dHPC: 0.60, p.adj. = 0.08; vHPC: 0.57 p.adj. = 0.01), while in YTHDC1 KOs, it is significantly downregulated in the mPFC (L2FC = -0.87, p.adj. = 0.003) and upregulated in the dHPC (L2FC = 0.37, p.adj. = 0.002). This is addressed in detail in the discussion section below.

4.2.9 Validation of NexCreERT2 induced YTHDC1 KO

To explore the effects of YTHDC1 in more detail, the conditional strain *Ythdc1*-NexCreERT2 was used for the analysis of KO induced changes in gene expression and splicing. The induction and sample collection followed the same procedure as described for the *Wtap*-NexCreERT2 strain. The results from the validation are summarized in Figure 68.

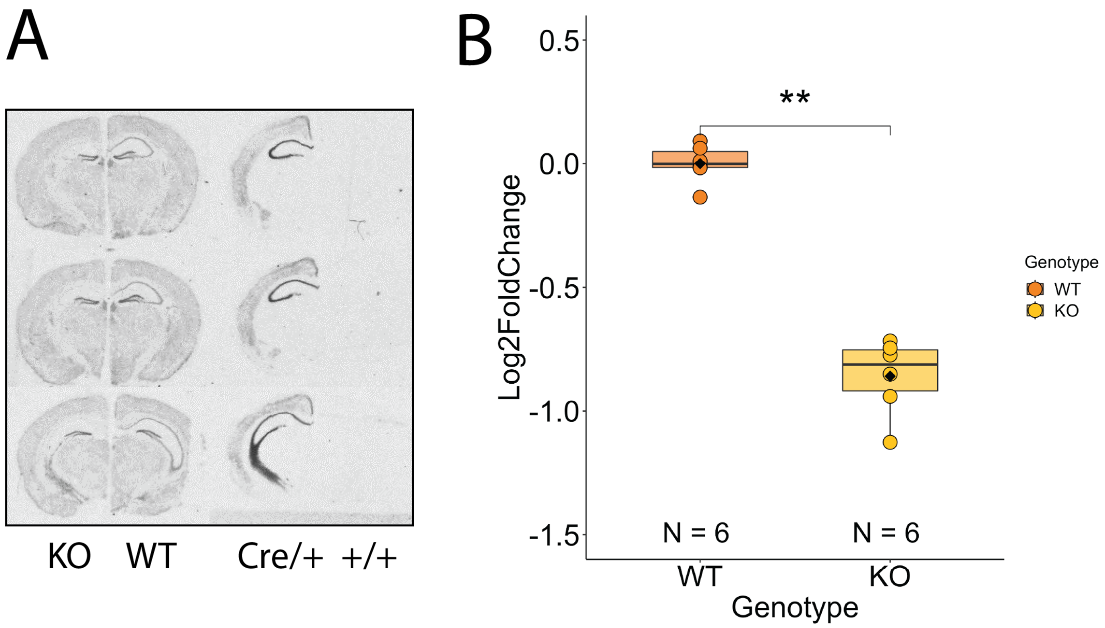

Figure 68: Tamoxifen treatment of NexCreERT2 carrying animals results in a depletion of the floxed *Ythdc1* exons

(A) ISH with a probe targeting the floxed exons 3-7 showing a clear reduction in *Ythdc1* signal in the HPC. **(B)** The KO efficacy for tissue used for gene expression analysis was validated using qPCR. Shown are the results for the samples that were used for RNA sequencing (WT = 6, KO = 6). Reported are the FDR adjusted p-values. ns = not significant, *: $p < 0.05$. **: $p < 0.01$, ***: $p < 0.001$, ****: $p < 0.0001$.

A clear reduction in *Ythdc1* expression was observed in the ISH (Figure 68, panel A). Similarly, a clear KO was determined for the qPCR validation (p.adj. < 0.01, Wilcoxon test, Figure 68, panel B). The samples for which the KO was validated with qPCR were used for subsequent gene expression analysis with poly-(A) sequencing.

4.2.10 YTHDC1 KO induces shift in gene expression

To determine whether YTHDC1 depletion results in changes in gene expression, poly(A) RNA sequencing was performed as described in the Methods section. In brief, libraries were prepared using the NEBNext Ultra II Directional RNA Library Prep Kit (Illumina) according to manufacturer’s instructions, starting from 200ng DNase I treated total RNA (WT = 6, KO = 6). Libraries were treated with Illumina's Free Adapter Blocking Reagent and sequenced on 1 x lane of the NovaSeq 6000 (2 x 100 paired end with an output of ~78 million reads per sample).

Genotype dependent correlation and separation in PCA space for YTHDC1 KOs

The global correlation coefficient amongst pairs of samples was calculated from the log2-transformed normalized counts of WT and KO samples and shows a pronounced separation of the genotypes (Figure 69, panel A).

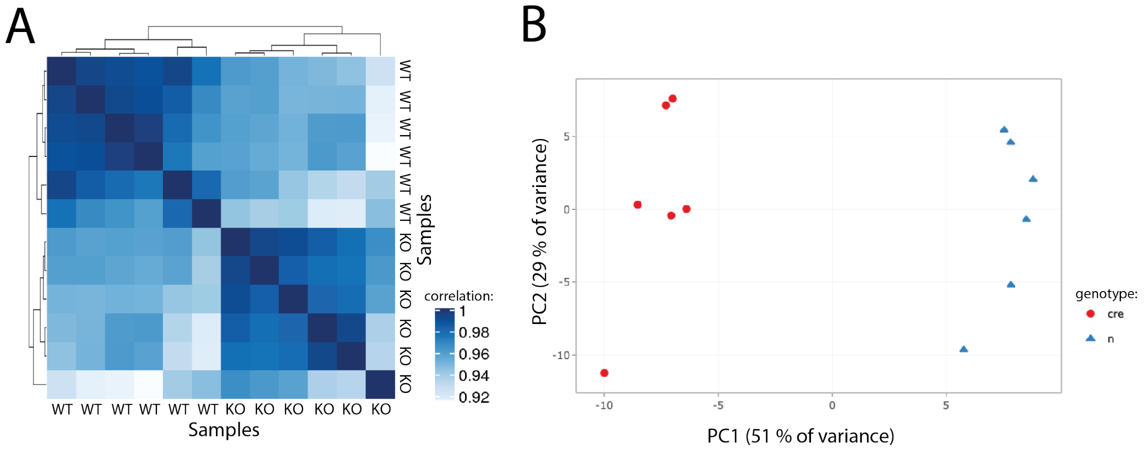

Figure 69: Sequenced samples show strong correlation within genotypes and clear separation in PC space **(A)** The sample correlations performed with the log2transformed normalized counts shows that samples of the same genotype are more similar to each other than to samples of the other genotype. **(B)** The PCA for the 1,000 most variably expressed genes shows that PC1 explains 51 % of the observed variance.

The results from the PCA performed with the 1,000 most variably expressed genes reveals a distinct clustering of WT and KO samples along principal component 1 (PC1), explaining 51 % of the variance and indicating the genotype driven effect of the KO (Figure 69, panel B).

NexCreERT2 YTHDC1 KO shifts gene expression

The depletion of YTHDC1 from NexCreERT2 expressing cells was observed to results in a strong shift in gene expression with 3,944 transcripts showing expression differences in the HPC region dCA1 (FDR < 0.05). For the current analysis, a cut off was applied and only genes showing differences matching Log2FoldChange > 0.5, FDR < 0.05 and a base mean ≥ 20 were considered. After filtering, 828 genes remain for subsequent exploration. The results are summarized in Figure 70.

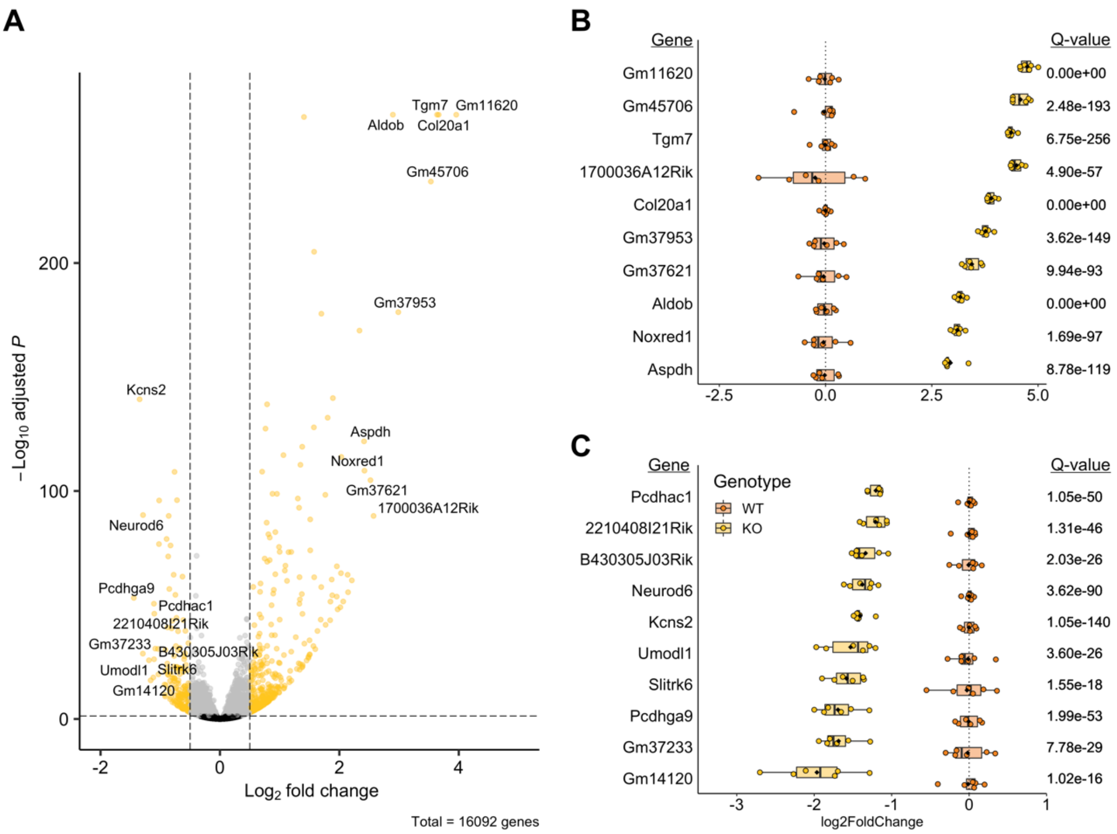

Figure 70: YTHDC1 KO animals show a strong shift in gene expression in the dCA1
(A) Volcano plot showing the comparison of KO vs WT animals for 16,092 detected genes. In total, 828 transcripts are differently expressed (FDR < 0.05, Log2FoldChange ≥ 0.5, base mean ≥ 20), with 531 transcripts being significantly upregulated and 297 transcripts significantly downregulated. **(B)** Top 10 genes with the greatest upregulation in YTHDC1 KO animals. **(C)** Top 10 genes with the greatest downregulation in YTHDC1 KO animals. Data is shown for WT = 6; KO = 6. For up- and downregulated genes, a cut off was applied (base mean ≥ 20, only genes detected for both genotypes).

Out of the 828 differentially expressed transcripts, 531 (64 %) were significantly up- and 297 (36 %) downregulated. The proportional change is similar to what has been observed for the WTAP NexCre-ERT2 KO (58 % up, 42 % down).

Gene Ontology analysis reveals enrichment for ion channel activity

To determine whether the observed changes are associated with particular biological functions or cellular components, a GO enrichment analysis was performed for the filtered results (FDR < 0.05, Log2FoldChange ≥ 0.5, base mean ≥ 20). The analysis for CC showed and enrichment for integral components of the plasma membrane (p.adj. < 0.0001) and for BP an enrichment for processes associated with cell-cell adhesion via plasma-membrane adhesion molecules (p.adj. = 0.025) was detected. The biggest number of enriched terms was determined for MF and is summarized in Figure 71. Detailed results can be found in Appendix 8.19.

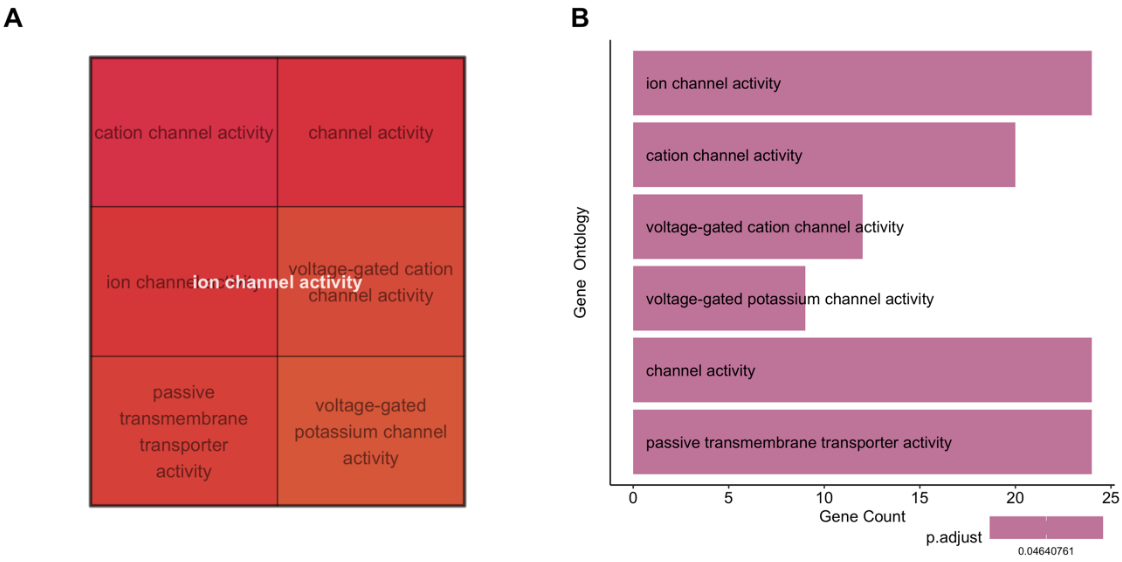

Figure 71: Differentially expressed genes in YTHDC1 KOs are enriched for ion channels activity
(A) Overview of the GO results for MF after application of semantic similarity analysis (FDR < 0.05). The enriched topics are all related to ion channel activity. **(B)** Bar plot showing the number of genes associated with identified GO terms and ranked by the adjusted p-value.

NexCreERT2 YTHDC1 animals show shift in differential exon usage

To determine whether the removal of YTHDC1 changes alternative splicing, the mRNA sequencing data were analyzed with the DEXSeq package as described for the *Wtap*-NexCreERT2 project. The DEXSeq analysis revealed a pronounce shift in exon usage after depletion of YTHDC1. Overall, 1,746 differentially expressed features, mapping to 1,054 genes (FDR < 0.05; Log2FolgChange ≥ 0.5; base mean ≥ 5) were identified. The results are summarized in Figure 72.

Of the 1,746 features, 653 (38 %) were significantly upregulated and 1,093 (62 %) were downregulated. In contrast, the changes in exon usage induced by the depletion of WTAP were more evenly distributed (52 % up, 48 % down).

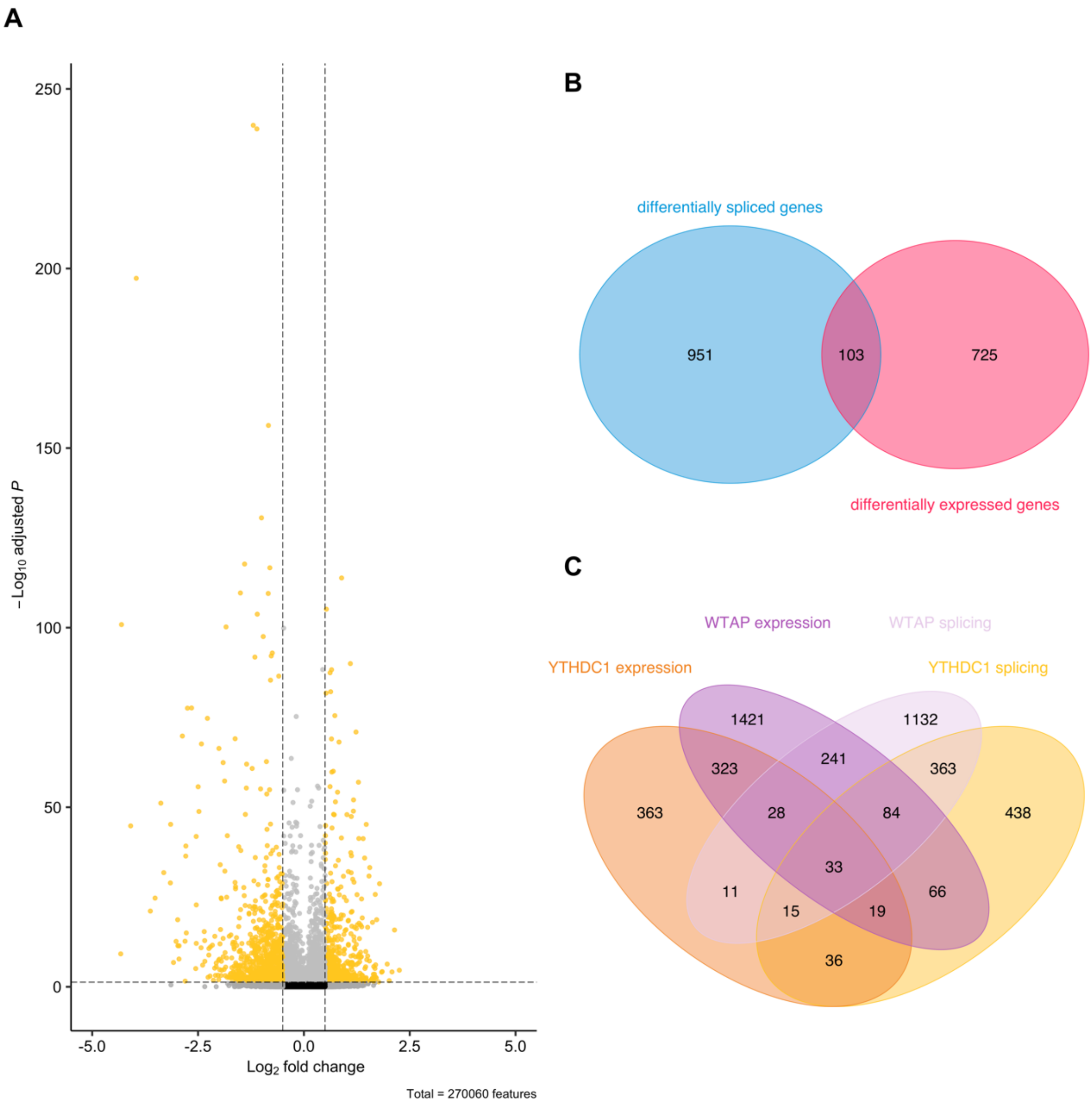

Figure 72: YTHDC1 KO results in large scale changes in exon usage

(A) YTHDC1 KO animals show differences in 1,746 exonic features mapping to 1,054 distinct genes (Log2FoldChance ≥ 0.5, FDR < 0.05, exon base mean ≥ 5). **(B)** Overlap of gene sets for which differential expression was detected (FDR < 0.05, Log2FoldChange ≥ 0.5, base mean ≥ 20) and genes for which differences in exon usage were observed genes (Log2FoldChance ≥ 0.5, FDR < 0.05, exon base mean ≥ 5). **(C)** Overlap and differences in the differential gene expression and splicing of WTAP and YTHDC1 KO animals.

Alternatively-spliced transcripts are enriched for synapse associated genes and mRNA metabolic processes

GO enrichment analysis was performed for genes for which a significantly different exon usage was determined (FDR < 0.05, Log2FoldChange ≥ 0.5, exon base mean ≥ 5). The GO analysis for BP revealed an enrichment for processes associated with the term ‘regulation of mRNA metabolic process’ (p.adj. = 0.047) and no enrichment was detected for MF associated ontologies. For CC, an enrichment was determined for synaptic components. An overview of this is shown in Figure 73. A list with all of the results can be found in Appendix 8.20.

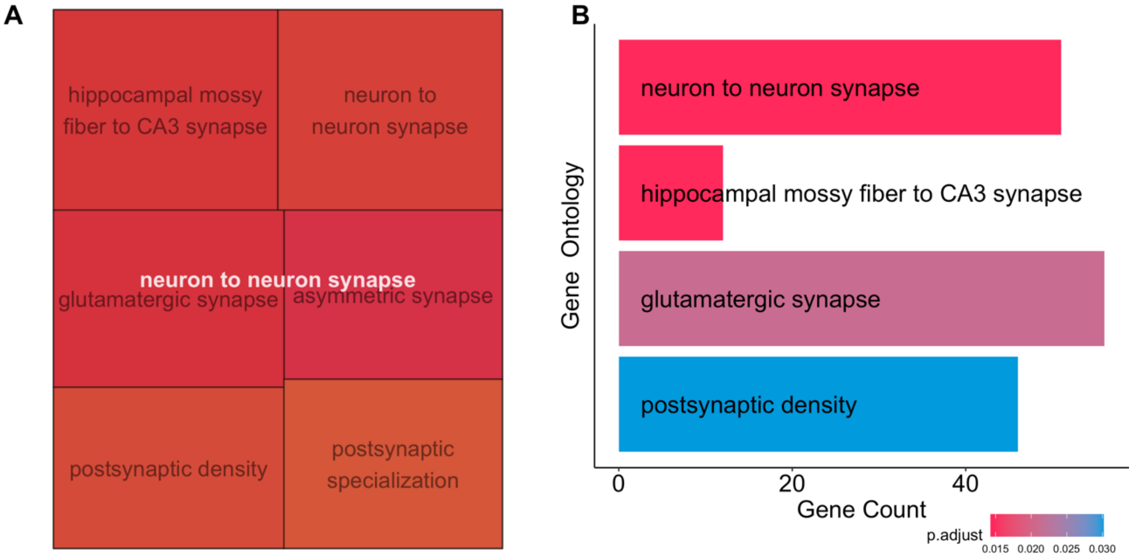

Figure 73: Differentially expressed exons in YTHDC1 KOs are enriched for synaptic genes
(A) Overview of the GO results for CC after application of semantic similarity analysis (FDR < 0.05) with the emerging topic neuron to neuron synapse. **(B)** Bar plot showing the number of genes associated with the top GO terms ranked by adjusted p-value.

4.2.11 NexCreERT2 YTHDC1 KO: behavioral assessment

Given the strong molecular phenotype with an enrichment for synaptic components, the implication for learning and memory and anxiety-like behaviors was assessed using FC, the OF and DL tests.

NexCreERT2 YTHDC1 KO animals show normal locomotion and anxiety-like behaviors

The OF test was conducted to assess overall differences in locomotion and explorative behavior between YTHDC1 WT and KO animals. The test was performed as described above, with a low light intensity (15 lux) and for a duration of 10 min. Group comparisons were tested using the independent two-sample t-test, Welch's t-test, or Wilcoxon test as appropriate and corrected for multiple testing using the Benjamini and Hochberg method. A summary of the results is shown in Figure 74.

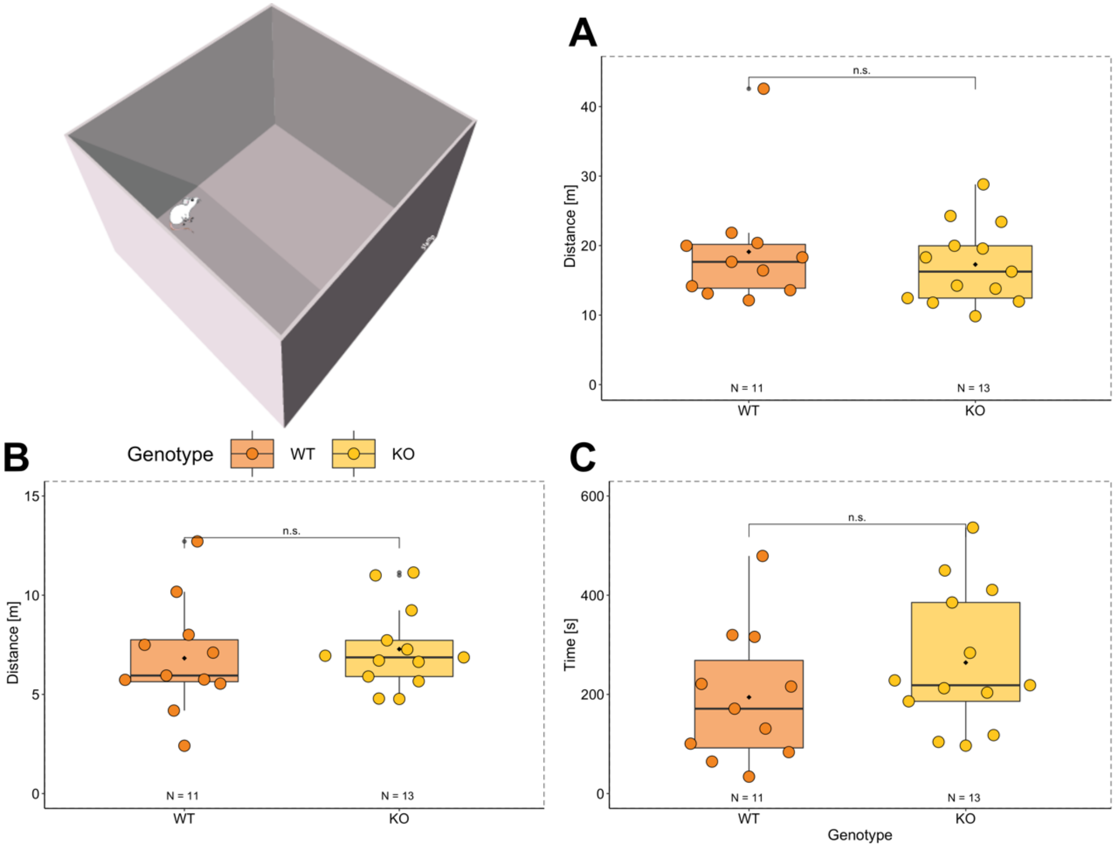

Figure 74: Open field test of NexCreERT2 YTHDC1 KO animals

(A) Total distance travelled. **(B)** Distance travelled in the center zone. **(C)** Time spent in the center. Individual results are plotted for both genotypes (WT N = 11, KO N = 13). ns= not significant, *: p.adj. < 0.05. ** p.dj < 0.01, *** p.adj. < 0.001, **** p.adj. < 0.000. Adjusted p-values were obtained using either the independent two-sample t-test, Welch's t-test, or Wilcoxon test as appropriate and corrected for multiple testing using the Benjamini and Hochberg method.

No significant differences were detected between WT and KO animals for the overall distance travelled (p.adj. = 0.68, Wilcox test), the distance travelled in the inner zone (p.adj. = 0.68, independent two-sample t-test) or the time spent in the inner zone (p.adj. = 0.68, independent two-sample t-test).

NexCreERT2 YTHDC1 KO animals show normal behavior in the DL test

Animals were subjected to the DL test to determine differences in the exploratory drive and anxiety. The test was performed with moderate lighting (~100 lux) in the lit chamber and total darkness in the dark chamber (< 5 lux) for a duration of 10 min. Group comparisons were tested using the independent two-sample t-test, Welch's t-test, or Wilcoxon test as appropriate and corrected for multiple testing using the Benjamini and Hochberg method. A summary of the results is shown in Figure 75.

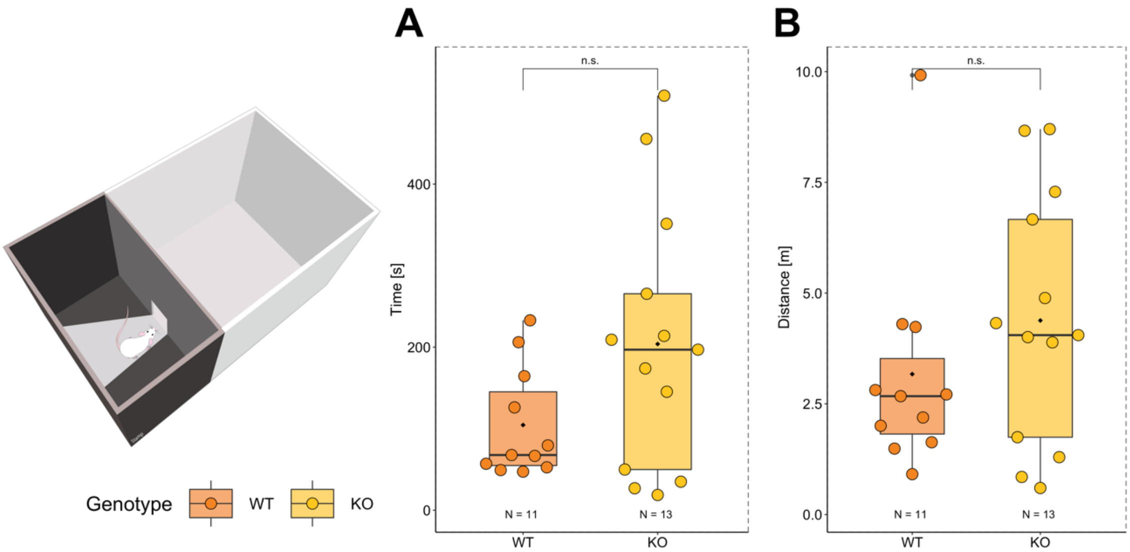

Figure 75: Open field test of NexCreERT2 YTHDC1 KO animals

(A) Time in the lit compartment. **(B)** Distance travelled in the lit compartment. Individual results are plotted for both genotypes (WT N = 11, KO N = 13). Ns = not significant, *: p.adj. < 0.05. ** p.dj < 0.01, *** p.adj. < 0.001, **** p.adj. < 0.000. Adjusted p-values were obtained using either the independent two-sample t-test, Welch's t-test, or Wilcoxon test as appropriate and corrected for multiple testing using the Benjamini and Hochberg method.

There were no significant differences for time spent in the light zone (p.adj. = 0.48, Wilcox test) or the distance travelled in the light zone (p.adj. = 0.48, Wilcox test).

NexCreERT2 YTHDC1 KO animals exhibit normal cue and contextual fear memory

Cortical and HPC functioning were tested using delay FC. For this, the paradigm and settings used were identical to the ones described for the *Wtap*-NexCreERT2 animals (foot shock: 1 s, 0.7 mA) and animals were tested 24 h (cue memory) and 48 h (contextual memory) after conditioning. The data were analyzed using logistic regression analysis with GAMs and the complete details of the fitted model can be found in Appendix 8.21.

Logistic regression analysis revealed that KO animals show comparable levels of freezing during the cue memory test compared to the control group (genotype:KO Estimate = 0.92, Z-value = 1.15, Pr(>|z|) = 0.25). Similarly, no difference between WT an KO animals was determined for the contextual memory 48 h after conditioning (genotype:KO Estimate = 0.55, Z-value = 0.51, Pr(>|z|) = 0.61). An overview of the results is shown in Figure 76.

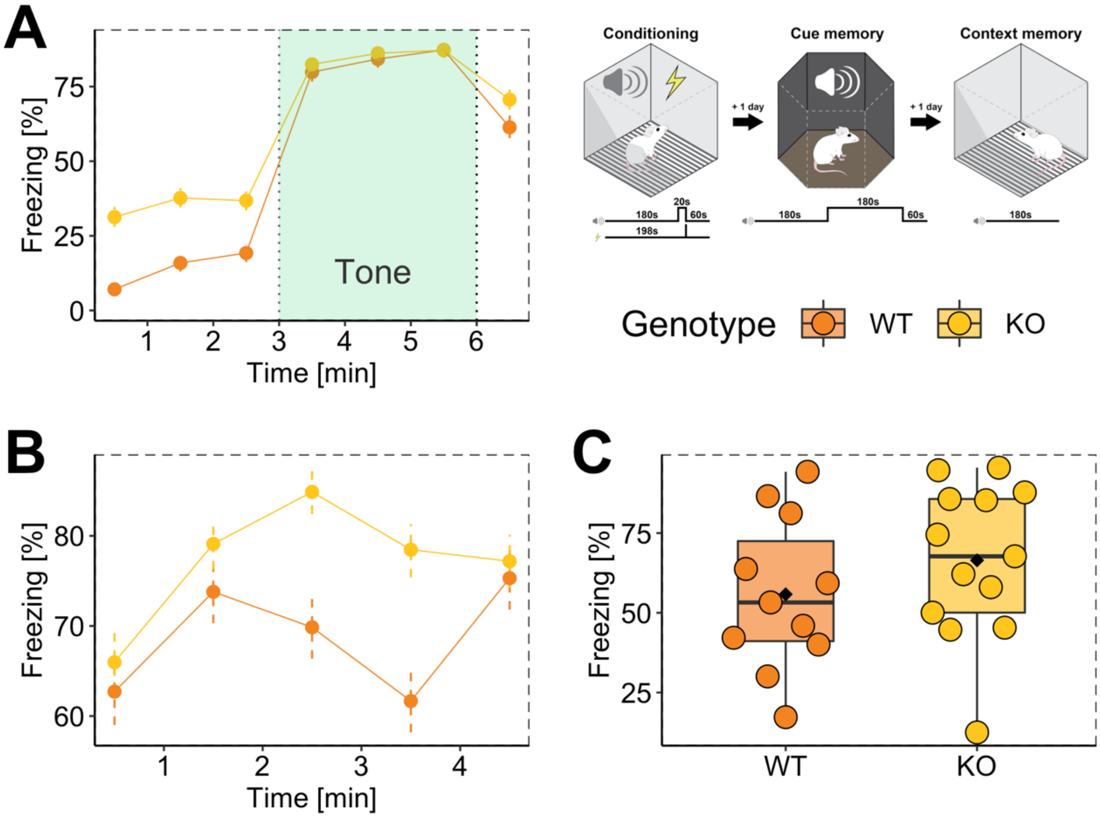

Figure 76: NexCreERT2 YTHDC1 KO animals show normal cue and contextual fear memory
(A) Cue memory, 24 h after conditioning. **(B)** Context memory 48 h after conditioning. **(C)** Mean contextual freezing across 5 min. Individual results are plotted for both genotypes (WT males N = 12, KO males N = 13). No significant difference between the two genotypes was determined.

While the data presented in Figure 76 might be suggestive of genotype driven differences, no significant difference is apparent in the statistical analysis. This is due to a high degree of variability in the recorded responses, as can be seen in Figure 76C. Initially, it looked like there might be a difference in the freezing during the habituation phase of the cue memory test. Freezing in a novel context can be indicative of fear generalization[203]. However, the differences seen here did not replicate in an independently tested cohort (data not included in this thesis).

5. Discussion

Previous research investigating the role of m^6A in the mammalian brain has focused on a limited number of key regulators, including METTL3[28,29], METTL14[26,150], FTO[28,146–148] and YTHDF1[30]. The contribution of WTAP and YTHDC1 to brain functioning has not been reported so far.

Therefore, the aim of this study is to provide the first insight into the role of WTAP and YTHDC1 in the regulation of adult brain functions. To achieve this, a detailed characterization of WTAP and YTHDC1 deficient animals was conducted, addressing the effect the KO has on different organizational levels of the brain. The molecular data collected for this study include a poly-(A) sequencing of dCA1 samples, label-free LC-MS measurements of the proteome in the mPFC, dHPC and vHPC and a targeted metabolic screening across these brain regions. Complementing this, structural MRI scans were acquired to reveal volumetric changes across the brain and electrophysiological recordings in the dCA1 and mPFC were performed to test for KO induced changes in signaling. Furthermore, A broad array of behavioral data sets looking at circadian activity, anxiety-like behavior, learning and memory was collected to reveal how the KO affects cognitive processes. Together, this multi-level experimental approach provides the first insight into the non-redundant role of WTAP and YTHDC1 in shaping adult brain functions.

In this section, I will briefly summarize and discuss the main results presented in this thesis within the context of the literature, assess how the presented findings expand the existing knowledge and suggest further areas of study.

5.1 Considerations regarding the targeted KO of m^6A regulators in the brain

In the presented research the Cre-lox recombination system was used to establish cell-type specific KOs in the brain of *Wtap* and *Ythdc1* floxed animals. For this, two different Cre driver lines were used. The developmentally regulated Camk2aCre, which starts inducing a KO around the 3rd postnatal week[149,187], when most of brain development has concluded[188], and NexCreERT2 which is tamoxifen inducible[151].

The rational for using a cell-type specific, postnatal deletion (conditional), instead of a global KO (constitutive), is twofold. First, many m^6A regulators are essential for early embryonic development and the full KO of WTAP and YTHDC1 has been reported to result in early embryonal lethality[64,65,72]. m^6A is required for normal brain development, as disturbances in m^6A patterns resulted in the premature differentiation of neuronal precursor cells[27] and prolonged postnatal cortical neurogenesis[26]. The postnatal deletion using a cell-type specific KO has the advantage that developmental effects can be minimized and the observed changes can be attributed to alterations in defined populations of cells, namely Camk2aCre/NexcreERT2 expressing neurons.

Secondly, it is important to note that findings obtained in constitutive KOs often differ from conditional deletions, due the effects constitutive KOs have on organismal development and the global nature of the depletion. An example for this is the constitutive KO of FTO which has been reported to result in increased anxiety-like behaviors[204]. In contrast, studies using conditional FTO KOs, targeting specifically the brain, did not find effects on anxiety-like behaviors[28,146]. Here we are interested in the contribution of WTAP and YTHDC1 to regulating the function of post-mitotic neurons in the adult brain. To avoid developmental driven effects and to compare our findings with previous studies targeting the brain, two Cre driver lines were chosen that allow the targeted depletion at postnatal stages.

Despite this precaution, both Camk2aCre induced KOs lines presented with genotype dependent differences in juvenile weight, shortly after the onset of Camk2aCre activity. This could indicate an effect of the KOs on late stages of brain maturation. Notably, no difference in the weight of pups was determined prior to the onset of the KO in either line (weight at P15: data not shown). Considering that the KO is restricted to the brain, the differences in weight might be due to KO induced changes in feeding behavior. In support of this, it was previously shown that the Camk2aCre driven depletions of transgenes in the brain may result in metabolic phenotypes associated with changes in body weight[205,206]. However, this was not systematically investigated here. Interestingly, the observed differences were more pronounced in males which suggests a sex-specific component that could be explored by future studies.

Since both Cre drivers employed in this research affect the expression of target genes within a rather large part of the brain, future studies using more targeted approaches, such as viral manipulations or more specific Cre lines, will be required to attribute the observed changes to specific brain areas.

5.2 WTAP is essential for regulating neurons and behavior

WTAP KO induced changes in gene expression

To determine the effect of WTAP depletion on neuronal gene expression, a poly-(A) sequencing of dCA1 samples from WT and KO animals was performed. The depletion of WTAP in the dCA1 was shown to result in the differential expression of thousands of genes, with 58 % of transcripts being upregulated in WTAP KO animals and 42 % being downregulated. The observed changes in gene expression were surprisingly consistent across biological replicates and the qPCR validation of selected candidates, performed in an independent cohort of animals, validated the observed differences regarding effect size and statistical robustness. This suggests that WTAP is integral to the regulation of gene expression.

A previously published study using a NexCreERT2 induced KO of METTL3 reported only very little differences in gene expression (84 genes: FDR < 0.1, Log2FoldChange ≥ 0.5). This is surprising, considering that both WTAP and METT3 depletion have been shown to induce changes in the expression of hundreds of genes *in vitro*[37] and could point towards a difference between these two regulators in the regulation of gene expression in the adult brain.

Given that one of the ascribed functions of m^{6}A is to regulate mRNA turnover[124], with m^{6}A serving as a mark for degradation, disruptions of the m^{6}A ‘writer complex’ are expected to increase the half-life of commonly methylated transcripts. Consequently, the upregulation of mRNAs as a result of WTAP depletion could partially be attributed to an attenuated mRNA decay. A limitation of the presented study is that the extent to which m^{6}A status determines gene expression and splicing has not been investigated. To address this, the m^{6}A landscape of the dCA1 could be characterized using m^{6}A-seq. and the observed changes in gene expression and splicing correlated with the presence of m^{6}A marks.

Considering that ~40 % of the observed changes are attributed to significantly downregulated transcripts, an impairment of mRNA degradation due to the depletion of m^{6}A is not sufficient to explain all results. Therefore, some of the observed changes might be attributed to other regulatory processes. In support of this, WTAP is known to interact with various cellular proteins such as WT1[61] VIRMA, RBM15, HAKAI and ZC3H13 and to be part of the MACOM complex, which has been suggested to be involved in m^{6}A-independent regulation[44]. The extent to which WTAP is affecting gene expression through m^{6}A-independent mechanisms remains to be determined. While the main finding of the gene expression characterization is that WTAP is crucial for normal expression levels of thousands of transcripts, a limitation of the presented results is that the reported changes are observational and the mechanisms underlying the observed changes remains to be determined by future studies.

WTAP controls the expression of m^{6}A 'writers' and 'readers'

A novel finding presented in this research thesis is that the depletion of WTAP alters the expression levels of key m^{6}A regulators. Specifically, the gene expression for the core-complex members *Mettl3* and *Mettl14* was found to be slightly but significantly downregulated in the sequencing, while components of the MACOM complex (*Rbm15*, *Virma*, *Zc3h13*) were found to be significantly upregulated. For the YTH-domain containing m^{6}A 'readers', a strong upregulation of *Ythdc1*, *Ythdf1/2* were detected and more subtle but significant regulations of *Ythdf3* and *Ythdc2*.

Previously published *in vitro* experiments manipulating the protein abundance of METTL3, showed that aberrant METTL3 levels alter WTAP expression[68], while another study using siRNA to knock down METTL3 and WTAP failed to detect reciprocal regulation[37]. Furthermore, a previous characterization of METTL3 KO in the adult mouse brain did not report any changes in the expression of m^{6}A regulators[28]. Considering these reports, the experiments carried out as part of this thesis are the first to demonstrate that WTAP exerts broad regulatory control over many m^{6}A regulators in the adult mouse brain. Furthermore, the changes in gene expression were reflected in large parts in alterations on the proteome level as discussed below.

In addition to the characterization of WTAP KO tissue, the expression of selected candidate genes was assessed in a METTL3-WTAP double KO. Surprisingly, the gene expression of the double KO animals was found to recapitulate the changes observed in WTAP KO animals. This suggests, at least for the selected candidate genes, no additive effect of a double KO. Given that none of the examined genes was reported to be differentially regulated in METTL3 KO brains[28], the observed changes might be entirely driven by the loss of WTAP. To determine how WTAP levels affect the expression of other m^{6}A regulatory genes, additional studies will be required. These could include overexpression experiments to determine the directionality of the regulation and 'rescue' experiments with a WTAP that has a defective m^{6}A core 'writer complex' interaction domain. The latter would provide information about the extent to which WTAP-dependent gene expression regulation depends on its interaction with the m^{6}A machinery.

WTAP KO changes splicing patterns

Among the principal functions that have been ascribed to m^{6}A, the regulation of pre-mRNA processing and specifically splicing stands out[37]. The present study confirmed this for the brain, with the depletion of WTAP resulting in the differential exon usage for over 1,900 genes in the dCA1. Interestingly, only a fraction of differentially expressed genes were also found to be differentially spliced (386 out of 1,889). This suggests that the observed changes in gene expression and splicing are mediated by distinct regulatory mechanisms. Previously, it has been shown that WTAP colocalizes with various splicing factors and regulates the alternative splicing of *Wtap* pre-mRNA[43]. Therefore, it is conceivable that WTAP might also be involved in m^{6}A independent regulation of splicing.

Considering that the temporal control of alternative splicing is essential for neuronal development[207], determines ion channel properties[208,209] and regulates the receptor composition at the synapse[210], the observed changes might affect the synaptic properties of KO neurons. In support of this, a strong enrichment for GO terms involved in regulating synaptic functions were identified among the differentially spliced transcripts. Given the abundance of changes induced by the KO, it will be difficult to disentangle the targeted regulation mediated by WTAP from compensatory effects. However, despite this limitation, this is the first data set to show that WTAP is crucial for regulating alternative splicing in the adult mouse brain.

WTAP shapes total protein abundance and membranome composition

Informed by the observation that differentially expressed genes in the WTAP KO dCA1 are enriched for integral components of the plasma membrane, a targeted analysis of membrane bound proteins was performed, followed by a largescale screening of the proteome in the mPFC, dHPC and vHPC. Considering the overwhelming number of differences that were observed, the results presented in this thesis focus on differences in respect to selected synaptic cell adhesion molecules, m^{6}A regulators and mitochondrial proteins.

For the membranome analysis, 216 proteins were determined to be altered in abundance in KO animals. Interestingly, many of the regulated proteins were also differentially expressed in the poly-(A) sequencing and a significant correlation ($R = 0.64$, $p < 0001$) of differences in mRNA levels and protein abundance was determined. This fits with previous studies, reporting a ~ 40-80 % accordance between mRNA and protein levels at steady state conditions[127]. Among the top regulated proteins were several synaptic adhesion molecules that are essential for the development and maintenance of synapses. Specifically, LRFN1 (SALM2) and LRFN2 (SALM1), which were significantly upregulated in KOs, have previously been reported to interact with PSD95 *in vitro*[211] and to promote the surface expression and clustering of NMDA receptors (SALM1, SALM2)[212] and the recruitment of AMPA receptors (SALM2)[211]. Both proteins have been shown to be involved the development and maturation of excitatory synapses[211,213], with an overexpression promoting neurite outgrowth *in vitro* and a depletion resulting in a reduction of neurite outgrowth[214]. Considering their interaction with AMPA and NMDA receptors, LRFN1 and LRFN2 could potentially be involved in the increased LTP observed here in WTAP KO animals. This could be systematically tested with ‘rescue’ experiments that restore the WT levels of either protein using siRNA. Another synaptic adhesion molecule that was significantly upregulated is Slitrk3, which selectively promotes inhibitory synapse development[193]. Consistent with the membranome analysis, SALM and SLITRK family members were also found to be differentially regulated across regions in the bulk analysis and the poly-(A) sequencing, supporting the idea that the depletion of WTAP might affect synaptic connections and neuronal morphology. Based on the presented findings, it would be interesting to determine whether the alteration of SALM and SLITRK proteins changes neuronal anatomy and connectivity using the traditional Sholl analysis, or state-of-the-art automatic reconstruction methods of neuron populations[215].

For the bulk screening, 2,924 unique proteins were determined to be differentially regulated across regions in WTAP KO animals. Interestingly, the identity of differentially regulated proteins differed greatly between regions with only about 9 % of commonly regulated proteins.

Corroborating the results from the gene expression analysis, the proteomic screening provides further evidence that the depletion of WTAP alters the expression levels of key m^{6}A regulators. Surprisingly, FTO, for which no difference in gene expression had been observed, was found to be significantly upregulated in the mPFC, dHPC and vHPC, while Virma showed a pronounced downregulation despite increased mRNA levels. These observations provide the first evidence that WTAP affects the gene expression and protein abundance of essential m^{6}A regulators in the brain.

The GO analysis performed with the results from the bulk tissue screening revealed a clear enrichment of downregulated proteins for mitochondrial processes, compartments and functions. Strikingly, this enrichment was present across regions, with the most consistent changes being observed in the mPFC.

Two topics emerging from the pathway analysis were the mitoribosomes and the respiratory chain complex. For both, a pronounced downregulation of critical components was observed with the strongest changes being associated with complex I (NADH-dehydrogenase). In contrast, very few changes were detected in respect to mitoribosomes and the respiratory chain complex in YTHDC1 KO tissue. Fitting these findings, the metabolic screening revealed a depletion of NAD^+ across regions in WTAP KO animals (discussed below). In contrast, no differences in NAD^+ levels were determined for YTHDC1 KO animals.

Interestingly, very little is known about the role of m^6A for mitochondrial functions. Previously, it has been suggested that the depletion of FTO attenuates mitochondrial biogenesis in skeletal muscle cells *in vitro*[216]. On the other hand, another study reported that the *in vitro* overexpression of FTO reduces the mitochondrial content in immortalized liver cells[217]. Furthermore, the yeast orthologue of METTL3 Ime4 has been suggested to be important for mitochondrial functioning, with the depletion of Ime4 resulting in decreased activity of the cytochrome c oxidase and mitochondrial fragmentation[218]. While these studies suggest a role of m^6A in regulating mitochondria *in vitro*, to the best of my knowledge, no studies investigating this *in vivo* have been published. Therefore, the results presented in this thesis provide the first evidence that WTAP and m^6A might be essential for the regulation of mitochondrial functions in the adult brain.

The presented findings suggest fundamental changes in mitochondrial function with most likely far-reaching consequences for the neuronal energy metabolism. However, considering that all of the significantly regulated mitochondrial proteins are downregulated, this could also point towards oxidative stress and mitochondrial damage. Therefore, it is important to determine whether mitochondria are selectively impaired in their function or non-specifically damaged. To assess mitochondrial functions, the seahorse assay of oxygen consumption rate is currently considered the gold standard. Together with a morphological characterization using electron microscopy, these questions could be addressed adequately.

WTAP is required for maintaining metabolic homeostasis

The proteomic characterization revealed a pronounced dysregulation of mitochondrial proteins. Considering that mitochondria are essential for the production of energy through the respiratory chain complex and the regulation of the cellular metabolism, it was hypothesized that the dysregulation of mitochondrial proteins would be reflected in the metabolic profile of WTAP KO animals. To test this systematically, a targeted metabolic screening of mPFC, dHPC and vHPC samples was performed.

Overall, 33 unique metabolites were identified with differing levels in the brains of KO animals. Strikingly, a high degree of accordance was observed for the most up- and downregulated candidates. Across brain regions early glycolysis products showed the strongest upregulation (glucose-1-phosphate, glucose-6-phosphate, fructose-6-phosphate). This fits with the observation that the glycolysis enzyme hexokinase (HK1) was detected to be downregulated in the brain of KO animals.

Interestingly, it has been reported previously that the levels of the m^6A demethylase FTO are regulated in accordance with glucose levels. Specifically, it was shown in mice that fasting is associated with a decrease in *Fto* expression, while glucose treatment is associated with an increase[58]. Consistently, in patients diagnosed with type 2 diabetes, high glucose levels were associated with elevated FTO protein levels[59]. Fitting these results, a pronounced upregulation of FTO in all three brain regions was observed while no differential regulation for the m^6A demethylase ALKBH5 was detected. Whether there is a causal relationship between FTO abundance and the upregulation of early glycolysis products remains to be determined. However, the fact that variants of *FTO* have been associated with body mass index and the risk for obesity[33,34] supports the idea that FTO is involved in regulating carbohydrate metabolism.

Among the significantly downregulated metabolites, NAD^+ showed the strongest downregulation across regions. NAD^+ is a universal cofactor used for the transfer of electrons from one molecule to another and required for the catalysis of redox reactions. Therefore, NAD^+ is essential for many metabolic processes including glycolysis, fatty acid oxidation, citric acid cycle and oxidative phosphorylation and ATP production. Dysregulations of NAD^+ levels have been associated with cancer, aging and neurodegenerative processes[219–221]. Fitting to the overall reduction in NAD^+ levels, we observed a significant downregulation of components of the NADH-dehydrogenase (complex I), which catalyzes the transfer of electrons from NADH to coenzyme Q (ubiquinone). Previously, the functional defect of complex I has been shown to result in reduced NAD+ levels[222]. Therefore, the reduction in NAD^+ might be the result of mitochondrial dysfunction. Considering that NAD^+ is required for the conversion of glyceraldehyde 3-phosphate to 1,3-bisphosphoglycerate, the depletion of NAD^+ might also explain the accumulation of early glycolysis products.

Overall, the results from the metabolic screening indicate that WTAP is required for regulating the energy metabolism and specifically the maintenance of physiological NAD^+ levels. Considering that the presented results are purely descriptive, no causal claims can be made, and additional experiments are required to determine whether the observed changes are due to mitochondrial defects. A limitation of the presented analysis is that the targeted screening of metabolites is restricted to a small number registered in the library. There are most likely many more differences that we were not able to detect and which an untargeted metabolic screening could help to identify.

Camk2aCre WTAP KO changes gray matter volume in the thalamus and auditory cortex

Camk2aCre WTAP KO animals underwent structural MRI scans to determine whether the observed molecular changes alter the architecture of the brain. Based on the Camk2aCre expression, it was hypothesized that structural changes would most likely be observed across the cortex and HPC. Surprisingly, WTAP KO animals showed a bilateral, locally restricted, increased gray matte volume in the thalamus and reduced gray matter volume in the auditory cortex. While the auditory cortex is targeted by Camk2aCre, no recombination was determined for the thalamic neurons using Ai9 reporter mice.

The thalamus is considered an important relay station and crucial for integrating sensory information. Except for olfaction, all sensory information is processed by the thalamus before being transmitted to the primary sensory areas in the cortex[223]. Primary sensory cortical areas in turn project to other cortical areas, as well as higher-order association nuclei in the thalamus, which transmit the information to higher order secondary sensory areas in the cortex[224]. This is illustrated in Figure 77. For example, the ventral division of the medial geniculate nucleus (MGN, the auditory thalamus) receives auditory input from the inferior colliculus residing in the brainstem and projects to the primary auditory cortex[225,226]. Fibers from the primary auditory cortex innervate the dorsal division of the MGN (feedforward and feedback), which in turn projects to secondary auditory areas in the cortex[224].

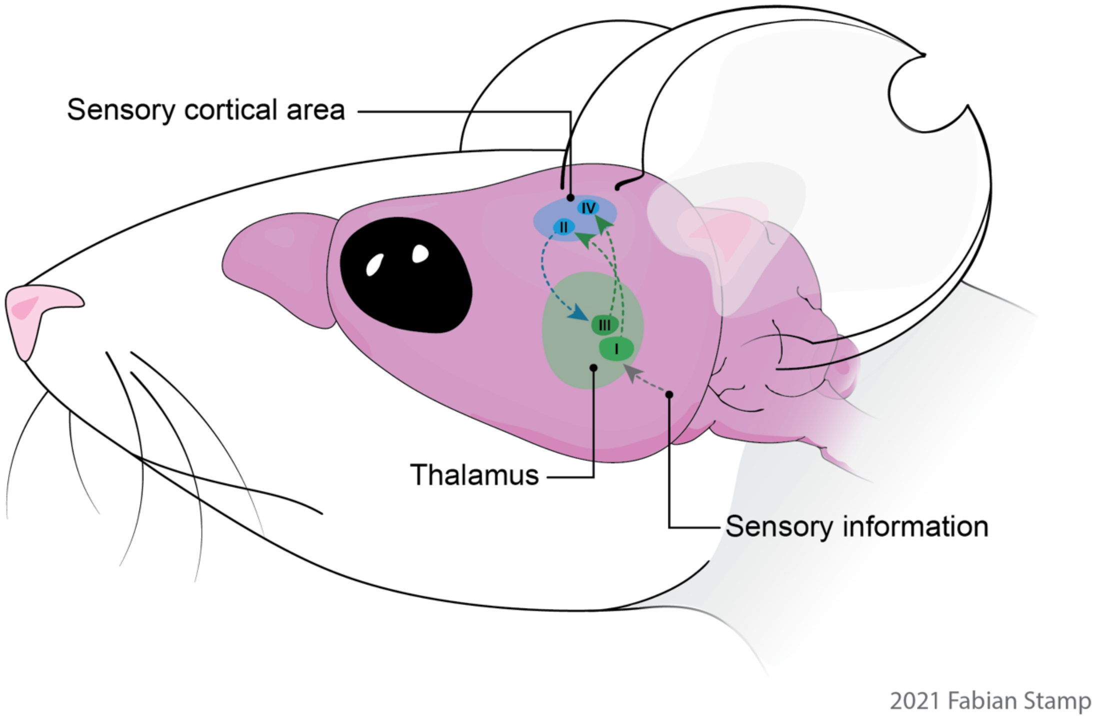

Figure 77: Thalamocortical and corticothalamic connectivity in the mouse brain
The thalamus is a relay station for all ascending sensory information, except olfaction. Thalamocortical projections (I) transmit sensory information to the primary sensory areas in the cortex where the information is processed (II). In turn feedback and feedforward projections from the primary sensory area connect to the higher-order thalamic areas where information is further processed (III) and forwarded to secondary sensory areas in the cortex (IV).

In the Camk2aCre-Ai9 expressing reporter mouse line the feedforward and feedback projections from cortical areas to the thalamus were clearly labelled. Consequently, KO driven alterations in the activity of corticothalamic projection neurons may explain the observed changes in the gray matter volume of the thalamus.

Considering that animal behavior is directed by sensory experiences, changes in thalamocortical and corticothalamic processing are expected to alter the behavioral output to sensory driven stimuli such as light or sound. Therefore, the differences observed in the DL test (discussed below) might be indicative of increased light sensitivity due to alterations in sensory processing. In support of this idea, the stimulation of the posterior thalamic nucleus has been shown to induce photophobic behavior, while anxiety-like behaviors remained unchanged[227].

In addition to sensory processing, the thalamus is also involved in the regulation of wakefulness and sleep rhythms[228–230]. Thus, the differences in arousal level in the EPM test, as well as the alterations in circadian activity might be caused by alterations in thalamic processing.

The results presented here are descriptive and functional experiments will be required that test these hypotheses. In this respect, the functional integrity of auditory thalamocortical and corticothalamic auditory circuitry could be tested using pre-pulse inhibition (PPI) of the acoustic startle response, which involves the medial geniculate nucleus and the reticular nucleus of the thalamus[231,232]. Furthermore, to determine the contribution of the thalamus to alterations in wakefulness and circadian activity, electroencephalogram (EEG) recordings in freely moving mice might provide insight into altered brain rhythms[233].

Camk2aCre WTAP KO alters circadian activity

The observation of animals within their home cage environment, using infrared activity sensors, revealed a disrupted circadian activity in Camk2aCre WTAP KO animals. WTAP deficient animals showed an overall increase in nocturnal activity and decrease in activity during the light phase. Most interestingly, the activity pattern of KOs did not follow the sinusoidal pattern that is expected and observed in the WT littermates. Instead, KOs appear to switch from a state of low activity to a state of high activity (bimodal activity pattern) at the beginning of the dark-phase (Figure 78).

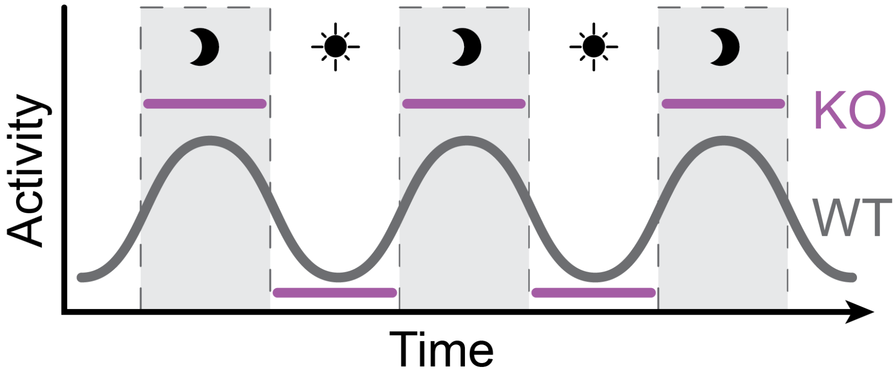

Figure 78: Disrupted circadian activity of WTAP KO animals

Camk2aCre WTAP KO animals show a disruption of circadian activity, with low levels of activity during the day and a switch to a highly active state during the early hours of the dark phase.

Previously it has been shown that, in the liver, m^6A patterns show circadian rhythmicity with increased methylation levels of transcripts during the dark phase[234]. Furthermore, the mRNA of various clock genes has been shown to carry m^6A[235] and mechanistically, m^6A has been suggested to be required for the timely processing of circadian transcripts, with disruptions resulting in processing delays and prolonged circadian periods[235]. Supporting this idea, the *in vitro* depletion of METTL3 was observed to increase the nuclear retention time of transcripts coding for circadian regulators[235]. *In vivo* experiments in which SAM-dependent methylation was inhibited in the SCN, the main regulator of circadian rhythms, resulted in prolonged locomotor activity in mice[235]. Together, these studies suggested that m^6A is essential for the regulation of circadian gene expression.

Investigations of circadian clock genes have shown that the disruptions of single genes can results in aberrant circadian regulation. For example, it was reported that the Camk2aCre driven KO of the circadian clock master regulator Bmal1 in the SCN (> 90 % KO efficacy) abolishes circadian rhythmicity under constant conditions (constant light or constant darkness)[236]. Another study showed that Bmal1 KO animals readily adapt their activity to experimenter controlled changes in the dark/light cycle, exhibiting a ‘switch-like’ adaptation in behavior that resembles the activity observed in WTAP KO animals[237]. Both of these studies highlight that the disruption of a single gene in the SCN can result in aberrant circadian activity.

Given that it has been reported that Camk2aCre can be used to target the SCN[236], the recombination pattern of Camk2aCre-Ai9 animals was examined. However, only a small number of Ai9 labelled cells were located within the area of the SCN. This is possibly the result of differences in the activity and specificity of the Cre driver lines[149,238]. This does not preclude that the observed phenotype involves SCN activity. However, due to the low penetrance, it seems likely that other effects contribute as well.

Considering the established role of m^6A in the regulation of circadian gene expression, and the similarity in the phenotypes of WTAP and Bmal1 KOs, the changes in home cage activity might be due to a disruption in the processing of critical clock transcripts. One way to further interrogate the circadian clock of WTAP KO animals, would be to monitor home cage activity under experimenter-controlled lighting conditions. If the internal pace maker is dysfunctional, it can be hypothesized, based on the discussed experiments, that the activity of KO animals should largely depend on external cues and could be manipulated by alterations in lighting. Lastly, due to the nature of the infrared tracking, animals had to be single-housed. It is well documented that social isolation affects various aspects of behavior in mice[239–241] and therefore future studies will be required to determine whether the observed differences are holding true in a social context. Furthermore, as discussed above, differences in the thalamus mediated regulation of the arousal and sleep might be causally involved and explain some of the observed differences.

WTAP KO results in aberrant behavior in classical anxiety tests

The characterization of locomotion, exploratory drive and anxiety levels using the OF, EPM and DL tests revealed complex behavioral alterations in WTAP KO animals. While KOs did not differ in their overall locomotion in the OF, they spent significantly less time in the center zone. In the DL test, animals preferred the dark compartment and spent significantly less time in the lit chamber. In contrast, in the EPM test, KOs exhibited increased overall locomotion, showing signs of heightened arousal (hyperlocomotion, hectic abrupt movements etc.) and spent increased time in the open arms. There are several points that need to be taken into consideration when interpreting these results.

First, all of the variables measured in the presented tests are derived from the movement of animals. Basal differences in locomotion are known confounds when testing animal behavior[242] and thus can interfere with the interpretation of locomotor-based tests. Regarding WTAP KOs, differences in the circadian activity and an overall increased locomotion in the EPM were observed. However, no difference in locomotion was detected in the OF. This suggests, that the observed changes in activity depend on the context and, with this possibly, on the arousal level. To determine differences in arousal during classical tests, defecation has previously been used as a proxy for corticosterone levels[243]. The defecation of animals during the OF was noted but no striking differences were observed.

Secondly, the interpretation of the OF, EPM and DL results as indicative of anxiety-like behavior is based on the observation that some anxiolytic drugs such as benzodiazepines change the performance in these tests[160,189,244]. However, it is important to note that alterations in sensory processes can affect animal behavior in a way that mimics behavioral phenotypes of anxiety. For example, blindness has previously been shown to resemble a low-anxiety phenotype in the EPM[201]. Similarly, an increased sensitivity to light can result in changes in the DL test irrespective of anxiety levels[227].

Considering, that the results from the OF, DL and EPM tests that are presented here do not exhibit a coherent picture, further tests are required to distinguish sensory-motor changes from differences in emotionality. Given the volumetric changes in the thalamus it is conceivable that various aspects of sensory processing are altered in KO animals and as a result affect behavioral readouts in the presented tests. In this respect, it has previously been shown that stimulation of the posterior thalamic nuclei results in light aversive behaviors while anxiety levels remain unchanged[227]. To address this, a systematic assessment of various sensory processes would be recommended. Specifically, to distinguish photophobia and anxiety, a systematic variation of the light intensity in the DL test has been used to test for differences in light sensitivity[245]. Furthermore, a test of visual acuity could be performed with the visible platform training, as conducted for the YTHDC1 KO animals.

Finally, within the research field of m^{6}A, no anxiety-like phenotypes have been reported for conditional KOs targeting the postnatal brain[28–30,146]. Behavioral phenotypes resulting from the conditional manipulation of m^{6}A regulators in the mouse brain have been reported to be subtle and mostly associated with learning and memory[28–30,146]. The results discussed above are, to the best of my knowledge, the first evidence for changes in sensory-driven and/or anxiety-like behaviors as a consequence of a postnatal deletion of a m^{6}A regulator in the mouse brain.

dCA1 WTAP KO alters neuronal activity but does not impair learning

The presented tests assessing learning and memory did not find differences in the cued and contextual FC and MWM test for animals with a depletion of WTAP in NexCreERT2 expressing neurons. In contrast, previous studies investigating the role of m^{6}A regulator proteins in the dHPC, reported that a depletion of METTL3 or YTHDF1 results in learning deficits and an attenuated LTP[29,30]. This study was not able to corroborate these findings and also did not find any differences in WTAP-METTL3 double KO animals. Interestingly, a significantly increased LTP was detected in the dHPC of NexCreERT2 WTAP KO animals. This could be the consequence of changes in the levels of AMPA and NMDA interacting surface molecules such as SALM and SLITRK family proteins that were observed in KO animals. Furthermore, significantly increased levels of the NMDA receptor agonist D-aspartate were observed in the mPFC, dHPC and vHPC of WTAP KO animals. Given that D-aspartate has previously been reported to enhance HPC-dependent LTP and compensate age-related impairments of synaptic plasticity in mice[246,247], the increased availability of this NMDA receptor agonist might be involved in the observed enhancement.

Lastly, considering that WTAP has been suggested to be involved in m^{6}A independent regulatory functions[44], the observed differences might be explained by a mechanism that has yet to be determined. Future studies using tools of increased sensitivity will be required to disentangle the individual contribution of m^{6}A regulators to learning and memory. A graphical summary of the main findings from the characterization of WTAP KOs is shown in Figure 79.

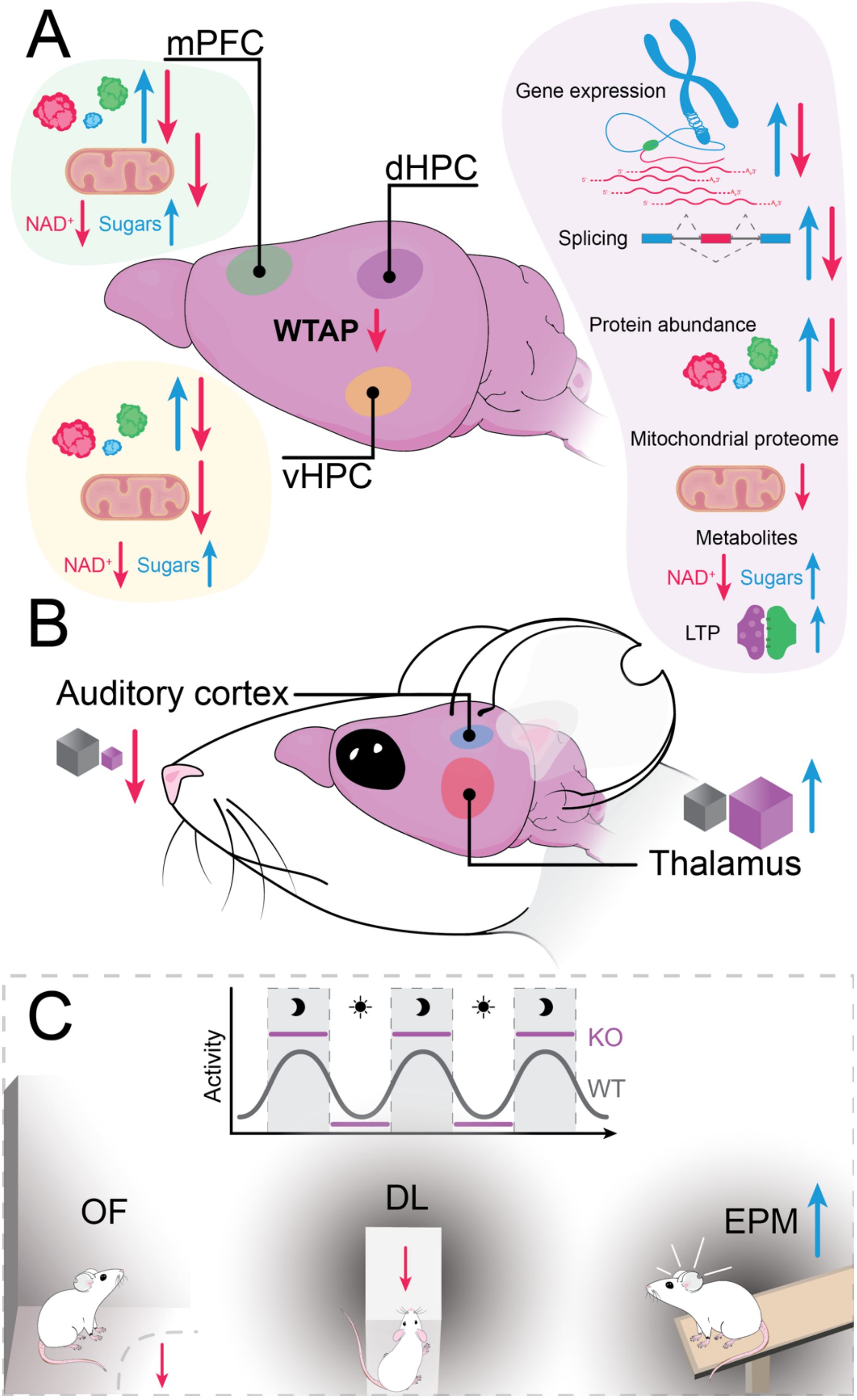

Figure 79: Graphical summary of the main findings from the characterization of WTAP KOs

(A) WTAO KO animals show pronounced changes in gene expression and splicing in the dCA1. The proteome of KO animals was drastically altered in the mPFC, dHPC and vHPC with mitochondrial proteins being overall downregulated. A differential regulation of metabolites was determined, with NAD$^+$ being significantly downregulated and sugars upregulated in KO animals. These changes affect neuronal activity which is reflected in an increase in LTP in the dHPC **(B)** KO animals show structural alterations in the brain as assessed by MRI. The gray matter volume in the thalamus of KOs is increased while the volume in the auditory cortex is decreased **(C)** KO animals show disrupted circadian activity, increased anxiety-like behavior in the OF, prefer the dark compartment in the DL and exhibit signs of hyperactivity in the EPM.

5.3 YTHDC1 is essential for adult survival and regulates brain functions

YTHDC1 regulates female reproductive success

When maintaining floxed Cre lines, it is important to consider the occurrence of selective germ line recombination, which can present with varying prevalence in the sexes. Specifically, for the Camk2aCre line used in this study[149] a germ line recombination efficacy of ~16 % in males and ~ 6 % in females has been reported[248]. However, internally we observed a recombination rate of > 90 % with the Camk2aCre kept in males. Therefore, for the purpose of this study, Camk2aCre was kept hemizygous in females only (+/Cre). In addition, each animal was genotyped for the WT, floxed and deleted allele.

For the *Ythdc1*-Camk2aCre line, it was observed that double floxed (lox/lox) Camk2aCre carrying females (i.e., YTHDC1 brain KO animals) do not breed well. In contrast, heterozygous floxed (+/lox, Cre/+) females bred normally. Interestingly, KO females did not appear to be infertile, given that about 50 % of breeding attempts gave rise to pregnancies that were carried to term. However, an overall impairment of breeding success was apparent, since only 13 % of breeding attempts resulted in litters that were weaned. Considering the prevalence of seizures and the overall changes in behaviors that are reported in this study, the attenuated breeding success might be the result of changes in female reproductive behavior. Since the breeding of experimental cohorts was conducted at the Max Planck breeding facility, a detailed study of mating behavior and maternal care taking was not possible. This is an interesting area that could be explored by future studies and for which, to the best of my knowledge, no m^{6}A related phenotypes have been described so far.

The postnatal loss of YTHDC1 in the brain results in seizures and premature death

Across cohorts of *Ythdc1*-Camk2aCre animals, an unexpected high number of sudden deaths was observed. The onset of sudden deaths appeared to be around the 10-12th week with animals having only a 50 % chance to become older than 4 months. This impairment of survivability was observed in both males and females, with no apparent difference in the survival rate of either sex. The term ‘sudden death’ is used purposefully here, since the majority of monitored animals did not show signs of suffering or behavioral impairments the day before. The post-mortem examination of animals that succumbed to sudden death did not find gross morphological differences in the organs or brain. A small number of observed KO animals presented with a sudden, rapid reduction or gain in weight as well as abnormal behavior. These animals were immediately sacrificed. Only in females, several KO animals exhibited pathological self-grooming, resulting in facial injuries. Close monitoring of this mouse line revealed that some KO animals develop spontaneous seizures in adulthood (> 8 weeks). Seizures appeared to sometimes manifest as an escalation of repetitive grooming behavior and were often followed by complete stiffness (tonic-clonic). Animals succumbing to seizures recovered within minutes and in many cases presented as ‘phenotypically normal’ on the next day. While most of the observed seizures appeared to occur at random, some of them were observed shortly after changing the cage or handling. It is likely that there is a connection between the seizures and sudden death, although this could not be confirmed during observational periods.

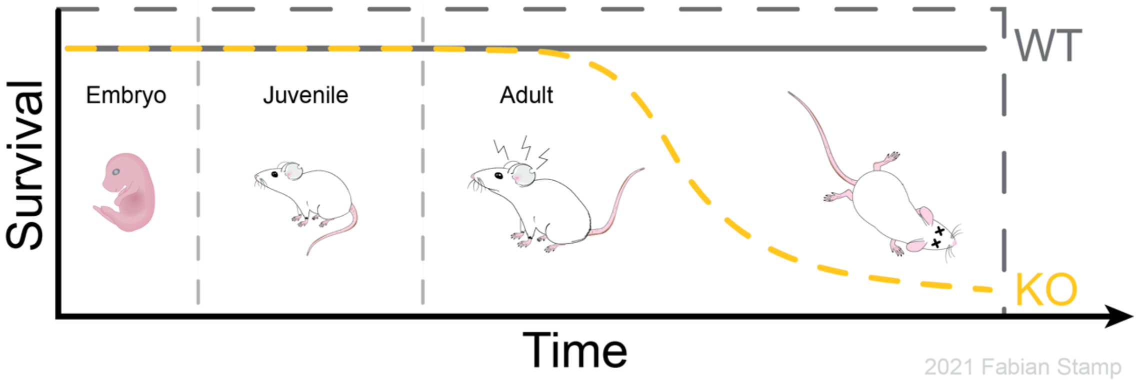

Figure 80: Unexplained sudden death in adult YTHDC1 KO animals

Camk2aCre YTHDC1 KO animals show reduced survivability in adulthood. KO animals show a normal development and no obvious health impairment throughout adolescence. In early adulthood sporadic seizures and unexplained sudden death were observed.

Sudden death has previously been associated with epilepsy in humans, affecting an estimated 0.1 % of adults diagnosed with epilepsy each year[249]. Interestingly, a major risk factor for sudden unexpected death in epilepsy is the occurrence of tonic-clonic seizures such as the ones observed in YTHDC1 KO animals. Mechanistically, it has been suggested that seizures can result in an irreversible wave of depolarization within brain stem areas controlling respiration resulting in cardiorespiratory arrest[250]. Patients experiencing 3 or more seizures per year have been reported to have a 15-fold increased risk for sudden death[249]. This supports the idea that YTHDC1 KO induced seizures are connected to the increased incidence of sudden death. Among the genetic factors that have been associated with seizures and epilepsy are various potassium[251] and sodium channels[252]. Interestingly, a marked dysregulation in the protein abundance of several risk factors was observed in YTHDC1 KO animals. Most prominently, the risk associated potassium channels KCNQ2, KCNQ3 as well as the sodium channel SCN1A and the risk associated ubiquitin ligase UBE3A[202] were dysregulated in the brains of KO animals. However, given that hundreds of proteins are significantly altered in their abundance (including many other channel proteins), this study was not able to determine the causative involvement of single candidates. More research will be required to determine which of the observed changes are causally involved.

Another area that has not been explored, is the overall sensitivity of KO animals to seizures. It would be interesting to determine whether KO animals are generally more sensitive to the induction of seizures. This could be for example tested by injecting animals with a low dosage of kainic acid, followed by manual scoring of the behavior[253]. In humans, EEGs are an important tool for the monitoring and diagnosis of epileptic seizures. Therefore, small wire-less devices such as the NeuroLogger could be used to monitor the occurrence of seizures in freely moving animals[233] and provide detailed information about the occurrence of seizures.

Previously published research manipulating the abundance of m^{6}A regulators in the adult brain did not report seizures and sudden death in KO animals[28–30,138,146,147]. A recent study that employed a comparable Camk2aCre driven KO to deplete METTL3 reported only subtle learning and memory deficits[29]. The fact that the other line investigated in this thesis (Camk2aCre-*Wtap)* exhibits normal breeding, health and survival, supports the idea that seizures and sudden death are driven by a YTHDC1 dependent, WTAP/METTL3-METTL14 independent mechanism.

A number of recent studies have shown that YTHDC1 is essential for regulating chromatin structure[27,79–82] through interacting with m^{6}A marks on caRNAs. Interestingly, some of this regulation has been suggested to involve METTL3-independent m^{6}A sites[82], which are possibly installed by a different m^6-methyltransferase. Whether the seizures are mediated by these METTL3-independent m^{6}A sites on caRNAs remains to be determined. Here, future studies could help to elucidate the influence of YTHDC1 KO on chromatin states in the brain through the characterization of chromatin modifications and chromatin status in YTHDC1 KO animals.

YTHDC1 KO induced changes in gene expression and splicing

The effect of the YTHDC1 KO on gene expression was determined using paired-end poly-(A) sequencing. In total, 828 transcripts were detected to be differentially regulated in the dCA1 of KO animals, with 64 % being significantly upregulated and 36 % being downregulated. While considerably less differences were observed than in the WTAP animals, the directionality was comparable (WTAP: 58 % up, 42 % down). Considering the ascribed role of YTHDC1 in mediating the nuclear export of m^{6}A tagged transcripts[76], the pronounced upregulation observed in KO animals, might be the result of increased nuclear retention and decreased cytoplasmic decay of m^{6}A carrying mRNA. Whether this is the case could be investigated by quantifying the m^{6}A content of the nuclear and cytoplasmic fraction.

It has previously been suggested that one of the primary functions of YTHDC1 is the regulation of alternative splicing of m^{6}A carrying transcripts. In support of this, YTHDC1 has been shown to interact with various splicing factors and to promote exon inclusion[73–76]. The results presented in this thesis show, that the depletion of YTHDC1 results in the differential usage of 1,746 exonic features mapping to 1,054 genes. Interestingly, 62 % of the observed changes were associated with a significant downregulation suggesting exon skipping events. This fits the ascribed function of YTHDC1 to promote exon inclusion. Given that exon skipping is only one of several alternative splicing events, this paired-end data could be used in the future for an in depth characterization of various differential splicing events with tools such as rMATS[254] or leafcutter[255]. In terms of functional enrichment, the GO analysis of differentially expressed and spliced transcripts revealed an enrichment for neuronal processes. Specifically, differentially expressed transcripts were enriched for ion channel activity related terms and alternatively spliced transcripts were enriched for transcripts associated with the synaptic compartment. Interestingly, very little overlap was detected between the differentially expressed and spliced genes. This suggests that YTHDC1 is involved in the regulation of two distinct pools of transcripts, possibly through its involvement in nuclear export and splicing. The comparison with the WTAP KO induced changes in gene expression and splicing revealed a large number of specific changes that are only present in one of the two KOs. This supports the idea that WTAP and YTHDC1 are non-redundant in their regulatory functions and provides a starting point for an in-depth analysis of the types of transcripts that are regulated by either factor.

YTHDC1 KO results in a pronounced reduction of many proteins

The LC-MS screening of YTHDC1 KO reported in this thesis showed KO induced changes in protein abundance across the mPFC, dHPC and vHPC. In total, 274 unique proteins were identified with most of the changes being detected in the dHPC and mPFC. Interestingly, the majority of changes (82 %) were associated with downregulation, while only 18 % of the changes were associated with significantly upregulated protein levels. Overall, this trend of increased downregulation is apparent across all three brain regions and differs from the WTAP KO results for which a more balanced differential regulation was observed. Furthermore, while also for the YTHDC1 KO a differential regulation of many mitochondrial proteins was observed, no overall enrichment was apparent in the GO analysis.

In the context of m^{6}A regulation, a global downregulation of proteins after depletion of METTL3 has previously been reported. A study using ^{35}S metabolic labeling, reported that the *in vitro* knockdown

METTL3 results in a ~ 30 % decrease of global protein levels[88,256]. A similar effect was observed upon the *in vitro* knockdown of the cytoplasmic m^{6}A ‘reader’ YTHDC2, which was associated with a 40 % reduction as quantified by pyromycin labelling[88]. In contrast, the depletion of the other cytoplasmic ‘readers’ YTHDF1-3 were reported to have only minute effects on global translation[88].

An interesting question is how the trend towards an upregulation of transcripts (64 % up, 36 % down) fits to the overall decrease in protein abundance. Considering that YTHDC1 has been demonstrated to play a role in the nuclear export of m^{6}A tagged transcripts, with the *in vitro* depletion of YTHDC1 resulting in the nuclear retention of methylated transcripts[76], the depletion of YTHDC1 might affect the number of mRNA templates available for translation in the cytosol. Consequently, an increased nuclear retention of methylated transcripts in YTHDC1 KO cells could result in a decreased translation rate in the cytoplasm. To test this, the predictive ability of methylation status on protein levels could be investigated. Specifically, the methylation status of transcripts coding for the down- and upregulated proteins.

YTHDC1 has recently been shown to be required for the synthesis of rRNA[82] implying a fundamental role in the global regulation of translation. Thus, alterations in YTHDC1 abundance might affect the translation efficiency of ribosomes. The extent to which either of these explanations is applicable in the adult mouse brain, remains to be determined by future studies.

YTHDC1 KOs show altered metabolism in the mPFC and dHPC

The assessment of the metabolome in YTHDC1 KO brains revealed that 17 out of 125 detected metabolites were differentially regulated in the mPFC and dHPC of YTHDC1 KOs. Interestingly, no differential regulation of metabolites was determined for the vHPC. Contrasting these results with the WTAP KO induced changes, considerably fewer differences were detected with less consistency across regions. Importantly, while a few carbohydrates were differentially regulated, no differences in NAD$^+$ levels were detected. This fits the observation that mitochondrial proteins, including those of the respiratory chain, are not as dysregulated in YTHDC1 KOs as they are in WTAP KOs.

D-aspartate stands out as the single metabolite that was differentially regulated in the mPFC and dHPC of YTHDC1 KOs as well as across all investigated regions in the WTAP KO. D-aspartate is an NMDA receptors agonist and involved in the release of luteinizing hormone and growth hormone[257]. Circulating D-aspartate has been shown to be developmentally regulated with high levels during embryonal development followed by a pronounced postnatal downregulation [258,259]. In mice, supplementation with D-aspartate has been reported to increase spine density and dendritic arborization[260], enhance HPC LTP and compensate for age-related deficits in synaptic plasticity[246,247]. The extent to which alterations in D-aspartate levels might contribute to some of the observed changes in neuronal excitability and behavior, remains to be determined by future studies.

YTHDC1 KO results in decreased gray matter volume in cortex and dHPC

For patients, diagnosed with temporal epilepsy, there have been reports of gray matter abnormalities in various brain regions and consistently in the HPC[261–263]. Given the occurrence of seizures and sudden death in YTHDC1 KO animals, a structural MRI scan was conducted to determine whether similar structural anomalies are present. The volumetric analysis of YTHDC1 KO animals revealed a striking reduction in gray matter volume across the prefrontal cortex and in the dHPC. A similar reduction in gray matter volume in the (olfactory bulb, cortex and HPC) has previously been reported in epileptic beagles[264]. Interestingly, the volumetric changes appear to be restricted to areas of Camk2aCre expression. This might suggest that local changes, rather than differences in network activity are responsible. The extent of observed gray matter volume changes could be indicative of atrophy. While the post-mortem investigation did not reveal any gross morphological differences, a detailed histological analysis would be required to determine whether the structural change is associated with apoptosis of KO neurons.

Comparing the YTHDC1 results to the WTAP data set, there appears to be very little overlap between the gray matter volume changes induced by the two KOs. This provides further support for the idea that these proteins are non-redundant in function. Given that these are the first data sets that investigate changes in gray matter volume of m^6A regulator KO animals, there is no point of reference to compare with these results. Future studies investigating the gray matter volume after depletion of METTL3, FTO and other regulators are required to better understand the relationship of the presented results within the context of m^6A.

Impaired neuronal excitability of YTHDC1 KO neurons

To determine whether the seizures and differences in the classical behavior tests are the result of altered neuronal activity, *ex-vivo* patch clamp recordings of layer V pyramidal neurons in the mPFC were performed. While, no differences in the input resistance and resting potential were detected, the rheobase and threshold potential were found to be significantly increased in YTHDC1 KO neurons. Both, the rheobase and threshold potential, are measures of membrane excitability and an increase is indicative of a decreased sensitivity towards stimulation. Furthermore, the AP amplitude was determined to be reduced in KO animals, while the half-width was found to be increased. In addition, the hyperpolarization following an AP showed a decreased undershoot in KO animals.

It is generally accepted that the amplitude and shape of an AP is not determined by the duration and intensity of the incoming stimulus but depends on the biophysical properties of the neuronal membrane. Thus, changes in the AP threshold, amplitude and kinetics depend on the composition and abundance of ion channels. Specifically, voltage gated sodium channels and voltage gated potassium channels are required for the generation and progression of an AP along the membrane. Given the overwhelming number of changes that were observed, particularly in respect to potassium channels, the presented study is not able to pin point the observed electrophysiological changes to any candidates. Future studies would be required to systematically test the involvement of candidates in the observed decrease in excitability.

It is important to emphasize that the electrophysiological recordings presented in this thesis provide only a snapshot insight at an early age. Given that seizures gradually manifest during adulthood it is possible that the decrease in excitability is indicative of an attempt by the system to contain the excitability within a physiological range. Consequently, the emergence of seizures could be the manifestation of a catastrophic event that is the result of this system failing. To address this further, electrophysiological characterizations capturing later time points could provide valuable insights.

YTHDC1 KO modulates behaviors in classical anxiety tests

The behavioral characterization of Camk2aCre-*Ythdc1* animals included an array of classical tests that are used to measure exploration, anxiety-like behaviors and learning and memory. With the exception of the OF test, a striking difference in the behavior of KO animals was observed across tests. For all behavior tests, males and females were used and compared for sex-specific differences.

Different to the WTAP KO animals, YTHDC1 KO animals did not avoid the center zone in the OF. This suggests that YTHDC1 animals do not have increased anxiety levels and supports the idea that YTHDC1 and WTAP are non-redundant in some aspects of their regulatory function. On the other hand, YTHDC1 showed an overall similar response to WTAP KOs in the EPM and DL tests. Specifically, YTHDC1 KO showed a comparable preference of the open arm, as well as elevated levels of activity and avoidance of the lit chamber in the DL test. As discussed above these differences might be the consequences of changes in sensory processing and locomotion. As demonstrated with the visible platform training, YTHDC1 animal can see and navigate towards a landmark. Interestingly, the results from the FC test suggest differences in overall activity when challenged, possibly due to differences in arousal. Taken together, it looks like KO animals show an overall difference in arousal and activity in the FC test and EPM, while avoiding bright areas in a place preference test. In contrast, the behavioral characterization of NexCreERT2 YTHDC1 KO animals did not determine differences in the OF, DL and FC tests. This underlines the importance of comparing the effect of different manipulations. Future studies will be required to determine the specificity of YTHDC1 mediated regulation across different brain areas. The analysis of the classical behavior tests presented in this thesis focused on small number of relevant readouts per test. Considering the complexity of animal behaviors and the multitude of variables that can be analyzed, future studies should continue the characterization and look at more complex behaviors such as those detected with the ‘Social Box’[265].

A graphical summary of the main findings from the characterization of YTHDC1 KOs is shown in Figure 81.

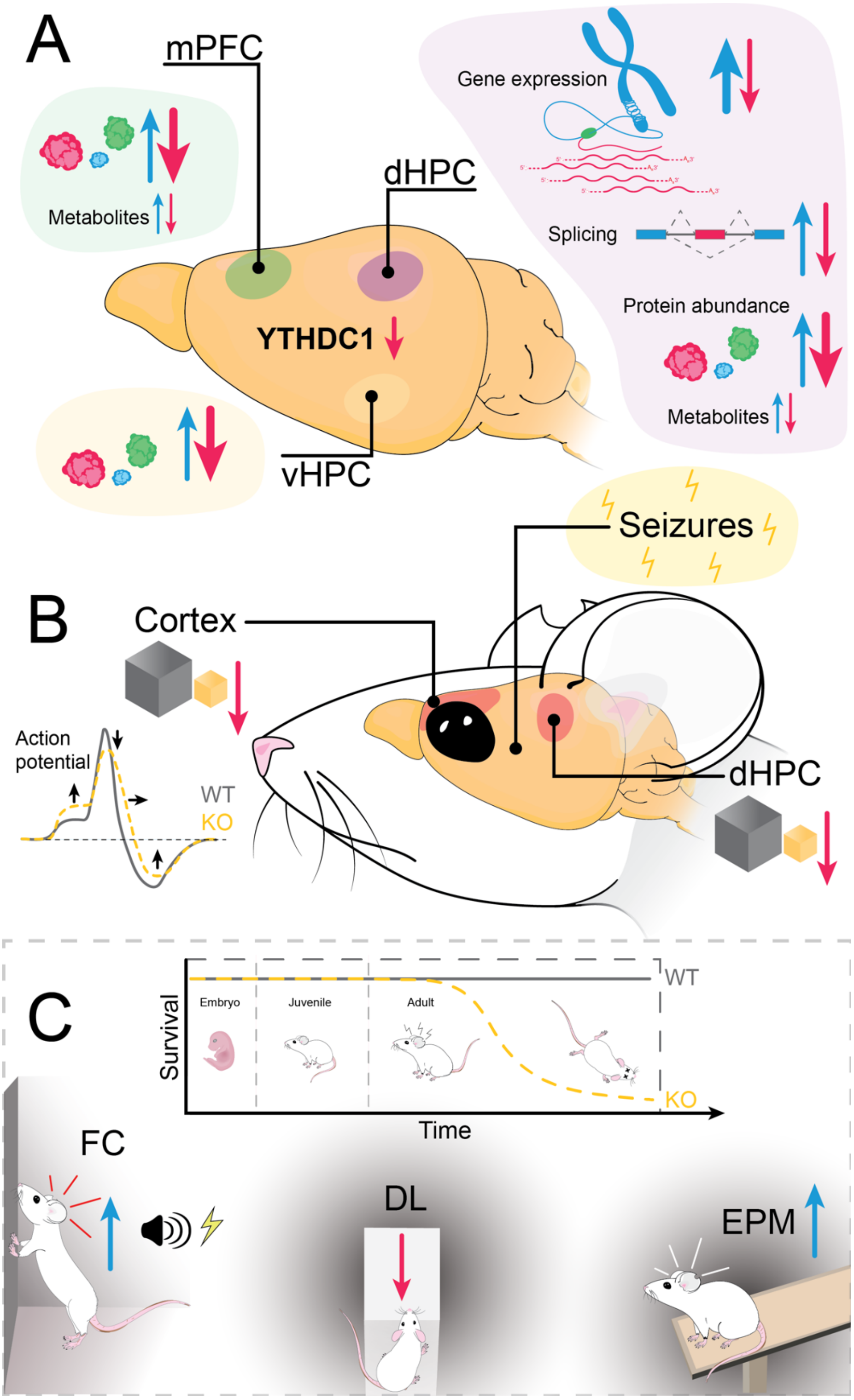

Figure 81: Graphical summary of the main findings from the characterization of YTHDC1 KOs
(A) YTHDC1 KO animals show pronounced changes in gene expression and splicing in the dCA1. The proteome of KO animals was altered in the mPFC, dHPC and vHPC with overall stronger down- than upregulation. Multiple metabolites were differentially regulated in the mPFC and dHPC but not the vHPC. **(B)** KO animals have a decreased gray matter volume in the cortex and dHPC. Basal properties of neurons are changed resulting in less excitability. **(C)** KO animals exhibit seizures in early adulthood and premature death. KO animals freeze less during fear memory retrieval, show increased activity in the EPM test and avoid the lit compartment in the DL test.

6. Conclusion and outlook

In recent years, the contribution of RNA modifications to fine tuning gene expression has attracted increasing interest across biological disciplines. An increasing number of studies suggest that the most abundant internal mRNA modification m^6A plays an important role in regulating neuronal processes[27–30,121,131,138,146–148]. However, research into the involvement of m^6A in the brain has focused on a few m^6A regulators, while the contribution of many other regulators remains undetermined. To date, the role of the m^6A 'writer' component WTAP and the m^6A 'reader' YTHDC1 in the brain has not been reported. Therefore, the aim of this project was to make a substantial contribution to our understanding of these two proteins in the adult mammalian brain.

To this end, this thesis provides a multidisciplinary study that characterizes the effect of WTAP or YTHDC1 deficiency on gene expression, splicing, protein abundance, the metabolism, neuronal signaling, brain anatomy and behavior of mice. The research presented here demonstrates that WTAP and YTHDC1 are non-redundant regulators of mammalian brain functioning.

The experiments conducted for this thesis show that the depletion of WTAP induces a massive shift in transcription and exon usage in the dHPC that has not been observed after the removal of the catalytic m^6A methyltransferase METTL3[28]. The KO-induced changes were shown to be highly consistent across experimental cohorts and predictive of changes in membrane associated proteins. On the protein level, hundreds of alterations were detected across the mPFC, dHPC and vHPC, many of which appear to be region-specific. A striking dysregulation of mitochondrial proteins constituting the mitoribosomes and components of the respiratory chain complex was observed. A metabolic screening revealed a depletion of the cofactor NAD^+ and an enrichment of carbohydrates suggestive of an arrest of glycolysis. The observed disturbances of the neuronal energy metabolism were accompanied by alterations in the circadian activity pattern of KO animals and structural changes in the thalamus and auditory cortex. Interestingly, the targeted deletion of WTAP in the cortex and HPC did not impair learning and memory, as previously reported for METTL3 and YTHDF1[28,29]. Together, the presented results demonstrate that WTAP is an important regulator of gene expression and neuronal functioning. The fact that a depletion of WTAP does not recapitulate the phenotypes that have previously been reported for other m^6A regulators, including impaired learning and a decreased LTP[28,29], suggest that WTAP is involved in METLL3-METTL14 independent regulation.

The direct comparison between YTHDC1 KO and WTAP KO that was done in this thesis suggests a currently unappreciated complexity in the regulatory role of m^6A proteins. Removing YTHDC1 postnatally in the brain impairs the reproductive success of females and results in sudden death in early adulthood. Given that neither of these changes has been observed after the postnatal deletion of METTL3 (Camk2aCre)[29] this might be a METTL3-METTL14 independent phenomenon. The frequent occurrence of seizures in KO animals, which is phenotypically similar to what is observed in epilepsy, is indicative of fundamental changes in the activity of KO neurons. This is reflected in the observed alterations of intrinsic membrane properties and impaired excitability of cells. Depleting YTHDC1 results in a pronounced shift in transcription and splicing that is enriched for neuron specific transcripts. Interestingly, the overlap with the changes observed after WTAP depletion is surprisingly small and suggests a specialization of these regulators. The volumetric changes observed in YTHDC1 KO animals are distinct from what was observed for the WTAP KO, providing further support for their non-redundant function.

There are clear limitations to the conclusions that can be drawn based on the presented results. The characterization presented here is observational and the mechanisms that mediate the observed changes remain elusive. Given the hundreds to thousands of genes that appear to be dependent on

WTAP and YTHDC1 functioning, it remains to be determined which of the observed changes are a direct consequence and which are due to network effects.

The focus of this thesis was to explore the functional consequences of depleting either regulator and the effect on methylation patters were not within the scope of the project. Therefore, the presented research does not address the link between methylation status and mRNA turnover which might explain, at least to some extent, the changes in gene expression and splicing.

The presented work provides a first glimpse into neuronal processes that depend on WTAP and YTHDC1 and raises many more questions for future studies. On the level of gene expression, it remains to be determined to which extend the methylation status under physiological conditions is predictive of splicing events that were observed in KO animals. Further exploration of the YTHDC1 KO paired-end sequencing data could provide insight into which types of splicing events (exon skipping, intron retention, etc.) are dysregulated and whether splicing sites are found in proximity of m^{6}A marks.

The protein screening that was conducted as part of this project, provides the first large scale assessment of changes in protein abundance in post-mitotic tissue, after the depletion of m^{6}A regulators. Given time restrictions, the presented analysis focused on one topic in particular, the alterations in mitochondrial proteins. The overall downregulation of components of the mitoribosomes and respiratory chain complexes raises the questions whether the mitochondria of KO cells are impaired in their physiology. Therefore, it would be interesting to determine the number and morphology of mitochondria using electron microscopy and study the mitochondrial metabolism using a method such as the seahorse assay.

The metabolic data presented in this thesis, provides a starting point for investigating how the changes in gene expression and protein abundance are linked to alterations in brain physiology and behavior. Here, a systematic matching of metabolites to alterations in protein levels would be helpful to identify dysregulated pathways and construct hypothesis for mechanistic studies. For example, it would be interesting to determine whether supplementing NAD$^+$ deficient WTAP KO animals with an NAD$^+$ donor, such as niacin, can ‘rescue’ the aberrant circadian activity observed under home cage conditions.

This thesis provides the first structural MRI data after m^{6}A dysregulation, showing a candidate specific change in the architecture of brain regions. Considering that gray matter volume is determined by various factors such as spine morphology, cell numbers and cell types[266] a histological analysis, could assist in identifying WTAP and YTHDC1 dependent signatures. While the manipulation used for this project is cell-type specific, the induced changes are expected to be diverse, which is something future studies could explore in more detail.

Lastly, the observed alterations in behavior do not recapitulate what has been observed in previous studies targeting METTL3, YTHDF1 or FTO[28,29,138,147]. Surprisingly, WTAP KO animals do not present with memory impairments. Increasing the sensitivity of the employed tools (e.g., MWM with less trials) and overexpression studies could be used to investigate this in more detail. Given that the behavioral tests used for this study heavily rely on locomotion, fundamental changes in spontaneous activity, as observed for the Camk2aCre WTAP KO animals, will limit the interpretation of the reported tests. Further studies will be required to determine whether the observed changes are specific to particular cognitive domains, or due to basal changes in activity. State-of-the-art behavior screening setups such as the ‘Social Box’ could provide a useful tool for future explorations of complex behavioral signatures[265].

In conclusion, this thesis presents the first comprehensive data sets that explore the potential role of WTAP and YTHDC1 in regulating functions of the adult mammalian brain. The presented experiments demonstrate that WTAP and YTHDC1 are non-redundant regulators of neuronal processes and raise many more questions for future investigations.

7. Bibliography

1. Crick F. “On protein synthesis.” *Symp Soc Exp Biol*. 1958;12.
2. Crick F. Central dogma of molecular biology. *Nature*. 1970;227(5258). doi:10.1038/227561a0
3. Moran LA. Basic Concepts: The Central Dogma of Molecular Biology. Published 2007. https://sandwalk.blogspot.com/2007/01/central-dogma-of-molecular-biology.html
4. Breiling A, Lyko F. Epigenetic regulatory functions of DNA modifications: 5-methylcytosine and beyond. *Epigenetics and Chromatin*. 2015;8(1). doi:10.1186/s13072-015-0016-6
5. McCown PJ, Ruszkowska A, Kunkler CN, Breger K, Hulewicz JP, Wang MC, Springer NA, Brown JA. Naturally occurring modified ribonucleosides. *Wiley Interdiscip Rev RNA*. 2020;11(5). doi:10.1002/wrna.1595
6. Mushtaq A, Mir US, Hunt CR, Pandita S, Tantray WW, Bhat A, Pandita RK, Altaf M, Pandita TK. Role of Histone Methylation in Maintenance of Genome Integrity. *Genes (Basel)*. 2021;12(7):1000. doi:10.3390/genes12071000
7. Verdone L, Agricola E, Caserta M, Di Mauro E. Histone acetylation in gene regulation. *Briefings Funct Genomics Proteomics*. 2006;5(3):209-221. doi:10.1093/bfgp/ell028
8. Lister R, Mukamel EA, Nery JR, Urich M, Puddifoot CA, Johnson ND, Lucero J, Huang Y, Dwork AJ, Schultz MD, Yu M, Tonti-Filippini J, Heyn H, Hu S, Wu JC, Rao A, Esteller M, He C, Haghighi FG, Sejnowski TJ, Behrens MM, Ecker JR. Global epigenomic reconfiguration during mammalian brain development. *Science (80-)*. 2013;341(6146). doi:10.1126/science.1237905
9. O’Donnell KJ, Meaney MJ. Epigenetics, Development, and Psychopathology. *Annu Rev Clin Psychol*. 2020;16. doi:10.1146/annurev-clinpsy-050718-095530
10. Carlile TM, Rojas-Duran MF, Zinshteyn B, Shin H, Bartoli KM, Gilbert W V. Pseudouridine profiling reveals regulated mRNA pseudouridylation in yeast and human cells. *Nature*. 2014;515(7525). doi:10.1038/nature13802
11. Charette M, Gray MW. Pseudouridine in RNA: What, where, how, and why. *IUBMB Life*. 2000;49(5). doi:10.1080/152165400410182
12. Safra M, Sas-Chen A, Nir R, Winkler R, Nachshon A, Bar-Yaacov D, Erlacher M, Rossmanith W, Stern-Ginossar N, Schwartz S. The m1A landscape on cytosolic and mitochondrial mRNA at single-base resolution. *Nature*. 2017;551(7679). doi:10.1038/nature24456
13. Dominissini D, Moshitch-Moshkovitz S, Schwartz S, Salmon-Divon M, Ungar L, Osenberg S, Cesarkas K, Jacob-Hirsch J, Amariglio N, Kupiec M, Sorek R, Rechavi G. Topology of the human and mouse m6A RNA methylomes revealed by m6A-seq. *Nature*. 2012;485(7397):201-206. doi:10.1038/nature11112
14. Liu J, Li K, Cai J, Zhang M, Zhang X, Xiong X, Meng H, Xu X, Huang Z, Peng J, Fan J, Yi C. Landscape and Regulation of m6A and m6Am Methylome across Human and Mouse Tissues. *Mol Cell*. 2020;77(2). doi:10.1016/j.molcel.2019.09.032
15. Meyer KD, Saletore Y, Zumbo P, Elemento O, Mason CE, Jaffrey SR. Comprehensive analysis of mRNA methylation reveals enrichment in 3′ UTRs and near stop codons. *Cell*. 2012;149(7):1635-1646. doi:10.1016/j.cell.2012.05.003
16. Fu Y, Dominissini D, Rechavi G, He C. Gene expression regulation mediated through reversible m6A RNA methylation. *Nat Rev Genet*. 2014;15(5). doi:10.1038/nrg3724
17. Perry RP, Kelley DE. Existence of methylated messenger RNA in mouse L cells. *Cell*. 1974;1(1):37-42. doi:10.1016/0092-8674(74)90153-6
18. Desrosiers R, Friderici K, Rottman F. Identification of methylated nucleosides in messenger RNA from Novikoff hepatoma cells. *Proc Natl Acad Sci U S A*. 1974;71(10):3971-3975. doi:10.1073/pnas.71.10.3971
19. Bokar JA, Shambaugh ME, Polayes D, Matera AG, Rottman FM. Purification and cDNA cloning of the AdoMet-binding subunit of the human mRNA (N6-adenosine)-methyltransferase. *RNA*. 1997;3(11):1233-1247.
20. Bujnicki JM, Feder M, Radlinska M, Blumenthal RM. Structure prediction and phylogenetic

analysis of a functionally diverse family of proteins homologous to the MT-A70 subunit of the human mRNA: m6A methyltransferase. *J Mol Evol*. 2002;55(4):431-444. doi:10.1007/s00239-002-2339-8

21. Jia G, Fu Y, Zhao X, Dai Q, Zheng G, Yang Y, Yi C, Lindahl T, Pan T, Yang YG, He C. N6-Methyladenosine in nuclear RNA is a major substrate of the obesity-associated FTO. *Nat Chem Biol*. 2011;7(12):885-887. doi:10.1038/nchembio.687

22. Schwartz S, Agarwala SD, Mumbach MR, Jovanovic M, Mertins P, Shishkin A, Tabach Y, Mikkelsen TS, Satija R, Ruvkun G, Carr SA, Lander ES, Fink GR, Regev A. High-resolution mapping reveals a conserved, widespread, dynamic meiotically regulated mRNA methylation program Schraga. *Cell*. 2013;155(6).

23. Batista PJ, Molinie B, Wang J, Qu K, Zhang J, Li L, Bouley DM, Lujan E, Haddad B, Daneshvar K, Carter AC, Flynn RA, Zhou C, Lim KS, Dedon P, Wernig M, Mullen AC, Xing Y, Giallourakis CC, Chang HY. m6A RNA modification controls cell fate transition in mammalian embryonic stem cells. *Cell Stem Cell*. 2014;15(6). doi:10.1016/j.stem.2014.09.019

24. Geula S, Moshitch-Moshkovitz S, Dominissini D, Mansour AAF, Kol N, Salmon-Divon M, Hershkovitz V, Peer E, Mor N, Manor YS, Ben-Haim MS, Eyal E, Yunger S, Pinto Y, Jaitin DA, Viukov S, Rais Y, Krupalnik V, Chomsky E, Zerbib M, Maza I, Rechavi Y, Massarwa R, Hanna S, Amit I, Levanon EY, Amariglio N, Stern-Ginossar N, Novershtern N, Rechavi G, Hanna JH. m6A mRNA methylation facilitates resolution of naïve pluripotency toward differentiation. *Science (80-)*. 2015;347(6225):1002-1006. doi:10.1126/science.1261417

25. Patil DP, Chen CK, Pickering BF, Chow A, Jackson C, Guttman M, Jaffrey SR. m6A RNA methylation promotes XIST-mediated transcriptional repression. *Nature*. 2016;537(7620):369-373. doi:10.1038/nature19342

26. Yoon KJ, Ringeling FR, Vissers C, Jacob F, Pokrass M, Jimenez-Cyrus D, Su Y, Kim NS, Zhu Y, Zheng L, Kim S, Wang X, Doré LC, Jin P, Regot S, Zhuang X, Canzar S, He C, Ming G li, Song H. Temporal Control of Mammalian Cortical Neurogenesis by m6A Methylation. *Cell*. 2017;171(4). doi:10.1016/j.cell.2017.09.003

27. Wang Y, Li Y, Yue M, Wang J, Kumar S, Wechsler-Reya RJ, Zhang Z, Ogawa Y, Kellis M, Duester G, Zhao JC. N6-methyladenosine RNA modification regulates embryonic neural stem cell self-renewal through histone modifications. *Nat Neurosci*. 2018;21(2). doi:10.1038/s41593-017-0057-1

28. Engel M, Eggert C, Kaplick PM, Eder M, Röh S, Tietze L, Namendorf C, Arloth J, Weber P, Rex-Haffner M, Geula S, Jakovcevski M, Hanna JH, Leshkowitz D, Uhr M, Wotjak CT, Schmidt M V., Deussing JM, Binder EB, Chen A. The Role of m6A/m-RNA Methylation in Stress Response Regulation. *Neuron*. 2018;99(2):389-403.e9. doi:10.1016/j.neuron.2018.07.009

29. Zhang Z, Wang M, Xie D, Huang Z, Zhang L, Yang Y, Ma D, Li W, Zhou Q, Yang YG, Wang XJ. METTL3-mediated N6-methyladenosine mRNA modification enhances long-term memory consolidation. *Cell Res*. 2018;28(11). doi:10.1038/s41422-018-0092-9

30. Shi H, Zhang X, Weng YL, Lu Z, Liu Y, Lu Z, Li J, Hao P, Zhang Y, Zhang F, Wu Y, Delgado JY, Su Y, Patel MJ, Cao X, Shen B, Huang X, Ming G li, Zhuang X, Song H, He C, Zhou T. m6A facilitates hippocampus-dependent learning and memory through YTHDF1. *Nature*. 2018;563(7730). doi:10.1038/s41586-018-0666-1

31. Gokhale NS, McIntyre ABR, Mattocks MD, Holley CL, Lazear HM, Mason CE, Horner SM. Altered m6A Modification of Specific Cellular Transcripts Affects Flaviviridae Infection. *Mol Cell*. 2020;77(3). doi:10.1016/j.molcel.2019.11.007

32. Yin H, Zhang X, Yang P, Zhang X, Peng Y, Li D, Yu Y, Wu Y, Wang Y, Zhang J, Ding X, Wang X, Yang A, Zhang R. RNA m6A methylation orchestrates cancer growth and metastasis via macrophage reprogramming. *Nat Commun*. 2021;12(1). doi:10.1038/s41467-021-21514-8

33. Frayling TM, Timpson NJ, Weedon MN, Zeggini E, Freathy RM, Lindgren CM, Perry JRB, Elliott KS, Lango H, Rayner NW, Shields B, Harries LW, Barrett JC, Ellard S, Groves CJ, Knight B, Patch AM, Ness AR, Ebrahim S, Lawlor DA, Ring SM, Ben-Shlomo Y, Jarvelin MR, Sovio U, Bennett AJ, Melzer D, Ferrucci L, Loos RJF, Barroso I, Wareham NJ, Karpe F, Owen KR, Cardon LR, Walker M, Hitman GA, Palmer CNA, Doney ASF, Morris AD, Smith GD, Hattersley AT, McCarthy MI. A common variant in the FTO gene is associated with body mass index and predisposes to childhood and adult obesity. *Science (80-)*. 2007;316(5826).

doi:10.1126/science.1141634

34. Dina C, Meyre D, Gallina S, Durand E, Körner A, Jacobson P, Carlsson LMS, Kiess W, Vatin V, Lecoeur C, Delplanque J, Vaillant E, Pattou F, Ruiz J, Weill J, Levy-Marchal C, Horber F, Potoczna N, Hercberg S, Le Stunff C, Bougnères P, Kovacs P, Marre M, Balkau B, Cauchi S, Chèvre JC, Froguel P. Variation in FTO contributes to childhood obesity and severe adult obesity. *Nat Genet*. 2007;39(6). doi:10.1038/ng2048

35. Linder B, Grozhik A V., Olarerin-George AO, Meydan C, Mason CE, Jaffrey SR. Single-nucleotide-resolution mapping of m6A and m6Am throughout the transcriptome. *Nat Methods*. 2015;12(8). doi:10.1038/nmeth.3453

36. Liu J, Yue Y, Han D, Wang X, Fu Y, Zhang L, Jia G, Yu M, Lu Z, Deng X, Dai Q, Chen W, He C. A METTL3-METTL14 complex mediates mammalian nuclear RNA N6-adenosine methylation. *Nat Chem Biol*. 2014;10(2):93-95. doi:10.1038/nchembio.1432

37. Ping XL, Sun BF, Wang L, Xiao W, Yang X, Wang WJ, Adhikari S, Shi Y, Lv Y, Chen YS, Zhao X, Li A, Yang Y, Dahal U, Lou XM, Liu X, Huang J, Yuan WP, Zhu XF, Cheng T, Zhao YL, Wang X, Danielsen JMR, Liu F, Yang YG. Mammalian WTAP is a regulatory subunit of the RNA N6-methyladenosine methyltransferase. *Cell Res*. 2014;24(2):177-189. doi:10.1038/cr.2014.3

38. Alarcón CR, Lee H, Goodarzi H, Halberg N, Tavazoie SF. N6-methyladenosine marks primary microRNAs for processing. *Nature*. 2015;519(7544). doi:10.1038/nature14281

39. Lin S, Choe J, Du P, Triboulet R, Gregory RI. The m6A Methyltransferase METTL3 Promotes Translation in Human Cancer Cells. *Mol Cell*. 2016;62.

40. Wang P, Doxtader KA, Nam Y. Structural Basis for Cooperative Function of Mettl3 and Mettl14 Methyltransferases. *Mol Cell*. 2016;63(2). doi:10.1016/j.molcel.2016.05.041

41. Slobodin B, Han R, Calderone V, Vrielink JAFO, Loayza-Puch F, Elkon R, Agami R. Transcription Impacts the Efficiency of mRNA Translation via Co-transcriptional N6-adenosine Methylation. *Cell*. 2017;169(2). doi:10.1016/j.cell.2017.03.031

42. Huang H, Weng H, Zhou K, Wu T, Zhao BS, Sun M, Chen Z, Deng X, Xiao G, Auer F, Klemm L, Wu H, Zuo Z, Qin X, Dong Y, Zhou Y, Qin H, Tao S, Du J, Liu J, Lu Z, Yin H, Mesquita A, Yuan CL, Hu YC, Sun W, Su R, Dong L, Shen C, Li C, Qing Y, Jiang X, Wu X, Sun M, Guan JL, Qu L, Wei M, Müschen M, Huang G, He C, Yang J, Chen J. Histone H3 trimethylation at lysine 36 guides m6A RNA modification co-transcriptionally. *Nature*. 2019;567(7748). doi:10.1038/s41586-019-1016-7

43. Horiuchi K, Kawamura T, Iwanari H, Ohashi R, Naito M, Kodama T, Hamakubo T. Identification of Wilms' tumor 1-associating protein complex and its role in alternative splicing and the cell cycle. *J Biol Chem*. 2013;288(46). doi:10.1074/jbc.M113.500397

44. Knuckles P, Lence T, Haussmann IU, Jacob D, Kreim N, Carl SH, Masiello I, Hares T, Villaseñor R, Hess D, Andrade-Navarro MA, Biggiogera M, Helm M, Soller M, Bühler M, Roignant JY. Zc3h13/Flacc is required for adenosine methylation by bridging the mRNA-binding factor RbM15/spenito to the m6 a machinery component Wtap/Fl(2)d. *Genes Dev*. 2018;32(5-6). doi:10.1101/gad.309146.117

45. Bawankar P, Lence T, Paolantoni C, Haussmann IU, Kazlauskiene M, Jacob D, Heidelberger JB, Richter FM, Nallasivan MP, Morin V, Kreim N, Beli P, Helm M, Jinek M, Soller M, Roignant JY. Hakai is required for stabilization of core components of the m6A mRNA methylation machinery. *Nat Commun*. 2021;12(1). doi:10.1038/s41467-021-23892-5

46. Brown JA, Kinzig CG, Degregorio SJ, Steitz JA. Methyltransferase-like protein 16 binds the 3'-terminal triple helix of MALAT1 long noncoding RNA. *Proc Natl Acad Sci U S A*. 2016;113(49). doi:10.1073/pnas.1614759113

47. Warda AS, Kretschmer J, Hackert P, Lenz C, Urlaub H, Höbartner C, Sloan KE, Bohnsack MT. Human METTL16 is a N6-methyladenosine (m6A) methyltransferase that targets pre-mRNAs and various non-coding RNAs. *EMBO Rep*. 2017;18(11). doi:10.15252/embr.201744940

48. Mendel M, Chen KM, Homolka D, Gos P, Pandey RR, McCarthy AA, Pillai RS. Methylation of Structured RNA by the m6A Writer METTL16 Is Essential for Mouse Embryonic Development. *Mol Cell*. 2018;71(6). doi:10.1016/j.molcel.2018.08.004

49. Ma H, Wang X, Cai J, Dai Q, Natchiar SK, Lv R, Chen K, Lu Z, Chen H, Shi YG, Lan F, Fan J,

Klaholz BP, Pan T, Shi Y, He C. N6-Methyladenosine methyltransferase ZCCHC4 mediates ribosomal RNA methylation. *Nat Chem Biol*. 2019;15(1). doi:10.1038/s41589-018-0184-3

50. Pendleton KE, Chen B, Liu K, Hunter O V., Xie Y, Tu BP, Conrad NK. The U6 snRNA m6A Methyltransferase METTL16 Regulates SAM Synthetase Intron Retention. *Cell*. 2017;169(5). doi:10.1016/j.cell.2017.05.003

51. Pinto R, Vågbø CB, Jakobsson ME, Kim Y, Baltissen MP, O'Donohue MF, Guzmán UH, Małecki JM, Wu J, Kirpekar F, Olsen J V., Gleizes PE, Vermeulen M, Leidel SA, Slupphaug G, Falnes PO. The human methyltransferase ZCCHC4 catalyses N6-methyladenosine modification of 28S ribosomal RNA. *Nucleic Acids Res*. 2020;48(2). doi:10.1093/nar/gkz1147

52. Zheng G, Dahl JA, Niu Y, Fedorcsak P, Huang CM, Li CJ, Vågbø CB, Shi Y, Wang WL, Song SH, Lu Z, Bosmans RPG, Dai Q, Hao YJ, Yang X, Zhao WM, Tong WM, Wang XJ, Bogdan F, Furu K, Fu Y, Jia G, Zhao X, Liu J, Krokan HE, Klungland A, Yang YG, He C. ALKBH5 Is a Mammalian RNA Demethylase that Impacts RNA Metabolism and Mouse Fertility. *Mol Cell*. 2013;49(1):18-29. doi:10.1016/j.molcel.2012.10.015

53. Thalhammer A, Bencokova Z, Poole R, Loenarz C, Adam J, O'Flaherty L, Schödel J, Mole D, Giaslakiotis K, Schofield CJ, Hammond EM, Ratcliffe PJ, Pollard PJ. Human AlkB homologue 5 is a nuclear 2-oxoglutarate dependent oxygenase and a direct target of hypoxia-inducible factor 1α (HIF-1α). *PLoS One*. 2011;6(1). doi:10.1371/journal.pone.0016210

54. Mauer J, Luo X, Blanjoie A, Jiao X, Grozhik A V., Patil DP, Linder B, Pickering BF, Vasseur JJ, Chen Q, Gross SS, Elemento O, Debart F, Kiledjian M, Jaffrey SR. Reversible methylation of m6Am in the 5′ cap controls mRNA stability. *Nature*. 2017;541(7637). doi:10.1038/nature21022

55. Mauer J, Sindelar M, Despic V, Guez T, Hawley BR, Vasseur JJ, Rentmeister A, Gross SS, Pellizzoni L, Debart F, Goodarzi H, Jaffrey SR. FTO controls reversible m6Am RNA methylation during snRNA biogenesis. *Nat Chem Biol*. 2019;15(4):340-347. doi:10.1038/s41589-019-0231-8

56. Wei J, Liu F, Lu Z, Fei Q, Ai Y, He PC, Shi H, Cui X, Su R, Klungland A, Jia G, Chen J, He C. Differential m6A, m6Am, and m1A Demethylation Mediated by FTO in the Cell Nucleus and Cytoplasm. *Mol Cell*. 2018;71(6):973-985.e5. doi:10.1016/j.molcel.2018.08.011

57. Fischer J, Koch L, Emmerling C, Vierkotten J, Peters T, Brüning JC, Rüther U. Inactivation of the Fto gene protects from obesity. *Nature*. 2009;458(7240). doi:10.1038/nature07848

58. Poritsanos NJ, Lew PS, Fischer J, Mobbs C V., Nagy JI, Wong D, Rüther U, Mizuno TM. Impaired hypothalamic Fto expression in response to fasting and glucose in obese mice. *Nutr Diabetes*. 2011;1(10). doi:10.1038/nutd.2011.15

59. Yang Y, Shen F, Huang W, Qin S, Huang J-T, Sergi C, Yuan B-F, Liu S-M. Glucose Is Involved in the Dynamic Regulation of m6A in Patients With Type 2 Diabetes. *J Clin Endocrinol Metab*. 2019;104(3):665-673. doi:10.1210/jc.2018-00619

60. Yu Q, Liu S, Yu L, Xiao Y, Zhang S, Wang X, Xu Y, Yu H, Li Y, Yang J, Tang J, Duan H-C, Wei L-H, Zhang H, Wei J, Tang Q, Wang C, Zhang W, Wang Y, Song P, Lu Q, Zhang W, Dong S, Song B, He C, Jia G. RNA demethylation increases the yield and biomass of rice and potato plants in field trials. *Nat Biotechnol*. Published online 2021. doi:10.1038/s41587-021-00982-9

61. Little NA, Hastie ND, Davies RC. Identification of WTAP, a novel Wilms' tumour 1-associating protein. *Hum Mol Genet*. 2000;9(15):2231-2239. doi:10.1093/oxfordjournals.hmg.a018914

62. Small TW, Bolender Z, Bueno C, O'Neil C, Nong Z, Rushlow W, Rajakumar N, Kandel C, Strong J, Madrenas J, Pickering JG. Wilms' tumor 1-associating protein regulates the proliferation of vascular smooth muscle cells. *Circ Res*. 2006;99(12). doi:10.1161/01.RES.0000252289.79841.d3

63. Small TW, Pickering JG. Nuclear degradation of Wilms tumor 1-associating protein and survivin splice variant switching underlie IGF-1-mediated survival. *J Biol Chem*. 2009;284(37). doi:10.1074/jbc.M109.034629

64. Horiuchi K, Umetani M, Minami T, Okayama H, Takada S, Yamamoto M, Aburatani H, Reid PC, Housman DE, Hamakubo T, Kodama T. Wilms' tumor 1-associating protein regulates G2/M transition through stabilization of cyclin A2 mRNA. *Proc Natl Acad Sci U S A*. 2006;103(46):17278-17283. doi:10.1073/pnas.0608357103

65. Fukusumi Y, Naruse C, Asano M. Wtap is required for differentiation of endoderm and mesoderm in the mouse embryo. *Dev Dyn*. 2008;237(3). doi:10.1002/dvdy.21444

66. Granadino B, Campuzano S, Sanchez L. The Drosophila melanogaster fl(2d) gene is needed for the female-specific splicing of Sex-lethal RNA. *EMBO J*. 1990;9(8). doi:10.1002/j.1460-2075.1990.tb07441.x

67. Schöller E, Weichmann F, Treiber T, Ringle S, Treiber N, Flatley A, Feederle R, Bruckmann A, Meister G. Interactions, localization, and phosphorylation of the m6A generating METTL3–METTL14–WTAP complex. *RNA*. 2018;24(4). doi:10.1261/rna.064063.117

68. Sorci M, Ianniello Z, Cruciani S, Larivera S, Ginistrelli LC, Capuano E, Marchioni M, Fazi F, Fatica A. METTL3 regulates WTAP protein homeostasis. *Cell Death Dis*. 2018;9(8). doi:10.1038/s41419-018-0843-z

69. Schwartz S, Mumbach MR, Jovanovic M, Wang T, Maciag K, Bushkin GG, Mertins P, Ter-Ovanesyan D, Habib N, Cacchiarelli D, Sanjana NE, Freinkman E, Pacold ME, Satija R, Mikkelsen TS, Hacohen N, Zhang F, Carr SA, Lander ES, Regev A. Perturbation of m6A writers reveals two distinct classes of mRNA methylation at internal and 5' sites. *Cell Rep*. 2014;8(1):284-296. doi:10.1016/j.celrep.2014.05.048

70. Zhang Z, Theler D, Kaminska KH, Hiller M, De La Grange P, Pudimat R, Rafalska I, Heinrich B, Bujnick JM, Allain FHT, Stamm S. The YTH domain is a novel RNA binding domain. *J Biol Chem*. 2010;285(19). doi:10.1074/jbc.M110.104711

71. Nayler O, Hartmann AM, Stamm S. The ER repeat protein YT521-B localizes to a novel subnuclear compartment. *J Cell Biol*. 2000;150(5). doi:10.1083/jcb.150.5.949

72. Kasowitz SD, Ma J, Anderson SJ, Leu NA, Xu Y, Gregory BD, Schultz RM, Wang PJ. Nuclear m6A reader YTHDC1 regulates alternative polyadenylation and splicing during mouse oocyte development. *PLoS Genet*. 2018;14(5). doi:10.1371/journal.pgen.1007412

73. Hartmann AM, Nayler O, Schwaiger FW, Obermeier A, Stamm S. The interaction and colocalization of Sam68 with the splicing-associated factor YT521-B in nuclear dots is regulated by the Src family kinase p59(fyn). *Mol Biol Cell*. 1999;10(11). doi:10.1091/mbc.10.11.3909

74. Xiao W, Adhikari S, Dahal U, Chen YS, Hao YJ, Sun BF, Sun HY, Li A, Ping XL, Lai WY, Wang X, Ma HL, Huang CM, Yang Y, Huang N, Jiang G Bin, Wang HL, Zhou Q, Wang XJ, Zhao YL, Yang YG. Nuclear m6A Reader YTHDC1 Regulates mRNA Splicing. *Mol Cell*. 2016;61(4):507-519. doi:10.1016/j.molcel.2016.01.012

75. Patil DP, Chen CK, Pickering BF, Chow A, Jackson C, Guttman M, Jaffrey SR. m6A RNA methylation promotes XIST-mediated transcriptional repression. *Nature*. 2016;537(7620). doi:10.1038/nature19342

76. Roundtree IA, Luo GZ, Zhang Z, Wang X, Zhou T, Cui Y, Sha J, Huang X, Guerrero L, Xie P, He E, Shen B, He C. YTHDC1 mediates nuclear export of N6-methyladenosine methylated mRNAs. *Elife*. 2017;6. doi:10.7554/eLife.31311

77. Xu C, Wang X, Liu K, Roundtree IA, Tempel W, Li Y, Lu Z, He C, Min J. Structural basis for selective binding of m6A RNA by the YTHDC1 YTH domain. *Nat Chem Biol*. 2014;10(11):927-929. doi:10.1038/nchembio.1654

78. Rafalska I, Zhang Z, Benderska N, Wolff H, Hartmann AM, Brack-Werner R, Stamm S. The intranuclear localization and function of YT521-B is regulated by tyrosine phosphorylation. *Hum Mol Genet*. 2004;13(15). doi:10.1093/hmg/ddh167

79. Liu J, Dou X, Chen C, Chen C, Liu C, Michelle Xu M, Zhao S, Shen B, Gao Y, Han D, He C. N6-methyladenosine of chromosome-associated regulatory RNA regulates chromatin state and transcription. *Science (80-)*. 2020;367(6477). doi:10.1126/science.aay6018

80. Liu J, Gao M, He J, Wu K, Lin S, Jin L, Chen Y, Liu H, Shi J, Wang X, Chang L, Lin Y, Zhao YL, Zhang X, Zhang M, Luo GZ, Wu G, Pei D, Wang J, Bao X, Chen J. The RNA m6A reader YTHDC1 silences retrotransposons and guards ES cell identity. *Nature*. 2021;591(7849). doi:10.1038/s41586-021-03313-9

81. Li Y, Xia L, Tan K, Ye X, Zuo Z, Li M, Xiao R, Wang Z, Liu X, Deng M, Cui J, Yang M, Luo Q, Liu S, Cao X, Zhu H, Liu T, Hu J, Shi J, Xiao S, Xia L. N6-Methyladenosine co-transcriptionally directs the demethylation of histone H3K9me2. *Nat Genet*. 2020;52(9). doi:10.1038/s41588-020-

0677-3

82. Chen C, Liu W, Guo J, Liu Y, Liu X, Liu J, Dou X, Le R, Huang Y, Li C, Yang L, Kou X, Zhao Y, Wu Y, Chen J, Wang H, Shen B, Gao Y, Gao S. Nuclear m6A reader YTHDC1 regulates the scaffold function of LINE1 RNA in mouse ESCs and early embryos. *Protein Cell*. 2021;12(6). doi:10.1007/s13238-021-00837-8

83. Jachowicz JW, Bing X, Pontabry J, Bošković A, Rando OJ, Torres-Padilla ME. LINE-1 activation after fertilization regulates global chromatin accessibility in the early mouse embryo. *Nat Genet*. 2017;49(10). doi:10.1038/ng.3945

84. Percharde M, Lin CJ, Yin Y, Guan J, Peixoto GA, Bulut-Karslioglu A, Biechele S, Huang B, Shen X, Ramalho-Santos M. A LINE1-Nucleolin Partnership Regulates Early Development and ESC Identity. *Cell*. 2018;174(2). doi:10.1016/j.cell.2018.05.043

85. Cuarenta A, Kigar SL, Henion IC, Karls KE, Chang L, Bakshi VP, Auger AP. Early life stress increases Line1 within the developing brain in a sex-dependent manner. *Brain Res*. 2020;1748. doi:10.1016/j.brainres.2020.147123

86. Cuarenta A, Kigar SL, Henion IC, Chang L, Bakshi VP, Auger AP. Early life stress during the neonatal period alters social play and Line1 during the juvenile stage of development. *Sci Rep*. 2021;11(1). doi:10.1038/s41598-021-82953-3

87. Wojtas MN, Pandey RR, Mendel M, Homolka D, Sachidanandam R, Pillai RS. Regulation of m6A Transcripts by the 3'→5' RNA Helicase YTHDC2 Is Essential for a Successful Meiotic Program in the Mammalian Germline. *Mol Cell*. 2017;68(2). doi:10.1016/j.molcel.2017.09.021

88. Mao Y, Dong L, Liu XM, Guo J, Ma H, Shen B, Qian SB. m6A in mRNA coding regions promotes translation via the RNA helicase-containing YTHDC2. *Nat Commun*. 2019;10(1). doi:10.1038/s41467-019-13317-9

89. Hsu PJ, Zhu Y, Ma H, Guo Y, Shi X, Liu Y, Qi M, Lu Z, Shi H, Wang J, Cheng Y, Luo G, Dai Q, Liu M, Guo X, Sha J, Shen B, He C. Ythdc2 is an N6-methyladenosine binding protein that regulates mammalian spermatogenesis. *Cell Res*. 2017;27(9). doi:10.1038/cr.2017.99

90. Jain D, Puno MR, Meydan C, Lailler N, Mason CE, Lima CD, Anderson K V., Keeney S. Ketu mutant mice uncover an essential meiotic function for the ancient RNA helicase YTHDC2. *Elife*. 2018;7. doi:10.7554/eLife.30919

91. Bailey AS, Batista PJ, Gold RS, Grace Chen Y, de Rooij DG, Chang HY, Fuller MT. The conserved RNA helicase YTHDC2 regulates the transition from proliferation to differentiation in the germline. *Elife*. 2017;6. doi:10.7554/eLife.26116

92. Choi J, Ieong KW, Demirci H, Chen J, Petrov A, Prabhakar A, O'Leary SE, Dominissini D, Rechavi G, Soltis SM, Ehrenberg M, Puglisi JD. N6-methyladenosine in mRNA disrupts tRNA selection and translation-elongation dynamics. *Nat Struct Mol Biol*. 2016;23(2). doi:10.1038/nsmb.3148

93. Kretschmer J, Rao H, Hackert P, Sloan KE, Höbartner C, Bohnsack MT. The m6A reader protein YTHDC2 interacts with the small ribosomal subunit and the 5′-3′ exoribonuclease XRN1. *RNA*. 2018;24(10). doi:10.1261/rna.064238.117

94. Wang X, Lu Z, Gomez A, Hon GC, Yue Y, Han D, Fu Y, Parisien M, Dai Q, Jia G, Ren B, Pan T, He C. N6-methyladenosine-dependent regulation of messenger RNA stability. *Nature*. 2014;505(7481):117-120. doi:10.1038/nature12730

95. Wang X, Zhao BS, Roundtree IA, Lu Z, Han D, Ma H, Weng X, Chen K, Shi H, He C. N6-methyladenosine modulates messenger RNA translation efficiency. *Cell*. 2015;161(6):1388-1399. doi:10.1016/j.cell.2015.05.014

96. Shi H, Wang X, Lu Z, Zhao BS, Ma H, Hsu PJ, Liu C, He C. YTHDF3 facilitates translation and decay of N6-methyladenosine-modified RNA. *Cell Res*. 2017;27(3):315-328. doi:10.1038/cr.2017.15

97. Zaccara S, Jaffrey SR. A Unified Model for the Function of YTHDF Proteins in Regulating m6A-Modified mRNA. *Cell*. 2020;181(7). doi:10.1016/j.cell.2020.05.012

98. Zhuang M, Li X, Zhu J, Zhang J, Niu F, Liang F, Chen M, Li D, Han P, Ji SJ. The m6A reader YTHDF1 regulates axon guidance through translational control of Robo3.1 expression. *Nucleic Acids Res*. 2019;47(9). doi:10.1093/nar/gkz157

99. Du H, Zhao Y, He J, Zhang Y, Xi H, Liu M, Ma J, Wu L. YTHDF2 destabilizes m6A-containing RNA through direct recruitment of the CCR4-NOT deadenylase complex. *Nat Commun*. 2016;7. doi:10.1038/ncomms12626

100. Ivanova I, Much C, Di Giacomo M, Azzi C, Morgan M, Moreira PN, Monahan J, Carrieri C, Enright AJ, O'Carroll D. The RNA m6A Reader YTHDF2 Is Essential for the Post-transcriptional Regulation of the Maternal Transcriptome and Oocyte Competence. *Mol Cell*. 2017;67(6). doi:10.1016/j.molcel.2017.08.003

101. Zhao BS, Wang X, Beadell A V., Lu Z, Shi H, Kuuspalu A, Ho RK, He C. m6A-dependent maternal mRNA clearance facilitates zebrafish maternal-to-zygotic transition. *Nature*. 2017;542(7642). doi:10.1038/nature21355

102. Zhou J, Wan J, Gao X, Zhang X, Jaffrey SR, Qian SB. Dynamic m6A mRNA methylation directs translational control of heat shock response. *Nature*. 2015;526(7574). doi:10.1038/nature15377

103. Cardelli M, Marchegiani F, Cavallone L, Olivieri F, Giovagnetti S, Mugianesi E, Moresi R, Lisa R, Franceschi C. A polymorphism of the YTHDF2 gene (1p35) located in an Alu-rich genomic domain is associated with human longevity. *Journals Gerontol - Ser A Biol Sci Med Sci*. 2006;61(6). doi:10.1093/gerona/61.6.547

104. Li A, Chen YS, Ping XL, Yang X, Xiao W, Yang Y, Sun HY, Zhu Q, Baidya P, Wang X, Bhattarai DP, Zhao YL, Sun BF, Yang YG. Cytoplasmic m6A reader YTHDF3 promotes mRNA translation. *Cell Res*. 2017;27(3):444-447. doi:10.1038/cr.2017.10

105. Zheng Q, Gan H, Yang F, Yao Y, Hao F, Hong L, Jin L. Cytoplasmic m1A reader YTHDF3 inhibits trophoblast invasion by downregulation of m1A-methylated IGF1R. *Cell Discov*. 2020;6(1). doi:10.1038/s41421-020-0144-4

106. Han SP, Tang YH, Smith R. Functional diversity of the hnRNPs: Past, present and perspectives. *Biochem J*. 2010;430(3). doi:10.1042/BJ20100396

107. Geuens T, Bouhy D, Timmerman V. The hnRNP family: insights into their role in health and disease. *Hum Genet*. 2016;135(8). doi:10.1007/s00439-016-1683-5

108. David CJ, Chen M, Assanah M, Canoll P, Manley JL. HnRNP proteins controlled by c-Myc deregulate pyruvate kinase mRNA splicing in cancer. *Nature*. 2010;463(7279). doi:10.1038/nature08697

109. Vance C, Rogelj B, Hortobágyi T, De Vos KJ, Nishimura AL, Sreedharan J, Hu X, Smith B, Ruddy D, Wright P, Ganesalingam J, Williams KL, Tripathi V, Al-Saraj S, Al-Chalabi A, Leigh PN, Blair IP, Nicholson G, De Belleroche J, Gallo JM, Miller CC, Shaw CE. Mutations in FUS, an RNA processing protein, cause familial amyotrophic lateral sclerosis type 6. *Science (80-)*. 2009;323(5918). doi:10.1126/science.1165942

110. Martinez FJ, Pratt GA, Van Nostrand EL, Batra R, Huelga SC, Kapeli K, Freese P, Chun SJ, Ling K, Gelboin-Burkhart C, Fijany L, Wang HC, Nussbacher JK, Broski SM, Kim HJ, Lardelli R, Sundararaman B, Donohue JP, Javaherian A, Lykke-Andersen J, Finkbeiner S, Bennett CF, Ares M, Burge CB, Taylor JP, Rigo F, Yeo GW. Protein-RNA Networks Regulated by Normal and ALS-Associated Mutant HNRNPA2B1 in the Nervous System. *Neuron*. 2016;92(4). doi:10.1016/j.neuron.2016.09.050

111. Liu N, Dai Q, Zheng G, He C, Parisien M, Pan T. N6-methyladenosine-dependent RNA structural switches regulate RNA-protein interactions. *Nature*. 2015;518(7540):560-564. doi:10.1038/nature14234

112. Zhou KI, Parisien M, Dai Q, Liu N, Diatchenko L, Sachleben JR, Pan T. N6-Methyladenosine Modification in a Long Noncoding RNA Hairpin Predisposes Its Conformation to Protein Binding. *J Mol Biol*. 2016;428(5):822-833. doi:10.1016/j.jmb.2015.08.021

113. Alarcón CR, Goodarzi H, Lee H, Liu X, Tavazoie S, Tavazoie SF. HNRNPA2B1 Is a Mediator of m6A-Dependent Nuclear RNA Processing Events. *Cell*. 2015;162(6):1299-1308. doi:10.1016/j.cell.2015.08.011

114. Wu B, Su S, Patil DP, Liu H, Gan J, Jaffrey SR, Ma J. Molecular basis for the specific and multivariant recognitions of RNA substrates by human hnRNP A2/B1. *Nat Commun*. 2018;9(1). doi:10.1038/s41467-017-02770-z

115. Pieretti M, Zhang F, Fu YH, Warren ST, Oostra BA, Caskey CT, Nelson DL. Absence of

expression of the FMR-1 gene in fragile X syndrome. *Cell*. 1991;66(4). doi:10.1016/0092-8674(91)90125-I

116. Tassone F, Hagerman RJ, Taylor AK, Gane LW, Godfrey TE, Hagerman PJ. Elevated levels of FMR1 mRNA carrier males: A new mechanism of involvement in the fragile-X syndrome. *Am J Hum Genet*. 2000;66(1). doi:10.1086/302720

117. Richter JD, Zhao X. The molecular biology of FMRP: new insights into fragile X syndrome. *Nat Rev Neurosci*. 2021;22(4). doi:10.1038/s41583-021-00432-0

118. Edupuganti RR, Geiger S, Lindeboom RGH, Shi H, Hsu PJ, Lu Z, Wang SY, Baltissen MPA, Jansen PWTC, Rossa M, Müller M, Stunnenberg HG, He C, Carell T, Vermeulen M. N6-methyladenosine (m6A) recruits and repels proteins to regulate mRNA homeostasis. *Nat Struct Mol Biol*. 2017;24(10). doi:10.1038/nsmb.3462

119. Zhang F, Kang Y, Wang M, Li Y, Xu T, Yang W, Song H, Wu H, Shu Q, Jin P. Fragile X mental retardation protein modulates the stability of its m6A-marked messenger RNA targets. *Hum Mol Genet*. 2018;27(22). doi:10.1093/hmg/ddy292

120. Edens BM, Vissers C, Su J, Arumugam S, Xu Z, Shi H, Miller N, Rojas Ringeling F, Ming G li, He C, Song H, Ma YC. FMRP Modulates Neural Differentiation through m6A-Dependent mRNA Nuclear Export. *Cell Rep*. 2019;28(4). doi:10.1016/j.celrep.2019.06.072

121. Worpenberg L, Paolantoni C, Longhi S, Mulorz MM, Lence T, Wessels H, Dassi E, Aiello G, Sutandy FXR, Scheibe M, Edupuganti RR, Busch A, Möckel MM, Vermeulen M, Butter F, König J, Notarangelo M, Ohler U, Dieterich C, Quattrone A, Soldano A, Roignant J. Ythdf is a N6-methyladenosine reader that modulates Fmr1 target mRNA selection and restricts axonal growth in Drosophila. *EMBO J*. 2021;40(4):e104975. doi:10.15252/embj.2020104975

122. Choe J, Lin S, Zhang W, Liu Q, Wang L, Ramirez-Moya J, Du P, Kim W, Tang S, Sliz P, Santisteban P, George RE, Richards WG, Wong KK, Locker N, Slack FJ, Gregory RI. mRNA circularization by METTL3–eIF3h enhances translation and promotes oncogenesis. *Nature*. 2018;561(7724). doi:10.1038/s41586-018-0538-8

123. Meyer KD, Patil DP, Zhou J, Zinoviev A, Skabkin MA, Elemento O, Pestova T V., Qian SB, Jaffrey SR. 5′ UTR m6A Promotes Cap-Independent Translation. *Cell*. 2015;163(4). doi:10.1016/j.cell.2015.10.012

124. Ke S, Pandya-Jones A, Saito Y, Fak JJ, Vågbø CB, Geula S, Hanna JH, Black DL, Darnell JE, Darnell RB. m6A mRNA modifications are deposited in nascent pre-mRNA and are not required for splicing but do specify cytoplasmic turnover. *Genes Dev*. 2017;31(10):990-1006. doi:10.1101/gad.301036.117

125. Rosa-Mercado NA, Withers JB, Steitz JA. Settling the m6A debate: Methylation of mature mRNA is not dynamic but accelerates turnover. *Genes Dev*. 2017;31(10):957-958. doi:10.1101/gad.302695.117

126. Garcia-Campos MA, Edelheit S, Toth U, Safra M, Shachar R, Viukov S, Winkler R, Nir R, Lasman L, Brandis A, Hanna JH, Rossmanith W, Schwartz S. Deciphering the “m6A Code” via Antibody-Independent Quantitative Profiling. *Cell*. 2019;178(3):731-747.e16. doi:10.1016/j.cell.2019.06.013

127. Liu Y, Beyer A, Aebersold R. On the Dependency of Cellular Protein Levels on mRNA Abundance. *Cell*. 2016;165(3):535-550. doi:10.1016/j.cell.2016.03.014

128. Chang M, Lv H, Zhang W, Ma C, He X, Zhao S, Zhang ZW, Zeng YX, Song S, Niu Y, Tong WM. Region-specific RNA m6A methylation represents a new layer of control in the gene regulatory network in the mouse brain. *Open Biol*. 2017;7(9). doi:10.1098/rsob.170166

129. Widagdo J, Anggono V. The m6A-epitranscriptomic signature in neurobiology: from neurodevelopment to brain plasticity. *J Neurochem*. 2018;147(2). doi:10.1111/jnc.14481

130. Merkurjev D, Hong WT, Iida K, Oomoto I, Goldie BJ, Yamaguti H, Ohara T, Kawaguchi SY, Hirano T, Martin KC, Pellegrini M, Wang DO. Synaptic N6-methyladenosine (m6A) epitranscriptome reveals functional partitioning of localized transcripts. *Nat Neurosci*. 2018;21(7). doi:10.1038/s41593-018-0173-6

131. Ma C, Chang M, Lv H, Zhang ZW, Zhang W, He X, Wu G, Zhao S, Zhang Y, Wang D, Teng X, Liu C, Li Q, Klungland A, Niu Y, Song S, Tong WM. RNA m6A methylation participates in

regulation of postnatal development of the mouse cerebellum. *Genome Biol*. 2018;19(1). doi:10.1186/s13059-018-1435-z

132. Wang CX, Cui GS, Liu X, Xu K, Wang M, Zhang XX, Jiang LY, Li A, Yang Y, Lai WY, Sun BF, Jiang G Bin, Wang HL, Tong WM, Li W, Wang XJ, Yang YG, Zhou Q. METTL3-mediated m6A modification is required for cerebellar development. *PLoS Biol*. 2018;16(6). doi:10.1371/journal.pbio.2004880

133. Li M, Zhao X, Wang W, Shi H, Pan Q, Lu Z, Perez SP, Suganthan R, He C, Bjørås M, Klungland A. Ythdf2-mediated m6A mRNA clearance modulates neural development in mice. *Genome Biol*. 2018;19(1). doi:10.1186/s13059-018-1436-y

134. Xu H, Dzhashiashvili Y, Shah A, Kunjamma RB, Weng Y lan, Elbaz B, Fei Q, Jones JS, Li YI, Zhuang X, Ming G li, He C, Popko B. m6A mRNA Methylation Is Essential for Oligodendrocyte Maturation and CNS Myelination. *Neuron*. 2020;105(2):293-309.e5. doi:10.1016/j.neuron.2019.12.013

135. Wu R, Li A, Sun B, Sun JG, Zhang J, Zhang T, Chen Y, Xiao Y, Gao Y, Zhang Q, Ma J, Yang X, Liao Y, Lai WY, Qi X, Wang S, Shu Y, Wang HL, Wang F, Yang YG, Yuan Z. A novel m6A reader Prrc2a controls oligodendroglial specification and myelination. *Cell Res*. 2019;29(1). doi:10.1038/s41422-018-0113-8

136. Altman J, Das GD. Autoradiographic and histological evidence of postnatal hippocampal neurogenesis in rats. *J Comp Neurol*. 1965;124(3). doi:10.1002/cne.901240303

137. Gage FH. Adult neurogenesis in mammals Neurogenesis in adulthood has implications for sense of self, memory, and disease. *Science (80-)*. 2019;364(6443). doi:10.1126/science.aav6885

138. Li L, Zang L, Zhang F, Chen J, Shen H, Shu L, Liang F, Feng C, Chen D, Tao H, Xu T, Li Z, Kang Y, Wu H, Tang L, Zhang P, Jin P, Shu Q, Li X. Fat mass and obesity-associated (FTO) protein regulates adult neurogenesis. *Hum Mol Genet*. 2017;26(13). doi:10.1093/hmg/ddx128

139. Chen J, Zhang YC, Huang C, Shen H, Sun B, Cheng X, Zhang YJ, Yang YG, Shu Q, Yang Y, Li X. m6A Regulates Neurogenesis and Neuronal Development by Modulating Histone Methyltransferase Ezh2. *Genomics, Proteomics Bioinforma*. 2019;17(2). doi:10.1016/j.gpb.2018.12.007

140. Van Battum EY, Brignani S, Pasterkamp RJ. Axon guidance proteins in neurological disorders. *Lancet Neurol*. 2015;14(5). doi:10.1016/S1474-4422(14)70257-1

141. Yu J, Chen M, Huang H, Zhu J, Song H, Zhu J, Park J, Ji SJ. Dynamic m6A modification regulates local translation of mRNA in axons. *Nucleic Acids Res*. 2018;46(3). doi:10.1093/nar/gkx1182

142. Weng YL, Wang X, An R, Cassin J, Vissers C, Liu Y, Liu Y, Xu T, Wang X, Wong SZH, Joseph J, Dore LC, Dong Q, Zheng W, Jin P, Wu H, Shen B, Zhuang X, He C, Liu K, Song H, Ming G li. Epitranscriptomic m6A Regulation of Axon Regeneration in the Adult Mammalian Nervous System. *Neuron*. 2018;97(2). doi:10.1016/j.neuron.2017.12.036

143. Kang H, Schuman EM. A requirement for local protein synthesis in neurotrophin-induced hippocampal synaptic plasticity. *Science (80-)*. 1996;273(5280). doi:10.1126/science.273.5280.1402

144. Bradshaw KD, Emptage NJ, Bliss TVP. A role for dendritic protein synthesis in hippocampal late LTP. *Eur J Neurosci*. 2003;18(11). doi:10.1111/j.1460-9568.2003.03054.x

145. Briz V, Zhu G, Wang Y, Liu Y, Avetisyan M, Bi X, Baudry M. Activity-dependent rapid local RhoA synthesis is required for hippocampal synaptic plasticity. *J Neurosci*. 2015;35(5). doi:10.1523/JNEUROSCI.2302-14.2015

146. Widagdo J, Zhao QY, Kempen MJ, Tan MC, Ratnu VS, Wei W, Leighton L, Spadaro PA, Edson J, Anggono V, Bredy TW. Experience-dependent accumulation of N6-methyladenosine in the prefrontal cortex is associated with memory processes in mice. *J Neurosci*. 2016;36(25). doi:10.1523/JNEUROSCI.4053-15.2016

147. Walters BJ, Mercaldo V, Gillon CJ, Yip M, Neve RL, Boyce FM, Frankland PW, Josselyn SA. The Role of The RNA Demethylase FTO (Fat Mass and Obesity-Associated) and mRNA Methylation in Hippocampal Memory Formation. *Neuropsychopharmacology*. 2017;42(7). doi:10.1038/npp.2017.31

148. Hess ME, Hess S, Meyer KD, Verhagen LAW, Koch L, Brönneke HS, Dietrich MO, Jordan SD,

Saletore Y, Elemento O, Belgardt BF, Franz T, Horvath TL, Rüther U, Jaffrey SR, Kloppenburg P, Brüning JC. The fat mass and obesity associated gene (Fto) regulates activity of the dopaminergic midbrain circuitry. *Nat Neurosci*. 2013;16(8). doi:10.1038/nn.3449

149. Minichiello L, Korte M, Wolfer D, Kühn R, Unsicker K, Cestari V, Rossi-Arnaud C, Lipp HP, Bonhoeffer T, Klein R. Essential role for TrkB receptors in hippocampus-mediated learning. *Neuron*. 1999;24(2). doi:10.1016/S0896-6273(00)80853-3

150. Koranda JL, Dore L, Shi H, Patel MJ, Vaasjo LO, Rao MN, Chen K, Lu Z, Yi Y, Chi W, He C, Zhuang X. Mettl14 Is Essential for Epitranscriptomic Regulation of Striatal Function and Learning. *Neuron*. 2018;99(2). doi:10.1016/j.neuron.2018.06.007

151. Agarwal A, Dibaj P, Kassmann CM, Goebbels S, Nave KA, Schwab MH. In vivo imaging and noninvasive ablation of pyramidal neurons in adult NEX-CreERT2 mice. *Cereb Cortex*. 2012;22(7):1473-1486. doi:10.1093/cercor/bhr214

152. Madisen L, Zwingman TA, Sunkin SM, Oh SW, Zariwala HA, Gu H, Ng LL, Palmiter RD, Hawrylycz MJ, Jones AR, Lein ES, Zeng H. A robust and high-throughput Cre reporting and characterization system for the whole mouse brain. *Nat Neurosci*. 2010;13(1):133-140. doi:10.1038/nn.2467

153. Falke LL, Broekhuizen R, Huitema A, Maarseveen E, Nguyen TQ, Goldschmeding R. Tamoxifen for induction of Cre-recombination may confound fibrosis studies in female mice. *J Cell Commun Signal*. 2017;11(2):205-211. doi:10.1007/s12079-017-0390-x

154. Ye R, Wang QA, Tao C, Vishvanath L, Shao M, McDonald JG, Gupta RK, Scherer PE. Impact of tamoxifen on adipocyte lineage tracing: Inducer of adipogenesis and prolonged nuclear translocation of Cre recombinase. *Mol Metab*. 2015;4(11):771-778. doi:10.1016/j.molmet.2015.08.004

155. Schmidt M V., Sterlemann V, Ganea K, Liebl C, Alam S, Harbich D, Greetfeld M, Uhr M, Holsboer F, Müller MB. Persistent neuroendocrine and behavioral effects of a novel, etiologically relevant mouse paradigm for chronic social stress during adolescence. *Psychoneuroendocrinology*. 2007;32(5):417-429. doi:10.1016/j.psyneuen.2007.02.011

156. Scharf SH, Liebl C, Binder EB, Schmidt M V., Müller MB. Expression and Regulation of the Fkbp5 Gene in the Adult Mouse Brain. Mueller F, ed. *PLoS One*. 2011;6(2):e16883. doi:10.1371/journal.pone.0016883

157. Gould TD, Dao DT, Kovacsics CE. *The Open Field Test*. Vol 42. Humana Press; 2009. doi:10.1007/978-1-60761-303-9_1

158. Walf AA, Frye CA. *Using the Elevated plus Maze as a Bioassay to Assess the Effects of Naturally Occurring and Exogenously Administered Compounds to Influence Anxiety-Related Behaviors of Mice*. Vol 42. Humana Press; 2009. doi:10.1007/978-1-60761-303-9_12

159. Takao K, Miyakawa T. Light/dark transition test for mice. *J Vis Exp*. 2006;(1):104. doi:10.3791/104

160. Hascoët M, Bourin M. *The Mouse Light-Dark Box Test*. Vol 42. Humana Press; 2009. doi:10.1007/978-1-60761-303-9_11

161. Wotjak CT. Sound check, stage design and screen plot – how to increase the comparability of fear conditioning and fear extinction experiments. *Psychopharmacology (Berl)*. 2019;236(1):33-48. doi:10.1007/s00213-018-5111-5

162. Morris RGM, Garrud P, Rawlins JNP, O'Keefe J. Place navigation impaired in rats with hippocampal lesions. *Nature*. 1982;297(5868):681-683. doi:10.1038/297681a0

163. R Core Team. A Language and Environment for Statistical Computing. *R Found Stat Comput Vienna, Austria*. Published online 2020:https://www.R-project.org. http://www.r-project.org

164. RStudio Team. Integrated development for R. *RStudio*. 2020;42. http://www.rstudio.com/

165. Duscha A, Gisevius B, Hirschberg S, Yissachar N, Stangl GI, Eilers E, Bader V, Haase S, Kaisler J, David C, Schneider R, Troisi R, Zent D, Hegelmaier T, Dokalis N, Gerstein S, Del Mare-Roumani S, Amidror S, Staszewski O, Poschmann G, Stühler K, Hirche F, Balogh A, Kempa S, Träger P, Zaiss MM, Holm JB, Massa MG, Nielsen HB, Faissner A, Lukas C, Gatermann SG, Scholz M, Przuntek H, Prinz M, Forslund SK, Winklhofer KF, Müller DN, Linker RA, Gold R, Haghikia A. Propionic Acid Shapes the Multiple Sclerosis Disease Course by an

Immunomodulatory Mechanism. *Cell*. 2020;180(6). doi:10.1016/j.cell.2020.02.035

166. Koster J, Rahmann S. Snakemake--a scalable bioinformatics workflow engine. *Bioinformatics*. 2012;28(19):2520-2522. doi:10.1093/bioinformatics/bts480

167. Martin M. Cutadapt removes adapter sequences from high-throughput sequencing reads. *EMBnet.journal*. 2011;17(1):10. doi:10.14806/ej.17.1.200

168. Dobin A, Davis CA, Schlesinger F, Drenkow J, Zaleski C, Jha S, Batut P, Chaisson M, Gingeras TR. STAR: Ultrafast universal RNA-seq aligner. *Bioinformatics*. 2013;29(1):15-21. doi:10.1093/bioinformatics/bts635

169. Anders S, Pyl PT, Huber W. HTSeq-A Python framework to work with high-throughput sequencing data. *Bioinformatics*. 2015;31(2):166-169. doi:10.1093/bioinformatics/btu638

170. Love MI, Huber W, Anders S. Moderated estimation of fold change and dispersion for RNA-seq data with DESeq2. *Genome Biol*. 2014;15(12):550. doi:10.1186/s13059-014-0550-8

171. Anders S, Reyes A, Huber W. Detecting differential usage of exons from RNA-seq data. *Genome Res*. 2012;22(10):2008-2017. doi:10.1101/gr.133744.111

172. Ashburner M, Ball CA, Blake JA, Botstein D, Butler H, Cherry JM, Davis AP, Dolinski K, Dwight SS, Eppig JT, Harris MA, Hill DP, Issel-Tarver L, Kasarskis A, Lewis S, Matese JC, Richardson JE, Ringwald M, Rubin GM, Sherlock G. Gene ontology: Tool for the unification of biology. *Nat Genet*. 2000;25(1):25-29. doi:10.1038/75556

173. Carbon S, Douglass E, Good BM, Unni DR, Harris NL, Mungall CJ, Basu S, Chisholm RL, Dodson RJ, Hartline E, Fey P, Thomas PD, Albou LP, Ebert D, Kesling MJ, Mi H, Muruganujan A, Huang X, Mushayahama T, LaBonte SA, Siegele DA, Antonazzo G, Attrill H, Brown NH, Garapati P, Marygold SJ, Trovisco V, dos Santos G, Falls K, Tabone C, Zhou P, Goodman JL, Strelets VB, Thurmond J, Garmiri P, Ishtiaq R, Rodríguez-López M, Acencio ML, Kuiper M, Lægreid A, Logie C, Lovering RC, Kramarz B, Saverimuttu SCC, Pinheiro SM, Gunn H, Su R, Thurlow KE, Chibucos M, Giglio M, Nadendla S, Munro J, Jackson R, Duesbury MJ, Del-Toro N, Meldal BHM, Paneerselvam K, Perfetto L, Porras P, Orchard S, Shrivastava A, Chang HY, Finn RD, Mitchell AL, Rawlings ND, Richardson L, Sangrador-Vegas A, Blake JA, Christie KR, Dolan ME, Drabkin HJ, Hill DP, Ni L, Sitnikov DM, Harris MA, Oliver SG, Rutherford K, Wood V, Hayles J, Bähler J, Bolton ER, de Pons JL, Dwinell MR, Hayman GT, Kaldunski ML, Kwitek AE, Laulederkind SJF, Plasterer C, Tutaj MA, Vedi M, Wang SJ, D'Eustachio P, Matthews L, Balhoff JP, Aleksander SA, Alexander MJ, Cherry JM, Engel SR, Gondwe F, Karra K, Miyasato SR, Nash RS, Simison M, Skrzypek MS, Weng S, Wong ED, Feuermann M, Gaudet P, Morgat A, Bakker E, Berardini TZ, Reiser L, Subramaniam S, Huala E, Arighi CN, Auchincloss A, Axelsen K, Argoud-Puy G, Bateman A, Blatter MC, Boutet E, Bowler E, Breuza L, Bridge A, Britto R, Bye-A-Jee H, Casas CC, Coudert E, Denny P, Es-Treicher A, Famiglietti ML, Georghiou G, Gos AN, Gruaz-Gumowski N, Hatton-Ellis E, Hulo C, Ignatchenko A, Jungo F, Laiho K, Le Mercier P, Lieberherr D, Lock A, Lussi Y, MacDougall A, Ma-Grane M, Martin MJ, Masson P, Natale DA, Hyka-Nouspikel N, Orchard S, Pedruzzi I, Pourcel L, Poux S, Pundir S, Rivoire C, Speretta E, Sundaram S, Tyagi N, Warner K, Zaru R, Wu CH, Diehl AD, Chan JN, Grove C, Lee RYN, Muller HM, Raciti D, van Auken K, Sternberg PW, Berriman M, Paulini M, Howe K, Gao S, Wright A, Stein L, Howe DG, Toro S, Westerfield M, Jaiswal P, Cooper L, Elser J. The Gene Ontology resource: Enriching a GOld mine. *Nucleic Acids Res*. 2021;49(D1):D325-D334. doi:10.1093/nar/gkaa1113

174. Yu G. clusterProfiler: statistical analysis and visualization of functional profiles for genes and gene clusters. Published online 2020. https://yulab-smu.top/biomedical-knowledge-mining-book/

175. Yu G, Li F, Qin Y, Bo X, Wu Y, Wang S. GOSemSim: an R package for measuring semantic similarity among GO terms and gene products. *Bioinformatics*. 2010;26(7):976-978. doi:10.1093/bioinformatics/btq064

176. Martinez-Sanchez A, Laugks U, Kochovski Z, Papantoniou C, Zinzula L, Baumeister W, Lučić V. Trans-synaptic assemblies link synaptic vesicles and neuroreceptors. *Sci Adv*. 2021;7(10). doi:10.1126/sciadv.abe6204

177. Rappsilber J, Mann M, Ishihama Y. Protocol for micro-purification, enrichment, pre-fractionation and storage of peptides for proteomics using StageTips. *Nat Protoc*. 2007;2(8). doi:10.1038/nprot.2007.261

178. Gabriel LR, Wu S, Melikian HE. Brain slice biotinylation: An ex vivo approach to measure region-

specific plasma membrane protein trafficking in adult neurons. *J Vis Exp*. 2014;(86). doi:10.3791/51240

179. Cox J, Mann M. MaxQuant enables high peptide identification rates, individualized p.p.b.-range mass accuracies and proteome-wide protein quantification. *Nat Biotechnol*. 2008;26(12). doi:10.1038/nbt.1511

180. Prianichnikov N, Koch H, Koch S, Lubeck M, Heilig R, Brehmer S, Fischer R, Cox J. Maxquant software for ion mobility enhanced shotgun proteomics. *Mol Cell Proteomics*. 2020;19(6). doi:10.1074/mcp.TIR119.001720

181. Yuan M, Breitkopf SB, Yang X, Asara JM. A positive/negative ion-switching, targeted mass spectrometry-based metabolomics platform for bodily fluids, cells, and fresh and fixed tissue. *Nat Protoc*. 2012;7(5). doi:10.1038/nprot.2012.024

182. Tyanova S, Temu T, Sinitcyn P, Carlson A, Hein MY, Geiger T, Mann M, Cox J. The Perseus computational platform for comprehensive analysis of (prote)omics data. *Nat Methods*. 2016;13(9). doi:10.1038/nmeth.3901

183. Engelhardt C, Boulat B, Czisch M, Schmidt M V. Lack of FKBP51 Shapes Brain Structure and Connectivity in Male Mice. *J Magn Reson Imaging*. 2021;53(5). doi:10.1002/jmri.27439

184. Ruat J, Heinz DE, Binder FP, Stark T, Neuner R, Hartmann A, Kaplick PM, Chen A, Czisch M, Wotjak CT. Structural correlates of trauma-induced hyperarousal in mice. *Prog Neuro-Psychopharmacology Biol Psychiatry*. 2021;111. doi:10.1016/j.pnpbp.2021.110404

185. Hikishima K, Komaki Y, Seki F, Ohnishi Y, Okano HJ, Okano H. In vivo microscopic voxel-based morphometry with a brain template to characterize strainspecific structures in the mouse brain. *Sci Rep*. 2017;7(1). doi:10.1038/s41598-017-00148-1

186. Manjón J V., Coupé P, Martí-Bonmatí L, Collins DL, Robles M. Adaptive non-local means denoising of MR images with spatially varying noise levels. *J Magn Reson Imaging*. 2010;31(1). doi:10.1002/jmri.22003

187. Refojo D, Schweizer M, Kuehne C, Ehrenberg S, Thoeringer C, Vogl AM, Dedic N, Schumacher M, Von Wolff G, Avrabos C, Touma C, Engblom D, Schütz G, Nave KA, Eder M, Wotjak CT, Sillaber I, Holsboer F, Wurst W, Deussing JM. Glutamatergic and dopaminergic neurons mediate anxiogenic and anxiolytic effects of CRHR1. *Science (80-)*. 2011;333(6051):1903-1907. doi:10.1126/science.1202107

188. Semple BD, Blomgren K, Gimlin K, Ferriero DM, Noble-Haeusslein LJ. Brain development in rodents and humans: Identifying benchmarks of maturation and vulnerability to injury across species. *Prog Neurobiol*. 2013;106-107. doi:10.1016/j.pneurobio.2013.04.001

189. Rodgers RJ, Dalvi A. Anxiety, defence and the elevated plus-maze. In: *Neuroscience and Biobehavioral Reviews*. Vol 21. ; 1997. doi:10.1016/S0149-7634(96)00058-9

190. Wang JZ, Du Z, Payattakool R, Yu PS, Chen CF. A new method to measure the semantic similarity of GO terms. *Bioinformatics*. 2007;23(10):1274-1281. doi:10.1093/bioinformatics/btm087

191. Yoboue ED, Devin A. Reactive oxygen species-mediated control of mitochondrial biogenesis. *Int J Cell Biol*. Published online 2012. doi:10.1155/2012/403870

192. Lie E, Li Y, Kim R, Kim E. SALM/Lrfn family synaptic adhesion molecules. *Front Mol Neurosci*. 2018;11. doi:10.3389/fnmol.2018.00105

193. Takahashi H, Katayama KI, Sohya K, Miyamoto H, Prasad T, Matsumoto Y, Ota M, Yasuda H, Tsumoto T, Aruga J, Craig AM. Selective control of inhibitory synapse development by Slitrk3-PTPδ trans-synaptic interaction. *Nat Neurosci*. 2012;15(3). doi:10.1038/nn.3040

194. Aruga J, Mikoshiba K. Identification and characterization of Slitrk, a novel neuronal transmembrane protein family controlling neurite outgrowth. *Mol Cell Neurosci*. 2003;24(1). doi:10.1016/S1044-7431(03)00129-5

195. Reinke H, Asher G. Crosstalk between metabolism and circadian clocks. *Nat Rev Mol Cell Biol*. 2019;20(4):227-241. doi:10.1038/s41580-018-0096-9

196. Hopp, Grüter, Hottiger. Regulation of Glucose Metabolism by NAD+ and ADP-Ribosylation. *Cells*. 2019;8(8). doi:10.3390/cells8080890

197. Kumar A. Long-term potentiation at CA3-CA1 hippocampal synapses with special emphasis on aging, disease, and stress. *Front Aging Neurosci*. 2011;3(MAY):1-20. doi:10.3389/fnagi.2011.00007

198. Vorhees C V., Williams MT. Morris water maze: Procedures for assessing spatial and related forms of learning and memory. *Nat Protoc*. 2006;1(2). doi:10.1038/nprot.2006.116

199. Kassambara A, Kosinski M, Biecek P. survminer: Drawing Survival Curves using ggplot2. Published online 2021. https://rpkgs.datanovia.com/survminer/index.html

200. Kaplan EL, Meier P. Nonparametric Estimation from Incomplete Observations. *J Am Stat Assoc*. 1958;53(282). doi:10.1080/01621459.1958.10501452

201. Genewsky A, Albrecht N, Bura S, Kaplick P, Heinz D, Nußbaumer M, Engel M, Grünecker B, Kaltwasser S, Riebe C, Bedenk B, Czisch M, Wotjak C. How much fear is in anxiety? *bioRxiv*. Published online 2018. doi:10.1101/385823

202. Fiumara A, Pittalà A, Cocuzza M, Sorge G. Epilepsy in patients with Angelman syndrome. *Ital J Pediatr*. 2010;36. doi:10.1186/1824-7288-36-31

203. Asok A, Kandel ER, Rayman JB. The neurobiology of fear generalization. *Front Behav Neurosci*. 2019;12. doi:10.3389/fnbeh.2018.00329

204. Spychala A, Rüther U. FTO affects hippocampal function by regulation of BDNF processing. *PLoS One*. 2019;14(2). doi:10.1371/journal.pone.0211937

205. Mang GM, Pradervand S, Du NH, Arpat AB, Preitner F, Wigger L, Gatfield D, Franken P. A neuron-specific deletion of the microRNA-processing enzyme dicer induces severe but transient obesity in mice. *PLoS One*. 2015;10(1). doi:10.1371/journal.pone.0116760

206. Zhou X, Gomez-Smith M, Qin Z, Duquette PM, Cardenas-Blanco A, Rai PS, Harper ME, Tsai EC, Anisman H, Chen HH. Ablation of LMO4 in glutamatergic neurons impairs leptin control of fat metabolism. *Cell Mol Life Sci*. 2012;69(5). doi:10.1007/s00018-011-0794-3

207. Weyn-Vanhentenryck SM, Feng H, Ustianenko D, Duffié R, Yan Q, Jacko M, Martinez JC, Goodwin M, Zhang X, Hengst U, Lomvardas S, Swanson MS, Zhang C. Precise temporal regulation of alternative splicing during neural development. *Nat Commun*. 2018;9(1). doi:10.1038/s41467-018-04559-0

208. Lipscombe D, Andrade A, Allen SE. Alternative splicing: Functional diversity among voltage-gated calcium channels and behavioral consequences. *Biochim Biophys Acta - Biomembr*. 2013;1828(7). doi:10.1016/j.bbamem.2012.09.018

209. Regan MC, Grant T, McDaniel MJ, Karakas E, Zhang J, Traynelis SF, Grigorieff N, Furukawa H. Structural Mechanism of Functional Modulation by Gene Splicing in NMDA Receptors. *Neuron*. 2018;98(3). doi:10.1016/j.neuron.2018.03.034

210. Dai J, Aoto J, Südhof TC. Alternative Splicing of Presynaptic Neurexins Differentially Controls Postsynaptic NMDA and AMPA Receptor Responses. *Neuron*. 2019;102(5). doi:10.1016/j.neuron.2019.03.032

211. Ko J, Kim S, Chung HS, Kim K, Han K, Kim H, Jun H, Kaang BK, Kim E. SALM Synaptic Cell Adhesion-like Molecules Regulate the Differentiation of Excitatory Synapses. *Neuron*. 2006;50(2). doi:10.1016/j.neuron.2006.04.005

212. Wang CY, Chang K, Petralia RS, Wang YX, Seabold GK, Wenthold RJ. A novel family of adhesion-like molecules that interacts with the NMDA receptor. *J Neurosci*. 2006;26(8). doi:10.1523/JNEUROSCI.3799-05.2006

213. Brouwer M, Farzana F, Koopmans F, Chen N, Brunner JW, Oldani S, Li KW, van Weering JR, Smit AB, Toonen RF, Verhage M. SALM 1 controls synapse development by promoting F-actin/PIP2-dependent Neurexin clustering. *EMBO J*. 2019;38(17). doi:10.15252/embj.2018101289

214. Wang PY, Seabold GK, Wenthold RJ. Synaptic adhesion-like molecules (SALMs) promote neurite outgrowth. *Mol Cell Neurosci*. 2008;39(1). doi:10.1016/j.mcn.2008.05.019

215. Quan T, Zhou H, Li J, Li S, Li A, Li Y, Lv X, Luo Q, Gong H, Zeng S. NeuroGPS-Tree: Automatic reconstruction of large-scale neuronal populations with dense neurites. *Nat Methods*. 2015;13(1). doi:10.1038/nmeth.3662

216. Wang X, Huang N, Yang M, Wei D, Tai H, Han X, Gong H, Zhou J, Qin J, Wei X, Chen H, Fang T, Xiao H. FTO is required for myogenesis by positively regulating mTOR-PGC-1α pathway-mediated mitochondria biogenesis. *Cell Death Dis*. 2017;8(3). doi:10.1038/cddis.2017.122

217. Kang H, Zhang Z, Yu L, Li Y, Liang M, Zhou L. FTO reduces mitochondria and promotes hepatic fat accumulation through RNA demethylation. *J Cell Biochem*. 2018;119(7). doi:10.1002/jcb.26746

218. Yadav PK, Rajasekharan R. The m6A methyltransferase Ime4 and mitochondrial functions in yeast. *Curr Genet*. 2018;64(2). doi:10.1007/s00294-017-0758-8

219. Xie N, Zhang L, Gao W, Huang C, Huber PE, Zhou X, Li C, Shen G, Zou B. NAD+ metabolism: pathophysiologic mechanisms and therapeutic potential. *Signal Transduct Target Ther*. 2020;5(1). doi:10.1038/s41392-020-00311-7

220. Katsyuba E, Romani M, Hofer D, Auwerx J. NAD+ homeostasis in health and disease. *Nat Metab*. 2020;2(1). doi:10.1038/s42255-019-0161-5

221. Navas LE, Carnero A. NAD+ metabolism, stemness, the immune response, and cancer. *Signal Transduct Target Ther*. 2021;6(1). doi:10.1038/s41392-020-00354-w

222. Lee CF, Caudal A, Abell L, Nagana Gowda GA, Tian R. Targeting NAD+ Metabolism as Interventions for Mitochondrial Disease. *Sci Rep*. 2019;9(1). doi:10.1038/s41598-019-39419-4

223. Schröder H, Moser N, Huggenberger S. The Mouse Thalamus. In: *Neuroanatomy of the Mouse: An Introduction*. Springer International Publishing; 2020:171-203. doi:10.1007/978-3-030-19898-5_8

224. Lee CC. Thalamic and cortical pathways supporting auditory processing. *Brain Lang*. 2013;126(1). doi:10.1016/j.bandl.2012.05.004

225. Anderson LA, Linden JF. Physiological differences between histologically defined subdivisions in the mouse auditory thalamus. *Hear Res*. 2011;274(1-2). doi:10.1016/j.heares.2010.12.016

226. Vasquez-Lopez SA, Weissenberger Y, Lohse M, Keating P, King AJ, Dahmen JC. Thalamic input to auditory cortex is locally heterogeneous but globally tonotopic. *Elife*. 2017;6. doi:10.7554/eLife.25141

227. Sowers LP, Wang M, Rea BJ, Taugher RJ, Kuburas A, Kim Y, Wemmie JA, Walker CS, Hay DL, Russo AF. Stimulation of Posterior Thalamic Nuclei Induces Photophobic Behavior in Mice. *Headache*. 2020;60(9). doi:10.1111/head.13917

228. Steriade M, McCormick DA, Sejnowski TJ. Thalamocortical oscillations in the sleeping and aroused brain. *Science (80-)*. 1993;262(5134). doi:10.1126/science.8235588

229. Gent TC, Bassetti C LA, Adamantidis AR. Sleep-wake control and the thalamus. *Curr Opin Neurobiol*. 2018;52. doi:10.1016/j.conb.2018.08.002

230. Urbain N, Fourcaud-Trocmé N, Laheux S, Salin PA, Gentet LJ. Brain-State-Dependent Modulation of Neuronal Firing and Membrane Potential Dynamics in the Somatosensory Thalamus during Natural Sleep. *Cell Rep*. 2019;26(6). doi:10.1016/j.celrep.2019.01.038

231. Zhang J, Engel JA, Ericson M, Svensson L. Involvement of the medial geniculate body in prepulse inhibition of acoustic startle. *Psychopharmacology (Berl)*. 1999;141(2). doi:10.1007/s002130050824

232. You Q long, Luo Z cai, Luo Z yi, Kong Y, Li Z lin, Yang J ming, Li X wen, Gao T ming. Involvement of the thalamic reticular nucleus in prepulse inhibition of acoustic startle. *Transl Psychiatry*. 2021;11(1). doi:10.1038/s41398-021-01363-1

233. Schuelert N, Dorner-Ciossek C, Brendel M, Rosenbrock H. A comprehensive analysis of auditory event-related potentials and network oscillations in an NMDA receptor antagonist mouse model using a novel wireless recording technology. *Physiol Rep*. 2018;6(16). doi:10.14814/phy2.13782

234. Wang CY, Yeh JK, Shie S Sen, Hsieh IC, Wen MS. Circadian rhythm of RNA N6-methyladenosine and the role of cryptochrome. *Biochem Biophys Res Commun*. 2015;465(1). doi:10.1016/j.bbrc.2015.07.135

235. Fustin JM, Doi M, Yamaguchi Y, Hida H, Nishimura S, Yoshida M, Isagawa T, Morioka MS, Kakeya H, Manabe I, Okamura H. RNA-methylation-dependent RNA processing controls the speed of the circadian clock. *Cell*. 2013;155(4). doi:10.1016/j.cell.2013.10.026

236. Izumo M, Pejchal M, Schook AC, Lange RP, Walisser JA, Sato TR, Wang X, Bradfield CA, Takahashi JS. Differential effects of light and feeding on circadian organization of peripheral clocks in a forebrain Bmal1 mutant. *Elife*. 2014;3. doi:10.7554/eLife.04617

237. Yang G, Chen L, Zhang J, Ren B, FitzGerald GA. Bmal1 deletion in mice facilitates adaptation to disrupted light/dark conditions. *JCI Insight*. 2019;4(10). doi:10.1172/jci.insight.125133

238. Casanova E, Fehsenfeld S, Mantamadiotis T, Lemberger T, Greiner E, Stewart AF, Schtz G. A CamKIIα iCre BAC allows brain-specific gene inactivation. *Genesis*. 2001;31(1). doi:10.1002/gene.1078

239. Ieraci A, Mallei A, Popoli M. Social Isolation Stress Induces Anxious-Depressive-Like Behavior and Alterations of Neuroplasticity-Related Genes in Adult Male Mice. *Neural Plast*. 2016;2016. doi:10.1155/2016/6212983

240. Koike H, Ibi D, Mizoguchi H, Nagai T, Nitta A, Takuma K, Nabeshima T, Yoneda Y, Yamada K. Behavioral abnormality and pharmacologic response in social isolation-reared mice. *Behav Brain Res*. 2009;202(1). doi:10.1016/j.bbr.2009.03.028

241. Medendorp WE, Petersen ED, Pal A, Wagner LM, Myers AR, Hochgeschwender U, Jenrow KA. Altered behavior in mice socially isolated during adolescence corresponds with immature dendritic spine morphology and impaired plasticity in the prefrontal cortex. *Front Behav Neurosci*. 2018;12. doi:10.3389/fnbeh.2018.00087

242. Stanford SC. The Open Field Test: Reinventing the wheel. *J Psychopharmacol*. 2007;21(2). doi:10.1177/0269881107073199

243. Gentsch C, Lichtsteiner M, Feer H. Locomotor activity, defecation score and corticosterone levels during an openfield exposure: A comparison among individually and group-housed rats, and genetically selected rat lines. *Physiol Behav*. 1981;27(1). doi:10.1016/0031-9384(81)90320-6

244. Prut L, Belzung C. The open field as a paradigm to measure the effects of drugs on anxiety-like behaviors: A review. *Eur J Pharmacol*. 2003;463(1-3). doi:10.1016/S0014-2999(03)01272-X

245. Thiels E, Hoffman EK, Gorin MB. A reliable behavioral assay for the assessment of sustained photophobia in mice. *Curr Eye Res*. 2008;33(5-6). doi:10.1080/02713680802130347

246. Errico F, Nisticò R, Napolitano F, Mazzola C, Astone D, Pisapia T, Giustizieri M, D'Aniello A, Mercuri NB, Usiello A. Increased d-aspartate brain content rescues hippocampal age-related synaptic plasticity deterioration of mice. *Neurobiol Aging*. 2011;32(12). doi:10.1016/j.neurobiolaging.2010.01.002

247. Errico F, Nisticò R, Palma G, Federici M, Affuso A, Brilli E, Topo E, Centonze D, Bernardi G, Bozzi Y, D'Aniello A, Di Lauro R, Mercuri NB, Usiello A. Increased levels of d-aspartate in the hippocampus enhance LTP but do not facilitate cognitive flexibility. *Mol Cell Neurosci*. 2008;37(2). doi:10.1016/j.mcn.2007.09.012

248. Luo L, Ambrozkiewicz MC, Benseler F, Chen C, Dumontier E, Falkner S, Furlanis E, Gomez AM, Hoshina N, Huang WH, Hutchison MA, Itoh-Maruoka Y, Lavery LA, Li W, Maruo T, Motohashi J, Pai ELL, Pelkey KA, Pereira A, Philips T, Sinclair JL, Stogsdill JA, Traunmüller L, Wang J, Wortel J, You W, Abumaria N, Beier KT, Brose N, Burgess HA, Cepko CL, Cloutier JF, Eroglu C, Goebbels S, Kaeser PS, Kay JN, Lu W, Luo L, Mandai K, McBain CJ, Nave KA, Prado MAM, Prado VF, Rothstein J, Rubenstein JLR, Saher G, Sakimura K, Sanes JR, Scheiffele P, Takai Y, Umemori H, Verhage M, Yuzaki M, Zoghbi HY, Kawabe H, Craig AM. Optimizing Nervous System-Specific Gene Targeting with Cre Driver Lines: Prevalence of Germline Recombination and Influencing Factors. *Neuron*. 2020;106(1). doi:10.1016/j.neuron.2020.01.008

249. Harden C, Tomson T, Gloss D, Buchhalter J, Cross JH, Donner E, French JA, Gil-Nagel A, Hesdorffer DC, Smithson WH, Spitz MC, Walczak TS, Sander JW, Ryvlin P. Practice guideline summary: Sudden unexpected death in epilepsy incidence rates and risk factors. *Neurology*. 2017;88(17). doi:10.1212/wnl.0000000000003685

250. Aiba I, Noebels JL. Spreading depolarization in the brainstem mediates sudden cardiorespiratory arrest in mouse SUDEP models. *Sci Transl Med*. 2015;7(282). doi:10.1126/scitranslmed.aaa4050

251. Jentsch TJ. Neuronal KCNQ potassium channels: Physislogy and role in disease. *Nat Rev Neurosci*. 2000;1(1). doi:10.1038/35036198

252. Kaplan DI, Isom LL, Petrou S. Role of sodium channels in epilepsy. *Cold Spring Harb Perspect Med*. 2016;6(6). doi:10.1101/cshperspect.a022814

253. Swahari V, Nakamura A, Hollville E, Stroud H, Simon JM, Ptacek TS, Beck M V., Flowers C, Guo J, Plestant C, Liang J, Kurtz CL, Kanke M, Hammond SM, He YW, Anton ES, Sethupathy P, Moy SS, Greenberg ME, Deshmukh M. MicroRNA-29 is an essential regulator of brain maturation through regulation of CH methylation. *Cell Rep*. 2021;35(1). doi:10.1016/j.celrep.2021.108946

254. Shen S, Park JW, Lu ZX, Lin L, Henry MD, Wu YN, Zhou Q, Xing Y. rMATS: Robust and flexible detection of differential alternative splicing from replicate RNA-Seq data. *Proc Natl Acad Sci U S A*. 2014;111(51). doi:10.1073/pnas.1419161111

255. Li YI, Knowles DA, Humphrey J, Barbeira AN, Dickinson SP, Im HK, Pritchard JK. Annotation-free quantification of RNA splicing using LeafCutter. *Nat Genet*. 2018;50(1). doi:10.1038/s41588-017-0004-9

256. Coots RA, Liu XM, Mao Y, Dong L, Zhou J, Wan J, Zhang X, Qian SB. m6A Facilitates eIF4F-Independent mRNA Translation. *Mol Cell*. 2017;68(3). doi:10.1016/j.molcel.2017.10.002

257. D'Aniello A, Di Fiore MM, Fisher GH, Milone A, Seleni A, D'Aniello S, Perna AF, Ingrosso D. Occurrence of D-aspartic acid and N-methyl-D-aspartic acid in rat neuroendocrine tissues and their role in the modulation of luteinizing hormone and growth hormone release. *FASEB J*. 2000;14(5). doi:10.1096/fasebj.14.5.699

258. Punzo D, Errico F, Cristino L, Sacchi S, Keller S, Belardo C, Luongo L, Nuzzo T, Imperatore R, Florio E, De Novellis V, Affinito O, Migliarini S, Maddaloni G, Sisalli MJ, Pasqualetti M, Pollegioni L, Maione S, Chiariotti L, Usiello A. Age-related changes in D-aspartate oxidase promoter methylation control extracellular D-aspartate levels and prevent precocious cell death during brain aging. *J Neurosci*. 2016;36(10). doi:10.1523/JNEUROSCI.3881-15.2016

259. Hashimoto A, Kumashiro S, Nishikawa T, Oka T, Takahashi K, Mito T, Takashima S, Doi N, Mizutani Y, Yamazaki T, Kaneko T, Ootomo E. Embryonic Development and Postnatal Changes in Free d-Aspartate and d-Serine in the Human Prefrontal Cortex. *J Neurochem*. 1993;61(1). doi:10.1111/j.1471-4159.1993.tb03575.x

260. Errico F, Nisticò R, Di Giorgio A, Squillace M, Vitucci D, Galbusera A, Piccinin S, Mango D, Fazio L, Middei S, Trizio S, Mercuri NB, Teule MA, Centonze D, Gozzi A, Blasi G, Bertolino A, Usiello A. Free D-aspartate regulates neuronal dendritic morphology, synaptic plasticity, gray matter volume and brain activity in mammals. *Transl Psychiatry*. 2014;4. doi:10.1038/tp.2014.59

261. Keller SS, Wieshmann UC, Mackay CE, Denby CE, Webb J, Roberts N. Voxel based morphometry of grey matter abnormalities in patients with medically intractable temporal lobe epilepsy: Effects of side of seizure onset and epilepsy duration. *J Neurol Neurosurg Psychiatry*. 2002;73(6). doi:10.1136/jnnp.73.6.648

262. Bonilha L, Rorden C, Castellano G, Pereira F, Rio PA, Cendes F, Li LM. Voxel-based morphometry reveals gray matter network atrophy in refractory medial temporal lobe epilepsy. *Arch Neurol*. 2004;61(9). doi:10.1001/archneur.61.9.1379

263. Beheshti I, Sone D, Farokhian F, Maikusa N, Matsuda H. Gray matter and white matter abnormalities in temporal lobe epilepsy patients with and without hippocampal sclerosis. *Front Neurol*. 2018;9(MAR). doi:10.3389/fneur.2018.00107

264. Frank L, Lüpke M, Kostic D, Löscher W, Tipold A. Grey matter volume in healthy and epileptic beagles using voxel-based morphometry - a pilot study. *BMC Vet Res*. 2018;14(1). doi:10.1186/s12917-018-1373-8

265. Forkosh O, Karamihalev S, Roeh S, Alon U, Anpilov S, Touma C, Nussbaumer M, Flachskamm C, Kaplick PM, Shemesh Y, Chen A. Identity domains capture individual differences from across the behavioral repertoire. *Nat Neurosci*. 2019;22(12). doi:10.1038/s41593-019-0516-y

266. Asan L, Falfán-Melgoza C, Beretta CA, Sack M, Zheng L, Weber-Fahr W, Kuner T, Knabbe J. Cellular correlates of gray matter volume changes in magnetic resonance morphometry identified by two-photon microscopy. *Sci Rep*. 2021;11(1). doi:10.1038/s41598-021-83491-8

267. Benoit K, Obeng A. readtext: Import and Handling for Plain and Formatted Text Files. Published online 2020. https://github.com/quanteda/readtext

268. Wickham H. tidyverse: Easily Install and Load the Tidyverse. Published online 2021. https://cran.r-project.org/package=tidyverse

269. Ryan JA, Ulrich JM. xts: eXtensible Time Series. Published online 2020. https://github.com/joshuaulrich/xts

270. Spinu V, Grolemund G, Wickham H. lubridate: Make Dealing with Dates a Little Easier. Published online 2021. https://cran.r-project.org/package=lubridate

271. Wood S. mgcv: Mixed GAM Computation Vehicle with Automatic Smoothness Estimation. Published online 2021. https://cran.r-project.org/package=mgcv

272. Harrell Jr. FE. Hmisc: Harrell Miscellaneous. Published online 2021. https://cran.r-project.org/package=Hmisc

273. Kuznetsova A, Bruun Brockhoff P, Haubo Bojesen Christensen R. lmerTest: Tests in Linear Mixed Effects Models. Published online 2020. https://github.com/runehaubo/lmerTestR

274. Bates D, Maechler M, Bolker B, Walker S. lme4: Linear Mixed-Effects Models using Eigen and S4. Published online 2021. https://github.com/lme4/lme4/

275. Therneau TM. survival: Survival Analysis. Published online 2021. https://github.com/therneau/survival

276. Carlson M. org.Mm.eg.db: Genome wide annotation for Mouse. Published online 2020.

277. Alexa A, Rahnenfuhrer J. topGO: Enrichment Analysis for Gene Ontology. Published online 2020.

278. Sayols S. rrvgo: a Bioconductor package to reduce and visualize Gene Ontology terms. Published online 2020. https://ssayols.github.io/rrvgo

279. Shen L, of Medicine at Mount Sinai IS. GeneOverlap: Test and visualize gene overlaps. Published online 2020. http://shenlab-sinai.github.io/shenlab-sinai/

280. Wickham H, Chang W, Henry L, Pedersen TL, Takahashi K, Wilke C, Woo K, Yutani H, Dunnington D. ggplot2: Create Elegant Data Visualisations Using the Grammar of Graphics. Published online 2020. https://cran.r-project.org/package=ggplot2

281. Kassambara A. ggpubr: ggplot2 Based Publication Ready Plots. Published online 2020. https://rpkgs.datanovia.com/ggpubr/

282. Blighe K, Rana S, Lewis M. EnhancedVolcano: Publication-ready volcano plots with enhanced colouring and labeling. Published online 2021. https://github.com/kevinblighe/EnhancedVolcano

283. Chen H. VennDiagram: Generate High-Resolution Venn and Euler Plots. Published online 2018. https://cran.r-project.org/package=VennDiagram

284. Wilke CO. cowplot: Streamlined Plot Theme and Plot Annotations for ggplot2. Published online 2020. https://wilkelab.org/cowplot/

285. Urbanek S. png: Read and write PNG images. Published online 2013. http://www.rforge.net/png/

286. Clarke E, Sherrill-Mix S. ggbeeswarm: Categorical Scatter (Violin Point) Plots. Published online 2017. https://github.com/eclarke/ggbeeswarm

287. Wu T, Hu E, Xu S, Chen M, Guo P, Dai Z, Feng T, Zhou L, Tang W, Zhan L, Fu X, Liu S, Bo X, Yu G. clusterProfiler 4.0: A universal enrichment tool for interpreting omics data. *Innov*. 2021;2(3). doi:10.1016/j.xinn.2021.100141

8. Appendix

8.1 Locus and genotyping information

Summary of the locus and genotyping information for *Mettl3* (Figure 82, Table 1), *Wtap* (Figure 83, Table 3) and *Ythdc1* (Figure 84,Table 5 and Table 6). Additionally, details for the genotyping of Ai9 (Figure 82,Table 2), NexCreERT2 (Figure 83,Table 4) and Camk2aCre (Figure 84, Table 7) are provided.

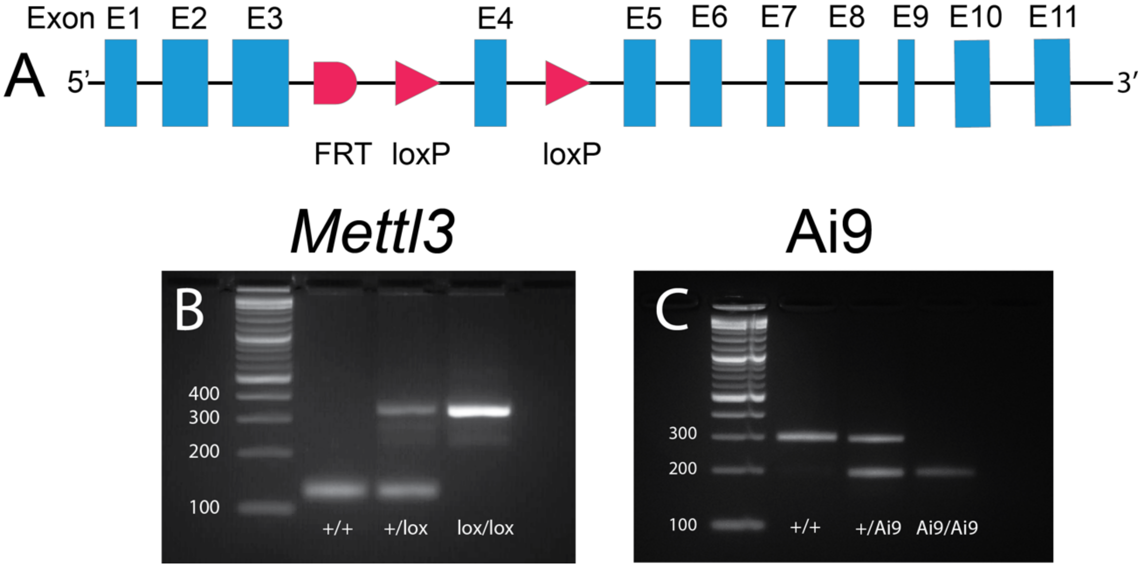

Figure 82: Locus and genotyping of *Mettl3* tm1c and genotyping of Ai9
(A) Overview of the tm1c *Mettl3* locus. **(B)** Genotyping of *Mettl3* animals: WT 128 bp (+/+), heterozygous 128 bp + 350 bp (+/lox) and homozygous 350 bp (lox/lox). **(C)** Genotyping of Ai9 carrying animals: WT 297 bp (+/+), heterozygous 297 bp + 196 bp (+/Ai9), and homozygous196 bp (Ai9/Ai9).

Table 1: Genotyping of *Mettl3*
Details on the genotyping for *Mettl3* tm1c, including primers, PCR settings and expected amplicons.

***Mettl3* tm1c PCR**	
Primer	**Sequence**
***Mettl3*_F**	5´-GTTGATGAAATTATCAGTACAATGGTTCTGA-3´
***Mettl3*_R**	5´-GTAAAGAACAACTCTGGTTATCGTCATCG-3´
PCR	**Amplicon**
95 °C 2 min [35x (95 °C 30 s, 59 °C 30 s, 72 °C 30 s)] 72 °C 2 min, 4 °C ∞	128 bp (+/+), 350 bp (tm1c)

Table 2: Genotyping for Ai9
Details on the genotyping for Ai9, including primers, PCR settings and expected amplicons.

Ai9 PCR	
Primer	**Sequence**
WT-F	5´-AAGGGAGCTGCAGTGGAGTA-3´
WT-R	5´-CCGAAAATCTGTGGGAAGTC-3´
Ai9-F	5´-CTGTTCCTGTACGGCATGG-3´
Ai9-R	5´-GGCATTAAAGCAGCGTATCC-3

PCR	**Amplicon**
95 °C 5 min [35x (95 °C 30 s, 57 °C 30 s, 72 °C 1 min)] 72 °C 5 min, 4 °C ∞	297 bp (+/+), 196 bp (Ai9)

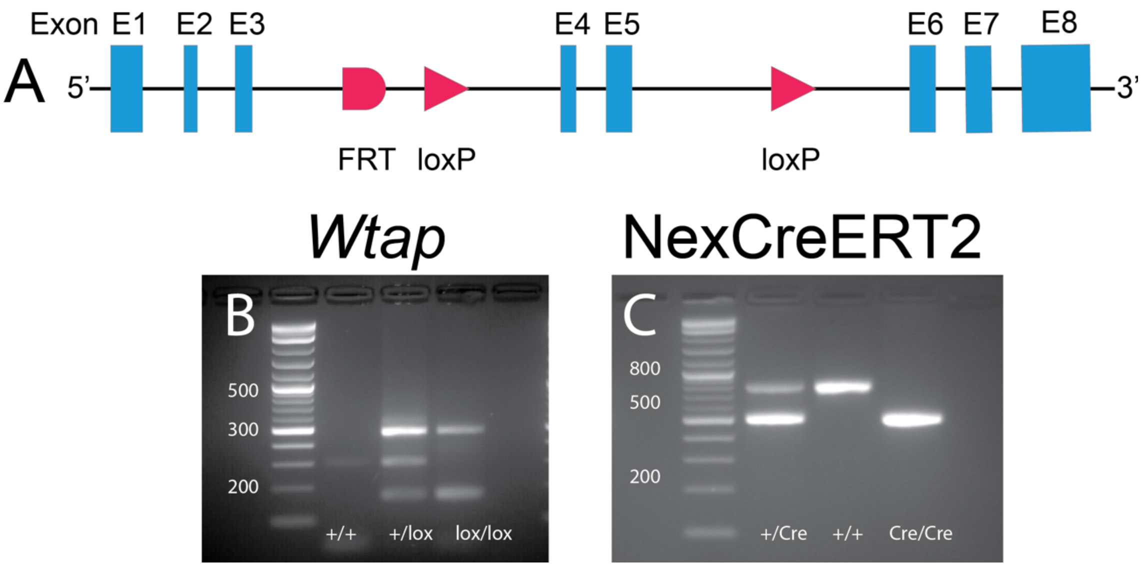

Figure 83: Locus and genotyping of *Wtap* tm1c animals and genotyping of NexCreERT2

(A) Overview of the tm1c *Wtap* locus. (**B**) Genotyping of *Wtap* animals: WT 295 bp (+/+), heterozygous 295 bp + 466 bp (+/lox) and homozygous 466 bp (lox/lox). The band below 200 bp is unspecific and not indicative of the genotype. (**C**) Genotyping of NexCreERT2 carrying animals: WT 770 bp (+/+), heterozygous 770 bp + 525 bp (+/CreERT2), and homozygous 525 bp (CreERT2/CreERT2).

Table 3: Genotyping for *Wtap*

Details on the genotyping for *Wtap* tm1a/tm1c, including primers, PCR settings and expected amplicons.

***Wtap* tm1a/tm1c PCR**	
Primer	**Sequence**
***Wtap*_5mut-R1**	5'-GAACTTCGGAATAGGAACTTCG-3'
***Wtap*_5arm-WTF**	5'-CCTCAAATTAGAGATCTCCCTTAGTC-3'
***Wtap*_Crit-WTR**	5'-GCTTGGCACCTTAGCAAGAC-3'
PCR	**Amplicon**
95 °C 3 min [39x (95 °C 30 s, 60 °C 30 s, 72 °C 1 min)] 72 °C 5 min, 4 °C ∞	169 bp (tm1a), 295 bp (+/+), 169 bp + 466 bp (tm1c)

Table 4: Genotyping for NexCreERT2

Details on the genotyping for NexCreERT2, including primers, PCR settings and expected amplicons.

NexCreERT2 PCR	
Primer	**Sequence**
WT/ NexCreERT2-F	5´-GAGTCCTGGAATCAGTCTTTTTC-3´
WT-R	5´-AGA ATGTGGAGTAGGGTGAC-3´
NexCreERT2-R	5´-CCGCATAACCAGTGAAACAG-3´
PCR	**Amplicon**
95 °C 5 min [35x (95 °C 30 s, 59 °C 30 s, 72 °C 1 min)] 72 °C 5 min, 4 °C ∞	770 bp (+/+), 525 bp (NexCreERT2)

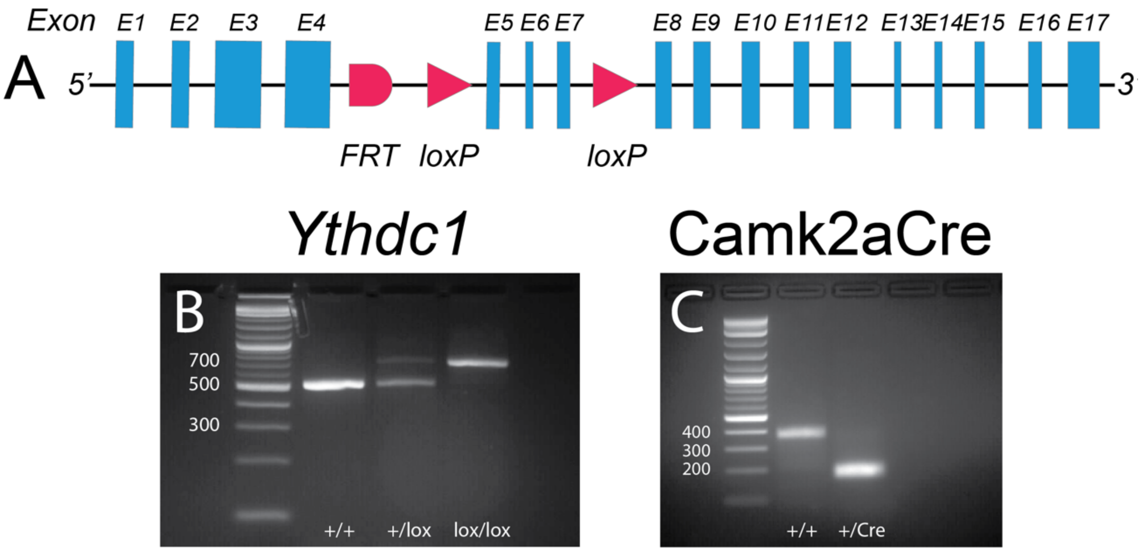

Figure 84: Locus and genotyping of *Ythdc1* tm1c animals and genotyping of Camk2aCre

(A) Overview of the tm1c *Ythdc1* locus. **(B)** Genotyping of *Ythdc1* animals: WT 488 bp (+/+), heterozygous 488 bp + 662 bp (+/lox) and homozygous 662 bp (lox/lox). **(C)** Genotyping of Camk2aCre carrying animals: WT 372 bp (+/+), heterozygous 372 bp + 183 bp (+/Cre). This PCR is not able to detect homozygous Cre.

Table 5: Genotyping for *Ythdc1*

Details on the genotyping for *Ythdc1* tm1a/tm1c, including primers, PCR settings and expected amplicons.

Ythdc1 tm1a/tm1c PCR	
Primer	**Sequence**
***Ythdc1*-F**	5'-TGAAGACATAGAAGTGGGGAAAC-3'
***Ythdc1*-R**	5'-ACAAACAAAAGATCCAGACAAGG-3'
***Ythdc1*-KO-R**	5'-ACCTTGGGCAAGAACATAAAGTG-3'
PCR	**Amplicon**
95 °C 5 min [35x (95 °C 30 s, 58 °C 30 s, 72 °C 30 s)] 72 °C 5 min, 4 °C ∞	488 bp (+/+), 662 bp (tm1c), 277 bp (tm1a)

Table 6: Genotyping for *Ythdc1* tm1d allele

Details on the genotyping for *Ythdc1* tm1d, including primers, PCR settings and expected amplicons.

***Ythdc1* tm1d PCR**	
Primer	**Sequence**
***Ythdc1*_tm1d_WT_F**	5'-TGTGTTGTGCCTGAGCTTTC-3'
***Ythdc1*_tm1d_WT _R**	5'-CCTTTGCTTTGGCAAGAGAC-3'
***Ythdc1*_tm1d_KO_F**	5'-AAGGCGCATAACGATACCAC-3'
***Ythdc1*_tm1d_KO_R**	5'-CCTAAACCCAGGTGACTGGA-3'
PCR	**Amplicon**
95 °C 5 min [35x (95 °C 30 s, 58 °C 30 s, 72 °C 30 s)] 72 °C 5 min, 4 °C ∞	245 bp (+/+), 199 bp (tm1d), 546 bp (unspecific regarding genotype)

Table 7: Genotyping for Camk2aCre

Details on the genotyping for Camk2aCre, including primers, PCR settings and expected amplicons.

Camk2aCre PCR

Primer	Sequence
Cre-F	5´-CCACCAGCCAGCTATCAACT-3´
Cre-R	5´-CAGCTTGCATGATCTCCGGT-3´
Thy1-F	5´-TCTGAGTGGCAAAGGACCTTAGG-3´
Thy1-R	5´-CCACTGGTGAGGTTGAGG-3´
PCR	**Amplicon**
95 °C 5 min [35x (95 °C 30 s, 57 °C 30 s, 72 °C 1 min)] 72 °C 5 min, 4 °C ∞	372 bp (+/+, Thy1 DNA control), 184 bp (Cre)

8.2 R packages

Overview of the main R packages used for data wrangling (Table 8), statistical analysis (Table 9), pathway analysis (Table 10) and data visualization (Table 11).

8.2.1.1 Data wrangling

Table 8: Packages used for data wrangling in R

Package	Version	Reference
readtext	0.8	[267]
tidyverse	1.3.1	[268]
xts	0.12	[269]
lubridate	1.7.1	[270]

8.2.1.2 Statistical analysis

Table 9: Packages used for statistical analysis in R

Package	Version	Reference
mgcv	1.8-35	[271]
Hmisc	4.5-0	[272]
lmertest	3.1-3	[273]
lme4	1.1-27	[274]
survival	3.2-11	[275]
survminer	0.4.9	[199]

8.2.1.3 Pathway analysis

Table 10: Packages used for pathway analysis in R

Package	Version	Reference
org.Mm.eg.db	3.12	[276]
clusterProfiler	3.19	[174]
topGO	2.42	[277]
rrvgo	1.2	[278]
GeneOverlap	1.26	[279]

8.2.1.4 Data visualization

Table 11: Packages used for data visualization in R

Package	Version	Reference
ggplot2	3.3.3	280
ggpubr	0.4.0	281
EnhancedVolcano	1.9.13	282
VennDiagram	1.6.20	283
cowplot	1.1.1	284
png	0.1-7	285
ggbeeswarm	0.6.0	286

8.3 Material and reagents

Overview of important materials and reagents used for immunostaining and histology (Table 12), RNA extraction and QC (Table 13), RT-qPCR and sequencing (Table 14), as well as the sequences of RT-qPCR primers used (Table 15).

8.3.1 Immunostaining and histology

Table 12: Reagents used for immunostaining and histology

Reagent or resource	Source	Identifier
DAPI Fluoromount-G®	SouthernBiotech	0100-20
Thermo Scientific™ SuperFrost Plus™ Adhesion slides	Thermo Scientific	J1800AMNZ
Coverslips Thickness: 1, 24 x 60 mm	Carl Roth	H878
Triton® X-100	Sigma Aldrich	9002-93-1
Normal Goat Serum	Sigma Aldrich	50062Z
Glycerol 86 %	Carl Roth	4043
Ethylene glycol	Sigma Aldrich	324558

8.3.2 RNA extraction and QC reagents

Table 13: Regents used for RNA extraction and quality control

Reagent or resource	Source	Identifier
RNaseZap™	Thermo Fisher Scientific	AM9780
Trichlormethan/Chloroform	Carl Roth	3313.1
Molecular Biology Grade Ethanol	Fisher BioReagents	BP2818-500
QIAzol Lysis Reagent	QIAGEN	79306
Nuclease-Free Water (not DEPC-Treated)	Ambion	AM9932
RNeasy Mini Ki	QIAGEN	74104
RNase-Free DNase Set	QIAGEN	79254
Zirconium Oxide Beads 0.5 mm	Next Advance	ZROB05
Diethyl pyrocarbonate	Sigma-Aldrich	D5758-100ML
TURBO DNase	Thermo Fisher Scientific	AM2238
Qubit™ RNA HS Assay Kit	Thermo Fisher Scientific	Q32855
Qubit™ RNA BR Assay	Thermo Fisher Scientific	Q10211

High Sensitivity RNA ScreenTape	Agilent	5067-5579
Agilent RNA 6000 Nano Kit	Agilent	5067-1511
RNA ScreenTape	Agilent	5067-5576

8.3.3 RT-qPCR, sequencing and m^{6}A

Table 14: Reagent used for RT-qPCR and sequencing

Reagent or resource	Source	Identifier
High-Capacity cDNA Reverse Transcription Kit with RNase Inhibitor	Applied Biosystems	4374966
QuantiFast SYBR Green PCR Kit	QIAGEN	204056; 204057
NEBNext Ultra II Directional RNA Library Prep Kit Illumina	New England Biolabs	E7760S
NEBNext® Multiplex Oligos for Illumina® (Index Primers Set 2); NEBNext® Multiplex Oligos for Illumina® (Index Primers Set 1)	New England Biolabs	7335S
NEBNext® Multiplex Oligos for Illumina® (Index Primers Set 2)	New England Biolabs	7500S
NEBNext® Poly(A) mRNA Magnetic Isolation Module	New England Biolabs	E7490L
Agilent High Sensitivity DNA Kit	Agilent	
EpiQuik m^{6}A RNA Methylation Quantification Kit (Colorimetric)	Epigentek	P-9005-48

8.3.4 qPCR primers

Table 15: RT-qPCR primers used in this study

Primer name	Sequence 5' 3'	Primer name	Sequence 5' 3'
Alkbh5_F2	ACAAGATTAGATGCACCGCG	Pgk1_E1E3_F	TGCCAAAATGTCGCTTTCCA
Alkbh5_R2	TGTCCATTTCCAGGATCCGG	Pgk1_E1E3_R	CCAGGTGGCTCATAAGGACA
Asphd2_E1E2_1_F	GTGTGCAGGAACGAGTCATC	Plcl2_E3E5_2_F	CTTAGTGAGCCCTACCCCAC
Asphd2_E1E2_1_R	TCCGGACCTGTATTGGGAAC	Plcl2_E3E5_2_R	AAAGCTCTCCACTGCCTTCT
Cbll1_E1E2_F	TCAAGACCACCCAAGGATCC	Polr2b_F1	CAAGACAAGGATCATATCTGATGG
Cbll1_E1E2_R	GACTGACTTCCGTTCCCACT	Polr2b_R1	AGAGTTTAGACGACGCAGGTG
Ckap4_E1E2_1_F	TCCTTCACGGCTTTCTCTGT	Rbm15_E1E2_F	AGGCCCATGTAAACTCCACA
Ckap4_E1E2_1_R	CTTCTCGGGCTGGTATGTCC	Rbm15_E1E2_R	TCTTCATGCCTTCCCACCTT
Drg1_E6E7_2_F	AGATGGGTACACAGTGAGGC	Rpl13a_F1	CACTCTGGAGGAGAAACGGAAGG
Drg1_E6E7_2_R	ACAGCTGACGACCTCATTGA	Rpl13a_R1	GCAGGCATGAGGCAAACAGTC
Ears2_E3E4_2_F	CTGCCTCCTCTAGACGGAAG	Sema6b_E9E10_F	CCACGTCATTCTTGCACACA
Ears2_E3E4_2_R	CCCTGTTTCTGTTTGCCACA	Sema6b_E9E10_R	TGGGGAAGCCACGTCTATTT
Epha7_all_E8E9_1_F	GTGTTCATGGTGTTCGGCTT	Slitrk3_E1E2_1_F	CAGGGGAATTGGGGTAGTCC
Epha7_all_E8E9_1_R	TCATCCCCTTCTTGGTCAGC	Slitrk3_E1E2_1_R	GACGGATACAATGCAGCCTC
Fto_F1	CTGAGGAAGGAGTGGCATG	Tomm34_E2E3_1_F	CGGATGCCACACTGTTATCG
Fto_R1	TCTCCACCTAAGACTTGTGC	Tomm34_E2E3_1_R	GCGTGCTACTTGAAGGATGG
Hnrnpa2b1_F1	GTGGAGGGAACTATGGTCCT	Ube2o_E13E14_2_F	CCAGCTCCTCTATCTTGGGG
Hnrnpa2b1_R1	TGAAGGCACCAACAAGAACT	Ube2o_E13E14_2_R	CAAAGTGGAAGTGGTGTGGG
Hnrnpc_F1	CAAACGTCAGCGTGTTTCAG	Uhrf1_E7E8_F	TGATGAGTGTGACATGGCCT
Hnrnpc_R1	TGGGGATGAGAAGGACAAGT	Uhrf1_E7E8_R	CTTCTCCCCTGCTTGTACCA
Hprt_E7E9_F	AGGACCTCTCGAAGTGTTGG	Vcpip1_E1E3_1_F	GCATCGACACACAACTCCAG

Hprt_E7E9_R	TTGCAGATTCAACTTGCGCT	Vcpip1_E1E3_1_R	GGAACTTCAGGAGCAAGCTG
Lrfn1_ E1E2_R	CGCCAGGTCATTCACTAGGA	Virma_F	CATTACGGCCGCTTAGTTCT
Lrfn1_E1E2_F	CTTGTGGCTGCTGAACTCAC	Virma_R	TACCACTGCCTCCACTAACA
Lrfn2_E1E2_1_F	CCACCATCTGCCTGCCTT	*Wtap*_E5E6_F	GTTGATCTCAGTTGGGCCAC
Lrfn2_E1E2_1_R	CCAAGCAGAGTCTCCATGGT	*Wtap*_E5E6_R	ACTAAAGCAGCAACAGCAGG
Mettl14_F1	AGACGCCTTCATCTCTTTGG	Ythdc1_E5E6_2_F	CTCGAGGCATATCACCCATT
Mettl14_R1	AGCCTCTCGATTTCCTCTGT	Ythdc1_E5E6_2_R	CAGCACGAACGGAAGATGATA
Mettl3_E4E3_F	AAAATTCTTGCACCTGGGCC	Ythdc2_F1	GTGGATACGCAAAGAAAGCC
Mettl3_E4E3_R	TGGCCTCTTCAGCATCAGAA	Ythdc2_R1	TCCATAGCCAGGAGTTCTGA
Mettl3_F1	ATTGAGAGACTGTCCCCTGG	Ythdf1_F1	CATTATGAGAAGCGCCAGGA
Mettl3_R1	AGCTTTGTAAGGAAGTGCGT	Ythdf1_R1	AGATGCAACAATCAACCCCG
Nceh1_E1E2_2_F	CTGGAAACTGATGCTGCTGG	Ythdf2_F1	ACCAACTCTAGGGACACTCA
Nceh1_E1E2_2_R	CGGACTTCTACCCCATCGAA	Ythdf2_R1	GGATAAGGAGATGCAACCGT
Nlgn2_PB1F	TGTCATGCTCAGCGCAGTAG	Ythdf3_F1	TGCACATTATGAAAAGCGTCA
Nlgn2_PB1R	GGTTTCAAGCCTATGTGCAGAT	Ythdf3_R1	AGATGCGCTGATGAAAACCA
Nrxn2_E15E16_F	TGCCCGAAATCTGGATCTCA	Zc3h13_E17E18_F	GCTGTTCTGCTACGAGTTGG
Nrxn2_E15E16_R	AAGCAGCCTTGAAAGCCATC	Zc3h13_E17E18_R	AAAGCAGCCATGTTGAGAGC

8.4 Circadian activity analysis: model summary

Overview of GAM model results from the home cage activity screening (Table 16, Table 17).

Table 16: Overview of the parameter estimates for home cage activity

ns = not significant, *: $p < 0.05$. **: $p < 0.01$, ***: $p < 0.001$, ****: $p < 0.0001$.

Effect	Estimate	Std. Error	CI.l	CI.u	t value	Pr(>|t|)	Symbol
(Intercept)	10.28	0.11	10.07	10.50	95.05	$0.0e^{+00}$	****
GenotypeKO	2.91	0.15	2.61	3.21	19.32	$1.2e^{-82}$	****
Formula: Genotype + s(as.numeric(time_bin_10min), k = 30) + s(as.numeric(time_bin_10min), by = as.ordered(Genotype), k = 30)							

Table 17: Overview of the smooth term estimates for home cage activity

ns = not significant, *: $p < 0.05$. **: $p < 0.01$, ***: $p < 0.001$, ****: $p < 0.0001$.

Smooth term	edf	Ref.df	F	p-value	Symbol
s(time_bin_10min)	28.98	29.00	114.07	0	****
s(time_bin_10min):as.ordered(Genotype)KO	26.60	28.51	27.62	0	****

8.5 Camk2aCre WTAP KO: proteomic GO analysis full results

Summary of all enrichment results for the mPFC (Table 18, Table 19, Table 20). dHPC (Table 21, Table 22, Table 23) and vHPC (Table 27, Table 28). Tables include the GeneRatio defined as number of input genes related to a selected GO term and divided by the total number of input genes (i.e., the ratio of input genes that are annotated for a given term) and the BgRatio, which is the size of the gene set divided by the size of the gene universe (i.e., the ratio of all genes that are annotated for a given term)[287].

mPFC: significantly downregulated proteins

Table 18: Camk2aCre WTAP KO: mPFC detailed results for BP

The analysis was performed with proteins for which a significant difference in the overall abundance was determined (FDR < 0.05).

ID	Description	GeneRatio	BgRatio	p.adjust
GO:0022900	electron transport chain	40/643	62/5690	0.0000
GO:0010257	NADH dehydrogenase complex assembly	26/643	39/5690	0.0000
GO:0032981	mitochondrial respiratory chain complex I assembly	26/643	39/5690	0.0000
GO:0007005	mitochondrion organization	77/643	293/5690	0.0000
GO:0046034	ATP metabolic process	49/643	157/5690	0.0000
GO:0006839	mitochondrial transport	35/643	132/5690	0.0001
GO:0043038	amino acid activation	17/643	42/5690	0.0002
GO:0043039	tRNA aminoacylation	17/643	42/5690	0.0002
GO:0006418	tRNA aminoacylation for protein translation	14/643	39/5690	0.0065
GO:0070585	protein localization to mitochondrion	18/643	63/5690	0.0172
GO:0043604	amide biosynthetic process	71/643	422/5690	0.0295
GO:0044281	small molecule metabolic process	117/643	775/5690	0.0343
GO:1990542	mitochondrial transmembrane transport	16/643	57/5690	0.0413

Table 19: Camk2aCre WTAP KO: mPFC detailed results for CC

The analysis was performed with proteins for which a significant difference in the overall abundance was determined (FDR < 0.05).

ID	Description	GeneRatio	BgRatio	p.adjust
GO:0098798	mitochondrial protein-containing complex	96/657	195/5731	0.0000
GO:0098803	respiratory chain complex	49/657	59/5731	0.0000
GO:0098800	inner mitochondrial membrane protein complex	63/657	96/5731	0.0000
GO:0070469	respirasome	50/657	63/5731	0.0000
GO:1990204	oxidoreductase complex	52/657	79/5731	0.0000

GO:0031975	envelope	147/657	627/5731	0.0000
GO:0070069	cytochrome complex	14/657	18/5731	0.0000
GO:0005759	mitochondrial matrix	52/657	183/5731	0.0000
GO:0000313	organellar ribosome	24/657	62/5731	0.0000

Table 20: Camk2aCre WTAP KO: mPFC detailed results for MF

The analysis was performed with proteins for which a significant difference in the overall abundance was determined (FDR < 0.05).

ID	Description	GeneRatio	BgRatio	p.adjust
GO:0016491	oxidoreductase activity	73/637	343/5647	0.0000
GO:0051539	4 iron, 4 sulfur cluster binding	10/637	21/5647	0.0015
GO:0004812	aminoacyl-tRNA ligase activity	14/637	40/5647	0.0025
GO:0016875	ligase activity, forming carbon-oxygen bonds	14/637	40/5647	0.0025
GO:0140101	catalytic activity, acting on a tRNA	18/637	66/5647	0.0088

dHPC: significantly downregulated proteins

Table 21: Camk2aCre WTAP KO: dHPC detailed results for BP

The analysis was performed with proteins for which a significant difference in the overall abundance was determined (FDR < 0.05).

ID	Description	GeneRatio	BgRatio	p.adjust
GO:0010257	NADH dehydrogenase complex assembly	17/548	41/5526	0.0002
GO:0032981	mitochondrial respiratory chain complex I assembly	17/548	41/5526	0.0002
GO:0022900	electron transport chain	20/548	60/5526	0.0004
GO:0007005	mitochondrion organization	49/548	278/5526	0.0111

Table 22: Camk2aCre WTAP KO: dHPC detailed results for CC

The analysis was performed with proteins for which a significant difference in the overall abundance was determined (FDR < 0.05).

ID	Description	GeneRatio	BgRatio	p.adjust
GO:0070469	respirasome	28/549	62/5563	0.0000
GO:0005746	mitochondrial respirasome	27/549	58/5563	0.0000
GO:0098803	respiratory chain complex	27/549	59/5563	0.0000
GO:0098798	mitochondrial protein-containing complex	49/549	184/5563	0.0000

GO:1990204	oxidoreductase complex	29/549	80/5563	0.0000
GO:0031975	envelope	93/549	601/5563	0.0001
GO:0000315	organellar large ribosomal subunit	11/549	35/5563	0.0085
GO:0005762	mitochondrial large ribosomal subunit	11/549	35/5563	0.0085
GO:0070069	cytochrome complex	7/549	17/5563	0.0159

Table 23: Camk2aCre WTAP KO: dHPC detailed results for MF

The analysis was performed with proteins for which a significant difference in the overall abundance was determined (FDR < 0.05).

ID	Description	GeneRatio	BgRatio	p.adjust
GO:0009055	electron transfer activity	20/538	58/5492	0.0001
GO:0016655	oxidoreductase activity, acting on NAD(P)H, quinone or similar compound as acceptor	10/538	31/5492	0.0329

vHPC: significantly downregulated proteins

Table 24: Camk2aCre WTAP KO: vHPC detailed results for CC (down)

The analysis was performed with proteins for which a significant difference in the overall abundance was determined (FDR < 0.05).

ID	Description	GeneRatio	BgRatio	p.adjust
GO:0005747	mitochondrial respiratory chain complex I	20/876	42/5792	0.0001
GO:0030964	NADH dehydrogenase complex	20/876	42/5792	0.0001
GO:0045271	respiratory chain complex I	20/876	42/5792	0.0001
GO:0098798	mitochondrial protein-containing complex	54/876	197/5792	0.0005
GO:1990204	oxidoreductase complex	28/876	81/5792	0.0006
GO:0070469	respirasome	23/876	64/5792	0.0015
GO:0000313	organellar ribosome	19/876	63/5792	0.0485
GO:0005761	mitochondrial ribosome	19/876	63/5792	0.0485

vHPC: significantly upregulated proteins

Table 25:Camk2aCre WTAP KO: vHPC detailed results for CC (UP)

The analysis was performed with proteins for which a significant difference in the overall abundance was determined (FDR < 0.05).

ID	Description	GeneRatio	BgRatio	p.adjust

GO:0099055	integral component of postsynaptic membrane	29/655	107/5792	0.0018
GO:0098936	intrinsic component of postsynaptic membrane	30/655	116/5792	0.0018
GO:0099572	postsynaptic specialization	59/655	337/5792	0.0171
GO:0043198	dendritic shaft	15/655	52/5792	0.0210
GO:0031301	integral component of organelle membrane	34/655	169/5792	0.0220
GO:0032590	dendrite membrane	10/655	31/5792	0.0496
GO:0034707	chloride channel complex	7/655	17/5792	0.0496

8.6 Camk2aCre WTAP KO: metabolite analysis full results

Summary of all results from the metabolite analysis for the mPFC (Table 26), dHPC (Table 27) and vHPC (Table 28).

Table 26: Camk2aCre WTAP KO: mPFC differentially regulated metabolites

The analysis was performed with metabolites for which a significant difference in the overall abundance was determined (FDR < 0.1).

Abbr.	**Name**	**p.adj.**	**L2FC**
CMP	CMP	0.0000	-1.1616
UMP	URIDINE-5-MONOPHOSPHATE	0.0000	-0.9747
NAD	NAD	0.0005	-1.7898
G6P	D-GLUCOSE 6-PHOSPHATE	0.0006	1.9691
F6P	D-FRUCTOSE 6-PHOSPHATE	0.0006	1.5541
ASP	D-ASPARTATE	0.0024	0.7370
GLY	GLYCINE	0.0056	0.7747
SER	L-SERINE	0.0096	-0.3397
LEU	LEUCINE	0.0127	0.5221
ADENOSINE	ADENOSINE	0.0253	0.4080
ADENINE	ADENINE	0.0254	0.8479
CIT	CITRULLINE	0.0326	-0.3335
ILE	L-ISOLEUCINE	0.0352	0.3910
URIDINE	URIDINE	0.0395	0.9451
UROCANATE	UROCANATE	0.0557	1.0103
4-GUANIDINOBUTANOATE	4-GUANIDINOBUTANOATE	0.0629	-0.4920
I	INOSINE	0.0665	0.5903
CYTIDINE	CYTIDINE	0.0665	0.5127
XAN	XANTHINE	0.0681	0.4887
GDP-mannose	GUANOSINE 5'-DIPHOSPHO-D-MANNOSE	0.0724	-0.2663

G1P	ALPHA-D-GLUCOSE 1-PHOSPHATE	0.0735	0.7693
OPH	OPHTHALMIC ACID	0.0836	-0.5668
PC(16:0/16:0)	PC(16:0/16:0)	0.0845	-0.5011
TML	NEPSILON,NEPSILON,NEPSILON-TRIMETHYLLYSINE	0.0845	-0.5264

Table 27: Camk2aCre WTAP KO: dHPC differentially regulated metabolites

The analysis was performed with metabolites for which a significant difference in the overall abundance was determined (FDR < 0.1).

Abbr.	Name	p.adj.	L2FC
NAD	NAD	0.0080	-1.3731
URIDINE	URIDINE	0.0189	0.5070
m1A	1-Methyladenosine	0.0189	-0.6068
SER	L-SERINE	0.0251	-0.4531
CMP	CMP	0.0251	-0.8802
INOSITOL	MYO-INOSITOL	0.0261	0.3995
F6P	D-FRUCTOSE 6-PHOSPHATE	0.0261	1.7054
CIT	CITRULLINE	0.0261	-0.6692
4-GUANIDINOBUTANOATE	4-GUANIDINOBUTANOATE	0.0261	-0.7908
Meglutol	3-HYDROXY-3-METHYLGLUTARATE	0.0261	-0.6868
G1P	ALPHA-D-GLUCOSE 1-PHOSPHATE	0.0393	1.8711
TML	NEPSILON,NEPSILON,NEPSILON-TRIMETHYLLYSINE	0.0519	-1.0987
ALA	D-ALANINE	0.0519	-0.3193
CREATINE	CREATINE	0.0519	-0.2339
5,6-DIHYDROURACIL	5,6-DIHYDROURACIL	0.0519	-0.3055
GLY	GLYCINE	0.0618	0.5005
GDP-mannose	GUANOSINE 5'-DIPHOSPHO-D-MANNOSE	0.0814	-0.9223
G6P	D-GLUCOSE 6-PHOSPHATE	0.0814	1.5870
ASP	D-ASPARTATE	0.0814	0.6041
AMP	ADENOSINE 5'-MONOPHOSPHATE	0.0814	-0.5518

Table 28: Camk2aCre WTAP KO: vHPC differentially regulated metabolites

The analysis was performed with metabolites for which a significant difference in the overall abundance was determined (FDR < 0.1).

Abbr.	Name	p.adj.	L2FC
CMP	CMP	0.0038	-1.0293
GLY	GLYCINE	0.0041	0.6221

UMP	URIDINE-5-MONOPHOSPHATE	0.0077	-0.7523
GUANOSINE	GUANOSINE	0.0077	0.6244
F6P	D-FRUCTOSE 6-PHOSPHATE	0.0120	1.5257
ASP	D-ASPARTATE	0.0120	0.5651
SER	L-SERINE	0.0140	-0.2379
G6P	D-GLUCOSE 6-PHOSPHATE	0.0265	1.7013
CYTIDINE	CYTIDINE	0.0334	0.5661
UROCANATE	UROCANATE	0.0429	0.6744
NAD	NAD	0.0442	-1.0463
DEOXYCYTIDINE	DEOXYCYTIDINE	0.0442	0.6856
URIDINE	URIDINE	0.0543	0.8248
G1P	ALPHA-D-GLUCOSE 1-PHOSPHATE	0.0543	0.8983
ADENINE	ADENINE	0.0663	0.7423
I	INOSINE	0.0740	0.4952
PC(16:0/16:0)	PC(16:0/16:0)	0.0789	-0.4179

8.7 NexCreERT2 expression validation using ISH

A representative example for the overlap of CreERT2 signal and the depletion of the floxed exon's signal (here *Wtap*) is shown in Figure 85.

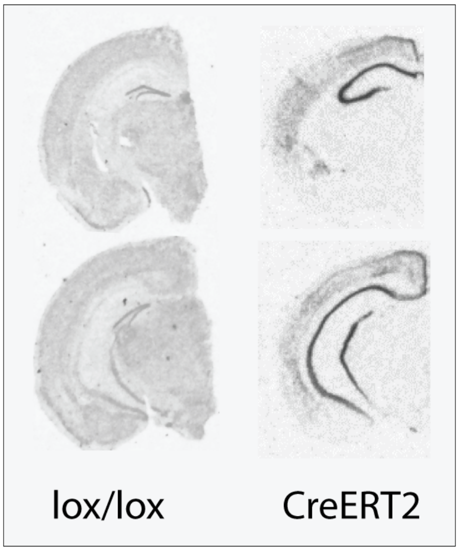

Figure 85: NexCreERT2 expression as detected with ISH

A representative example for the overlap of CreERT2 signal and the depletion of the floxed exon (here *Wtap*) after tamoxifen induction.

ISH probes

Overview of oligonucleotides used for ISH in the presented thesis (Table 29).

Table 29: ISH oligonucleotides used in this study

Oligonucleotides	Sequence	Source
ISH probe *Mettl3* exon 4 (175 bp)	TCAGTCAGGAGATCCTAGAGCTATT; CTGAAGTGCAGCTTGCGACA	28
ISH probe *Wtap* exon 4-7 (423bp)	GCATATGTTCAAGCTTTGGAGGG; CAGCTGCCTTCCAAGCTCTT	This thesis
ISH probe *Wtap* exon 4-5 (170bp)	GAAGCATATGTTCAAGCTTTGGAG; CACTCTTGCATCTCCTGCTCT	This thesis
ISH probe *Ythdc1* exon 4-8 (585bp)	CAGTGGTTCTTCTGAACAGGG; GGCAATGTGGACCATACACC	This thesis
ISH probe *Ythdc1* exon 5-7 (232bp)	AGAAAAAGAAGGAAAGGAAGAGAGC; TTGCTTTGGCAAGAGACACA	This thesis

8.8 Comparison of KO efficacy in bulk HPC, dHPC slices and dCA1

The efficacy of the NexCreERT2 induced KO of *Wtap* in the HPC was validated using qPCR for bulk HPC, dHPC slices and dissected dCA1 (Figure 86).

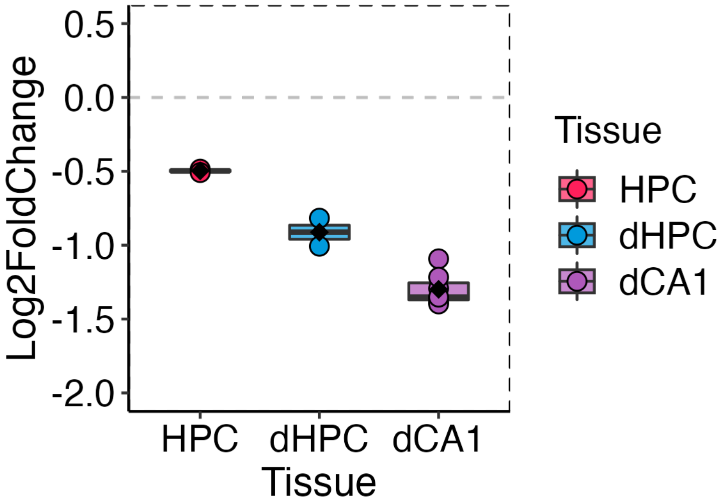

Figure 86: Comparison of *Wtap* KO efficacy in the HPC

qPCR validation of KO efficacy, comparing total HPC RNA to, dHPC and dissected dCA1. HPC = 2, dHPC = 2, dCA1 = 7. The WT expression level of *Wtap* is indicated by the dashed line.

8.9 NexCreERT2 WTAP KO: qPCR validation of LTP cohort

For the KO validation of animals used for the LTP experiment, the tissue was collected on dry ice after recordings. The dCA1 was punched using a cryostat, the RNA extracted and qPCR performed as described in the Methods section. The results of the validation are shown in Figure 87.

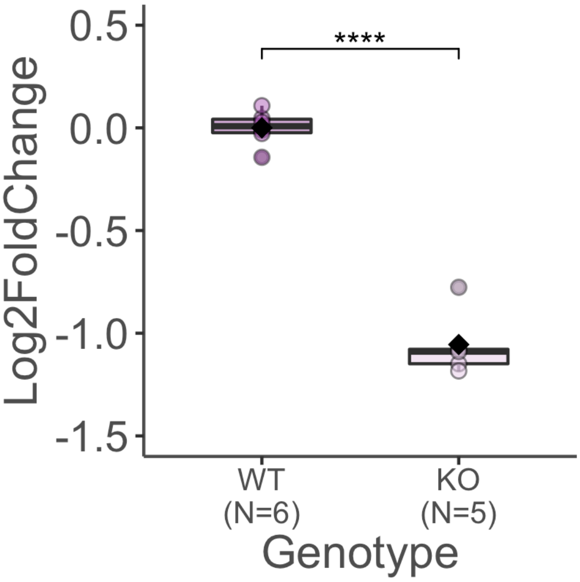

Figure 87: RT-qPCR validation of *Wtap* KO efficacy for the LTP cohort
The qPCR validation of the animals used for LTP recordings shows a clear depletion of the floxed *Wtap* exons (WT = 6, KO = 5; p.adj. < 0.001, independent two-sample t-test).

8.10 NexCreERT2 WTAP KO: DESeq2 GO full results

Summary of all results from the enrichment analysis for CC (Table 30) and MF (Table 31).

Table 30: NexCreERT2 WTAP KO: detailed results for CC (DESeq2)
The analysis was performed with genes for which a significant difference in the overall expression was detected (FDR < 0.05, Log2FoldChange ≥ 0.5, base mean ≥ 20), Reported below are the results p.adj. < 0.05.

ID	Description	GeneRatio	BgRatio	p.adj.
GO:0005887	integral component of plasma membrane	181/1659	944/13930	0.0000
GO:0034702	ion channel complex	51/1659	242/13930	0.0020
GO:1990351	transporter complex	51/1659	257/13930	0.0057
GO:0008076	voltage-gated potassium channel complex	18/1659	67/13930	0.0183

Table 31: NexCreERT2 WTAP KO: detailed results for MF (DESeq2)
The analysis was performed with genes for which a significant difference in the overall expression was detected (FDR < 0.05, Log2FoldChange ≥ 0.5, base mean ≥ 20), Reported below are the results p.adj. < 0.05.

ID	Description	GeneRatio	BgRatio	p.adj.
GO:0022843	voltage-gated cation channel activity	33/1638	113/13653	0.0002
GO:0005244	voltage-gated ion channel activity	40/1638	152/13653	0.0002
GO:0022832	voltage-gated channel activity	40/1638	152/13653	0.0002
GO:0004930	G protein-coupled receptor activity	50/1638	219/13653	0.0008
GO:0046873	metal ion transmembrane transporter activity	65/1638	323/13653	0.0016
GO:0004993	G protein-coupled serotonin receptor activity	10/1638	19/13653	0.0016

GO:0008146	sulfotransferase activity	13/1638	35/13653	0.0048

8.11 NexCreERT2 WTAP KO: DEXSeq GO full results

Summary of all results from the enrichment analysis for BP (Table 32), CC (Table 33) and MF (Table 34).

Table 32: NexCreERT2 WTAP KO: detailed results for BP (DEXSeq)

The analysis was performed with genes for which a significantly different exon usage had been observed (FDR < 0.05, Log2FoldChange ≥ 0.5, exon base mean ≥ 5). Reported below are the results p.adj. < 0.05.

ID	Description	GeneRatio	BgRatio	p.adj.
GO:0050808	synapse organization	114/1774	451/13808	0.0000
GO:0099536	synaptic signaling	143/1774	664/13808	0.0000
GO:0048812	neuron projection morphogenesis	135/1774	630/13808	0.0000
GO:0032990	cell part morphogenesis	141/1774	670/13808	0.0000
GO:0007416	synapse assembly	52/1774	174/13808	0.0000
GO:0000904	cell morphogenesis involved in differentiation	147/1774	717/13808	0.0000
GO:0051960	regulation of nervous system development	188/1774	977/13808	0.0000
GO:0051963	regulation of synapse assembly	39/1774	114/13808	0.0000
GO:0000902	cell morphogenesis	185/1774	975/13808	0.0000
GO:0050803	regulation of synapse structure or activity	69/1774	272/13808	0.0000
GO:0050807	regulation of synapse organization	67/1774	263/13808	0.0000
GO:0099177	regulation of trans-synaptic signaling	105/1774	484/13808	0.0000
GO:0010975	regulation of neuron projection development	120/1774	583/13808	0.0000
GO:0060322	head development	124/1774	610/13808	0.0000
GO:1902414	protein localization to cell junction	38/1774	122/13808	0.0000
GO:0007420	brain development	113/1774	559/13808	0.0001
GO:0120035	regulation of plasma membrane bounded cell projection organization	140/1774	734/13808	0.0001
GO:0001764	neuron migration	44/1774	165/13808	0.0002
GO:1901888	regulation of cell junction assembly	50/1774	199/13808	0.0002
GO:0022604	regulation of cell morphogenesis	101/1774	500/13808	0.0002
GO:0042391	regulation of membrane potential	81/1774	379/13808	0.0002
GO:0010769	regulation of cell morphogenesis involved in differentiation	73/1774	333/13808	0.0003
GO:0099003	vesicle-mediated transport in synapse	56/1774	242/13808	0.0006
GO:0060080	inhibitory postsynaptic potential	11/1774	20/13808	0.0008
GO:0030534	adult behavior	39/1774	150/13808	0.0009
GO:0034329	cell junction assembly	77/1774	370/13808	0.0009
GO:0050877	nervous system process	145/1774	811/13808	0.0012

GO:0007610	behavior	112/1774	596/13808	0.0013
GO:0099601	regulation of neurotransmitter receptor activity	21/1774	62/13808	0.0013
GO:0021954	central nervous system neuron development	25/1774	88/13808	0.0056
GO:0007612	learning	37/1774	154/13808	0.0066
GO:2000463	positive regulation of excitatory postsynaptic potential	14/1774	37/13808	0.0069
GO:0044087	regulation of cellular component biogenesis	150/1774	883/13808	0.0091
GO:0007215	glutamate receptor signaling pathway	24/1774	87/13808	0.0105
GO:0031644	regulation of nervous system process	36/1774	154/13808	0.0122
GO:0032688	negative regulation of interferon-beta production	8/1774	16/13808	0.0181
GO:0035176	social behavior	15/1774	46/13808	0.0204
GO:0051703	intraspecies interaction between organisms	15/1774	46/13808	0.0204
GO:0097479	synaptic vesicle localization	18/1774	61/13808	0.0224
GO:2001257	regulation of cation channel activity	35/1774	154/13808	0.0228
GO:1903539	protein localization to postsynaptic membrane	17/1774	57/13808	0.0265
GO:0010996	response to auditory stimulus	9/1774	21/13808	0.0293
GO:0016082	synaptic vesicle priming	10/1774	26/13808	0.0390
GO:0006836	neurotransmitter transport	44/1774	214/13808	0.0405

Table 33: NexCreERT2 WTAP KO: detailed results for CC (DEXSeq)
The analysis was performed with genes for which a significantly different exon usage had been observed (FDR < 0.05, Log2FoldChange ≥ 0.5, exon base mean ≥ 5). Reported below are the results p.adj. < 0.05.

ID	Description	GeneRatio	BgRatio	p.adj.
GO:0098978	glutamatergic synapse	123/1784	492/13930	0.0000
GO:0098794	postsynapse	157/1784	690/13930	0.0000
GO:0030424	axon	144/1784	655/13930	0.0000
GO:0032279	asymmetric synapse	99/1784	396/13930	0.0000
GO:0097060	synaptic membrane	101/1784	428/13930	0.0000
GO:0036477	somatodendritic compartment	172/1784	919/13930	0.0000
GO:0043025	neuronal cell body	125/1784	637/13930	0.0000
GO:0098685	Schaffer collateral-CA1 synapse	34/1784	110/13930	0.0000
GO:0043679	axon terminus	44/1784	163/13930	0.0000
GO:0097447	dendritic tree	125/1784	647/13930	0.0000
GO:0044297	cell body	135/1784	722/13930	0.0001
GO:0044306	neuron projection terminus	46/1784	184/13930	0.0001
GO:0098982	GABA-ergic synapse	30/1784	101/13930	0.0001
GO:0032589	neuron projection membrane	20/1784	63/13930	0.0014
GO:0030427	site of polarized growth	46/1784	204/13930	0.0014
GO:0071004	U2-type prespliceosome	8/1784	15/13930	0.0032

GO:0071010	prespliceosomeå	8/1784	15/13930	0.0032
GO:1990351	transporter complex	53/1784	257/13930	0.0040
GO:0060077	inhibitory synapse	10/1784	23/13930	0.0040
GO:0034702	ion channel complex	50/1784	242/13930	0.0053
GO:0008328	ionotropic glutamate receptor complex	15/1784	53/13930	0.0239
GO:0098831	presynaptic active zone cytoplasmic component	8/1784	20/13930	0.0245
GO:0098878	neurotransmitter receptor complex	15/1784	54/13930	0.0270
GO:0032809	neuronal cell body membrane	10/1784	30/13930	0.0313
GO:0060076	excitatory synapse	19/1784	77/13930	0.0323
GO:0034708	methyltransferase complex	23/1784	101/13930	0.0373

Table 34: NexCreERT2 WTAP KO: detailed results for MF (DEXSeq)
The analysis was performed with genes for which a significantly different exon usage had been observed (FDR < 0.05, Log2FoldChange ≥ 0.5, exon base mean ≥ 5). Reported below are the results p.adj. < 0.05.

ID	Description	GeneRatio	BgRatio	p.adj.
GO:0060589	nucleoside-triphosphatase regulator activity	59/1753	281/13653	0.0312
GO:0019904	protein domain specific binding	126/1753	717/13653	0.0312
GO:0035254	glutamate receptor binding	20/1753	66/13653	0.0312
GO:0022843	voltage-gated cation channel activity	29/1753	113/13653	0.0312
GO:0022836	gated channel activity	51/1753	242/13653	0.0312
GO:0042054	histone methyltransferase activity	17/1753	55/13653	0.0312
GO:0015085	calcium ion transmembrane transporter activity	27/1753	107/13653	0.0312
GO:0005244	voltage-gated ion channel activity	35/1753	152/13653	0.0312
GO:0022832	voltage-gated channel activity	35/1753	152/13653	0.0312
GO:0016773	phosphotransferase activity, alcohol group as acceptor	104/1753	596/13653	0.0446
GO:0043425	bHLH transcription factor binding	10/1753	26/13653	0.0452
GO:0005246	calcium channel regulator activity	12/1753	35/13653	0.0452

8.12 Membranome preparation: enrichment for membrane associated terms

An enrichment analysis for the proteins detected in the membranome preparation was performed to determine the success of the enrichment. For this all detected proteins (2594) were use as input and the genes detected in the mRNA sequencing as background (15826). The analysis was run for CC and the results for p.adj. < 0.05 are shown in Figure 88.

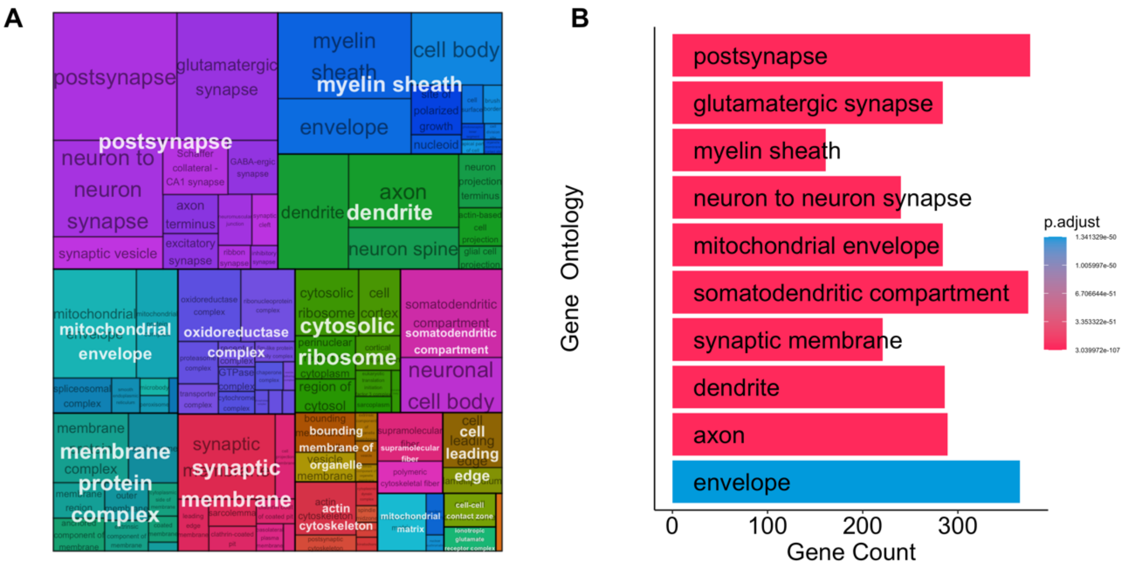

Figure 88: Strong enrichment for membrane related cellular components in the membranome isolation **(A**) Overview of the GO results for CC after application of semantic similarity analysis. Among the emerging topics are membrane associated terms such as post synapse, myelin sheath, dendrite and membrane protein complex. **(B)** Bar plot showing the number of significantly differentially expressed genes associated with individual GO terms and their respective q-value.

8.13 NexCreERT2 WTAP KO: GAM model details for cue and contextual fear memory analysis

Overview of GAM model results from the cue (Table 35) and context memory tests (Table 36).

Table 35: NexCreERT2 WTAP KO: summary of the GAM model for cue memory
ns = not significant, *: p < 0.05. **: p < 0.01, ***: p < 0.001, ****: p < 0.0001.

Effect	Estimate	Std. Error	CI.l	CI.u	z value	Pr(>|z|)	Symbol
(Intercept)	0.79	0.91	-1.02	2.61	0.87	0.382	ns
GenotypeKO	-0.10	0.90	-1.91	1.71	-0.11	0.914	ns
Formula: Freezing ~ Genotype + s(Time, by = Tone) + s(Animal, bs = "re")							

Table 36: NexCreERT2 WTAP KO: summary of the GAM model for contextual memory
ns = not significant, *: p < 0.05. **: p < 0.01, ***: p < 0.001, ****: p < 0.0001.

Effect	Estimate	Std. Error	CI.l	CI.u	z value	Pr(>|z|)	Symbol
(Intercept)	1.32	0.40	0.51	2.13	3.27	0.00108	**
GenotypeKO	0.01	0.56	-1.11	1.13	0.01	0.98860	ns
Formula: Freezing ~ Genotype + s(Time) + s(Animal, bs = "re")							

8.14 NexCreERT2 WTAP METTL3 KO: GAM model details for cue and contextual fear memory analysis

Overview of GAM model results from the cue (Table 37) and context memory tests (Table 38).

Table 37: NexCreERT2 WTAP-METTL3 KO: summary of the GAM model for cue memory
ns = not significant, *: $p < 0.05$. **: $p < 0.01$, ***: $p < 0.001$, ****: $p < 0.0001$.

Effect	Estimate	Std. Error	CI.l	CI.u	z value	Pr(>|z|)	Symbol
(Intercept)	-1.95	3.50	-8.96	5.05	-0.56	0.577	ns
GenotypeKO	-0.34	0.84	-2.02	1.33	-0.41	0.681	ns
Formula: Freezing ~ Genotype + s(Time, by = Tone) + s(Animal, bs = "re")							

Table 38: NexCreERT2 WTAP-METTL3 KO: summary of the GAM model for contextual memory
ns = not significant, *: $p < 0.05$. **: $p < 0.01$, ***: $p < 0.001$, ****: $p < 0.0001$.

Effect	Estimate	Std. Error	CI.l	CI.u	z value	Pr(>|z|)	Symbol
(Intercept)	-0.24	0.63	-1.49	1.02	-0.38	0.705	ns
GenotypeKO	0.30	0.87	-1.44	2.04	0.35	0.730	ns
Formula: Freezing ~ Genotype + s(Time) + s(Animal, bs = "re")							

8.15 Camk2aCre YTHDC1 weight at P15 and week 12

Several litters of YTHDC1 animals were weighed before weaning (P15) to determine whether the observed differences in the weight of KO animals are already present before the onset of Camk2aCre expression. Here, no genotype driven difference in weight was determined for either sex (males: p = 0.96, independent two-sample t-test; females: p = 0.74, independent two-sample t-test). In addition, a group of adult males was weighed at 12 weeks of age to see whether the differences in weight that were observed between weeks 4-8 are retained throughout adulthood. At 12 weeks of age, no difference in the weight of WT and KO males was detected (p = 0.12, independent two-sample t-test). The results are shown in Figure 89.

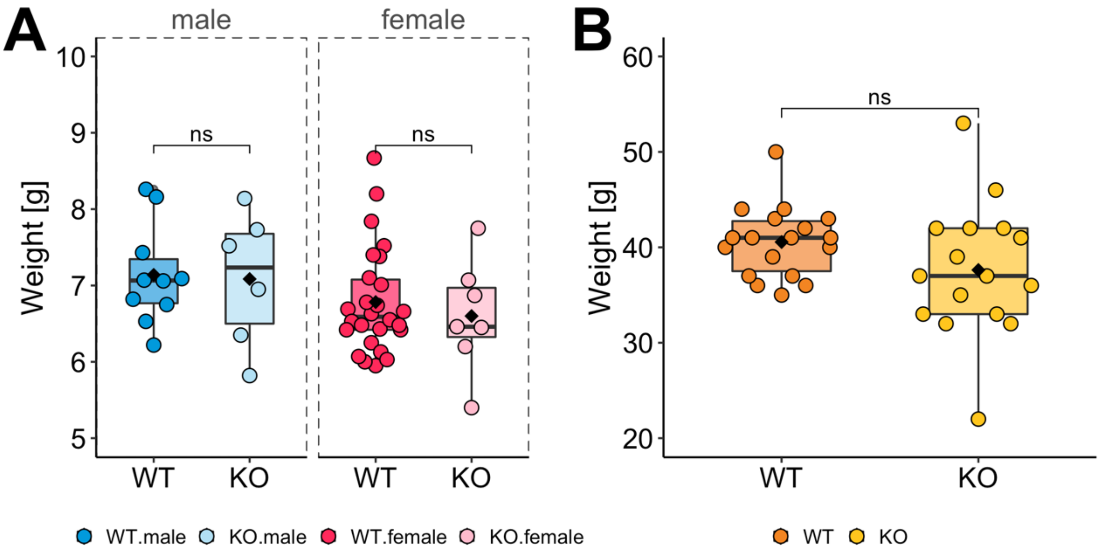

Figure 89: YTHDC1 weight at P15 and week 12

(A) Weight of males and females before the onset of Camk2aCre expression at P15 (males: WT = 10, KO = 6, KO; females WT = 26, KO = 7, KO). **(B)** Weight of male animals at 12 weeks of age (WT = 18, KO = 16).

8.16 Camk2aCre YTHDC1 KO: GAM model details for cue and contextual fear memory analysis

Overview of GAM model results from the cue (Table 39) and context memory tests (Table 40).

Table 39: Camk2aCre YTHDC1 KO: summary of the GAM model for cue memory

ns = not significant, *: p < 0.05. **: p < 0.01, ***: p < 0.001, ****: p < 0.0001.

Effect	**Estimate**	**Std. Error**	**CI.l**	**CI.u**	**z value**	**Pr(>|z|)**	**Symbol**
(Intercept)	0.71	4.86	-9.01	10.44	0.15	$8.84e^{-01}$	ns
GenotypeKO	-1.70	0.23	-2.16	-1.25	-7.52	$5.54e^{-14}$	****
Sexfemale	-1.01	6.77	-14.55	12.54	-0.15	$8.82e^{-01}$	ns
GenotypeKO:Sexfemale	1.31	0.28	0.76	1.87	4.72	$2.41e^{-06}$	****
Formula: Freezing ~ Genotype * Sex + s(Time, by = Tone) + s(Animal, bs = "re")							

Table 40: Camk2aCre YTHDC1 KO: summary of the GAM model for context memory

ns = not significant, *: p < 0.05. **: p < 0.01, ***: p < 0.001, ****: p < 0.0001.

Effect	**Estimate**	**Std. Error**	**CI.l**	**CI.u**	**z value**	**Pr(>|z|)**	**Symbol**
(Intercept)	-2.09	3.40	-8.89	4.71	-0.62	$5.38e^{-01}$	ns
GenotypeKO	-2.27	0.30	-2.88	-1.66	-7.46	$8.36e^{-14}$	****
Sexfemale	-0.40	4.79	-9.97	9.18	-0.08	$9.34e^{-01}$	ns
GenotypeKO:Sexfemale	2.70	0.35	2.00	3.41	7.65	$2.08e^{-14}$	****
Formula: Freezing ~ Genotype * Sex + s(Time) + s(Animal, bs = "re")							

8.17 Camk2aCre YTHDC1 KO: patch clamp recordings full results

Summary of the results from the patch clamp recordings of layer V pyramidal neurons in the mPFC (Table 41).

Table 41: Camk2aCre YTHDC1 KO: all parameters measured in layer V pyramidal neurons of the mPFC

measurement	mean ± sd [WT = 23]	mean ± sd [KO = 24]	test	p-adj.	symbol
AP amplitude [mV]	66.6 ± 7.15	58.88 ± 10.7	t-test	0.021	*
AP half-width [ms]	0.87 ± 0.12	1.05 ± 0.18	Wilcox	0.005	**
CN [pF]	146.48 ± 23.96	162.58 ± 33.15	t-test	0.117	ns
fAHP [mV]	9.97 ± 4.15	11.5 ± 4.74	t-test	0.336	ns
AP overshoot [mV]	22.83 ± 6.03	20.08 ± 8.47	Welch	0.325	ns
Rheobase [pA]	90.57 ± 25.07	106.75 ± 20.52	t-test	0.042	*
Rin [MΩ]	228.37 ± 49.76	220.91 ± 48.28	Wilcox	0.494	ns
Vrest [mV]	-80.13 ± 6.9	-79 ± 6.92	Wilcox	0.425	ns
Rs [MΩ]	8.61 ± 0.14	8.63 ± 0.2	Wilcox	0.831	ns
AP threshold [mV]	-43.77 ± 2.85	-38.79 ± 6.09	Welch	0.005	**
AP undershoot [mV]	-53.74 ± 3.88	-50.29 ± 4.76	t-test	0.026	*

8.18 YTHDC1 Camk2aCre KO: metabolite analysis full results

Summary of all results from the metabolite analysis for the mPFC (Table 42) and dHPC (Table 43).

Table 42: Camk2aCre YTHDC1 KO: mPFC differentially regulated metabolites

The analysis was performed with metabolites for which a significant difference in the overall abundance was determined (FDR < 0.1).

abbr.	name	p.adj.	L2FC
D-ASPARTATE	D-ASPARTATE	0.0026	-0.8705
ALPHA-D-GALACTOSE 1-PHOSPHATE	ALPHA-D-GALACTOSE 1-PHOSPHATE	0.0027	1.4457
D-GLUCOSE 6-PHOSPHATE	D-GLUCOSE 6-PHOSPHATE	0.0194	0.2117
MYO-INOSITOL	MYO-INOSITOL	0.0434	-0.3449
BETAINE	BETAINE	0.0467	-0.3127
L-SERINE	L-SERINE	0.0690	0.2762
FUMARATE	FUMARATE	0.0755	0.4091
D-FRUCTOSE 6-PHOSPHATE	D-FRUCTOSE 6-PHOSPHATE	0.0755	1.1207

Table 43: Camk2aCre YTHDC1 KO: dHPC differentially regulated metabolites

The analysis was performed with metabolites for which a significant difference in the overall abundance was determined (FDR < 0.1).

abbr.	Name	p.adj.	L2FC

D-ASPARTATE	D-ASPARTATE	0.0017	0.3683
L-CYSTATHIONINE	L-CYSTATHIONINE	0.0017	0.6583
XANTHINE	XANTHINE	0.0360	0.5525
MYO-INOSITOL	MYO-INOSITOL	0.0360	-0.8220
ADENOSINE	ADENOSINE	0.0369	-0.8503
N-ACETYL-D-GLUCOSAMINE	N-ACETYL-D-GLUCOSAMINE	0.0496	-0.7583
ALLANTOIN	ALLANTOIN	0.0647	-0.7995
HYPOXANTHINE	HYPOXANTHINE	0.0647	-0.6692
CREATININE	CREATININE	0.0647	-0.3289
URACIL	URACIL	0.0647	-0.3575
URIDINE	URIDINE	0.0871	-0.7214

8.19 NexCreERT2 YTHDC1 KO: DESeq2 GO full results

Summary of all results from the enrichment analysis for BP (Table 44), CC (Table 45) and MF (Table 46).

Table 44: NexCreERT2 YTHDC1 KO: detailed results for BP (DESeq2)

The analysis was performed with genes for which a significant difference in the overall expression was detected (FDR < 0.05, Log2FoldChange ≥ 0.5, base mean ≥ 20), Reported below are the results p.adj. < 0.05.

ID	Description	GeneRatio	BgRatio	p.adjust
GO:0098742	cell-cell adhesion via plasma-membrane adhesion molecules	19/487	169/13919	0.0253

Table 45: NexCreERT2 YTHDC1 KO: detailed results for CC (DESeq2)

The analysis was performed with genes for which a significant difference in the overall expression was detected (FDR < 0.05, Log2FoldChange ≥ 0.5, base mean ≥ 20), Reported below are the results p.adj. < 0.05.

ID	Description	GeneRatio	BgRatio	p.adjust
GO:0005887	integral component of plasma membrane	75/489	966/14045	0.0000

Table 46: NexCreERT2 YTHDC1 KO: detailed results for MF (DESeq2)

The analysis was performed with genes for which a significant difference in the overall expression was detected (FDR < 0.05, Log2FoldChange ≥ 0.5, base mean ≥ 20), Reported below are the results p.adj. < 0.05.

ID	Description	GeneRatio	BgRatio	p.adjust
GO:0005216	ion channel activity	24/472	314/13767	0.0464
GO:0005261	cation channel activity	20/472	253/13767	0.0464
GO:0022843	voltage-gated cation channel activity	12/472	113/13767	0.0464
GO:0005249	voltage-gated potassium channel activity	9/472	68/13767	0.0464

GO:0015267	channel activity	24/472	334/13767	0.0464
GO:0022803	passive transmembrane transporter activity	24/472	334/13767	0.0464

8.20 NexCreERT2 YTHDC1 KO: DEXSeq GO full results

Summary of all results from the enrichment analysis for BP (Table 47) and CC (Table 48).

Table 47: NexCreERT2 YTHDC1 KO: detailed results for BP (DEXSeq)
The analysis was performed with genes for which a significantly different exon usage had been observed (FDR < 0.05, Log2FoldChange ≥ 0.5, exon base mean ≥ 5). Reported below are the results p.adj. < 0.05.

ID	Description	GeneRatio	BgRatio	p.adjust
GO:1903311	regulation of mRNA metabolic process	35/955	235/13919	0.0469

Table 48: NexCreERT2 YTHDC1 KO: detailed results for CC (DEXSeq)
The analysis was performed with genes for which a significantly different exon usage had been observed (FDR < 0.05, Log2FoldChange ≥ 0.5, exon base mean ≥ 5). Reported below are the results p.adj. < 0.05.

ID	Description	GeneRatio	BgRatio	p.adjust
GO:0098984	neuron to neuron synapse	51/962	423/14045	0.0143
GO:0098686	hippocampal mossy fiber to CA3 synapse	12/962	47/14045	0.0143
GO:0098978	glutamatergic synapse	56/962	493/14045	0.0211
GO:0014069	postsynaptic density	46/962	392/14045	0.0302

8.21 NexCreERT2 YTHDC1 KO: GAM model details for cue and contextual fear memory analysis

Overview of GAM model results from the cue (Table 49) and context memory tests (Table 50).

Table 49: NexCreERT2 YTHDC1 KO: summary of the GAM model for cue memory
ns = not significant, *: p < 0.05. **: p < 0.01, ***: p < 0.001, ****: p < 0.0001.

Effect	Estimate	Std. Error	CI.l	CI.u	z value	Pr(>|z|)	Symbol
(Intercept)	4.85	3.24	-1.63	11.34	1.50	0.134	ns
GenotypeKO	0.92	0.81	-0.69	2.54	1.15	0.251	ns
Formula: Freezing ~ Genotype + s(Time, by = Tone) + s(Animal, bs = "re")							

Table 50: NexCreERT2 YTHDC1 KO: summary of the GAM model for context memory

ns = not significant, *: p < 0.05. **: p < 0.01, ***: p < 0.001, ****: p < 0.0001.

Effect	Estimate	Std. Error	CI.l	CI.u	z value	Pr(>|z|)	Symbol
(Intercept)	1.16	0.79	-0.42	2.74	1.47	0.141	ns
GenotypeKO	0.55	1.07	-1.60	2.69	0.51	0.611	ns
Formula: Freezing ~ Genotype + s(Time) + s(Animal, bs = "re")							

9. List of figures

Figure 1: The flow of genetic information from DNA to protein..2
Figure 2: Research into N^6-Methyladenosine has exponentially grown since 2010 3
Figure 3: The conversion of adenosine to N^6-methyladenosine by ‘writers’ and the removal through ‘erasers’ 5
Figure 4: Overview of the m^{6}A regulation by ‘writers’, ‘readers’ and ‘erasers’ 7
Figure 5: Tentative roles of m^{6}A in regulating neuronal functions 15
Figure 6: Fresh tissue dissection for molecular analysis..22
Figure 7: Differential exon usage analyzed with the DEXSeq R package 29
Figure 8: Camk2aCre expression across the adult mouse brain..38
Figure 9: Camk2aCre WTAP KO juvenile males show decreased weight................................39
Figure 10: WTAP Camk2aCre WT KO animals show altered circadian activity dynamics.........41
Figure 11: Camk2aCre-Ai9 labelling of the suprachiasmatic nucleus.......................................42
Figure 12: Camk2aCre WTAP KO animals in the open field test 43
Figure 13: Camk2aCre WTAP KO animals in the EPM test..44
Figure 14: Camk2aCre WTAP KO animals in the DL test...45
Figure 15: Camk2aCre WTAP KO results in volumetric changes in the thalamus and auditory cortex 46
Figure 16: WTAP KO animals show a dysregulated proteome in the mPFC, dHPC and vHPC.47
Figure 17: Detailed overview of proteomic changes in the mPFC, dHPC and vHPC of WTAP KO animals...47
Figure 18: Downregulated proteins in the mPFC of WTAP KOs are enriched for mitochondrial processes 48
Figure 19: Downregulated proteins in the mPFC of WTAP KOs are enriched for mitochondrial compartments..49
Figure 20: Downregulated proteins in the mPFC of WTAP KOs are enriched for mitochondrial functions 49
Figure 21: Downregulated proteins in the dHPC of WTAP KOs are enriched for mitochondrial processes 50
Figure 22: Downregulated proteins in the dHPC of WTAP KOs are enriched for mitochondrial compartments..50
Figure 23: Downregulated proteins in the dHPC of WTAP KOs are enriched for mitochondrial functions 51
Figure 24: Downregulated proteins in the vHPC of WTAP KOs are enriched for mitochondrial compartments..51
Figure 25: Upregulated proteins in the vHPC of WTAP KOs are enriched for neuron-specific terms 52
Figure 26: Downregulation of mitoribosome components in the mPFC of WTAP KO animals...52
Figure 27: Mitochondrial encoded proteins are downregulated in WTAP KO tissue..................53
Figure 28: WTAP KO effects on respiratory chain components in the mPFC of WTAP KO animals 54
Figure 29: Differential abundance of m^{6}A ‘regulators’ and ‘readers’ in WTAP KO animals........55
Figure 30: Differential regulation of synaptic scaffolding molecules 55
Figure 31: Metabolic dysregulation in Camk2aCre WTAP KO brains 56
Figure 32: Tamoxifen induces NexCreERT2 recombination in projection neurons of the cortex and HPC...58
Figure 33: Tamoxifen treatment of NexCreERT2-*Wtap* animals results in a depletion of the floxed exons and WTAP protein 59
Figure 34: WTAP depletion in the dCA1 reduces m^{6}A levels...60
Figure 35: Sequenced samples show strong correlation within genotypes and clear separation in PC space...61

Figure 36: WTAP KO results in a massive transcriptional shift in the dCA1 62
Figure 37: Differentially expressed genes in WTAP KOs are enriched for integral components of the plasma membrane 63
Figure 38: Differentially expressed genes in WTAP KOs are enriched for voltage-gated ion channels and G protein-coupled receptors 63
Figure 39: WTAP regulates expression of the m^{6}A ‘writer complex’ components and m^{6}A ‘readers’ 64
Figure 40: WTAP-METTL3 double KO effects on gene expression of m^{6}A regulators and ‘readers’ 65
Figure 41: NexCreERT2 activity does not alter gene expression in WT animals.......................66
Figure 42: WTAP KO results in large scale changes in exon usage 67
Figure 43: Differentially expressed exons in WTAP KOs are enriched for biological processes associated with synaptic functions and morphogenesis 68
Figure 44: Differentially expressed exons in WTAP KOs are enriched for neuron specific cellular components...68
Figure 45: Differentially expressed exons in WTAP KOs are enriched for calcium transport and voltage-gated channel activity 69
Figure 46: The depletion of WTAP alters the composition of the membranome........................70
Figure 47: qPCR validation of differentially expressed membrane associated proteins.............71
Figure 48: NexCreERT2 WTAP KO animals exhibit increased LTP in the dHPC......................72
Figure 49: Wtap-NexCreERT2 KO animals show normal delay fear memory 73
Figure 50: Double KO *Wtap-Mettl3*-NexCreERT2 animals exhibit normal cue and contextual fear memory 74
Figure 51: NexCreERT2 WTAP KO animals show normal learning in the MWM test................76
Figure 52: Breeding impairments and premature death in YTHDC1 Camk2aCre KO females ..78
Figure 53: Reduced weight in juvenile YTHDC1 KO animals 79
Figure 54: YTHDC1 Camk2aCre KO animals exhibit a decreased survival probability in adulthood 80
Figure 55. YTHDC1 KO males and females exhibit normal behavior in the open field test........82
Figure 56: YTHDC1 KO animals spent an increased duration in the open arm of the EPM.......83
Figure 57: YTHDC1 KO animals spent more time in the dark in the DL test 84
Figure 58: *Ythdc1*-Camk2aCre KO animals don’t show impairments of vision in the visible platform training...85
Figure 59: YTHDC1 Camk2aCre KO animals show differences in the fear conditioning response 87
Figure 60: Camk2aCre YTHDC1 KO results in reduced gray matter volume in PFC and dHPC88
Figure 61: Camk2aCre YTHDC1 KO animals show a reduced excitability of layer V pyramidal neurons in the mPFC...89
Figure 62: YTHDC1 Camk2aCre KO animals show altered protein abundance in the mPFC, dHPC and vHPC...90
Figure 63: Detailed overview of changes observed in the LC-MS proteomic screening of YTHDC1 KO in the mPFC, dHPC and vHPC...90
Figure 64: YTHDC1 Camk2aCre KO animals have normal levels of mitoribosomal proteins in the mPFC...91
Figure 65: YTHDC1 KO animals show minor changes in the composition of respiratory chain complex..92
Figure 66: Metabolic dysregulation in Camk2aCre YTHDC1 KO animals 93
Figure 67: Overlap of differentially regulated metabolites across brain regions for WTAP and YTHDC1 KOs 94
Figure 68: Tamoxifen treatment of NexCreERT2 carrying animals results in a depletion of the floxed *Ythdc1* exons...95
Figure 69: Sequenced samples show strong correlation within genotypes and clear separation in PC space...96

Figure 70: YTHDC1 KO animals show a strong shift in gene expression in the dCA1...............97
Figure 71: Differentially expressed genes in YTHDC1 KOs are enriched for ion channels activity 98
Figure 72: YTHDC1 KO results in large scale changes in exon usage 99
Figure 73: Differentially expressed exons in YTHDC1 KOs are enriched for synaptic genes...100
Figure 74: Open field test of NexCreERT2 YTHDC1 KO animals...101
Figure 75: Open field test of NexCreERT2 YTHDC1 KO animals...102
Figure 76: NexCreERT2 YTHDC1 KO animals show normal cue and contextual fear memory103
Figure 77: Thalamocortical and corticothalamic connectivity in the mouse brain.....................110
Figure 78: Disrupted circadian activity of WTAP KO animals 111
Figure 79: Graphical summary of the main findings from the characterization of WTAP KOs..114
Figure 80: Unexplained sudden death in adult YTHDC1 KO animals 116
Figure 81: Graphical summary of the main findings from the characterization of YTHDC1 KOs121
Figure 82: Locus and genotyping of *Mettl3* tm1c and genotyping of Ai9 142
Figure 83: Locus and genotyping of *Wtap* tm1c animals and genotyping of NexCreERT2......143
Figure 84: Locus and genotyping of *Ythdc1* tm1c animals and genotyping of Camk2aCre 144
Figure 85: NexCreERT2 expression as detected with ISH 154
Figure 86: Comparison of *Wtap* KO efficacy in the HPC 155
Figure 87: RT-qPCR validation of *Wtap* KO efficacy for the LTP cohort 156
Figure 88: Strong enrichment for membrane related cellular components in the membranome isolation 160
Figure 89: YTHDC1 weight at P15 and week 12..162

10. List of tables

Table 1: Genotyping of *Mettl3* 142
Table 2: Genotyping for Ai9 142
Table 3: Genotyping for *Wtap* 143
Table 4: Genotyping for NexCreERT2 143
Table 5: Genotyping for *Ythdc1* 144
Table 6: Genotyping for *Ythdc1* tm1d allele 144
Table 7: Genotyping for Camk2aCre 144
Table 8: Packages used for data wrangling in R 145
Table 9: Packages used for statistical analysis in R 145
Table 10: Packages used for pathway analysis in R 145
Table 11: Packages used for data visualization in R 146
Table 12: Reagents used for immunostaining and histology 146
Table 13: Regents used for RNA extraction and quality control 146
Table 14: Reagent used for RT-qPCR and sequencing 147
Table 15: RT-qPCR primers used in this study 147
Table 16: Overview of the parameter estimates for home cage activity 148
Table 17: Overview of the smooth term estimates for home cage activity 148
Table 18: Camk2aCre WTAP KO: mPFC detailed results for BP 149
Table 19: Camk2aCre WTAP KO: mPFC detailed results for CC 149
Table 20: Camk2aCre WTAP KO: mPFC detailed results for MF 150
Table 21: Camk2aCre WTAP KO: dHPC detailed results for BP 150
Table 22: Camk2aCre WTAP KO: dHPC detailed results for CC 150
Table 23: Camk2aCre WTAP KO: dHPC detailed results for MF 151
Table 24: Camk2aCre WTAP KO: vHPC detailed results for CC (down) 151
Table 25:Camk2aCre WTAP KO: vHPC detailed results for CC (UP) 151
Table 26: Camk2aCre WTAP KO: mPFC differentially regulated metabolites 152
Table 27: Camk2aCre WTAP KO: dHPC differentially regulated metabolites 153
Table 28: Camk2aCre WTAP KO: vHPC differentially regulated metabolites 153
Table 29: ISH oligonucleotides used in this study 155
Table 30: NexCreERT2 WTAP KO: detailed results for CC (DESeq2) 156
Table 31: NexCreERT2 WTAP KO: detailed results for MF (DESeq2) 156
Table 32: NexCreERT2 WTAP KO: detailed results for BP (DEXSeq) 157
Table 33: NexCreERT2 WTAP KO: detailed results for CC (DEXSeq) 158
Table 34: NexCreERT2 WTAP KO: detailed results for MF (DEXSeq) 159
Table 35: NexCreERT2 WTAP KO: summary of the GAM model for cue memory 160
Table 36: NexCreERT2 WTAP KO: summary of the GAM model for contextual memory 160
Table 37: NexCreERT2 WTAP-METTL3 KO: summary of the GAM model for cue memory 161
Table 38: NexCreERT2 WTAP-METTL3 KO: summary of the GAM model for contextual memory 161
Table 39: Camk2aCre YTHDC1 KO: summary of the GAM model for cue memory 162
Table 40: Camk2aCre YTHDC1 KO: summary of the GAM model for context memory 162
Table 41: Camk2aCre YTHDC1 KO: all parameters measured in layer V pyramidal neurons of the mPFC 163
Table 42: Camk2aCre YTHDC1 KO: mPFC differentially regulated metabolites 163
Table 43: Camk2aCre YTHDC1 KO: dHPC differentially regulated metabolites 163
Table 44: NexCreERT2 YTHDC1 KO: detailed results for BP (DESeq2) 164
Table 45: NexCreERT2 YTHDC1 KO: detailed results for CC (DESeq2) 164
Table 46: NexCreERT2 YTHDC1 KO: detailed results for MF (DESeq2) 164

Table 47: NexCreERT2 YTHDC1 KO: detailed results for BP (DEXSeq)................................165
Table 48: NexCreERT2 YTHDC1 KO: detailed results for CC (DEXSeq) 165
Table 49: NexCreERT2 YTHDC1 KO: summary of the GAM model for cue memory..............165
Table 50: NexCreERT2 YTHDC1 KO: summary of the GAM model for context memory 166

11. Declaration of author contributions

Project conceptualization: Fabian Stamp, Alon Chen, Elisabeth Binder

Tissue dissections: Fabian Stamp

mRNA Seq. experiments: Fabian Stamp

mRNA Seq. data processing (DESeq, DEXSeq): Eviatar Weizman

mRNA Seq. downstream data analyses and visualization (enrichment, etc.): Fabian Stamp

Primer design: Fabian Stamp

RT-qPCR: Fabian Stamp, Laura Pohlenz

MRI: Fabian Stamp, Daniel Heinz, Lea Bartmann, Tibor Stark

Electrophysiology: Danusa Menegaz, Silvio Calcagnini, Mathias Eder, Fabian Stamp (statistics and visualization)

Animal behavior: Fabian Stamp

Immunostaining: Fabian Stamp

m^{6}A quantification: Fabian Stamp

Microscopy: Fabian Stamp, Laura Pohlenz

ISH: Fabian Stamp, Carola Eggert

Western Blot: Fabian Stamp

Proteomic Screening: Fabian Stamp, Daniel Heinz, Andreas Zellner, Nils Gassen

Metabolomics Screening: Jinqiu Xiao (analysis), Fabian Stamp (visualization and interpretation)

Dissertation writing and graphics: Fabian Stamp